Multi component Bose-Einstein condensates

From mean field physics to strong correlations

Dissertation
zur Erlangung des Doktorgrades
des Departments Physik
der Universität Hamburg

vorgelegt von
Christoph Becker
aus Lahnau

Hamburg
2008

Gutachterin/Gutachter der Dissertation:	Prof. Dr. Klaus Sengstock Prof. Dr. Werner Neuhauser
Gutachter der Disputation:	Prof. Dr. Klaus Sengstock Prof. Dr. Günter Huber
Datum der Disputation:	28.01.2009
Vorsitzender des Prüfungsausschusses:	Dr. Klaus Petermann
Vorsitzender des Promotionsausschusses:	Prof. Dr. Robert Klanner
Dekan der Fakultät für Mathematik, Informatik und Naturwissenschaften:	Prof. Dr. Arno Frühwald

Für Lotta

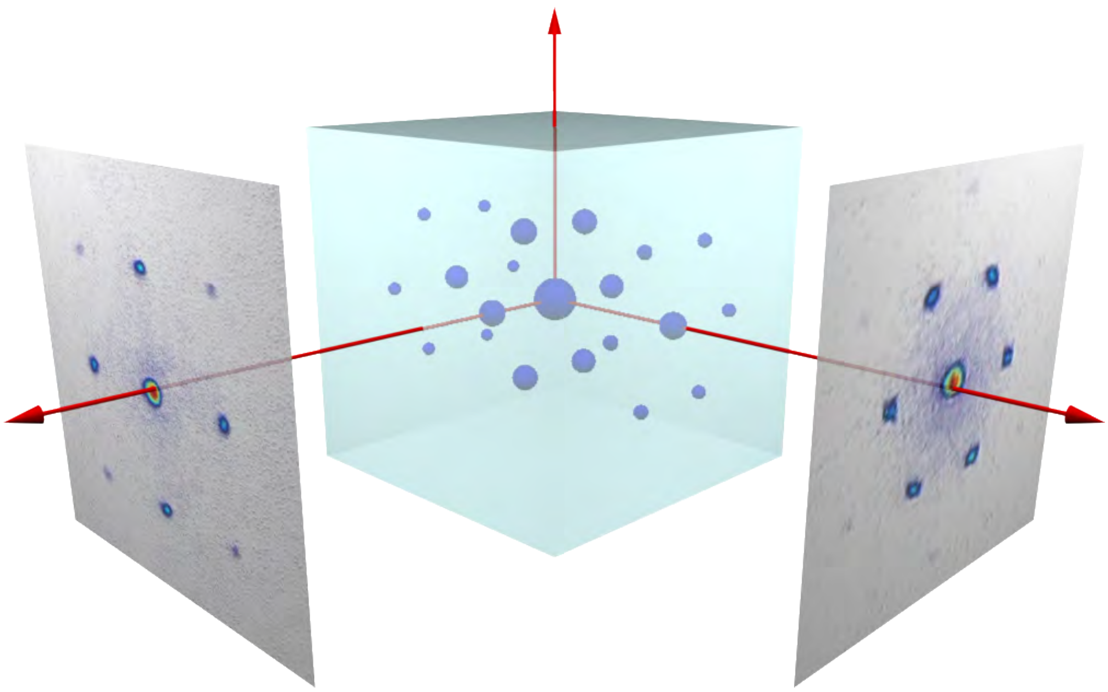

Zusammenfassung

Die Physik ultrakalter Quantengase stellt sich heutzutage als ein hochaktives und vielseitiges Forschungsfeld dar. Im Rahmen dieser Dissertation konnten fundamentale Erkenntnisse zu unterschiedlichen Phänomenen in Bose-Einstein Kondensaten gewonnen werden, welche völlig verschiedenen Wechselwirkungsbereichen zuzuordnen sind.

Erstmals wurden Experimente durchgeführt, die als eines der Paradigmen nichtlinearer Physik die Dynamik extrem langlebiger dunkler Solitonen zeigen. Solitonen, die sich als formstabile Wellenpakete auszeichnen, resultieren aus einer Kompensation der Dispersion durch eine entgegengerichtet wirkende nichtlineare Wechselwirkung. Oszillationen von dunklen Solitonen in elongierten Bose-Einstein Kondensaten wurden beobachtet und eine sehr gute Übereinstimmung mit der theoretisch erwarteten Oszillationsfrequenz von $\omega/\sqrt{2}$ wurde gefunden. Desweiteren konnten im Verlauf dieser Arbeit Experimente durchgeführt werden, bei denen die Kollisionen unterschiedlich tiefer dunkler Solitonen untersucht wurden. Es war dadurch möglich die Solitonen über den Kollisionszeitpunkt hinaus zu verfolgen. Als ein zentrales Ergebnis wurde gezeigt, dass Solitonen sich im Verlauf der Kollision durchdringen ohne einen nennenswerten Einfluss aufeinander auszuüben, was in Übereinstimmung mit der theoretischen Beschreibung von Solitonen als schwach wechselwirkende Quasiteilchen steht. Darüber hinaus konnten diese Studien durch Untersuchungen an 'gefüllten' Solitonen abgerundet werden.

Als ein wesentliches Forschungsziel wurde im Verlauf dieser Dissertation ein optisches Gitter mit einer Dreieckssymmetrie aufgebaut, um die experimnetelle Grundlage für die Untersuchung stark korrelierter ultrakalter Atome in einer neuartigen Geometrie zu schaffen. Es konnte eine Polarisationsabhängigkeit des periodischen Potentials herausgestellt werden, welche die Untersuchung neuartiger magnetischer Phasen ermöglichen sollte. Experimente zum Quantenphasenübergang zwischen Superfluid und Mott-Isolator in drei- als auch zweidimensionalen Systemen mit Dreieckssymmetrie wurden durchgeführt und analysiert. Unterschiede als auch Gemeinsamkeiten zu früheren Ergebnissen, die in kubischen Gittern gewonnen wurden, konnten nachgewiesen und auf Unterschiede der entscheidenden Gitterparameter, wie etwa Tunnelenergie und Wechselwirkung, zurückgeführt werden.

Ein weiterer Teil der vorliegenden Arbeit widmet sich Untersuchungen zur Dynamik von mehrkomponentigen Spinor Bose-Einstein Kondensaten. In entsptrechend spinunabhängigen Fallenpotentialen, wie sie durch optische Dipolfallen realisiert werden können, lässt sich die Physik Bose-kondensierter Materie auf eine zusätzliche Dynamik der inneren Freiheitsgrade, in diesem Fall des Spins, erweitern. Die im Rahmen dieser Dissertation durchgeführten Experimente zur Physik mehrkomponentiger Quantengase konzentrieren sich auf die kohärente zeitliche Entwicklung des vektoriellen Ordnungsparameters eines Spinor Kondensates, gemeinhin als Spindynamik bezeichnet. ^{87}Rb Kondensate mit Spin-1 als auch Spin-2 wurden untersucht und als ein zentrales Ergebnis konnte erstmals eine Spindynamikresonanz vermessen werden, welche aus der Konkurrenz zwischen spinabhängiger Wechselwirkung and quadratischem Zeemaneffekt heraus entsteht.

Abstract

During the last decade the physics of ultracold quantum gases has matured into a highly active and versatile field of research. Within the framework of this thesis experiments dedicated to the physics of Bose-Einstein condensates have been performed and diverse phenomena, which are distinguished by fundamentally different regimes of interaction, could be investigated.

For the first time the dynamical evolution of long-lived dark solitons has been studied as a paradigm of non-linear physics. Solitons, characterized as non-spreading wave packets, are stabilized against dispersion by a suitable non-linear interaction. It has been possible to observe oscillations of dark solitons in elongated Bose-Einstein condensates and good agreement with the theoretically predicted oscillation frequency of $\omega/\sqrt{2}$ has been obtained. Moreover experiments have been conducted which address the collision of two dark solitons distinguished by different depths. This particular feature enabled the identification of the individual solitons beyond the actual collision process and as a central result it could be shown, that these peculiar entities interpenetrate without significantly influencing each other. The theoretical description of solitons as weakly interacting quasi particles is in good agreement with these findings. Continuative studies on vectorial "dark-bright" solitons and their dynamical properties complement the investigations on dark solitons.

A central goal of this dissertation has been the design and implementation of an optical lattice with an underlying triangular symmetry in order to investigate strongly correlated ultracold atoms in a novel experimental geometry. Exhibiting an explicit polarization dependence the optical lattice realized here should allow for the creation and analysis of thus far unexplored magnetic phases. Experiments attending to the quantum phase transition from a superfluid to a Mott-insulating state in a three- as well as in a two-dimensional system with triangular symmetry have been performed. Similarities as well as differences to the findings obtained in cubic lattices have been worked out and could be attributed to the inherent differences in the crucial lattice parameters such as tunneling energy J and onsite interaction U.

Devoted to the dynamics of spinor condensates, a third part of this thesis concerns the physics of multi component quantum gases. Employing suitable spin-independent trapping potentials the physics of Bose-Einstein condensates may be extended to the investigation of the static and dynamical properties of internal degrees of freedom, in this case the spin of the atoms. The measurements presented here concentrate on the coherent dynamical evolution of the vectorial order parameter of a spinor condensate. ^{87}Rb condensates with $F = 1$ and $F = 2$ have been studied and the existence of a spin dynamics resonance, caused by the competition between spin-dependent non-linear interaction and quadratic Zeeman effect was demonstrated for the first time.

Publikationen

Im Rahmen der vorliegenden Arbeit sind die folgenden wissenschaftlichen Veröffentlichungen entstanden.

Publications

The following research articles have been published in the course of this thesis.

[1] C. Becker, P. Soltan-Panahi, S. Dörscher, J. Kronjäger, K. Bongs and K. Sengstock, *Mott insulator transition in a triangular optical lattice*, to be submitted to Phys. Rev. Lett.

[2] S. Stellmer, C. Becker, P. Soltan-Panahi, E. M. Richter, S. Dörscher, M. Baumert, J. Kronjäger, K. Bongs and K. Sengstock, *Collisions of dark solitons in elongated Bose-Einstein condensates*, Phys. Rev. Lett. **101** 202020 (2008)

[3] C. Becker, S. Stellmer, P. Soltan-Panahi, S. Dörscher, M. Baumert, E. M. Richter, J. Kronjäger, K. Bongs and K. Sengstock, *Oscillations and interactions of dark and dark-bright solitons in Bose-Einstein condensates*, Nature physics **4** 496 – 501 (2008)

[4] J. Kronjäger, C. Becker, P. Navez, K. Bongs and K. Sengstock, *Magnetically tuned spin dynamics resonance*, Phys. Rev. Lett. **97** 110404 (2006)

[5] J. Kronjäger, C. Becker, M. Brinkmann, R. Walser, P. Navez, K. Bongs and K. Sengstock. *Evolution of a spinor condensate: Coherent dynamics, dephasing, and revivals*, Phys. Rev. A **72**, 063619 (2005)

Vorträge und Poster

Im Rahmen der vorliegenden Arbeit wurden folgende wissenschaftliche Vorträge und Poster präsentiert.

Talks and posters

The following talks and posters have been presented in the course of this thesis.

Workshop on Strong Correlations in Multiflavor Ultracold Quantum Gases C. Becker, *Physics with Spinor Bose-Einstein Condensates*, **talk**; München, 10/2008,

DPG Frühjahrstagung C. Becker, *Spinor BEC in triangular optical lattices*, **talk**; Düsseldorf, 3/2007

YAO Meeting C. Becker, *Spinor Bose Einstein Condensates*, **talk**; Innsbruck, 3/2004

Workshop on Disorder in Ultracold Quantum Gases C. Becker, *Spinor Condensates: Magnetization Waves, Triangular Lattices and Solitons*, **poster**; Leiden, 9/2007

Workshop on Disorder in Ultracold Quantum Gases C. Becker, *Spinor BEC in triangular optical lattices*, **poster**; Barcelona, 2/2007

Workshop on Spinor Bose Einstein Condensates J. kronjäger and C. Becker, *Evolution of Spinor BEC in External Fields*, **poster**; Barcelona, 9/2005

Ecole predoctorale Laser cooling and applications C. Becker, *Spinor physics with cold* ^{87}Rb *quantum gases*, **poster**; Les Houches, 9/2004

Contents

Contents i

List of Figures v

List of Tables vii

1 Introduction 1

2 Theory of Bose-Einstein condensation 7
2.1 Thermodynamic properties . . . 7
2.2 The Gross-Pitaevskii equation . . . 8
2.2.1 The Thomas-Fermi regime . . . 9
2.2.2 Collective excitations . . . 10

3 Experimental setup 11
3.1 The core of the BEC machine . . . 11
3.2 A versatile dipole trap setup . . . 12
3.2.1 The dipole force . . . 12
3.2.2 Gaussian beams . . . 16
3.2.3 Astigmatic single beam dipole trap . . . 20
3.2.4 Single Gaussian beam dipole trap . . . 21
3.2.5 Crossed beam dipole trap (XDT) . . . 21
3.2.6 Elongated crossed dipole trap (EXDT) . . . 24
3.3 Detection of Spinor BEC . . . 24
3.3.1 Absorption imaging . . . 24
3.3.2 Spin-selective detection . . . 27
3.4 Controlling magnetic fields . . . 28
3.5 State preparation and analysis . . . 31
3.5.1 Rf- and microwave pulses and sweeps . . . 32
3.5.2 Raman laser system . . . 35
3.5.3 Spatial light modulator . . . 38
3.5.4 Bragg laser system . . . 39
3.6 Setup for an optical lattice . . . 43
3.6.1 A Ti:Sapphire laser system . . . 44
3.6.2 Intensity stabilization . . . 47
3.6.3 Phase noise elimination . . . 48
3.6.4 Adjusting the lattice . . . 50

4 Dynamics of Spinor Bose-Einstein condensates **53**
4.1 Single atom spin-1 and spin-2 physics . . . 54
4.1.1 Theory of single spins in a magnetic field . . . 54
4.2 Interacting spinor Bose-Einstein condensates . . . 62
4.2.1 Theoretical description of spinor BEC . . . 63
4.2.2 Dynamical evolution of a stretched state . . . 66
4.3 Future perspectives . . . 73

5 Spinor BEC in optical lattices **75**
5.1 Generation of periodic potentials . . . 76
5.1.1 The standing wave - textbook physics . . . 76
5.1.2 Three-beam lattices in two dimensions . . . 78
5.2 Single particle in a periodic potential . . . 84
5.3 Revealing the momentum distribution . . . 87
5.4 Calibration of the lattice depth . . . 89
5.5 SF-MI transition . . . 90
5.5.1 The Bose-Hubbard model . . . 92
5.5.2 Ground states and quantum phase transition . . . 94
5.5.3 The Mott-insulator at finite J . . . 97
5.5.4 Thermodynamics of cold atoms in optical lattices . . . 97
5.6 Experimental observation of the SF-MI transition of cold atoms in a triangular optical lattice . . . 100
5.6.1 Adiabatic loading of the lattice . . . 100
5.6.2 SF-MI transition in an array of 2D condensates . . . 101
5.6.3 The SF-MI transition in a 3D system . . . 110
5.7 The hexagonal lattice . . . 111
5.8 Observation of noise correlations in a triangular lattice . . . 113
5.9 Spin dynamics in a triangular optical lattice . . . 115
5.9.1 Experimental sequence . . . 116
5.9.2 Below the phase transition: modified mean-field physics? . . . 116
5.9.3 Spin dynamics in the MI regime . . . 121
5.10 A Zeeman-Bragg resonance - polarization effects . . . 123
5.11 Conclusion and Outlook . . . 126

6 Dynamics of matter-wave solitons **129**
6.1 Theoretical prerequisites for the understanding of solitons . . . 130
6.1.1 Quasi-1D condensates . . . 130
6.1.2 Dark solitons in Bose-Einstein condensates . . . 131
6.1.3 Dark-bright solitons in multi-component condensates . . . 134
6.1.4 Stability of solitons in Bose-Einstein condensates . . . 136
6.1.5 Collisions of solitons . . . 137
6.2 Generation of solitons in a BEC . . . 138
6.2.1 Engineering of super cold elongated BEC . . . 138
6.2.2 Generating dark solitons . . . 139
6.2.3 Filling the notch: creation of dark-bright solitons . . . 141
6.3 Oscillations and collisions of dark solitons . . . 144
6.3.1 Extraction of soliton parameters . . . 144
6.3.2 Oscillations . . . 148

6.3.3 Collisions 151
6.4 Dark-bright solitons in multi-component BEC 154
6.4.1 Collisions of two dark-bright solitons 159
6.5 Outlook 159

A ^{87}Rb **data** **162**

B Atom-light interaction in the two-level picture **165**

C Determination of ensemble parameters **166**
C.1 Bimodal density distribution of a partly condensed Bose gas 166

D Mathematical material for Spinor condensates **168**
D.1 Representation of Projection operators 168
D.2 Equations of motion for spinor condensates 168
D.3 Spin dependent scattering lengths 169

Bibliography **170**

List of Figures

3.1 m_F-dependence of the dipole force . . . 15
3.2 Beam shaping concepts . . . 18
3.3 Gravitational sag in a crossed dipole trap . . . 19
3.4 Schematic beam geometries of the optical dipole traps . . . 21
3.5 Schematic beam geometries of the optical dipole traps . . . 22
3.6 Reduction of interference fringes by post-processing . . . 26
3.7 Structured spinor BEC at $B = 0$ . . . 29
3.8 Gradient compensation (crossed-beam trap) . . . 31
3.9 Rabi oscillations in $F = 1$ . . . 32
3.10 State preparation by rf adiabatic passage . . . 33
3.11 State preparation by microwave sweeps (schematic) . . . 34
3.12 State preparation by microwave sweeps (examples) . . . 34
3.13 Raman transitions in a Λ-system . . . 35
3.14 Experimental setup to apply arbitrary optical potentials using a SLM. . . . 39
3.15 Setup used for focusing of the SLM optics . . . 40
3.16 Scheme for Bragg spectroscopy and -interferometry . . . 41
3.17 Rabi-oscillations between two momentum states . . . 42
3.18 Measuring the coherence length of a BEC employing a Bragg $\pi/2$ - $\pi/2$ interferometer . . . 44
3.19 Setup of the laser system used to generate the optical lattice . . . 45
3.20 Estimate of the line width of the Ti:Sa laser . . . 46
3.21 Power spectrum of one of the lattice beams . . . 47
3.22 Set up for stabilizing the phase . . . 48
3.23 OPPL beat note . . . 49

4.1 Experimental rf pulse sequence for Rabi and Ramsey oscillations . . . 56
4.2 Rabi oscillations with quadratic Zeeman effect . . . 57
4.3 Rabi oscillations of a BEC in $F = 1$ . . . 58
4.4 Ramsey fringes including quadratic Zeeman effect . . . 59
4.5 The Bloch sphere . . . 60
4.6 Ramsey experiment in $F = 1$ . . . 61
4.7 Ground state phase for ^{87}Rb spinor condensates. . . . 65
4.8 Resonance in $F = 1$ spin dynamics . . . 68
4.9 Population oscillations in a ^{87}Rb $F = 1$ BEC . . . 69
4.10 Resonance phenomenon in $F = 2$ . . . 72

5.1 1D lattice . . . 77
5.2 Properties of symmetric three-beam lattices . . . 80
5.3 Contour plots of triangular and hexagonal potential . . . 81

5.4 Lattice potential along directions of high symmetry 82
5.5 Potential well ordering in different lattices 83
5.6 Band structure of a 1D lattice 86
5.7 Band structure of the triangular lattice 87
5.8 TOF images of atoms released from a triangular optical lattice. 88
5.9 Calibrating the lattice depth 91
5.10 Parameters of the Bose Hubbard model 93
5.11 Phase Diagram of atoms inside an optical lattice 96
5.12 Phase Diagram of atoms inside an optical lattice at finite temperature . . . 98
5.13 SF-MI transition in a 2D system 101
5.14 Visibility across the 2D phase transition 103
5.15 Simple model for the determination of a Mott-shell structure 105
5.16 Bimodal fits to the peak structure 107
5.17 First order perturbation theory for a MI-state 108
5.18 Visibility across the 3D phase transition 111
5.19 TOF images of atoms released from an hexagonal lattice 112
5.20 Example of noise correlation data 114
5.21 Experimental cycle for spin dynamics measurements 116
5.22 Spin dynamics of a ^{87}Rb $F = 1$ spinor condensate in optical lattices of various depth. 118
5.23 Spin dynamics oscillation amplitude and period for various lattice depths . 119
5.24 Spin dynamics in the MI regime 122
5.25 Scheme for Zeeman-Bragg processes 124
5.26 Measurements of first- and second-order Zeeman-Bragg resonances 125
5.27 Magnetic field calibration. 125
5.28 Observation of Rabi oscillations between different magnetic- and momentum sub-states 127

6.1 Density and phase distribution of dark solitons. 132
6.2 Density distribution of dark-bright solitons. 135
6.3 Generation of dark solitons. 140
6.4 Basic principle of the generation of dark-bright solitons. 142
6.5 Rotation of the quantization axis 143
6.6 Exemplary fit to the data for dark soliton experiments 145
6.7 Exemplary fit to the data for dark-bright soliton experiments 146
6.8 Oscillations of the condensate. 147
6.9 Lifetimes of BEC for the soliton experiments 148
6.10 Oscillation of dark solitons in a BEC. 149
6.11 Stability diagram for dark solitons 151
6.12 Experimental scheme for the investigation of dark soliton collisions. 152
6.13 Collision of two dark solitons 153
6.14 Chase scenario for two dark solitons 155
6.15 Examples of extremely longlived dark solitons 156
6.16 Oscillation of a dark-bright soliton in a two-component BEC. 157
6.17 Interaction of a dark and a dark-bright soliton. 158
6.18 Interaction of two dark-bright solitons. 160

List of Tables

3.1 Analysis of the astigmatic dipole trap 20
3.2 Trapping frequencies of the crossed-, elongated crossed-,astigmatic- and single-beam dipole trap 23
3.3 Parameters of the magnetic field compensation coils 28
3.4 Separation d of the interference fringes in Fig. 3.18 as a function of the evolution time t_e between the $\frac{\pi}{2}$-pulses. 43

5.1 Radii and particle numbers in different Mott-shells. 105
5.2 Average Thomas-Fermi densities in different lattice regimes 117
5.3 Particle numbers in different Mott-shells for typical N_{tot}. 121

A.1 Fundamental physical constants (taken from 1998 CODATA [6]) 162
A.2 ^{87}Rb physical properties (taken from [7] and references therein) 163
A.3 ^{87}Rb $D_2(5^2S_{1/2} \rightarrow 5^2P_{3/2})$ 164
A.4 ^{87}Rb $D_1(5^2S_{1/2} \rightarrow 5^2P_{1/2})$ 164

D.1 Scattering lengths for ^{87}Rb 169
D.2 Coupling parameters for ^{87}Rb 169

Chapter 1

Introduction

The Nobel prize winning experimental realization of Bose-Einstein condensation in cold atomic vapors back in 1995 [8, 9] has been the foundation for a whole new field of physics. Quickly after the first experiments had been conducted the theoretical as well as experimental interest and progress in understanding Bose-Einstein condensates has been tremendous.

It was realized that Bose-Einstein condensates provide the experimentalist with a very high degree of control over all experimental parameters and that they constitute an almost ideal model system for the investigation of all kinds of non-linear phenomena. Ground breaking experiments exploiting the properties of the coherent macroscopic wave function, like the interference of independent BEC, measurements of collective excitations or the first realization of an atom laser have been performed. Prime examples of non-linear phenomena like the generation of vortices [10] and vortex lattices in rotating condensates or the creation of dark [11, 12] and bright [13] *solitons* – non-spreading wave packets – have been realized in Bose-Einstein condensates.

Today the variety and diversity of experiments involving Bose condensed atoms is huge. Precision measurements, quantum information, macroscopic entanglement or the interaction of BEC with mesoscopic solid state systems are only few examples.

Two very well recognized fields of research attending to Bose-Einstein condensation are the investigation of quantum magnetism in multi-component *spinor condensates* and the realization of condensates inside *optical lattices* formed by interfering laser beams. Although the aforementioned experiments rely on the utilization of Bose-Einstein condensates they can be assigned quite different areas of physics.

In the context of this thesis three different kinds of experiments have been performed. On the one hand experiments attending to the generation and investigation of various species of solitons as one of the most intriguing examples of a generic non-linear phenomenon have been performed. On the other hand the coherent dynamics of multi-component spinor BEC, combining the benefits of BEC and the exploration of quantum magnetism, has been studied in detail.

Finally an optical lattice has been set up in a new triangular geometry aiming at the investigation of magnetic quantum gases inside periodic potentials, that promise such fascinating prospects like geometric frustration or spin-state dependent potentials to create magnetically ordered states.

This introduction intends to provide the reader with a well-founded survey of the historical development in all of these three fields as well as to emphasize which contributions have been made in the framework of this thesis.

Matterwave solitons

Solitons are characterized as wave packets that do not change their shape and propagate with a constant velocity in homogeneous systems. In linear systems a wave packet may be represented by a super position of plane waves that is liable to dispersion tending to spread the wave packet due to different group velocities. On the contrary in non-linear media this dispersion may be balanced by a suitable focusing or defocusing non-linear interaction leading to form stability.
Solitons were first recognized over 150 years ago by J. Scott Russell, a Scottish engineer trying to determine the most efficient design for canal boats when he observed an unusual non-spreading water wave in a narrow channel. He traced the wave that he called "wave of translation" for several miles along the channel before he lost its track [14].
Some 50 years later in 1895 Korteweg and deVries finally formulated the famous Korteweg-deVries equation which is capable of describing the physics of water waves in narrow channels and predicts the existence of solitons. It was not before 1965 when Zabusky and Kruskal found in numerical simulations that solitary waves do not change their shape or velocity after collisions: Asymptotically far away from the collision vertex solitons retain their identity and the interaction during the collision manifests itself only in a phase shift of the trajectories of the individual solitons [15]. They established the term soliton to express the generic quasi-particle like properties of these peculiar objects. Three years later the same authors came up with the inverse scattering method that allowed for an analytical solution of the Korteweg-deVries and the related non-linear Schrödinger equation [16].
As a phenomenon inherent to many different non-linear systems in nature solitons are nowadays recognized in many areas of research such as oceanography and meteorology [17], molecular biology [18] and astrophysics [19] to name only a few. The most prominent example of soliton physics is however the field of non-linear optics (see e.g. [20]) where the physical concept of soliton propagation in optical fibers has matured into an international standard for telecommunication.
Weakly interacting Bose-Einstein condensates that can be described within the framework of the Schrödinger equation exhibiting a cubic non-linearity represent an especially well suited system to investigate solitons. Shortly after the experimental achievement of Bose-Einstein condensation, first experiments on dark [11, 12, 21] and bright [22, 13, 23] solitons were accomplished by different groups. Moreover bright band-gap solitons in a repulsive BEC inside a one-dimensional optical lattice could be established by engineering a suitable dispersion thus creating an effectively attractive interaction [24, 25]. So-called dark-bright solitons, vectorial solitons in multi-component condensates where a bright soliton in one component is stabilized by a dark soliton in the other disregarding the repulsive interaction of the BEC have been realized as well [21].
At the same time a huge amount of theoretical work concerning all kinds of solitons in Bose-Einstein condensate appeared (see e.g. [26] for bright, [27, 28, 29, 30, 31, 32, 33, 34, 35, 36, 37, 38] for dark and [39] for dark-bright solitons). Dynamical as well as thermodynamical stability of solitons was studied and it was found that quasi-one dimensional condensates at ultra low temperatures would provide the most promising approach in order to study the wealth of physical phenomena connected to solitons. An oscillatory behavior of dark solitons in trapped condensates was predicted be several authors all arriving at a characteristic oscillation frequency given by $\omega/\sqrt{2}$ where ω is the trapping frequency. The lifetimes of the experimentally generated solitons had however been rather short and none

of the fascinating quasi-particle like features like oscillation in a trap or recurrence of the initial shape after a collision could be observed.

In the framework of this thesis very long-lived dark and dark-bright solitons could be produced, Unsurpassed experimental conditions allow for lifetimes of up to several seconds for both kinds of solitons. The oscillation of dark and dark-bright solitons in an elongated optically trapped ^{87}Rb BEC could be observed for the first time and the theoretically predicted oscillation period was recovered in these experiments. Experiments devoted to the collision of two dark solitons were performed and *no* discernible influence of the solitons on each other was observed: The solitons pass through each other as if they where transparent. Theoretically predicted shifts in the trajectory of the individual solitons are too small to be optically resolved in our experiment but are compatible with the zero shift that we observe.
Chapter 6 of this thesis describes the experimental results as well as a comparison to theoretical simulations and discusses further aspects of solitons in BEC .[1]

Magnetism in quantum gases – Spinor Condensates

Spinor condensates are distinguished by an additional internal degree of freedom represented by the spin of the atoms. The collisional properties among the atoms of a spinor condensate depend on their relative spin orientation and Hamiltonians similar to those originating from the exchange interaction known in solid state magnetism result for the theoretical description of spinor condensates. Suitable spin-independent trapping potentials are necessary to investigate spinor physics in Bose-Einstein condensates that had become accessible with the first realization of BEC in an optical dipole trap [41]. Shortly after the first realization of BEC the first experiments on spinor condensate composed out of ^{23}Na were performed at MIT. Basic properties like the phase diagram of the magnetic ground state [42] as well as the miscibility of different magnetic substates [43] were investigated. It was realized that spin conservation and the influence of the quadratic Zeeman effect play a major role in understanding the physics of spinor Bose-Einstein condensates Quantum tunneling across artificially created spin domains driven by magnetic gradients fields was studied [44] and could beautifully be described by a simple quantum mechanical model.
At the same time ground breaking theoretical work by Ho [45] and Ohmi*et. al* [46] concerning magnetic ground states and Law *et. al* [47] with regard to the first theoretical investigation of coherent spin mixing paved the way for a concise understanding of the static and dynamical properties of spinor condensates. The mean-field description of spinor BEC developed in [45, 46] was further established by the impressive agreement between the MIT experiments and the theoretical predictions for the specific atomic parameters of ^{23}Na and made it the standard theoretical model for harmonically trapped spinor condensates in the upcoming years.
Concurrently a different experimental approach was taken at JILA where quasi-spin 1/2 condensates composed out of two simultaneously magnetically trappable hyperfine states of ^{87}Rb were analyzed [48]. A whole wealth of phenomena was discovered ranging from

[1] Shortly after the experiments presented here had been finished, we learned about experiments performed by the Heidelberg group, who was able to produce long lived dark solitons as well and observed oscillations of dark solitons and modifications of these oscillations by interactions of two dark solitons and dimensionality effects [40].

phase separation [49, 50], Rabi oscillations [51] to spin waves in a non-condensed spinor gas [52] and spin-dependent interaction between normal and condensed atoms [53, 54]. Furthermore a resonance shifts of a two-photon transition induced by spin-dependent interaction effects [55] and the generation of solitons [21] and vortex lattices [56] could be shown .

A few years after the first seminal experiments several groups started to devote their work again to spinor condensates. The focus was mainly on ^{87}Rb where the static and dynamic properties of $F = 1$ [57, 58] and $F = 2$ [59, 57, 60] spinor condensates were investigated. The ground state phases of $F = 2$ were identified and the corresponding phase diagram was first calculated in our group by H. Schmaljohann [59] accompanied by measurements supporting the *anti-ferromagnetic* nature of $F = 2$. On the contrary $F = 1$ is found to interact *ferromagnetically*.

The investigation of spin mixing dynamics in all of the experiments listed above suffered from a disadvantageous choice of the initial state leading to a severe limitation of the observability of coherent dynamics. Starting from any pure m_F-state, spin dynamics is triggered by small residual "seed"-populations in the other magnetic substates which cannot be prepared satisfactorily. Moreover for reproducible initial conditions the relative phases of different m_F-substates have to be controlled, which is not possible by preparation relying on rapid adiabatic passage which has been the case in some of the above mentioned experiments.

It was only one year later when it was realized in our group that choosing a particular transversely magnetized state leads to a much more controllable and reproducible coherent dynamical evolution of a spinor BEC. It turned out that also theoretically this particular case is analytically soluble and allows for a direct comparison of experiment and theory. In the framework of this thesis measurements on $F = 1$ [5] and $F = 2$ [4] were performed together with J. Kronjäger and as a striking feature the existence of a resonance phenomenon driven by a competition between spin dependent interaction and quadratic Zeeman effect was demonstrated.

Similar results for $F = 1$ were obtained at the same time at Georgia Tech [61] where moreover an analogy to the physics of a non-rigid classical pendulum was raised [62] providing a beautiful figurative picture of the intriguing dynamics of spinor condensates.

In the Berkley group a non-destructive spin-dependent phase contrast method was developed that allows for an in-situ analysis of the *transverse* magnetization [63]. Thereupon spontaneous symmetry breaking in ferromagnetic ^{87}Rb $F = 1$ spinor condensate was observed in terms of spontaneous formation of spin domains and vortices [64]. As another striking result this group was able to observe are dipolar effects in the evolution of spin textures artificially modulated on a ^{87}Rb spinor BEC [65].

An important step towards the long standing goal of a dipolar quantum gas [66] interacting *anisotropically* as opposed to the usual isotropic contact interaction present in BEC has been taken by the realization of Bose-Einstein condensation in ^{52}Cr with a magnetic moment of $6\mu_{\mathrm{B}}$ [67]. First experiments [68, 69] including the generation of a purely dipolar interacting gas [70] promise interesting physics to be discovered in this fascinating area of research. A fundamentally different approach towards dipolar gases is the utilization of ground state molecules with a large permanent electric dipole moment (see e.g. [66]).

The breakdown of the widely applied single mode approximation, where spin and spatial degrees of freedom are decoupled, manifests itself through the formation of spatially varying spin structures and is currently investigated experimentally and theoretically with high effort in several groups [64, 71]. At the Hamburg spinor experiments the formation

of spin domains in an elongated *anti-ferromagnetic* $F = 2$ condensate has been observed and interpreted as a dynamical instability [71].
The Mainz group performed several interesting experiments on the dynamics of spinor condensates confined to the individual wells of a deeply Mott-insulating state [72, 73, 74]. The observed coherent dynamics could be explained by interaction driven Rabi oscillations in a pure two-body picture.

In the context of this PhD thesis several tools to manipulate spinor BEC are discussed in Chapter 3: magnetic field control, Rabi and Ramsey like experimental techniques employing rf and microwave fields similar to those known from NMR and optical manipulation schemes using a Raman laser system. Chapter 4 is devoted to the theoretical basics and experiments attending to the coherent evolution of spin dynamics in ^{87}Rb $F = 1$ and $F = 2$ condensates. As a central result a spin dynamics resonance in $F = 2$ has been studied for the very first time. Spin dynamics of ^{87}Rb in $F = 1$ in a triangular optical lattice of various depth has been investigated in the course of this thesis. Since the mean-field picture valid in large condensates and the two-body picture valid at individual lattice sites with double occupancy exhibit conceptually different solutions it is interesting to study the cross over between those two regimes and develop a deeper understanding of how the characteristic properties of spin changing oscillations are modified when a periodic potential is applied.
Measurements on spin dynamics in a triangular optical lattice which address this question are presented at the end of Chapter 5

Optical lattices and strongly correlated systems

Cold atoms in optical lattices have been in the focus of interest in the atomic physics community for almost 2 decades. While early experiments worked in dissipative lattices to cool atoms further relying on sub-Doppler colling mechanisms [75, 76] with mean single site occupation numbers $\bar{n} \ll 1$ the advent of Bose-Einstein condensation in 1995 [8, 9, 77] paved the way to three-dimensional optical lattice systems with occupation numbers $\bar{n} \geq 1$. The concept of *crystals of light* was born.
When ultracold gases are loaded in deep optical lattices quantum fluctuations start to play a dominant role and it is no longer possible to describe the interacting atoms as non-interacting quasi particles as usually done for Bose-Einstein condensates in the Bogoliubov approach – an unambiguous sign of entering a strongly correlated regime. It is remarkable that this is possible utilizing gaseous samples of ultracold atoms, were interactions usually play an inferior role by definition.
After the identification that atoms in an optical lattice represent an ideal realization of the Bose-Hubbard model [78, 79] well known in solid state physics the theoretical and experimental effort in exploring these systems gained an enormous boost. When the first experimental evidence for the quantum phase transition from a superfluid to a Mott-insulating state in a 3D optical lattice had been found [80] this interest did even grow further. Commonly accepted cold atoms in optical lattices are supposed to represent an ideal play ground to test fundamental solid state theories, e.g. attending to super conductivity or quantum magnetism (see [81] for a detailed overview). The parameters of the system like tunneling strength and interatomic interactions can be conveniently controlled by changing the laser power or additionally employing Feshbach resonances. The translational symmetry of the lattice can be changed by employing different beam geometries

and by choosing the laser polarization properly, magnetic lattices can be realized [82]. It is assumed that by loading atoms in an optical lattice adiabatically an almost perfect crystal system without any impurities or defects can be created. This very fact has moreover lead to several promising proposals for quantum computing schemes relying on the existence of a perfect Mott-insulating state [83].
The dimensionality of the underlying physical systems can be well-controlled making use of optical lattices. Atoms in two-dimensional [84, 85] as well as quasi one-dimensional systems [86] up to the point of the Tonks-Girardeau regime [87] have been realized and investigated. Experiments related to ultracold chemistry have already been conducted and are continued e.g. the creation of molecules by loading two atoms to an individual lattice site and performing association via a two-photon process [88] or by employing sweeps across a Feshbach resonance [89]. powerful and very promising detection methods like noise correlation spectroscopy capable of revealing exotic phases of cold atoms in optical lattices have been proposed [90, 91, 92, 93] and already applied in experiments on bosonic [94] and fermionic atoms [95, 96].

Most of the experiments accomplished or proposed in optical lattices rely very much on the fact that cold atoms in optical lattice provide a perfect experimental environment. To specify to which degree this assumption is justified it is inevitable to precisely understand the underlying physics. Despite circumventing a lot of the problems inherently assigned to solid state systems, new problems like e.g. inhomogeneities in harmonically trapped systems appear and have to be understood and hopefully controlled to comply with the high aims listed above.
The underlying thesis contributes to this goal by investigating the properties of cold atoms in a triangular optical lattice system for the first time. The necessary experimental tools have been designed and implemented as outlined in Chapter 3 and first measurements proving that the optical lattice can be well-controlled were performed. So far experiments on ultracold atoms in periodic potentials had been restricted to simple cubic lattices. In Chapter 5 of this work experiments on the superfluid to Mott-insulator transition in the triangular lattice are presented. A full three-dimensional system as well as the investigation of the quantum phase transition in a reduced two-dimensional regime is concerned.
Very first measurements on spin dynamics in the triangular lattice are presented to motivate further work dedicated to quantum magnetism in this particularly interesting physical system. Numerous theoretical proposals for ultracold atoms with and without spin degree of freedom confined in triangular optical lattices anticipate new and fascinating experiments attending to e.g. rich ground state phases like supersolids [97, 98], frustrated states [99] or exotic stripe ordered phases characterized by various spontaneously broken symmetries [100, 101].
The realization of a Mott-insulating phase of atoms with spin degree of freedom in a triangular lattice achieved in this work is a first step towards the understanding of these so far largely unexplored physical systems.

Chapter 2

Theory of Bose-Einstein condensation

The theory of Bose-Einstein condensation has been established almost a hundred years ago by and N. Bose and A. Einstein who generalized the statistics of photons found by Bose to massive particles. The phenomenon of Bose-Einstein condensation, namely the macroscopic occupation of *one* single-particle state, for temperatures $T_c \gg \hbar\omega_0$ is a purely statistical effect. In this chapter a brief introduction to the general theoretical concepts and key findings of thermodynamic properties and the dynamics of the order parameter in the mean-field approximation will be given. Special topics, like reduced dimensionality or multi-component dynamics will be treated in detail in the corresponding chapters. Useful formulas, used throughout this thesis will be quoted here for completeness.

2.1 Thermodynamic properties of trapped BEC

In order to get an idea of how Bose-Einstein condensation appears we will have a look at the ideal Bose gas. The average occupancy of a single-particle state can be written as

$$\bar{n}_i = \frac{1}{\exp\beta(\epsilon_i - \mu) - 1}, \tag{2.1}$$

where $\beta = 1/(k_B T)$, μ the chemical potential and ϵ_i the energy associated with the single particle state i. As one starts to increase the number of particles N of the system at a given temperature T, the normalization condition $N = \sum_i \bar{n}_i$ leads a macroscopic occupation of the lowest state $i = 0$. This can be understood as a saturation of the thermal distribution. As $N \to \infty$ the chemical potential μ approaches ϵ_0 indicating an exponential growth of $\bar{n}_0$.

The criterion for Bose-Einstein condensation can also be recast in terms of phase space density

$$\lambda_T^3 n = g_{3/2}(1) = 2.612 \tag{2.2}$$

indicating that inter particle spacing n^{-3} and thermal deBroglie wavelength λ_T need to be of the same order of magnitude.

In experiments cold atoms are usually trapped in magnetic or optical dipole traps, whose potential can often be approximated harmonically. The critical temperature of a Bose gas in a harmonic trap is one of the key results of the thermodynamic approach and can be calculated by setting the number of thermal atoms $N_T = \sum_{\bar{n}_i, i \neq 0} = N$ leading to [102]

$$k_{\mathrm{B}} T_c = 0.94\, \hbar\bar{\omega} N^{1/3}. \tag{2.3}$$

Directly related to the critical temperature is the condensate fraction

$$\frac{N_0}{N} = 1 - \left(\frac{T}{T_c}\right)^3, \tag{2.4}$$

where $N_0 = \bar{n}_0$. For typical parameters at our experiment the critical temperature varies between 50 and 300 nK. It has to be emphasized again at this point, that Bose-Einstein condensation occurs at temperatures $k_{\mathrm{B}} T_c \gg \hbar\bar{\omega}$ and should not be confused with the much stronger constraint $k_{\mathrm{B}} T_c \ll \hbar\bar{\omega}$ which would lead to a macroscopic occupation of the lowest single-particle state in a trivial way. Although the above expressions have been derived assuming a non-interacting system, corrections to the *thermodynamic* properties of a BEC due to interactions and finite size stay small, typically amounting to only a few percent. [1]

2.2 Mean-field physics: the Gross-Pitaevskii equation

In harsh contrast to the preceding paragraph interactions play a dominant role in determining the behavior of the order parameter of the condensate, which can be described by a mean-field equation for reasonably large particle numbers. The Hamiltonian for a non-uniform interacting BEC takes the following form

$$\hat{H} = \int \left(\frac{\hbar^2}{2m} \nabla\hat{\Psi}^\dagger(\mathbf{r})\nabla\hat{\Psi}(\mathbf{r})\right) d\mathbf{r} + \frac{1}{2}\int \hat{\Psi}^\dagger(\mathbf{r})\hat{\Psi}^\dagger(\mathbf{r}')V(\mathbf{r}-\mathbf{r}')\hat{\Psi}(\mathbf{r})\hat{\Psi}(\mathbf{r}')\, d\mathbf{r}\, d\mathbf{r}' \tag{2.5}$$

The field operator $\hat{\Psi}(\mathbf{r})$ obeys the Heisenberg equation of motion and commutation relation

$$i\hbar\partial_t \hat{\Psi}(\mathbf{r},t) = [\hat{\Psi}(\mathbf{r},t), \hat{H}] \quad \text{and} \quad [\hat{\Psi}(\mathbf{r},t), \hat{\Psi}^\dagger(\mathbf{r}',t)] = \delta(\mathbf{r}-\mathbf{r}') \tag{2.6}$$

Following the ideas of the Bogoliubov expansion one can replace the field operator for the lowest state simply by a c number $\hat{\Psi} \to \psi_0$ yielding the famous Gross-Pitaevskii equation for the order parameter

$$i\hbar\partial_t \psi_0(\mathbf{r},t) = \left(-\frac{\hbar^2\nabla^2}{2m} + V_{\mathrm{ext}}(\mathbf{r},t) + g|\psi_0(\mathbf{r},t)|^2\right)\psi_0(\mathbf{r},t). \tag{2.7}$$

Here

$$g = \frac{4\pi\hbar^2 a}{m} \tag{2.8}$$

is the interaction parameter for a given s-wave scattering length a, which completely determines the interaction at sufficiently low temperatures. For stationary solutions the time-dependence can be separated leading to the widely used form

$$\left(-\frac{\hbar^2\nabla^2}{2m} + V_{\mathrm{ext}}(\mathbf{r},t) - \mu + g|\psi_0(\mathbf{r},t)|^2\right)\psi_0(\mathbf{r},t) = 0, \tag{2.9}$$

[1] This is only true as long as interactions are not dramatically increased as e.g. in the vicinity of Feshbach resonances. Working with ^{87}Rb condensates far away from any Feshbach resonance, interactions are determined by the background s-wave scattering length a. In this case the thermodynamic properties are well given within the non-interacting model.

emphasizing that the time evolution of a condensate is governed by the chemical potential μ which turns out to be a key quantity in the description of BEC. The density of the condensate is easily found as $n(\mathbf{r},t) = |\psi_0(\mathbf{r},t)|^2$.
By equating the kinetic- and interaction energy term an important length scale for the physics of a condensate the *healing length* ξ is found[2].

$$\xi = \frac{\hbar}{\sqrt{2mgn}} \tag{2.11}$$

The density of the condensate cannot change over distances that are smaller than ξ without destroying superfluidity, because E_{kin} will take values corresponding to velocities beyond the critical velocity for superfluididty otherwise. If on the other hand $E_{\text{kin}} \ll \hbar^2/(2m\xi^2)$ the kinetic energy can safely be neglected compared to the interaction energy yielding the important Thomas-Fermi approximation (see next section).
Another useful quantity is the *Bogoliubov speed of sound* in the condensate describing the propagation of phonon-like excitations

$$c = \sqrt{\frac{gn}{m}}, \tag{2.12}$$

at low momenta. Sound propagation will be of importance for the generation of dark solitons and is thus described in more detail in Chapter 6.
For inhomogeneous systems ξ as well as c can usually be replaced by their *local* values $\xi(\mathbf{r})$ and $c(\mathbf{r})$ respectively (local density approximation (LDA)). Very useful relations between the three key parameters of a BEC μ, ξ and c are given by

$$\mu = mc^2 = \frac{\hbar^2}{2m\xi^2} \tag{2.13}$$

$$\xi = \tfrac{\hbar}{\sqrt{2}mc} = \frac{\hbar}{\sqrt{2m\mu}}. \tag{2.14}$$

2.2.1 The Thomas-Fermi regime

The Thomas-Fermi limit already mentioned above is reached if $Na/a_{\text{ho}} \gg 1$ where $a_{\text{ho}} = \sqrt{\hbar/(m\omega_{\text{ho}})}$ is the harmonic oscillator length. In other words, the interaction greatly dominates the kinetic energy. Without loss of generality we will assume harmonic trapping

$$V_{\text{ext}}(\mathbf{r}) = \sum_{i=x,y,z} \frac{1}{2} m\omega_i^2 r_i^2 \tag{2.15}$$

for the rest of this section. The GPE can then conveniently be reduced to

$$n_{\text{TF}}(\mathbf{r}) = \frac{1}{g}(\mu_{\text{TF}} - V_{\text{ext}}(\mathbf{r})). \tag{2.16}$$

[2] ξ also indicates the transition from phonon like to particle like excitations according to the Bogoliubov dispersion law of a condensate

$$\epsilon(\vec{p}) = \sqrt{\frac{p^2}{2m}\left(\frac{p^2}{2m} + 2gn\right)}. \tag{2.10}$$

Equating the two quantities in parentheses leads to the same expression for the healing length.

The above result shows, that the density of the condensate resembles the inverted trapping potential to keep the chemical potential constant across the BEC. The chemical potential is found to be

$$\mu_{\mathrm{TF}} = \frac{\hbar\omega_{\mathrm{ho}}}{2}\left(\frac{15Na}{a_{\mathrm{ho}}}\right)^{2/5}. \tag{2.17}$$

Note that Equ. 2.17 is one of the most important equations for an experimentalist since it allows for the evaluation of one of the key measures for trapped BEC by simply plugging in experimentally accessible numbers. Another helpful expression relating the radii R_i of the condensate and the chemical potential can be derived from Equ. 2.16 through the fact that $n(R_i) = 0$:

$$\mu_{\mathrm{TF}} = \frac{1}{2}m\omega_i^2 R_i^2 \tag{2.18}$$

Since the radii and the particle number can be determined independently in an experiment, the two preceding expressions can be readily used to cross check the value obtained for μ.

2.2.2 Collective excitations

Besides topological excited states like vortices and solitons, which will be treated in great detail in Chapter 6, sound and low-lying modes of the collective spectrum are the most widely observed excitations in BEC experiments. Low-lying modes corresponding to excitations with wavelength on the order of the condensate size $k^{-1} \approx R$ show up as center-of-mass- or shape oscillations. Sound propagation on the other hand takes place at higher wavenumbers $\xi \ll k^{-1} \leq R$ and is associated with the generation and propagation of phonons in a quantum mechanical sense. Two prominent examples of low lying modes that have been vastly measured at our experiment are the dipole (DP) mode and the quadrupole (QP) mode. They will thus be presented here for completeness. The lowest collective oscillation of the condensate simply corresponds to an oscillation of the center-of-mass at the trap frequency.

$$\omega_{\mathrm{DP}} = \omega_{\mathrm{trap}} \tag{2.19}$$

In fact this oscillation is readily used to determine the trapping frequencies in our experiment. The most prominent example for a higher-order oscillation is the QP mode proportional to $Y_{l=2,m=0}(\theta,\phi)$ or *breathing* mode, where $Y_{l,m}(\theta,\phi)$ are spherical harmonics. It is characterized by a shape oscillation of the BEC at a frequency

$$\omega_{\mathrm{DP}} = \sqrt{\frac{5}{2}}\,\omega_{\mathrm{trap}}. \tag{2.20}$$

The breathing mode is an artifact that often appears when the BEC is perturbed by any kind of mode mismatch or effective shear force and is especially pronounced in elongated condensates. We will come back to this point in Chapter 6.

Chapter 3

Experimental setup and tools for analysis of Spinor BEC

The measurements presented in this thesis have been performed at the Spinor BEC experimental setup at the University of Hamburg. In the course of this work the experiment, originally designed and built as described in [7, 103], has been rebuild in a new laboratory in the Institut fuer Laser-Physik and significantly upgraded, considering mechanical and thermal stability, experimental options and analysis tools. The influence of electromagnetic interference has been minimized as much as possible. Some of these features have already been described in great detail in [71] and will only be briefly sketched here. The present chapter focuses on the basics, design and implementation of optical dipole traps and optical lattices which have been a significant portion of this PhD thesis. Optical design considerations as well as the implementation of accurate servo loops controlling phase, frequency and intensity of the laser light employed for the dipole traps have been accomplished during this work and will be discussed. Essential tools to manipulate external and internal degrees of freedom of multi component BEC have been significantly refined in the course of this work and are presented.

3.1 The core of the BEC machine

The experimental apparatus employed throughout this work represents a complete and very reliable tool for the generation of ^{87}Rb Bose-Einstein condensates with large and reproducible particle numbers. ^{87}Rb BEC are prepared by first collecting up to 10^{10} atoms in a 2D-3D double-MOT system. After further cooling in an optical molasses the atoms are optically pumped to $|F, m_F\rangle = |1, -1\rangle$ and loaded in a magnetic trap of hybrid D-cloverleaf type. After compression of the trap to increase the radial steepness the atoms are cooled by radio-frequency (rf) forced evaporative cooling for 20 s. Residual atoms in $|2, +2\rangle$ are removed by a very-low intensity resonant laser beam during the first of three linear rf ramps. After an overall cycle time of 40 s we finally end up with almost pure BEC of several 10^6 particles in the magnetic trap. For all measurements presented in later chapters the atoms are transferred to an optical dipole trap. For this purpose we evaporate to a rf value corresponding to a temperature slightly above the critical temperature for BEC and superimpose an optical dipole trap with moderate optical power along the axial direction of the magnetic trap. By applying a magnetic offset field B_{off} the radial trapping frequencies are drastically lowered and the atoms condense in the much steeper optical

dipole potential. Deliberately switching off the magnetic trap and lowering the optical power of the dipole trap produces BEC of up to 3×10^5 atoms in a well defined m_F-state without any discernible thermal fraction. The atoms can subsequently be imaged with different kinds of CCD cameras from various directions, leading to an overall cycle time of $50 - 60\,\mathrm{s}$.
A much more detailed description of the basic experimental setup can be found in [7, 103].

3.2 A versatile dipole trap setup

Many experiments involving ultracold atoms are performed using magnetic traps (MT) which are capable of trapping many atoms and allows for efficient and fast evaporative cooling schemes. However, despite these advantages the investigation of magnetic properties of ultracold atoms demands for an m_F-state independent trapping potential in order to liberate the spin degree of freedom, which is not provided by MT's since only low field seeking states can be trapped in the local magnetic field minimum, thereby freezing the spin. An optical dipole trap (ODT) on the other hand can fulfill this requirement if the laser polarization is linear with respect to the quantization axis and/or the detuning with respect to the atomic resonance is fairly large as we will see soon. An ODT can be easily implemented by focusing down a laser beam to a Gaussian waist. The size of the waist, optical power and laser detuning determine the properties of the trap usually given in terms of trap frequencies in a harmonic approximation. However as will be shown later very cold BEC require very shallow traps, where the harmonic approximation breaks down and the gravitational sag starts to play a significant role.

3.2.1 The dipole force

Basic equations

The interaction between light and atoms is the essence of quantum optics. When laser light is irradiated onto an atom, two distinct physical processes will take place. The radiation pressure force which results from absorption and spontaneous emission of photons is essential for laser cooling [104] and represents the imaginary part of the polarizability. The non dissipative dipole force on the other hand is a result of the interaction of the dipole moment of the atom induced by the electric field of the laser $\mathbf{p}_\mathrm{ind} = \alpha\mathbf{E}$ with this electric field and can be written as

$$U(\mathbf{r}) = -\frac{1}{2}\langle \mathbf{p}_\mathrm{ind} \cdot \mathbf{E}(\mathbf{r})\rangle = -\frac{1}{2\epsilon_0 c}\mathrm{Re}\,(\alpha) I(\mathbf{r}), \tag{3.1}$$

where brackets $\langle ... \rangle$ denote time-averaging over fast oscillating terms. $U(\mathbf{r})$ is intrinsically connected with the real part of the polarizability $\mathrm{Re}\,(\alpha)$. If the detuning $\Delta = \omega_L - \omega_0$, defined as the difference between the atomic resonance frequency and the laser frequency, is greater than zero, the induced atomic dipole moment follows the electric field in phase and the atom will be accelerated towards regions of high intensity. When $\Delta < 0$ the induced dipole moment oscillates out of phase with the electric field of the laser and a repulsion away from the region of highest intensity is the result. Obviously a trap for cold atoms can be created by employing laser light fields with a suitable inhomogeneous intensity distribution $I(\mathbf{r})$, as it is given e.g. in the waist of a Gaussian beam. A quantum mechanical description of a two level atom in the frame work of the *dressed atom* picture

[104] results in the analytical expression for the dipole potential

$$U_{\text{dip}}(\mathbf{r}) = -\frac{3\pi c^2}{2\omega_0^3} \cdot \left(\frac{\Gamma}{\omega_0 - \omega_L} + \frac{\Gamma}{\omega_0 + \omega_L} \right) I(\mathbf{r}), \tag{3.2}$$

where Γ denotes the decay rate of the excited state. If the detuning is not too large $|\Delta| \ll \omega_0$ the above expression can be simplified in the *rotating wave approximation* (RWA) yielding

$$U(\mathbf{r}) = \frac{3\pi c^2}{2\omega_0^3} \cdot \left(\frac{\Gamma}{\Delta} \right) I(\mathbf{r}). \tag{3.3}$$

A comparison with the corresponding expression for the photon scattering rate Γ_{sc} which is easily derived in an analogous way

$$\Gamma_{\text{sc}}(\mathbf{r}) = \frac{3\pi c^2}{2\hbar\omega_0^3} \cdot \left(\frac{\Gamma}{\Delta} \right)^2 I(\mathbf{r}) \tag{3.4}$$

reveals an important prerequisite for the design of any optical dipole trap: For a purely conservative, spin independent trap it is best to choose large laser powers and large detunings since the ratio $U_{\text{dip}}/\Gamma_{\text{sc}} \sim \Delta$ and therefor grows with increasing detuning which minimizes heating processes mediated by laser light. Please note that while providing useful qualitative insight in the physics involved in ODT design, the RWA is explicitly not valid for detunings on the order of the atomic resonance frequency as in our experiment, where the beams are derived from a Nd:YAG laser at a wavelength of 1064 nm and the error involved with the RWA is already larger than 10%. All calculations shown in this section therefor take into account both terms of Equ. 3.2, while for ease of notation all equations presented from now on are denoted in the RWA.

The simplification to a two-level system is of course too rough to account for a precise description of the dipole forces involved with real-world multi-level atoms like the alkali's, which are widely used in cold atom experiments. ^{87}Rb is an alkali atom with a nuclear spin $I = 3/2$ and has two hyperfine ground states with $F = 1$ and $F = 2$ respectively. To obtain the dipole potential for a given ground state level the sum over all allowed transitions to excited states has to be formed.

$$U_{\text{dip}}(\mathbf{r}) = 3\pi c^2 \left(\sum \frac{|c_{CG,i}|^2}{\omega_{0,i}^3} \frac{2\Gamma_i \Delta_i}{\Gamma_i^2 + 4\Delta_i^2} \right) I(\mathbf{r}) \tag{3.5}$$

The $c_{CG,i}$ denote the Clebsch-Gordon coefficients involved with each specific transition. For laser detunings large compared to the excited state hyperfine splitting for the D1- ($\Delta'_{\text{HFS}} = 800\,\text{MHz}$) and the D2-line ($\Delta''_{\text{HFS}} = 500\,\text{MHz}$) respectively, as is the case for all purposes discussed in this thesis, one can sum over all transitions within a given excited-state hyper-fine manifold which results in

$$U_{\text{dip}}(\mathbf{r}) = \frac{\pi c^2 \Gamma}{2\omega_0^3} \left(\frac{1 - \mathcal{P} g_F m_F}{\Delta_{D1}} + \frac{2 + \mathcal{P} g_F m_F}{\Delta_{D2}} \right) I(\mathbf{r}). \tag{3.6}$$

Here Δ_{D1} and Δ_{D2} identify the detuning with respect to the center of the D1 and D2 hyperfine manifold respectively, while Γ is the total decay rate of the excited state which is F' as well as m'_F independent. $\mathcal{P} = 0, \pm 1$ characterizes the laser polarization $\pi, \sigma^\pm$ respectively which gives a first clear indication that for circular polarization the dipole potential will obey a spin dependence, which vanishes asymptotically for infinite detuning.

Note that linear- and unpolarized light does not lead to an m_F dependent potential. If the laser detuning is slightly larger than the fine structure splitting $\Delta_{\rm FS} = \omega_{\rm D1} - \omega_{\rm D2}$ the expression for the dipole force can be further simplified yielding

$$U_{\rm dip}(\mathbf{r}) = \frac{3\pi c^2}{2\omega_0^3}\frac{\Gamma}{\Delta}\left(1+\frac{1}{3}\mathcal{P}g_F m_F \frac{\Delta_{\rm FS}}{\Delta}\right) I(\mathbf{r}). \tag{3.7}$$

Effective field picture

As already recognized by Cohen-Tannoudji and co-workers [105] the $m_{\rm F}$ dependence of the dipole force can also be regarded as an imaginary effective magnetic field acting on the atomic sublevels just like a real magnetic field does. [1] With the help of

$$U_{\rm dip}^{\rm mag}(\mathbf{r}) = -\mu \cdot \mathbf{B}_{\rm eff}(\mathbf{r}) \tag{3.8}$$

$$= -\mu_{\rm B} g_F m_F \frac{\hat{\mathbf{F}}}{F}\cdot \mathbf{B}_{\rm eff}(\mathbf{r}) \tag{3.9}$$

and Equ. 3.5 this effective magnetic field evaluates to

$$\mathbf{B}_{\rm eff}(\mathbf{r}) = i(\mathbf{e}_{\mathcal{P}}^* \times \mathbf{e}_{\mathcal{P}})\frac{\Gamma\pi c^2}{2\omega_0^3\mu_{\rm B}}\frac{\Delta_{\rm HFS}}{\Delta^2} I(\mathbf{r}). \tag{3.10}$$

Note that the dipole force exerted by sufficiently far detuned circular polarized light is equivalent to the *linear* Zeeman effect. For typical experimental conditions inside the hexagonal optical lattice (see Chapter 5) values of $B_{\rm eff}^{\rm max} = 0.5\,{\rm mG\,cm^2/mW}\cdot I$ are easily achieved. The corresponding value for the magnetic dipole potential yields $U_{\rm dip}^{\rm LZ} = 2\pi\hbar \cdot m_F \cdot 0.35\,{\rm kHz/mW}\cdot I$. Finally the dipole potential can be written as [2].

$$U_{\rm dip}(\mathbf{r}) = \frac{3\pi c^2}{2\omega_0^3}\frac{\Gamma}{\Delta}\left(|\mathbf{e}_{\mathcal{P}}|^2 + g_F m_F \frac{i}{3}(\mathbf{e}_{\mathcal{P}}^*\times\mathbf{e}_{\mathcal{P}})\cdot\frac{\hat{\mathbf{F}}}{F}\frac{\Delta_{\rm FS}}{\Delta}\right) I(\mathbf{r}) \tag{3.11}$$

$$= U_{\rm dip}^0(\mathbf{r}) + U_{\rm dip}^{\rm LZ}(\mathbf{r}). \tag{3.12}$$

It has to be emphasized, that with the help of optical lattice configurations involving circular polarization, magnetic potential landscapes with optical wavelength resolution can be designed.

Fig. 3.1 spotlights the effect of circular polarized light for different m_F-states. Another interesting possibility to mimic the effect of a classical field using laser light occurs for the case of relatively small detuning $\Gamma \ll \Delta < \Delta'_{\rm HFS}$, π^0 polarized light and transitions of the kind $|F\rangle \rightarrow |F' = F\rangle$. Especially the D1-transition $|F=2\rangle \rightarrow |F'=2\rangle$ in ^{87}Rb is a promising candidate for the realization of an optically induced *quadratic* Zeeman effect, since an effective energy shift of

$$U_{\rm dip}^{\rm QZ}(\mathbf{r}) = \frac{\pi c^2}{6\omega_0^3}\frac{\Gamma}{\Delta_{D1}}\frac{4m_F^2}{(2\hat{I}+1)^2} I(\mathbf{r}) \tag{3.13}$$

[1] The polarizability inEqu. 3.1 is in general polarization as well as spin-state dependent. This is conveniently expressed in terms of irreducible tensors leading to the effective field picture [105, 106].

[2] The assumptions made to derive Equ. 3.11 are valid for all optical dipole potentials employed in the course of this thesis. The only exception to this statement is the optically induced phase evolution used throughout the soliton experiments described in Chapter 6. There Equ. 3.5 has to be used without further approximations.

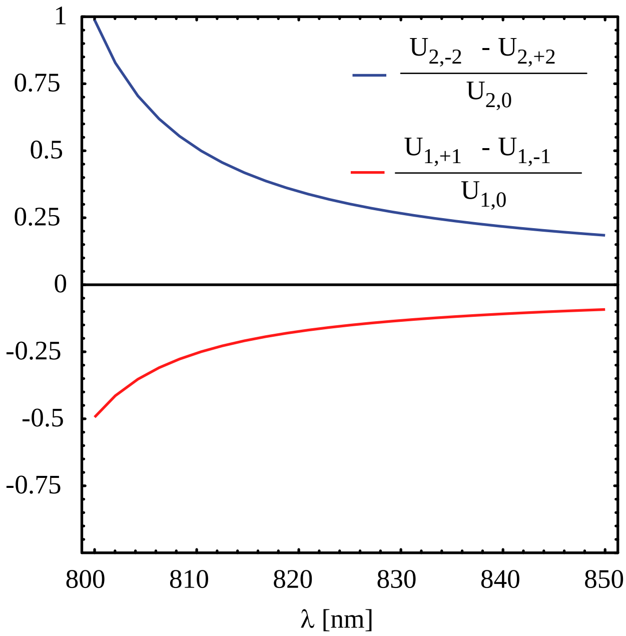

Figure 3.1: Maximal difference in the dipole potential experienced by opposed stretched states $|F, \pm F_{\max}\rangle$ for σ^--polarized light normalized to the dipole potential felt by the $|F, 0\rangle$ state. The use of σ^+-polarized light results in a change of sign. Linear polarized light generates a dipole potential that doesn't exhibit any significant m_F-dependence for any detuning. Even larger differences are obtained for smaller detunings, yet limiting the lifetime of the atomic samples through spontaneously scattered photons. Detunings larger than the shown range finally lead to a vanishing of the spin dependence of the dipole force, regardless of the polarization.

can be calculated. Comparison to the expression for the usual quadratic Zeeman effect

$$U_{\mathrm{LZ}} = \frac{\mu_B^2 B_0^2}{\Delta_{\mathrm{HFS}}} \left(1 - \frac{4m_F^2}{(2\hat{I}+1)^2} \right) \tag{3.14}$$

leads to an expression for the imaginary magnetic field of

$$B_{\mathrm{eff}}^2 = \frac{\pi c^2}{6\mu_B^2 \omega_0^3} \frac{\Delta_{\mathrm{HFS}}}{\Delta_{D1}} \Gamma\, I(\mathbf{r}). \tag{3.15}$$

Unlike the usual quadratic Zeeman shift, the sign of $U_{\mathrm{dip}}^{\mathrm{QZ}}$ can easily be chosen by detuning the laser to the red (+) or the blue (-) of the atomic resonance respectively. Typical values that can be achieved using a moderately detuned laser ($\Delta \approx \pm 100\,\mathrm{Mhz}$) with a beam waist of 1 cm are of the order of $|B_{\mathrm{eff}}|^2 = 3.3\,\mathrm{G}^2/\mathrm{mW} \cdot I$ corresponding to $U_{\mathrm{dip}}^{\mathrm{QZ}} = 2\pi\hbar \cdot 1\,\mathrm{kHz/mW} \cdot I$.
The overall quadratic Zeeman shift relative to the shift of $|2, 0\rangle$ can then be written as

$$U^{\mathrm{QZ}}(\mathbf{r}) = \frac{\mu_B^2}{\Delta_{\mathrm{HFS}}} (B^2 - B_{\mathrm{eff}}^2) \left(\frac{4m_F^2}{(2\hat{I}+1)^2} \right) \tag{3.16}$$

Most importantly the detuning to the $|F' = 2\rangle$ state must be much smaller than that to the $|F' = 1\rangle$ state, which limits the range of applicable values to $\Delta < \Delta'_{\mathrm{HFS}} \overset{\mathrm{D1}}{\approx} 800\,\mathrm{MHz}$. It has already been suggested in [103, 107] and implemented in [108] to compensate or even invert the quadratic Zeeman effect in coherent spinor dynamics by a suitable laser- or microwave dipole potential in cold atom experiments.
Further details regarding the dipole force can be deduced from [109, 104, 105, 110].

3.2.2 Gaussian beams

Basic properties

The starting point for the design of beam shaping optics for the creation of optical dipole traps is the propagation of Gaussian laser beams through various kinds of optical elements. Since the atoms will be finally trapped in the waist of such a Gaussian laser beam w_0, it is quite useful to give a short reminder of the involved expressions. More information can be found in standard optics text books (see e.g. [111]). The intensity distribution of a Gaussian beam traveling in the z-direction can be written as

$$I(\mathbf{r}) = \frac{2P}{\pi w(z)^2} \exp -2\left(\frac{x^2+y^2}{w_x^2(z)w_y^2(z)}\right). \tag{3.17}$$

P is the optical power of the beam, whereas the $w_i(z)$ are the beam waists in direction i at the axial position z. They are connected to the minimal waist $w_{i,0}$ through $w(z) = w_0\sqrt{1+(z/z_{\mathbf{R}})^2}$, where the Rayleigh range is given by $z_{\mathrm{R}} = (\pi w_0^2)/\lambda$ and defines the distance over which $w(z)$ grows by a factor of $\sqrt{2}$.

ABCD matrix optics

The propagation through optical elements like lenses, mirrors, etc. can be described by the use of $ABCD$-matrices, known from paraxial ray optics. Here the distance r from the optical axis and the angle of inclination α of a ray transform according to

$$\begin{pmatrix} r' \\ \alpha' \end{pmatrix} = \begin{pmatrix} A & B \\ C & D \end{pmatrix} \begin{pmatrix} r \\ \alpha \end{pmatrix}. \tag{3.18}$$

The most common examples when working with out-of-the-box lenses are the matrices for a thin lens and propagation in free space:

$$\hat{\mathbf{M}}_{\mathrm{lens}} = \begin{pmatrix} 1 & 0 \\ -1/f & 1 \end{pmatrix}, \hat{\mathbf{M}}_{\mathrm{free}} = \begin{pmatrix} 1 & d \\ 0 & 1 \end{pmatrix}. \tag{3.19}$$

Any optical system can consequently be written as a (non-commutative) product of matrices $\prod_i \hat{\mathbf{M}}_{\mathrm{i}}$ of individual optical elements, where the right-most matrix corresponds to the optical element adjacent to the beam input. The resulting matrix features some very convenient properties, that can be summarized as follows:

- If the optical elements are arranged such that they fulfill an imaging condition, then $B = 0$.
- If $B = 0$, then simultaneously the magnification can be obtained through $D = 1/A = M$.
- If $B = 0$, the resulting focal length of the optical system is given by $C = -1/f$.

A thorough analysis reveals that the crucial measure for Gaussian beams is the complex beam parameter $\tilde{q}(z)$ defined as

$$\frac{1}{\tilde{q}(z)} \equiv \frac{1}{R(z)} - i\frac{\lambda}{\pi w_0^2}. \tag{3.20}$$

This complex beam parameter transforms exactly like the radius of curvature $R(z)$ does in spherical-wave optics:

$$\tilde{q}_2 = \frac{A\tilde{q}_1 + B}{C\tilde{q}_1 + D}. \tag{3.21}$$

Since $R(z)$ can be written as $R(z) = z + z_{\mathrm{R}}^2/z$ the entire physics of Gaussian beams can be characterized by the minimal beam waist w_0 and the wavelength λ.
With the help of Equ. 3.21 and Equ. 3.20 a normalized thin lens formula for Gaussian beams can be derived [112]

$$b/f = 1 + \frac{g/f\ -1}{(g/f\ -1)^2 + (z_{\mathrm{R}}/f)^2}, \tag{3.22}$$

where g is the b is the image distance In Gaussian optics an imaging condition is derived for $b = g = f$. This is in contrast to geometrical optics, where a similar calculation reveals $b = g = 2f$ as a special combination of object- and image distances. Moreover for $g = f$ in geometrical optics, one obtains a perfectly collimated beam, a construct that does *not* exist for real Gaussian beams. Maybe the most striking feature of Equ. 3.22 is the fact that for $z_{\mathrm{R}}/f \geq 1$ the image distance b depends on the object distance g only very weakly and is basically equal to f. Basically a rule of thumb can be declared, that the smaller the waist behind the final lens shall be, the bigger the waist in front of the lens has to be.

Design considerations

Since a TEM_{00} mode Gaussian laser beam is the highly desired beam shape for the creation of optical dipole traps or optical lattice beams, some attention has to be paid to the creation of such a beam. The goal for the design of the XDT beam shaping telescopes was the creation of a Gaussian waist $w_0 \approx 40\,\mu$m a distance of 400 mm away from the focusing lens. A very elegant and flexible approach consists in the use of optical single mode (SM) fibers, which deliver the optical power to any desired destination in the experimental setup. Another advantage is, that the laser beam emerging from a SM fiber is almost perfectly Gaussian. carefully designed beam shaping optics may image the Gaussian waist without losses in beam quality. Special care has to be taken when placing apertures in the optical path. To avoid any loss in power and undesired interference due to diffraction the apertures must not be smaller than $4.4 \times w_0$ [113]. Taking this into account and with the help of Equ. 3.21 beam shaping telescopes for the crossed-beam dipole trap and the optical lattice beams have been designed using commercially available achromatic and aspherical lenses (MELLES GRIOT, THORLABS, LINOS). It has proven, that the crucial condition for superb beam quality is a preferably high numerical aperture (NA) of the first lens, which in addition necessarily has to be of aspherical type to minimize aberration [3]. Two different concepts concerning the interim collimation of the beam have been traced throughout this work. They are sketched and explained in Fig. 3.2. The resulting beam waists have been analyzed along the optical path with a laser beam analysis device (BEAMview by COHERENT) to further characterize the trapping potential. An essential quality requirement was a very low $|M|^2$ factor which determines the deviation of a laser beam from the idealized Gaussian shape. Taking images of the waist along the

[3]The NA is a measure of the angular acceptance of an optical system. It is widely defined as $NA = n \cdot \sin(\arctan(D/2f))$, where n is the index of refraction, D the open aperture of the optical system and f the focal length.

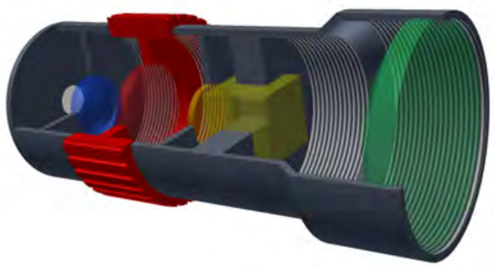

(a) 2-lens collimation scheme realized in the 2D-lattice telescopes. An aspherical lens (blue) with $f = 4.5\,\mathrm{mm}$ placed at a distance of $f/2$ in front of the fiber end virtually decreases the NA by a factor of two. An $f = 8\,\mathrm{mm}$ achromatic lens (red) subsequently collimates the beam without diffraction effects. Additional polarizing optics (yellow) are used to adjust the polarization, before a $f = 400\,\mathrm{mm}$ achromatic lens creates a spot of size $w_0 = 125\,\mu\mathrm{m}$

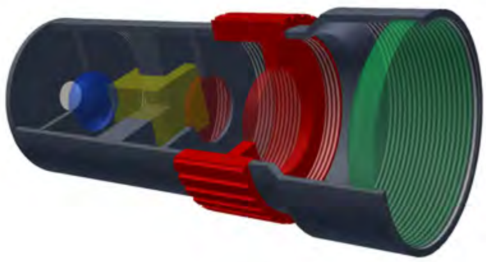

(b) 1-lens plus magnification-telescope scheme as used for the crossed dipole trap. An aspherical lens (blue) with $f = 4.5\,\mathrm{mm}$ collimates the beam which is expanded by a factor of ≈ 6 with a telescope (red) consisting of an $f = 8\,\mathrm{mm}$ aspherical and an $f = 50\,\mathrm{mm}$ achromatic lens, which is externally adjustable. Finally an $f = 300\,\mathrm{mm}$ achromatic lens (green) focuses the beam down to the desired spot size of $w_0 = 40\,\mu\mathrm{m}$. A polarizing beam splitter cube (yellow) is used to eliminate any residual elliptic polarization.

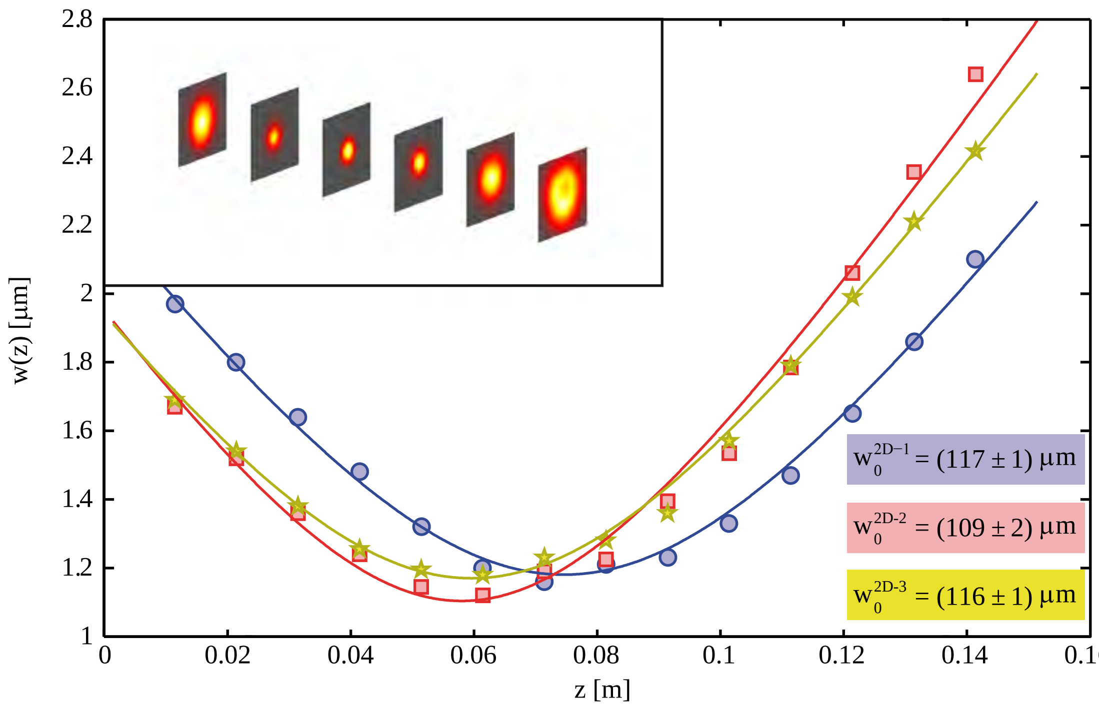

(c) Fits to measured spot sizes to determine w_0. Data for the the three 2D lattice telescopes is shown. Equal waist sizes have been a major design prerequisite. The inset shows beam waists of a typical Gaussian laser beam measured along the optical axis with a beam profile analyzing camera (COHERENT BEAMview).

Figure 3.2: Different approaches for the generation of small Gaussian waists. Measurements of the spot size along the optical axis and determined minimal waists are shown.

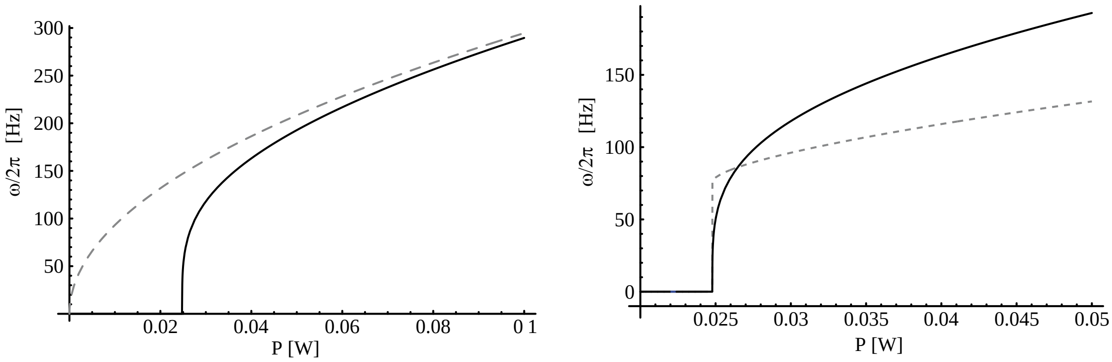

(a) Influence of gravity on ω_z (b) Comparison of ω_z and $\omega_{x,y}$ in a XDT

Figure 3.3: Plot of the trap frequencies for a shallow crossed-beam optical dipole trap as implemented in our experiment. The influence of gravity is clearly seen for low optical power. The gray dashed curve shows the expected $\sqrt{I}$ dependence of ω. Fig. 3.3b shows the vertical (full black) and horizontal (gray dashed) trap frequencies. For a specific value of P all trap frequencies become equal resulting in a spherical potential.

---

optical path ensured good control of this parameter. Wavefront distortions in the vicinity of the focus of the beam transform into intensity modulations in the far field ($z \gg z_{\mathrm{R}}$) and can therefor by detected and eliminated. The measured spot sizes for the two Since we expect, that ultracold atoms will occupy the lowest level of a given potential, it is very useful to write the potential in a harmonic approximation, which yields trapping frequencies:

$$\omega_\rho = \sqrt{\frac{4U_{\mathrm{dip}}^{\mathrm{max}}}{mw_0^2}} \text{ and } \omega_z = \sqrt{\frac{2U_{\mathrm{dip}}^{\mathrm{max}}}{mz_{\mathrm{R}}^2}} \tag{3.23}$$

$U_{\mathrm{dip}}^{\mathrm{max}}$ denotes the dipole potential evaluated at the point of maximum intensity. The aspect ratio of BEC in a single Gaussian beam trap is given by $\sqrt{2}\pi w_0/\lambda$ and takes very large values for $w_0 \gg \lambda$ as usually fulfilled. The expected scaling with optical power follows the simple law $\omega \propto \sqrt{P}$ but is explicitly violated for very low trap depth, where the gravitational sag $\Delta z = 2g/\omega_z^2$ starts to play a dominant role and shifts the zero of the potential away from the optical axis. This breaks the cylindrical symmetry of the potential and lowers the effective trap frequencies. The gradient $\partial\omega_z/\partial P$ is especially steep for very low laser power as can be taken from Fig. 3.3 , which is unfortunately the working point in the experiments throughout this thesis. It has therefor proven indispensable to stabilize the intensity of the trap laser to a high degree of accuracy in order to get reproducible and stable experimental conditions. Fig. 3.3 further illustrates the change in the trap properties due to gravity and low optical power for a crossed dipole trap. The trap frequencies decrease faster than the naively expected $1/\sqrt{I}$-law and furthermore an inversion of the aspect ratio of the trap takes place. As the main conclusion one has to bear in mind, that trap frequencies measured at an arbitrary trap depth must not simply be scaled, when working at different optical power. Instead it has proven inescapable to determine the trap frequencies at the working point.

Table 3.1: Comparison of average frequencies of the astigmatic dipole trap, obtained by various methods. $\bar{\omega}$ is scaled according to Tab. 3.2, $\bar{\omega}^{(T)}$ and $\bar{\omega}^{(n)}$ are calculated from measured critical temperatures and densities, respectively (see text for details).

power	experimental data				calculated from data			scaled
[mW]	$T/\,\mathrm{nK}$	$N/10^5$	$N_0/10^5$	$n/\,\mathrm{cm}^{-3}$	$T_c/\,\mathrm{nK}$	$\bar{\omega}^{(T)}/\,\mathrm{s}^{-1}$	$\bar{\omega}^{(n)}/\,\mathrm{s}^{-1}$	$\bar{\omega}/\,\mathrm{s}^{-1}$
44	64	5.0	3.8	0.68×10^{14}	104	$2\pi \times 29$	$2\pi \times 23$	$2\pi \times 106$
107	205	8.3	2.9	1.9×10^{14}	229	$2\pi \times 54$	$4\pi \times 96$	$2\pi \times 165$

3.2.3 Astigmatic single beam dipole trap

A first dipole trap setup has been implemented at the Hamburg Spinor experiment employing an astigmatic single beam dipole trap. Three prerequisites have to be met in order to study spinor physics of ^{87}Rb BEC in $|F = 2\rangle$ and $|F = 1\rangle$:

1. a trap potential as conservative and spin independent as possible is required.
2. the trap has to be sufficiently strong in the vertical direction to support the atoms against gravity.
3. the resulting atomic density in the condensate has to be low enough to reduce three-body losses, especially important for $|F = 2\rangle$, to a reasonable level.

The first requirement is met by the use of a far red detuned Nd:YAG laser (Innolight Mephisto) at a wavelength of 1064 nm and purely linear polarization. At reasonable trap depths the spontaneous scattering rate evaluates to less than $0.1\,\mathrm{s}^{-1}$. To fulfill the latter two conditions an astigmatic trap has been designed which has a tight focus in the vertical direction, while providing a relatively relaxed overall tightness defined through the geometric average of the trap frequencies $\bar{\omega} = \sqrt[3]{\omega_x \omega_y \omega_z}$. The atomic density is then defined through $\bar{\omega}$ according to Equ. 2.16. A laser beam emerging from an optical single-mode fiber (THORLABS) is first collimated to a beam diameter of ≈ 50 mm and then focused to a small Gaussian beam waist of $w_0 \approx 6\,\mu$m using a spherical achromatic lens ($f = 250$ mm). A moderate astigmatism is introduced by placing a cylindrical lens behind the focusing achromat. Its major effect is a displacement of the horizontal- relative to the vertical focus position along the optical axis of $\Delta z \approx 4$ mm. The horizontal beam waist at the position of the vertical focus has been determined to be $w^y(z = \Delta z) \approx 400\,\mu$m. The resulting optical potential is shown in Fig. 3.4a.

To characterize the potential, trap frequencies have been measured using dipole oscillations (see also Fig. 3.5) as well as parametric heating [114] which is in particular feasible for tight traps and high trap frequencies as for the astigmatic trap. Trap frequencies obtained in this way can be cross checked by determination of the critical temperature via $N_0/N = 1 - (T/T_c)^3$ which is then used to calculate the trap frequencies through $k_B T_c = 0.94\hbar\bar{\omega}^{(T)} N^{1/3}$. Neither this method nor the comparison to direct measurements of the average density $\langle n \rangle$ through spin changing dynamics related to the trap frequencies according to $\bar{\omega}^{(\bar{n})} = \hbar/(ma^2)(14\pi\langle n \rangle a^3)^{5/6}(15N_0)^{-1/3}$ show an acceptable agreement with the directly measured frequencies as documented in Tab. 3.1. Since the above expressions do only weakly depend on the particle number N, which is afflicted with some experimental errors due to imperfections in the detection process, the major reason for the disagreement seems to be something else. The already mentioned breakdown of the

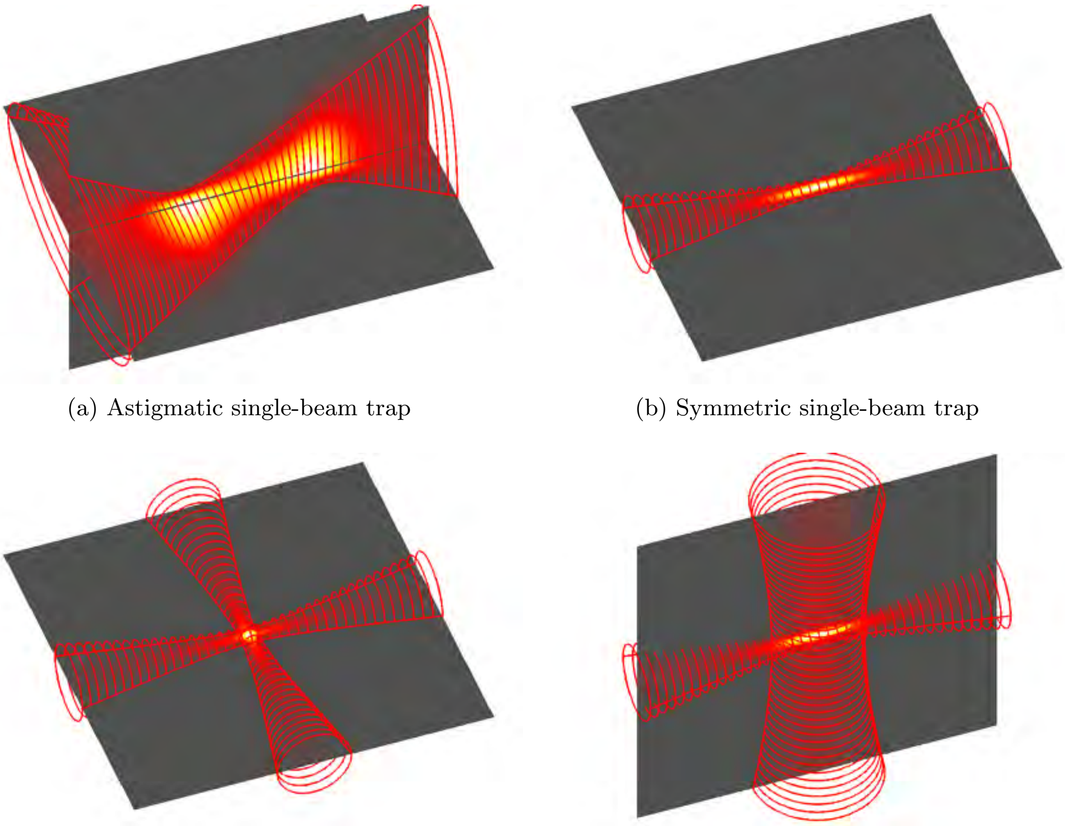

(a) Astigmatic single-beam trap

(b) Symmetric single-beam trap

(c) Crossed-beam trap

(d) Elongated crossed-beam trap

Figure 3.4: Schematic beam geometries of the astigmatic- and symmetric single-beam, crossed-beam and elongated crossed-beam optical dipole traps. Shown are the $1/e^2$ beam diameter (red wire frame) and the intensity distribution (colored sections).

---

harmonic approximation for low trap depth, which forms the basis of all of the above calculations, seems to be a promising candidate to explain the remarkable disagreement.

3.2.4 Single Gaussian beam dipole trap

For measurements in very elongated BEC, e.g. the experiments concerning spin domain formation presented in Chapter 4 only one of the crossed-beam dipole trap beams can be employed in order to achieve a very high aspect ratio (see Fig. 3.4b). Axial condensate extensions of up to 1 mm can be achieved in this way. The axial beam frequency involved with such a trap is in the sub-Hz regime and cannot be measured by usual excitation of dipole oscillations. However by determination of the gravitational sag as a function of the tilt angle of the beam with respect to the horizontal direction the axial trapping frequency can be measured with very high accuracy [115]. Measurements in a typical trap yield an axial trapping frequency of $\omega_x = 0.8\,\mathrm{Hz}$ and ≈ 100 for the aspect ratio.

3.2.5 Crossed beam dipole trap (XDT)

In the framework of this thesis the Hamburg Spinor experiment has been upgraded with an optical lattice. The need for an almost isotropic but spin-independent trapping poten-

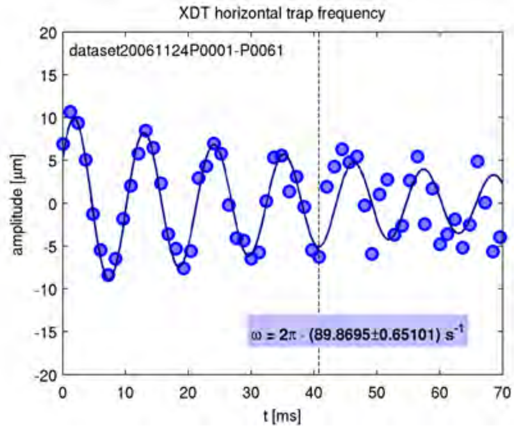

(a) Horizontal trapping frequency XDT

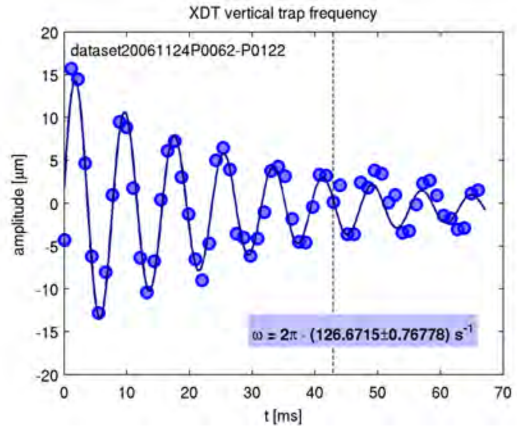

(b) Vertical trapping frequency XDT

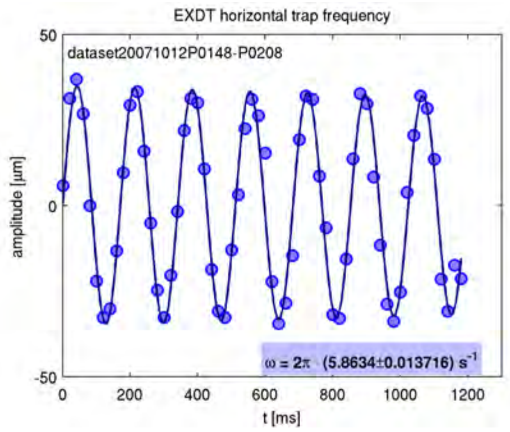

(c) Horizontal trapping frequency EXDT

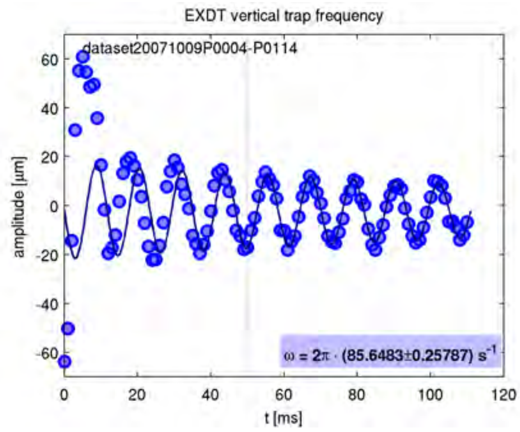

(d) Vertical trapping frequency EXDT

Figure 3.5: Center of mass oscillations of a BEC in two different trap geometries. Shown are measurements of the vertical and horizontal trap frequencies in a symmetric crossed dipole trap (XDT) employed for the lattice experiments and in an elongated crossed dipole trap (EXDT) used in the framework of soliton dynamics. The vertical dotted (dashed) lines mark the lower (upper) bound of the fit interval.

tial as the starting point for all later experiments could be satisfied with the setup of a crossed-beam optical dipole trap as depicted in Fig. 3.4c. As an improvement to the single beam trap ALL trapping frequencies are determined by the transverse confinement of the beams and can therefor be independently adjusted. By choosing suitable waist sizes of the two beams almost arbitrary aspect ratios can be achieved. The most symmetric case is of course realized by taking two beams with equal waist size. Once again the optical power is delivered by single mode fibers which terminate with beam shaping telescopes as shown in Fig. 3.2b. In our experiment two Gaussian laser beams with a beam waist of $w_0 = 40\,\mu$m each, intersect at the point of minimal beam waist. In this way a trapping potential with an aspect ratio of $1 : 1 : \sqrt{2}$ is created. The potential can even be made more symmetric due to the following fact: In order to produce and maintain a condensate in an optical dipole trap at very low temperatures two different methods can be employed. Cooling of the atomic ensemble by selective parametric excitation [116] removes only atoms in higher vibrational trap levels and has proven to work well in the astigmatic trap. However a

Table 3.2: Trapping frequencies and expected power scaling of the optical dipole traps used in this work. Data for the astigmatic trap is taken from [71]. For the crossed beam traps, compare Fig. 3.5.

	at power	ω_x	ω_y	ω_z
astigmatic	$P = 48\,\mathrm{mW}$	$2\pi \times 16.7\,\mathrm{Hz}$	$2\pi \times 118\,\mathrm{Hz}$	$2\pi \times 690\,\mathrm{Hz}$
symmetric	$P = 43\,\mathrm{mW}$	$2\pi \times 0.8\,\mathrm{Hz}$	$2\pi \times 133\,\mathrm{Hz}$	$2\pi \times 86\,\mathrm{Hz}$
XDT	$P_x = P_y = 38\,\mathrm{mW}$	$2\pi \times 90\,\mathrm{Hz}$	$2\pi \times 89\,\mathrm{Hz}$	$2\pi \times 127\,\mathrm{Hz}$
EXDT	$P_x = 43\,\mathrm{mW}, P_{2D-1} = 8\,\mathrm{mW}$	$2\pi \times 5.8\,\mathrm{Hz}$	$2\pi \times 133\,\mathrm{Hz}$	$2\pi \times 86\,\mathrm{Hz}$
	optical power	ω_x	ω_y	ω_z
single beam	P	$\propto \sqrt{P}$	$\propto \sqrt{P}$	$\propto \sqrt{P}$
XDT	P_x, P_y	$\propto \sqrt{P_y}$	$\propto \sqrt{P_x}$	$\propto \sqrt{P_x + P_y}$
EXDT	P_x, P_{2D-1}	$\propto \sqrt{P_{2D-1}}$	$\propto \sqrt{P_x}$	$\propto \sqrt{P_x}$

more straight forward approach is to reduce the trap depth to such a low level that all excited atoms are immediately spilled out of the trap. Moreover this technique provides a continuous cooling mechanism throughout the whole experimental sequence. As shown in Fig. 3.3b, very low trap power leads to a convergence of the horizontal and vertical trapping frequencies for a small range of optical power settings. Working in this regime is an ideal starting point for loading cold atoms in an optical lattice. Fig. 3.5 shows exemplary measurements of vertical and horizontal dipole oscillations in the crossed dipole trap.
For the sake of reproducibility, stability and experimental ease the two XDT laser beams are intensity stabilized. Moreover intensity noise at Fourier components of twice the trapping frequencies ω_i may lead to heating through parametric excitation. Fortunately the output of the Nd:YAG laser (INNOLIGHT Mephisto) already features a very high suppression of intensity fluctuations, so that the main task consists in keeping them low along the optical path of the beams. Rigid design of all opto-mechanical elements, especially the fiber couplers and a thorough design of the fiber laying guarantees a very low level of intensity fluctuations [71]. To ensure a reproducible constant power level of the laser, independent of e.g. the fiber coupling efficiency, a simple servo loop has been set up as described below. A small portion of light is picked off the beam with a pellicle beam splitter in front of the last focusing lens [4]. A pure integral servo controller actuating an acousto optical modulator (AOM) in front of the fiber regulates the beam intensity to within less than 10^{-3}. This ensures excellent experimental conditions, necessary for reliable creation of very cold BEC with constant and controllable particle number.

Tab. 3.2 summarizes measured trap frequencies and expected power scaling for all of the optical traps used for the experiments presented in this work. However, due to the aforementioned reasons the power scaling has to be treated with great care when trying to estimate trapping frequencies for different trap depth.

[4] A pellicle beam splitter is used to eliminate any ghosting.

3.2.6 Elongated crossed dipole trap (EXDT)

The experiments on solitons in Bose-Einstein condensates presented in Chapter 6 demand for a very elongated trap geometry in order to reach the regime of quasi one-dimensional BEC. One of the major goals of these measurements was the observation of soliton oscillations in a trapped BEC. The single waist dipole trap fulfills the requirement of very high aspect ratio but due to the very low axial trapping frequency of $\omega_z \leq 2\pi\, 1\,\mathrm{Hz}$ it is quiet demanding to observe soliton oscillations expected with a frequency $\Omega = \omega_z/\sqrt{2}$. To independently control the axial trapping frequency we have added one of the beams of the triangular optical lattice (see Chapter 5 for more details) traveling in the vertical direction. The large waist size of $w_0 = 117\,\mu\mathrm{m}$ together with a sensitive intensity controller allows for a precise adjustment of the axial trapping frequency. The experiments have been performed at an identical aspect ratio to keep the experimental conditions constant throughout the different series. The trapping frequencies of this configuration are listed in Tab. 3.2.

3.3 Detection of Spinor BEC

The usual way to detect Bose-Einstein condensates in current experiments is to image them with resonant or off-resonant light on a CCD camera. Depending on the specific experimental demands absorption or phase-contrast imaging can be the best choice to determine the desired parameter as accurate as possible. Absorption imaging is superior in terms of experimental ease and is distinguished by the highest sensitivity to particle number. Unfortunately it is a destructive detection method, which makes the non-destructive phase-contrast imaging the method of choice, when in-situ measurements with high temporal or spatial solution are required. An excellent introduction to both techniques is given in [117]. The reader is referred there for details. A collection of useful formulas used to determine particle numbers is given in Appendix C. Other detection methods for cold atoms like e.g. diffraction-contrast [118] imaging have been considered in proof-of-principle experiments but have not been made standard practice. In the course of this work absorption imaging has been employed vastly even though phase-contrast methods have been occasionally tested. In the following some particularities concerning imaging of multi component quantum gases as well as a little discussion of image post-processing techniques are presented. More details concerning specific methods used at our experiment can also be found in [103, 71, 119].
The investigation of static and dynamical properties of spinor BEC demand for additional information on the internal state or the magnetization respectively. The method of Stern-Gerlach separation prior to absorption imaging has been vastly employed at our experiment and will be discussed.

3.3.1 Absorption imaging

The master experimental setup for absorption imaging consists of a fiber coupled illuminating laser beam, expanded to a diameter of several centimeters, a custom-designed 5 (7)-lens detection optics (B. Halle), with a magnification of 2.58 (9.9) and a CCD camera (SenSys 3200ME) with a pixel size of $6.8\,\mu\mathrm{m}$. The resolving capacity of the detection optics is on the order of $2\,\mu\mathrm{m}$ [120], enabling spatially well resolved studies of spinor BEC important for experiments on dark solitons and magnetic domain formation as discussed later. To obtain an absorption image that is free of interference fringes and/or other effects of inhomogeneities in the detection beam or dust particles on the surfaces of optical elements three distinct images are recorded. An absorption image containing the shadow casted by the atomic cloud, a reference image without any atoms and a dark image without any illumination. The optical column density is then easily calculated according to Beer's law

$$n_{\mathrm{OD}} = -\ln\left(\frac{I^{\mathrm{abso}} - I^{\mathrm{dark}}}{I^{\mathrm{ref}} - I^{\mathrm{dark}}}\right). \tag{3.24}$$

Unfortunately the read-out-time of the camera amounts to 4 s, which leads to an unavoidable shift of the interference pattern between two pictures due to mechanical vibrations of the whole apparatus. As a result a residual fringe pattern is always visible, possibly obscuring the visibility of spatial details in the atomic density distribution and reducing the maximal achievable precision in the determination of particle numbers. Possibilities to minimize the effect of interference fringes are discussed below.
An alternative Slave detection setup is capable of imaging the atomic cloud along the quantization axis and therewith perpendicular to the triangular optical lattice as described in Section 3.6. A second CCD camera (PCO Pixelfly QE) with a pixel size of 6 μm capable of taking two absorption images within 50 μs is used here in conjunction with a 1:1 imaging optics consisting of two commercially available achromatic lenses (Melles Griot). For technical reasons the minimal distance of the first lens to the glass cell is approximately 40 cm limiting the resolving power considerably to not more than 6 μm. However, throughout this work only absorption images incorporating fairly long times of flight have been employed, so that the constrain imposed by the reduced resolution was of no consequence.

Fringe reduction

We have measured the temporal correlation of the fringe pattern and found a significant decrease already on a millisecond scale [119]. The only way to circumvent image post-processing is therefor to take the absorption- and reference picture on a time scale considerably shorter than 1 ms. This technique is indeed used in the Slave detection setup employing the double-shutter option of the PCO camera. The repetition rate in this mode is rather high eliminating most of the interference fringes.
In the case that the fringe pattern can be unambiguously traced back to the interference between two distinct optical elements, the insertion of a quarter wave-plate between those two elements may significantly decrease the fringe contrast. In our experimental set up the interference between the glass cell and the surface of the CCD chip has proven to be the most prominent source of fringes. Still, the quality of the images couldn't be improved to a satisfying level by eliminating these interferences. Since the above mentioned restrictions can not always be fulfilled image post-processing as briefly sketched below may fairly reduce the residual interference pattern. One very fact that is at the heart of the algorithm used to reduce fringes is the observation that the patterns only move very little with recurrence of their initial phase after a certain time, depending on whose opto-mechanical element's vibration or thermal expansion is responsible for the movement. For these reasons it is possible to construct a new reference image $\tilde{I}_{\mathrm{ref}}$ as a linear combination out of only ≈ 50 images from the same experimental series $\tilde{I}_{\mathrm{ref}} = \sum_n c_n I_{\mathrm{ref},n}$. The first step is to construct a basis set of orthogonal images from all available images from one experimental series. Since an CCD image can simply be regarded as a vector in a $\mathbb{R}^{N_x \times N_y}$ vector space, algebraic methods like the Gram-Schmidt orthonormalization scheme [121]

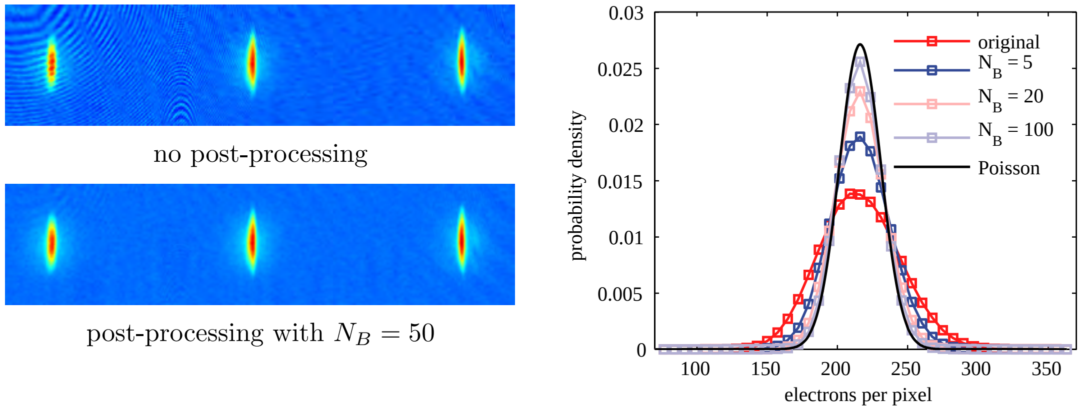

(a) Example for the effect of post-processing. (b) Histograms of pixel noise.

Figure 3.6: Reduction of interference fringes by post-processing with an N_B-element basis. Histograms are based on a 200×200 pixel section from 10 random test images. For these histograms, the artificial reference image has been subtracted from the test images, instead of dividing the test images by the artificial reference image.

---

can be used to build the basis set B_n of pictures that fulfill the orthogonality condition $(B_n, B_m) = \delta_{n,m}$. The final best-fit reference image $\tilde{I}_{\text{ref}}$ is then constructed under the additional restriction that the integrated atom number outside the regions that contains atoms is equal to zero:

$$\tilde{I}^{\text{ref}} = \sum_n \left(I^{\text{abso}}, B^n\right) B^n. \tag{3.25}$$

The particle number restriction is necessary to be able to determine atom numbers by just summing the column density over the desired regions of the image. Significant errors occur if this last post-processing step is omitted. Fig. 3.6a shows the impressive improvement that can be achieved in optical quality of the images and in terms of shot-noise limited photon counting. Fig. 3.6b has been obtained from a homogeneously illuminated region of a set of arbitrary test pictures. The expected Poissonian distribution of the counts-per-pixel is very well approximated already for moderate basis sizes. A very detailed and exhaustive presentation of the underlying physical and technical aspects of imaging of BEC can be found in the Diploma thesis of M. Brinkmann [119]. Other interesting aspects of fringe reduction in absorption imaging like imaging with spatially incoherent light have been raised at the Hamburg spinor experiment. However they have been presented in a very illustrative way in Jochen Kronjäger's PhD thesis [71] and will be omitted here.

Double exposure detection

A particularly useful detection method for $|1, m_f\rangle$-$|2, m_F\rangle$ has been employed in the framework of the filled solitons experiments. In order to distinguish the two components on a single image a double-exposure technique has been employed. The atoms are first exposed to light resonant with $|2, m_F\rangle$-states only. After a short wait time of 2 ms the atoms in $|1, m_F\rangle$ are optically pumped to $|2, m_F\rangle$ and subsequently imaged with a second resonant light pulse. The advantage of this method is the possibility to directly compare the particle number and axial structure of the two components without any further post-processing. Some attention has to be paid to the determination of the optical density, since the new images $\tilde{I}^{\text{abso}}$ and $\tilde{I}^{\text{ref}}$ contain more light than desired by Equ. 3.24:

$$\tilde{I}^{\text{abso}} = I^{\text{abso}} + I^{\text{ref}} \tag{3.26}$$

$$\tilde{I}^{\text{ref}} = 2 \cdot I^{\text{ref}} \tag{3.27}$$

Assuming that the dark image can be neglected [5] , the correct optical density can be easily calculated as

$$n_{\text{OD}} = -\ln\left(2e^{-\tilde{n}_{\text{OD}}} - 1\right). \tag{3.28}$$

3.3.2 Spin-selective detection

When dealing with Spinor BEC one of the most interesting experimental measures is the distribution of the atomic density among the different m_F-states. One technique to distinguish between the different magnetic states is magnetization dependent phase-contrast imaging [63, 122] based on the Faraday rotation of light polarization through a magnetized gas [123]. More details attending to the application of this method can be found in [124]. At our experiment in contrast the method of choice is the separation of m_F-states through the application of a Stern-Gerlach-like magnetic field gradient during time-of-flight. Different m_F-states are separated according to the law $F = -\mu_{\text{B}} g_F m_F \nabla B$ which allows for an independent determination of the particle number in different states. Note however, that the relative phases needed for a complete characterization of the quantum mechanical state are not determined in this way and remain unknown. Only the diagonal elements can be specified. In principal tomographic methods imaging the sample in the way described above from $4F + 1$ different directions could be merged to obtain the complete density matrix [125, 126]. This technical demanding detection setup has not been implemented in our apparatus however.
In order to have a well defined quantization axis during the Stern-Gerlach separation, a sufficiently large magnetic offset field has to be applied. Some attention has to be paid to the switching of this offset field. A rise of the axial offset field $\dot{B}_{\text{off},x}/|\mathbf{B}|$ slow compared to the transverse Larmor frequency $g_F\mu_B/\hbar|B_\perp|$ will lead to adiabatic rotation of the spin. If , on the other hand the field is switched non-adiabatically, i.e. $\dot{B}_{\text{off},x}/|\mathbf{B}| \ll g_F\mu_B/\hbar|B_\perp|$ the spin states are projected onto the new quantization axis defined by $B_{\text{off},x}$. The rise-time of the current in the coils generating the offset field is on the order of $0.1\,\text{G}/\mu\text{s}$ leading to non-adiabatic switching for transverse fields $|B_\perp| \ll 150\,\text{mG}$, which is usually well fulfilled in our experiment when all residual magnetic fields are well compensated. This important fact is extensively used when zeroing the magnetic field, where it is crucial to correctly interpret Stern-Gerlach pictures in order to compensate residual offset fields as good as possible (see Section 3.4). When the angle between the magnetic field $\mathbf{B}_{\text{ini}}$ before switching the offset field and $B_{\text{off},x}$ is small, the effect of projection can safely be neglected. For the interpretation of all measurements on spin dynamics presented in this work, this is the fundamental precondition, i.e. the measured spin-state distribution is

[5] The dark count rate for the SenSys CCD camera employed for this detection method is very low. Together with the very short exposure time, the dark counts per pixel are always in the range of one or two and can safely be ignored.

Table 3.3: Characteristics of the compensation coil cube, calculated using Ampère's law. The measured value for B_x is $275 \pm 1\,\mathrm{mG/A}$, in good agreement with the calculation. The comparison may serve as an error estimate for the remaining coefficients.

coil pair	quantity	coefficient	unit
Helmholtz horizontal	B_x, B_y	0.286	G/A
Anti-Helmholtz horizontal	$\partial B_x/\partial x$	0.034	G/(A cm)
Helmholtz vertical	B_z	0.521	G/A

equal to the spin-state distribution before the Stern-Gerlach separation.

3.4 Controlling magnetic fields

The investigation of magnetic properties like ground state phases and spin mixing dynamics of Spinor BEC demands for a very well controlled magnetic field. The energy scale of spin dependent interactions in ^{87}Rb corresponds to magnetic fields of the order of several mG. Moreover state preparation is often achieved by pulse techniques employing magnetically sensitive transitions. A clean and reproducible initialization of any experiment involving multi-component BEC is therefor indispensably connected to a highly stable finite magnetic offset field $\mathbf{B}_0$. To achieve a magnetic field as low/accurate as the above conditions ask for a thorough compensation of interfering fields from various sources has to be performed. The earth's magnetic field makes the largest contribution with values of typically 0.5 G [127], while technical sources like power supplies, permanent magnets of ion pumps and residual (weak) magnetization of steel parts of the apparatus contribute considerably less. The most annoying technically induced stray fields are ac fluctuations with peak-to-peak amplitudes on the order of $2-4\,\mathrm{mG}$. Since the experiments take place inside an ultra-high vacuum chamber, no magnetic sensor can be placed at the position of the BEC, rendering the determination of the magnetic field with conventional methods impossible. For this reason we have developed a method of calibrating our magnetic fields, using the atoms themselves as a magnetic sensor.

The precondition for the procedure described below is a working BEC machine with condensates produced in an optical dipole trap and subsequent Stern-Gerlach analysis. In our experiment various multi purpose coils can be used in an approximate Helmholtz- or anti-Helmholtz configuration in order to generate homogeneous fields or pure magnetic field gradients. It has proven sufficient to compensate for the offset field components B_x, B_y and B_z and only two components of the magnetic field gradient tensor $\partial_i B_j$ namely $\partial_x B_x$ and $\partial_z B_x$. As described earlier in this chapter the atoms reside in the $|1, -1\rangle$-state when loaded from the magnetic trap into the optical dipole trap. For sufficiently large offset fields $\mathbf{B}_0$ only one spin component should be detectable in Stern-Gerlach separation (SGS). This required initial condition is usually fulfilled, since the preceding optical molasses also demand for a quite well compensated magnetic field. In a next step $\mathbf{B}_0$ is being set to zero which should lead to an occupation of more or less all spin states after SGS. This means that the residual magnetic field is mainly transverse, and the maladjustment for the axial compensation coils current is not too large. Following this check the offset field is set to a reasonably low value of typically 100 mG or even less depending on the quality

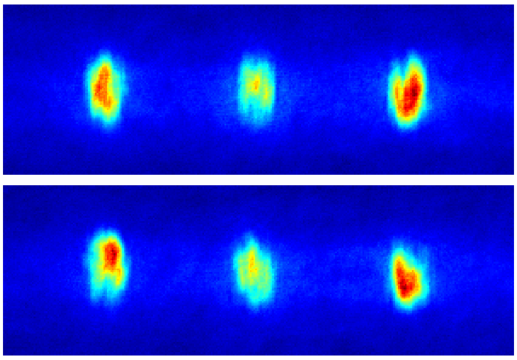

(a) Elongated geometry

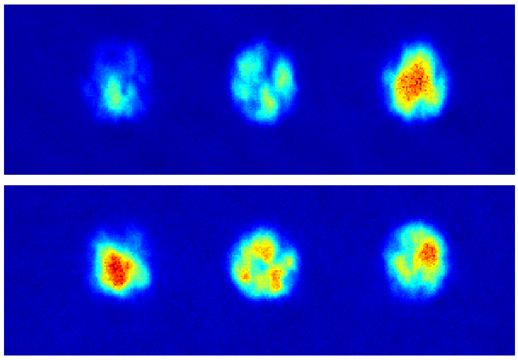

(b) Isotropic geometry

Figure 3.7: Typical structured spinor condensates in the crossed dipole trap at zero offset field, indicating optimum stray field and gradient compensation. Gradient compensation currents are those deduced from Fig. 3.8. The pattern as well as the relative population of spin states varies randomly from shot to shot, probably due to AC stray fields. Since the hold time at zero offset field is comparatively long, the line trigger is ineffective in this case.

---

of the initial compensation. The offset field is lowered until the $|1,0\rangle$-state gets weakly populated after SGS. As described in Section 3.3 the population of other spin states is a result of the projection of the $|1,-1\rangle$-state along the initial B-field direction onto the experiment's symmetry axis defined by the Stern-Gerlach field. If the angle between the initial and the final magnetic field is sufficiently large, populations in other spin states will be observed. This very fact can be employed to calibrate the transverse components of the compensation field. Properly reducing the transverse part of the residual field will make the additional $|1,0\rangle$ component disappear. A successive iteration of these steps is employed until no further improvement can be observed. Usually a careful application of this algorithm leads to a minimal offset field of 6 mG corresponding to a current of not more than 20 mA. At this point the sensitivity to current maladjustment's in the transverse direction is on the order of the resolution of the precision current sources which is 1 mA - less than one mG. In a last step the axial compensation field is adjusted by again setting $\mathbf{B}_0$ to zero while simultaneously changing one of the currents through the transverse coils by about 20 mA. The resulting field should be purely transverse, leading to a spin distribution symmetric with respect to $m_F = 0$. If this is not the case, the axial compensation field is adjusted in order to achieve a distribution as symmetric as possible. Since the above method does not allow to compensate the axial field as precise as the transverse fields (sensitivity is about $3 - 5\,\text{mA} \approx 2\,\text{mG}$), two additional steps should be added to improve the overall magnetic field compensation. A good cross check for the compensation is to set the offset field equal to zero and study the resulting spin state distribution. A well compensated magnetic field leads to population of all three spin states which in addition should be spatially structured (see Fig. 3.7).

The latter implies, that the variations of the field across the condensate are on the same order of magnitude as the residual field itself. Moreover variations of the magnetic field are not restricted to the spatial domain, but change also with time, so that the patterns observed differ from shot-to-shot. Once the magnetic field has been compensates very well, rf-pulses can be used to transfer population between different m_F-states (see Section 3.5). We have determined the parameters and frequencies necessary to perform π-pulses transferring the atoms from $|1,-1\rangle$ to $|1,+1\rangle$. Since a π-pulse is a relatively fragile method to prepare states, its transfer efficiency crucially depends on the chosen frequency. Once determined the frequency needed for a perfect π-pulse can be checked for different offset fields, which delivers another tool to check for the quality of the compensation. The degree of compensation that can be achieved for the axial field in this way amounts to roughly 2 mG. Finally the lowest achievable offset field that can be safely chosen to work with has been $10\,\mathrm{mG} \mathrel{\hat{=}} 30\,\mathrm{mA}$. Better compensations can be achieved for short times, but it seems that background fields drift in time, so that lower, well-defined offset fields cannot be established over times long enough to perform thorough measurements. The ac-stray fields mentioned at the beginning of this section are obviously on the same order of magnitude or even larger than the residual dc-fields after the compensation procedure. They can be avoided as much as possible by keeping line-operated laboratory electronics as far away from the vacuum chamber as possible. In an attempt to provide even more reproducible experimental conditions we have implemented a line trigger that synchronizes the whole experimental sequence to the mains cycle: After we have prepared a BEC in the desired spin state distribution we wait a short time on the order of the inverse mains frequency and trigger the beginning of the evolution time of the atomic sample to a zero crossing in the mains cycle. This really does improve the reproducibility, but unfortunately only on a time scale as short as approximately 1-2 mains cycles. The main reason for that, is that the mains frequency is only 50 Hz on average but varies significantly on even short time scales. We have checked the influence by performing Ramsey experiments without and with the line trigger and observed significant improvement in terms of smaller deviations from the desired resonance frequency (see [71] for details).

For even more homogeneous magnetic fields, the next step in the compensation procedure is to cancel for the variations of the magnetic field across the condensate. The tensor of the magnetic field gradient $\partial B_{x,y,z}/\partial x, y, z$ cannot be totally canceled with realistic experimental effort. However, under the restriction $\nabla \cdot \mathbf{B} = 0$ the most limiting components of the tensor $\partial_i B_j$ can be tackled and minimized. Many experiments presented in this thesis deal with condensates which are considerably elongated along the axis of symmetry (the x-direction), the most important gradient will therefor be along the x-direction. In addition at a finite offset field $\mathbf{B}_{\mathrm{off}} = B_0 \cdot \mathbf{e}_x$ axial deviations contribute linearly to the absolute value of the magnetic field, whereas transverse fluctuations enter only quadratically. A pair of compensation coils is used in anti-Helmholtz configuration to generate a more or less pure gradient field without the addition of a considerably large offset field. Fig. 3.8 shows the influence of the $\partial_x B_x$ compensation in absorption images. A displacement of the $|1,\pm1\rangle$ condensates relative to their thermal clouds can be observed. A current of $0.5 \pm 0.1\,\mathrm{mA}$ is needed for optimum cancellation where the displacement vanishes, indicating a gradient of $\partial_x B_x \approx 15\,\mathrm{mG/cm}$. The remaining uncertainty of $\Delta\partial_x B_x \approx 3\,\mathrm{mG/cm}$ corresponds to a Zeeman energy difference between adjacent m_F-states of $2\pi \cdot 20\,\mathrm{Hz}$ for typical condensate extensions of $100\,\mu\mathrm{m}$. By using a small pair of off-axis Helmholtz-like coils, $\partial_z B_x$ has been compensated for few experiments. However, driving a current through these coils adds an offset field in the x-direction of several hundred mG, demanding for a new calibration of the homogeneous compensation field as well. Usually the effort connected to this procedure is not worth the enhancement and is often abandoned. For completeness it should be mentioned that currents of $1-2\,\mathrm{A}$ assure an optimum compensation. Fig. 3.8 finally illustrates how gradient compensation influences the inhomogeneous patterns observed for

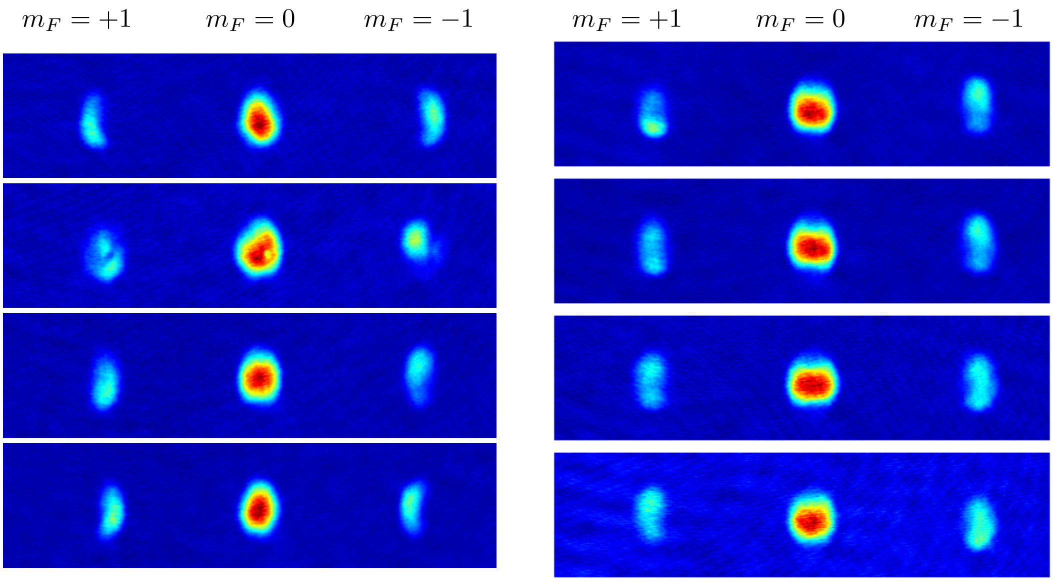

(a) Varying $\partial_x B_x$ (top to bottom: 1 A . . . 0 A in steps of 0.2 A) at zero $\partial B_x/\partial z$ compensation

(b) Varying $\partial_z B_x$ (top to bottom: 0 A . . . 3 A in steps of 1 A) at optimum $\partial_z B_x$

Figure 3.8: Selected images of spinor condensates in the crossed dipole trap at zero offset field, demonstrating gradient compensation. This kind of experiment has been used to find the optimum compensation currents. In the left column, it can be seen how the $m_F = \pm 1$ components separate under the influence of the magnetic field gradient and swap places when it changes sign (from both "outwards" with respect to $m_F = 0$ at the center to both "inwards"). In the right column, similar behavior can be seen in the vertical direction depending on the vertical gradient. Optimum compensation currents deduced from these images are 0.5 A for $\partial B_x/\partial x$ (left) and 2 A for $\partial B_x/\partial z$ (right).

---

almost perfect magnetic field compensation and how these images can be employed to cancel the desired gradients as good as possible.

3.5 State preparation and analysis

The preparation of well defined initial states is at the heart of every quantum mechanical experiment. When dealing with multi-component systems the spatial and internal degrees of freedom can often be prepared separately. Our experimental setup provides a variety of preparation and analysis tools that will be briefly sketched in this section. For the preparation of distinct m_F-state distributions or spinors rf pulses and sweeps are employed. On the other hand micro-wave techniques are used to transfer atoms between different hyperfine states. Spatially resolved phase and state preparation can be achieved by the usage of a Raman laser system together with a spatial light modulator. Finally a Bragg laser system is presented enabling us to determine coherence properties and momentum spectroscopy of BEC.

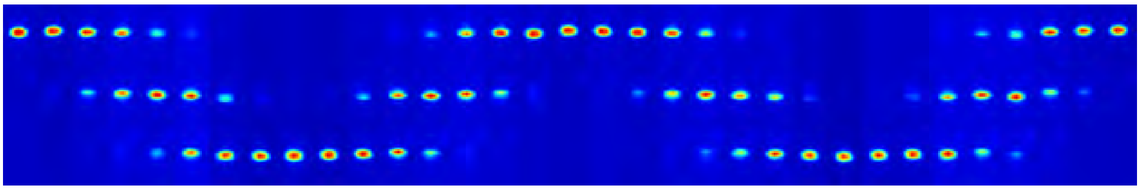

Figure 3.9: Rabi-like oscillations in $F = 1$, driven by continuously applied rf. The condensate is initially prepared in $F = 1, m_F = -1$ (top row) and is driven through a superposition of all three m_F-states to a pure $m_F = +1$ state, before the dynamics is reversed. The pictures are taken at intervals of $10\,\mu$s. Note that only a small fraction of all possible superpositions of the three m_F-states are situated on the Bloch sphere and therefor appear in the Rabi cycle.

3.5.1 Rf- and microwave pulses and sweeps

Spin rotations

At small magnetic offset fields the quadratic Zeeman splitting is usually negligible compared to the Rabi frequency of the rf coupling (a few kHz). The dynamics of an initially stretched state is then well described within the classical spin picture (Section 4.1.1). In the rotating frame, applying rf power induces a rotation around the x-axis at the rate of the Rabi frequency, while waiting and doing nothing corresponds to a rotation around the z-axis at the rate of the detuning between radio and Larmor frequency. Arbitrary points on the Bloch sphere can be addressed by nested rf pulse sequences. Sophisticated techniques and error resistant sequences have been developed in the context of nuclear magnetic resonance (NMR) [128].
In practice the correct Larmor frequencies and pulse durations are roughly known from experience. A first rough estimate for the Larmor frequency can be obtained by using text book values for the Zeeman splitting of ^{87}Rb . In a next step more precise values for the Larmor frequency are found by choosing an approximate π-pulse of $80\,\mu$s and adjusting the frequency for maximum rotation away from the initial $|F, -F\rangle$-state. A perfect π-pulse at zero detuning will transfer all atoms to the opposite stretched state $|F, +F\rangle$. The Rabi frequency is then adjusted by varying the amplitude such that a pulse duration of $40\,\mu$s corresponds to a $\pi/2$ pulse, i.e. leads to a symmetric distribution of the population over all m_F states. If necessary the procedure is iterated. Using this protocol, the Larmor frequency can be obtained to a precision of about 1 kHz. For improved precision, the π-pulse is replaced by a Ramsey sequence, with wait times between the two $\pi/2$-pulses from $10\,\mu$s up to 1 ms. The frequency is then continuously adjusted for maximum population of the $|F, +F\rangle$-state as before. Care has to be taken not to increase the waiting time by more than a factor of two in each step, in order to keep the rotation due to detuning always within $\pm\pi$. The resulting uncertainty of the Larmor frequency is decreased to 100 Hz in this way.

The specific advantage of spin rotations is that the relative phases of different m_F components are well defined, which makes it superior to sweeping techniques concerning the initialization of superposition states. Note that preparation using rf-pulses is neither limited to stretched states nor to $\pi/2$ pulses. E.g., a $\pi/2$ pulse applied to a pure $|F = 2, m_F = 0\rangle$ state can be used to prepare a superposition of $m_F = \pm 2$ and $m_F = 0$ only, a state that is characterized by the absence of g_1 coupling (Section 4.2.1); other useful examples can be found in [71]. Pulses corresponding to very small population transfer can be employed to generate small “seed” populations in m_F states adjacent to a single

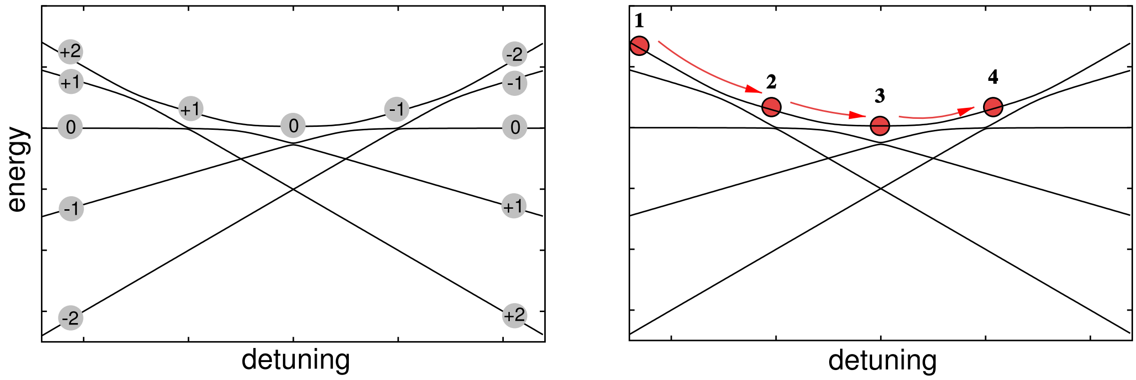

Figure 3.10: Schematic level diagram of dressed m_F states versus detuning $\Delta = \omega_{\mathrm{rf}} - \omega_{\mathrm{L}}$. LEFT: The quadratic Zeeman effect lifts the degeneracy of the resonance. Without it, all levels would intersect at zero detuning. Coupling of adjacent levels ($\Delta m_F = \pm 1$) turns level intersections into avoided crossings. RIGHT: Sweeping the radio frequency, a population prepared in $m_F = +2$ adiabatically follows the dressed state across avoided intersections and ends as a pure $m_F = -1$ population when the sweep is interrupted between resonances. (see also [103])

strongly populated one at a well defined phase.
A $\pi/2$-pulse is also employed to prepare the particular superpositions $\zeta_{\pi/2} = (1/2, 1/\sqrt{2}, 1/2)$ in $F = 1$ and $\zeta_{\pi/2} = (1/4, 1/2, \sqrt{3/8}, 1/2, 1/4)$ in $F = 2$ which are the initial states of choice for the experiments on spin dynamics presented in Chapter 4. Both states are fully transversely magnetized states, $\zeta_{\pi/2} = e^{i\frac{\pi}{2}\mathbf{F}_y}\zeta_{-F}$ where $\zeta_{-F} = (0,0,1)$ or $(0,0,0,0,1)$, respectively.

Rf adiabatic passage

The characteristic regime for spin rotations is that of a negligible quadratic Zeeman effect. As a result, *all* transitions between adjacent m_F levels are degenerate. At larger offset field, where the quadratic Zeeman effect is of the order of 100 kHz and thus much larger than the Rabi frequency of the rf coupling, this degeneracy is lifted. Transitions between specific m_F levels can be selectively addressed by tuning the radio frequency (Fig. 3.10). Rf *sweeps* can be used to adiabatically transfer population between specific m_F substates, enabling access to non-stretched states, e.g. $|1,-1\rangle \rightarrow |1,0\rangle$. Superpositions can be prepared as well by sweeping more quickly, violating adiabaticity; however, in this case the relative phases are not well defined. This technique has been used extensively in early experiments of our group [7, 103]. The offset field is chosen at 26 G, corresponding to a linear Zeeman splitting of 18 MHz and transition frequencies between m_F components spaced at 47 kHz due to the quadratic Zeeman effect. Sweeping over 50 kHz in 1 ms is sufficient to ensure adiabaticity [103].
While the use of quick rf sweeps to generate mixtures is problematic, adiabatic sweeps employed for the preparation of pure m_F-states are an invaluable tool due to their robustness against small changes in crucial experimental parameters, e.g. magnetic offset field or rf power. Used to prepare initial states for subsequent rotation by pulses, they also greatly increase the range of mixtures accessible by the latter technique (see also [71]).

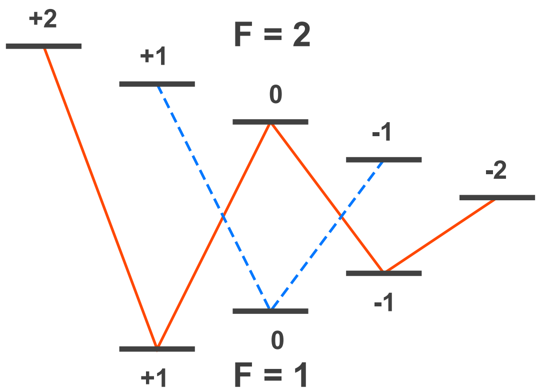

Figure 3.11: Preparation scheme using microwave sweeps. Each colored path can be completed in a single sweep, taking the population along from one $|F, m_F\rangle$ state to the next. In the example below, we start in $|2, -2\rangle$ and follow the solid path to $|2, +2\rangle$.

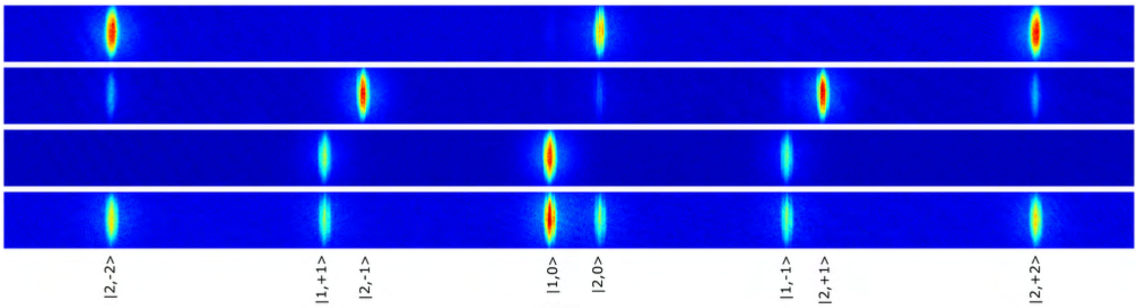

(a) Various superpositions of $F = 2$ and $F = 1$, used to calibrate Stern-Gerlach imaging. $F = 1$ and $F = 2$ positions differ due to the quadratic Zeeman effect.

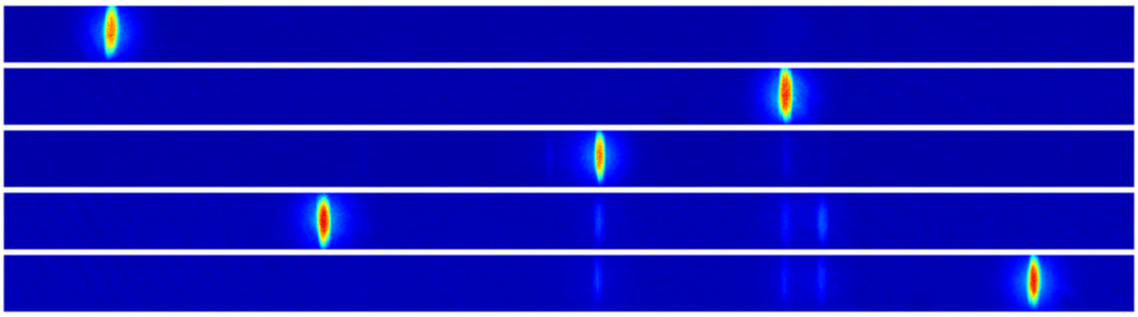

(b) Successive preparations using successive microwave sweeps. From top to bottom: $|2, -2\rangle \rightarrow |1, -1\rangle \rightarrow |2, 0\rangle \rightarrow |1, +1\rangle \rightarrow |2, +2\rangle$. The individual sweeps can also be combined into a single one spanning all transitions.

Figure 3.12: Preparation of $F = 2$ and $F = 1$ using microwave sweeps.

Hyperfine changing microwave sweeps $F = 1 \leftrightarrow F = 2$

By the implementation of a rectangular wave guide suited for microwave (mw) fields in the range of $5 - 8\,\text{GHz}$ transitions between different hyperfine states $|1, m_F\rangle \leftrightarrow |2, m_F \pm 1\rangle$ can be driven as well. Similar to the rf techniques presented above pulse as well as sweep schemes may be used. Even at small offset field, m_F levels can be selectively addressed by precisely tuning the microwave frequency since the individual transitions are now separated by the hyperfine splitting plus or minus multiples of the *linear* Zeeman energy. Due to this very fact the atom can be regarded as an effective two-level system, simplifying the underlying physics. Selection rules and mw polarizations at the position of the atoms limit possible transitions to $\Delta m_F = \pm 1$. E.g., starting from $|1, -1\rangle$ it is thus possible

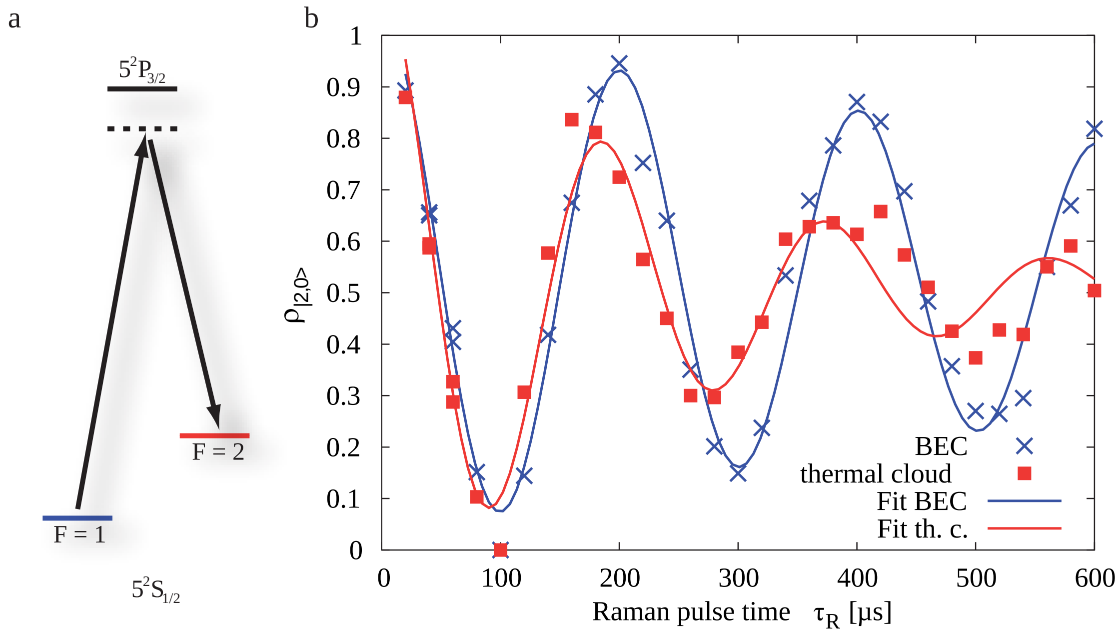

Figure 3.13: Rabi oscillations on the two-photon Raman transition in the Λ-system $|F = 1, m_F = 0\rangle \leftrightarrow |F = 2, m_F = 0\rangle$. The plot shows the relative population of $|2, 0\rangle$ versus the duration of the laser pulse at resonance (Taken from [103]).

to transfer to $|2, 0\rangle$ or $|2, -2\rangle$ in a single sweep. Fig. 3.12 shows how by continuation of this sweep, the population can be successively transferred through all available m_F values, alternating between $F = 1$ and $F = 2$. The achievable Rabi frequency for the $|1, -1\rangle \leftrightarrow |2, -2\rangle$ transition is approximately $\Omega_0 = 2\pi \times 10\,\mathrm{kHz}$, a fully adiabatic sweep may cover a range of detunings of 400 kHz in 0.5 ms.

Apart from the possibility of preparing mixtures, the advantage of using microwave transitions is that switching between $F = 1$ and $F = 2$ is possible without changing anything in the experimental sequence before loading the dipole trap. In particular loading and evaporating in the magnetic trap is always done in $F = 1$.

3.5.2 Raman laser system

In the course of this work it has proven necessary to prepare the internal state of Bose-Einstein condensates *spatially* selective with high resolution. While one possibility would be the use of strong magnetic field gradients tuning the atoms in and out of resonance on a μm scale, we have employed a more elegant and general approach by the use of a Raman laser system. Atoms can coherently be transferred from one hyperfine state $|1\rangle$ to another $|2\rangle$ by a two-photon process in a Λ-scheme via a virtual intermediate state $|3\rangle$ (see Fig. 3.13). Under the restriction that the detuning Δ_e of intermediate and any real excited state is large enough to avoid any population of the upper state, the intermediate state can be eliminated adiabatically [129]. The three level system is therefor reduced to an effective two-level system consisting of the two ground states $|1\rangle$ and $|2\rangle$. Under the additional assumption that the two-photon detuning $\delta = \omega_1 - \omega_2$ is zero, a simple expression for the resulting two-photon Rabi frequency can be derived:

$$\Omega_R = \frac{\Omega_1 \Omega_2}{2\Delta_e}. \tag{3.29}$$

The introduction of a Rabi frequency already anticipates that the whole Rabi picture can be applied to the physical behavior of coherent two-photon processes. The spontaneous scattering rate for the excited level reads

$$\Gamma_{\mathrm{sc}} = \frac{\gamma_e}{4\Delta_e^2}\left(\frac{\tilde{\Omega}_1^2\rho_{11} + \tilde{\Omega}_2^2\rho_{22}}{\rho_{11}+\rho_{22}}\right), \tag{3.30}$$

emphasizing again the need for a preferably large detuning Δ_e. Of course, increasing Δ_e demands for more laser power, which will ultimately set the upper experimental limit for the detuning. γ_e is the lifetime of the excited state, while the ρ_{ii} denote the occupation of the two ground state levels. Note that the $\tilde{\Omega}_i$'s are modified Rabi frequencies which include all one-photon allowed excited levels, that do not necessarily contribute to the two-photon process but unfortunately increase the decoherence, namely $\tilde{\Omega}_i \geq \Omega_i$ – a consequence of the fact that real-world atoms do not represent a perfect Λ-system. Since the width of the two-photon resonance is only on the order of $1-2$ kHz an important effect is the differential ac-Stark shift, which shifts the resonance frequency away from the bare hyperfine splitting Δ_{HFS}. The main reasons for that are again the different modified Rabi frequencies $\tilde{\Omega}_i$ and the different detunings due to the cross coupling of laser 1 to $|2\rangle$ and vice versa:

$$\begin{aligned}
\Delta_{\mathrm{ac-Stark}} &= U_{\mathrm{dip}}^1 - U_{\mathrm{dip}}^2 && (3.31)\\
&= \frac{\hbar}{4}\left\{\left(\frac{\tilde{\Omega}_1^2}{\Delta_e} + \frac{\tilde{\Omega}_2^2}{\Delta_e - \Delta_{\mathrm{HFS}}}\right) - \left(\frac{\tilde{\Omega}_1^2}{\Delta_e + \Delta_{\mathrm{HFS}}} + \frac{\tilde{\Omega}_2^2}{\Delta_e}\right)\right\} && (3.32)\\
&= \frac{\hbar}{4}\left(\frac{\tilde{\Omega}_1^2 - \tilde{\Omega}_2^2}{\Delta_e} + \frac{\tilde{\Omega}_2^2}{\Delta_e - \Delta_{\mathrm{HFS}}} - \frac{\tilde{\Omega}_1^2}{\Delta_e + \Delta_{\mathrm{HFS}}}\right). && (3.33)
\end{aligned}$$

For typical experimental conditions as for the filled solitons experiments, $\Delta_{\mathrm{ac-Stark}}$ usually stays quite small, on the order of a few kHz. However, to achieve a fully modulated perfect π-pulse, the resonance frequency has to be adjusted with an accuracy of a few hundred Hz. It has to be emphasized here, that symmetry considerations lead to a significant constraint concerning allowed two-photon transitions. If the detuning from the excited state hyperfine manifold is much larger then the excited state hyperfine splitting Δ'_{HFS} itself, the detuning to all excited state hyperfine levels $|F'\rangle$ is approximately the same. In that particular case, which is usually realized in our experiments, the overall Rabi frequency can be simplified by rewriting the dipole matrix elements by application of the Wigner-Eckart theorem. It is thus possible to express the Rabi frequency for a specific transition as $\Omega = -\mathrm{E}_0/\hbar \cdot \langle F, m_F|e\mathbf{r}|F', m'_F\rangle$ in terms of the reduced matrix element [6] $\langle J\|e\mathbf{r}\|J'\rangle$ and a separate angular momentum term, which can be calculated by brute force using the Wigner-Eckart theorem or simply looked up in atomic physics tables as e.g. found in [109]. For simplicity this factor will be termed Clebsch Gordon coefficient $c_{CG}(...)$ here, leading to $\Omega = -\mathrm{E}_0/\hbar\ c_{CG}(F, m_F, \mathcal{P}; F', m'_F) \cdot \langle J\|e\mathbf{r}\|J'\rangle$. The two-photon

[6] Reduced matrix elements are usually determined through excited state lifetime measurements[109] following the dependence $\tau \sim |\langle J\|e\mathbf{r}\|J'\rangle|^{-2}$

Rabi frequency can thus be expressed as

$$\Omega_R = \frac{\Omega_1\Omega_2}{2\Delta_e}. \tag{3.34}$$

$$= \frac{\mathrm{E}_{0,1}\mathrm{E}_{0,2}}{2\hbar^2\Delta_e}\sum_{F',\mathcal{P}}\langle 1|e\mathbf{r}|F'\rangle\langle F'|e\mathbf{r}|2\rangle \tag{3.35}$$

$$= \frac{\sqrt{I_1 I_2}}{c\epsilon_0\hbar^2\Delta_e}|\langle J\|e\mathbf{r}\|J'\rangle|^2\sum_{F',\mathcal{P}} c_{CG}(|1\rangle,\mathcal{P};F',m_F')\cdot c_{CG}(|2\rangle,\mathcal{P};F',m_F'). \tag{3.36}$$

Here the electric field amplitude of the laser beams has been expressed in terms of the intensity $I = c\epsilon_0\mathrm{E}_0^2/2$. The most important observation from this expression is that destructive interference between different interaction paths may cancel a two-photon transition strength, even though the involved one-photon processes are all allowed according to the usual selection rules. We will come back to this point later, when discussing the technical prerequisites for the generation of filled solitons.

Fig. 3.13 shows an example of Raman-Rabi oscillations between the to ground state hyperfine states $|1,0\rangle$ and $|2,0\rangle$. The two σ^+-polarized Raman laser beams have been irradiated onto the condensate along the quantization axis. The particular experimental geometry employed for the generation of filled solitons is presented in Chapter 6 in more detail. The different damping rates for the condensate and the thermal cloud emphasize the importance of decoherence, since the spatial extension of the thermal cloud is much larger than that of the condensate, so that inhomogeneities of magnetic fields and/or the Raman laser beam profiles play a much more important role. Moreover severe constraints concerning the coherence – in other words: quality of the phase-lock – of the two Raman lasers are defined by the required coherence time for a specific experiment. Typical Rabi frequencies that can be realized with our experimental setup range from $\Omega = 5 - 10\,\mathrm{kHz}$. A preferably high Rabi frequency is needed for an *instantaneous* manipulation of the condensate on a time scale given by the correlation time $\tau_{\mathrm{corr}} = \hbar/\mu$ as will be seen later.

The setup for the Raman laser system consists of two phase-locked extended cavity diode lasers (ECDL) which are actively stabilized to a fixed frequency difference equal to the hyperfine splitting in ^{87}Rb at around 6.84 GHz. The master laser can be used either free running, locked to an fm-spectroscopy signal or to a cavity via Pound-Drever-Hall (PDH) stabilization. The latter method has been vastly employed in our experiments: The cavity itself is locked to a laser, resonant with the cycling transition of ^{87}Rb by a very simple but sufficient side-of-fringe locking scheme in *transmission*. At the same time the Raman master laser is used as usual in *reflection* to generate the well-known PDH error signal. Note that the polarization of the two lasers has to be perpendicular in order to distinguish the two beams [7]. The advantage of this scheme is the possibility to arbitrarily detune the Raman master by multiples of the free spectral range of the cavity, 4 GHz in this case. Offset-lock techniques can only safely be employed up to detunings of 10 GHz due to the availability of suitable electronics. It has proven in our experiments that larger detunings between 20 and 30 GHz are favorable for coherent population transfer between $|F=1\rangle$ and $|F=2\rangle$. The two laser beams are superimposed and coupled into the same optical single mode fiber, which delivers the light to the experiment. Phase-locked AOM's as well as mechanical shutters allow to switch the light on and off, quickly and reliable. The optical power available at the experiment is limited to about $4-5\,\mathrm{mW}$ per beam and limits the

[7] Since the frequency difference between those two lasers is usually on the order of tens of GHz it is not possible to separate them by the use of dichroic mirrors or similar optics.

maximum two-photon Rabi frequency Ω to the values mentioned above.
A very detailed description of the Raman laser system can be found in the PhD thesis of Dr. Jochen Kronjäger. Concluding, the quality of the phase-lock can be characterized by the rms-phase error $\langle\phi^2\rangle$ Employing different methods,$\langle\phi^2\rangle$ has been determined to be $25°$ (see Section 3.6 for further information). The width of the beat note of the two lasers has been recorded to be less than 1 Hz before coupling them into an optical fiber [8]. That means, the coherence time of the laser is more than sufficient, at least for the requirements set by the generation of filled solitons, where pulse times in the $100 - 1000\,\mu$s range are employed.

3.5.3 Spatial light modulator

Up to date the application of optical dipole potentials on ensembles of ultracold atoms has mainly been realized by exposing them *globally* to laser light. The range of applications runs from optical dipole traps [110] and lattices [80] to the generation of vortices by stirring with a laser beam [10]. Other applications, like e.g. phase imprinting methods [11] demand for the possibility to *locally* manipulate a BEC. So far this has been mainly achieved by imaging some rigid, possibly etched, mask onto the atoms or focusing of Gaussian beams to very small waists. New applications already appear at the horizon: disorder potentials with sub-micron resolution, double-well systems [130, 131] to the point of potentials that can be arbitrarily shaped in space and time.
The rapid developments in the field of video projectors and display production have opened up new possibilities to engineer cold atoms with laser light [132]. The use of spatial light modulators (SLM), characterized by high efficiency, fast switching times and small pixel sizes may be the beginning of a new era of versatile manipulation. We have implemented an experimental setup that enables us to use an SLM together with a very-high-quality optical imaging system with 1/10-fold magnification. That allows us to generate almost arbitrary optical potentials with a resolution limited by the resolving capacity of the imaging system to about $2\,\mu$m [9]. Structures of the size of the healing length of the condensate $\xi \approx 1-2\,\mu$m can therefor be created – essential for the generation of topological structures like solitons and vortices [11, 12, 134]. Single site addressing in tilted optical lattice – one of the holy grails of quantum information in optical lattices – would also be a very "hot" application of SLM's in cold atom experiments to name only one example. The SLM's utilized in our experiment (Fa. HOLOEYE, LC-R 1080) are of *liquid crystal on silicon* (LCoS) *normally black* type and work in reflection as compared to a normal LCD, which works in transmission: Basically the SLM works like a 8-bit voltage controlled wave plate in front of a mirror. The active medium is passed twice in this way. Consequently 256 different phase retardation values for the slow axis can be addressed. In order to achieve amplitude modulation, polarizing optics has to be placed in front of the SLM as shown in Fig. 3.14. The pixel size of the SLM amounts to $8.1\,\mu$m, which is effectively lowered by a factor of ten through the 1/10-fold magnification of the imaging optics. The display provides 1920×1200 pixel (WUXGA-format), which corresponds to an effective controllable area of $1500 \times 970\,\mu$m – large enough to address every position in any conceivable BEC that can

[8] The resolution of the spectrum analyzer used here (Fa. RHODE & SCHWARZ UPV) is 1 Hz. This value can therefor be given as an upper bound for the real width of the beat note.

[9] Obviously the effective pixel size would be smaller than the optical resolution and is consequently convoluted with the modulation transfer function of the imaging system. A detailed characterization of the whole optical setup [133] has indeed shown, that the theoretical possible limit for the resolution of $2\,\mu$m is almost reached in our experiment.

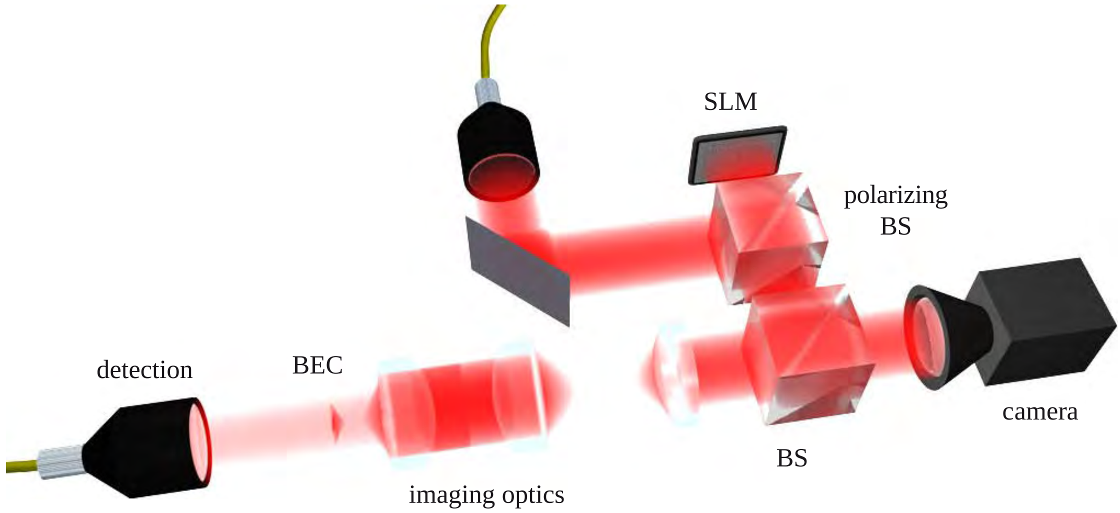

Figure 3.14: Scheme of the setup to optically imprint arbitrary SLM patterns onto the BEC. The high-resolution detection optics is also used to image the SLM patterns. Polarization optics is needed to translate the rotated polarization into intensity modulation

be generated with our machine. The shape of the potential can be changed at will from shot-to-shot, allowing for measurement series that e.g. spatially scan the condensate with some potential barrier. The repetition rate of the SLM's display amounts to 60 Hz and sets the upper limit for changing the optical potential on-line. Unfortunately this rate is too low to manipulate a BEC *in-situ* and dynamically engineer excitations or shift potential minima. Possibly future SLM's will overcome these restrictions and pave the way for even more versatile experiments and unlimited control over Bose-Einstein condensates in the spatial and temporal domain.
A particularly useful experimental setup used to precisely focus the SLM onto the BEC is shown and explained in Fig. 3.15. For the generation of structures of the size of the healing length it is crucial to focus the SLM optics as good as possible. The SLM is mounted on a three-screw mirror holder with precision screws which allows for an excellent control over tilt and focusing position. It has shown that a focusing to within less than half a millimeter is necessary in order to generate deep and reproducible dark solitons. That means that the focus adjustment has to be on the order of approximately one full revolution of the mirror holder screws.
More concrete examples and applications will be given in Chapter 6, where the SLM has been vastly employed together with the Raman laser system to generate dark and dark-bright solitons.

3.5.4 Bragg laser system

Many features of Bose-Einstein condensates have been discovered and studied in detail over the last decade. A valuable tool in this context has been the possibility to track the dispersion of various kinds of excited collective modes, sound velocities and the momentum distribution inside the BEC in general. Bragg spectroscopy provides access to all of the above mentioned quantities and has been employed in the past to prove many the-

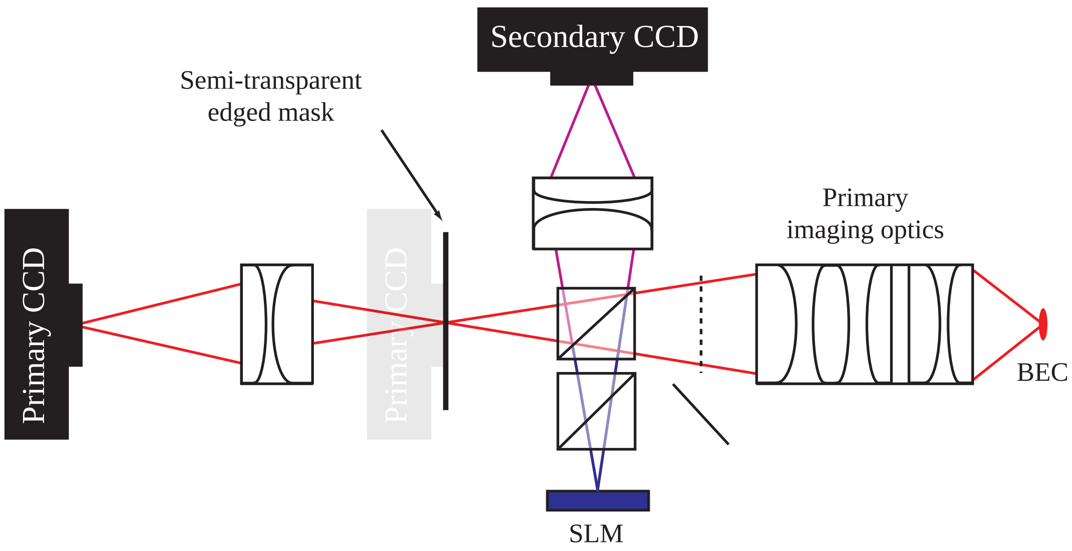

Figure 3.15: Scheme of the setup used to focus the SLM optics. The optical path lengths between CCD camera and BEC and SLM and BEC must be equal in order to have an image of the SLM at the position of the BEC. The primary CCD camera (gray shaded camera) is taken away and the image of the BEC I at the position of the CCD chip is imaged again by another supplementary imaging system $SIS1$ to yield the final image I'. Now an auxiliary semi transparent edged mask is placed at the position of the intermediate image I and adjusted until it is focused. Finally the edged mask and the SLM can be imaged simultaneously employing a secondary CCD camera and another supplementary imaging system $SIS2$. The SLM is now adjusted until both edged mask and SLM are focused,

oretical predictions concerning momentum distribution [135], coherence properties [136] and superfluid flows [137] to name only a few examples. Future applications include measurements on quasi momentum distributions in optical lattices to unambiguously identify novel phases or quasi-particles.

In the course of this PhD thesis a Bragg laser system has been set up together with Dipl. Phys. Thomas Garl. Details concerning theoretical and experimental details can be taken from his Diploma thesis. Here, only a brief overview is given, in order to basically understand how Bragg spectroscopy works.

Analogously to the well-known Bragg refraction of X-ray radiation on a solid state crystal lattice, matter waves with a de-Broglie wavelength λ_{dB} may be diffracted off a standing light wave, generated by a laser of wavelength λ_{L} according to $\lambda_{\mathrm{L}} \cos\theta = n\lambda_{\mathrm{dB}}$ If one of the laser beams is slightly detuned in frequency by $\Delta E/h$ the lattice is moving relative to the atoms and the diffraction of atoms occurs only for distinct detunings fulfilling the condition:

$$\hbar\Delta\omega = \frac{(2\hbar k)^2}{2m}. \tag{3.37}$$

Regarding the Bragg diffraction as a two-photon process (see Fig. 3.16) similar to the Raman transitions discussed earlier in this chapter, this relation becomes even more evident: Assuming two counter propagating beams, the atom virtually absorbs one photon from one laser beam and is stimulated to emit another photon into the other beam. If the detuning to the excited state δ is large enough to neglect any upper-state population, this state can

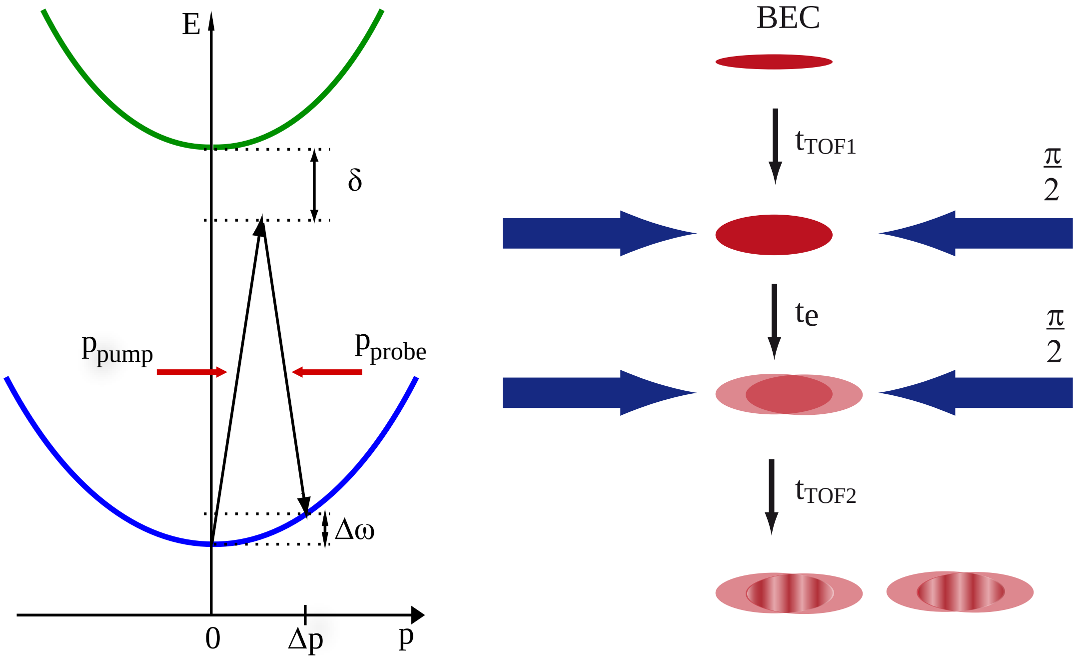

Figure 3.16: (a) Schematic illustration of a first-order Bragg process in terms of a two-photon process on the basis of the dispersion of a free particle. Only if the detuning $\Delta\omega$ between the two Bragg beams matches the energy corresponding to the transferred momentum $\Delta p = 2\hbar k$, a notable transfer to $|2\hbar k\rangle$ will occur. (b) Principle of a $\pi/2 - \pi/2$ interferometer based on Bragg-pulses to investigate the coherence properties of a BEC.

---

be adiabatically eliminated and the problem reduces to that of an effective two-level Rabi system with all its well-known properties. An overall momentum transfer of $\Delta p = 2\hbar k$ occurs in this process. In the case of free particles such a momentum transfer demands for a change in energy of $\Delta\omega = (2\hbar k)^2/(2m)$ in order to fulfill energy conservation.

When pursuing spectroscopy on trapped systems, the corresponding dispersion $\Delta E(k)$ is probed and can be precisely traced. For atoms moving with an initial velocity v and Bragg beams enclosing an angle of θ a more general version of Equ. 3.37 can be quoted as

$$\Delta E = \frac{(2\hbar k \sin(\theta/2))^2}{2m} - 2kv\sin(\theta/2). \tag{3.38}$$

More details on transition probabilities and higher-order Bragg diffraction can be found in [138].
The original experimental setup for the Bragg laser is also well described in [138], while some newer features have been added and are explained in [139]. An ECDL, which can be used either free running or stabilized to a reference cavity locked to the ^{87}Rb cycling

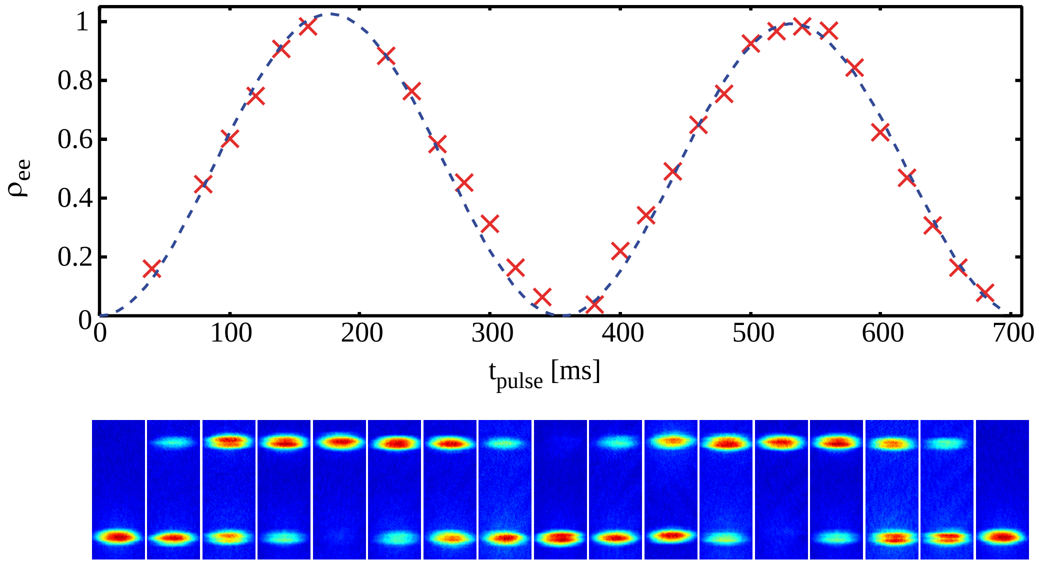

Figure 3.17: Rabi-oscillations between states with momentum 0 and $2\hbar k$. Shown are experimental results together with a fit employing a squared sine. The obtained Rabi frequency $\Omega \simeq 2\pi \cdot 14\,\mathrm{kHz}$ is in reasonable agreement with the theoretically expected one regarding the uncertainty in the determination of the beam intensities at the position of the condensate..

---

transition, is coupled into an optical fiber, guided to the experiment and split up into two optical paths. Every beam passes through one of two phase-locked AOMs. In this manner the frequency difference between the two beams can easily be adjusted to the Hz-level, while providing a very high degree of coherence between the two laser fields [10]. The beams are finally expanded to a diameter of $1-2\,\mathrm{mm}$ and irradiated onto the atoms.

As a proof-of-principle experiment, Rabi oscillations between the momentum-states with $|0\rangle$ and $|2\hbar k_\mathrm{L}\rangle$ have been driven successfully over several periods as shown in Fig. 3.17. Continuative experiments in our group were aiming at the coherence properties of multi-component condensates. One possibility to measure the spatial coherence of a BEC is to split it up into two, displace the two parts with respect to each other by a certain distance and let them finally interfere. If the coherence length l_coh is larger than the displacement d, then a visible interference contrast will be observed. One elegant possibility to do this is the use of a $\pi/2-\pi/2$ interferometer sequence by using two Bragg pulses: After switching off all trapping potentials and a wait time long enough to convert mean-field- in kinetic energy the atoms are exposed to a short $\pi/2$ Bragg pulse, splitting the condensate wave function in a superposition of $|0\rangle$ and $|2\hbar k_\mathrm{L}\rangle$. After an evolution time t_e a second $\pi/2$ pulse recombines the two condensate parts and enables them to interfere. Since the atoms travel a distance $\Delta x = (2\hbar k/m)\cdot t_e$ in between the two pulses the coherence properties can be investigated continuously by varying t_e. Fig. 3.16 shows the experimental scheme for a $\pi/2-\pi/2$ interferometer, while the results of measurements performed in the astigmatic single beam dipole trap are presented in Fig. 3.18. After a mean-field energy release time of

[10]It should be emphasized, that first splitting the two beams and then coupling them into a fiber results in considerable phase noise, broadening the beat note to $1-2\,\mathrm{kHz}$. This should in any case be avoided. Using the same fiber with crossed polarization also doesn't show the desired result (see Section 3.6 and [138]).

5.5 ms a first Bragg pulse with a duration of 80 μs has been applied. We wait for a variable evolution time t_e ranging from 0.5 ms to 5.5 ms before we apply the second $\pi/2$-pulse. The atoms are imaged after an overall TOF of $t_{\mathrm{TOF}} = (33.5 - 2t_{\pi/2} - t_e)$ to assure equal expansion parameters for all evolution times. The finite beam size represents a serious problem, since the atoms fall down a notable distance under the influence of gravity in between the two pulses and experience a smaller intensity during the second pulse. As a result the Rabi frequencies for the two pulses may not be the same and especially change with increasing t_e. This can be re-adjusted by increasing the laser intensity but more homogeneous beams would avoid that problem ab initio.
As can be deduced from the measurements interference fringes appear, whose spacing d should obey the law [11]

$$d = \frac{h}{m\Delta v} = \frac{h}{m\alpha(t)\Delta x} = \frac{\lambda_{\mathrm{L}}}{2}\frac{1}{\alpha(t)t_e}. \tag{3.39}$$

Here λ_{L} denotes the laser wave length and $\alpha(t) = \dot{b}(t)/b(t)$ describes the expansion of the condensate relative to its initial size (taken from [102]). Qualitatively this can be confirmed regarding the present measurements summarized in Tab. 3.5.4.

t_e [ms]	2,5	3.0	3,5	4.0	4,5	5.0	5.5
Δx [μm]	29.4	35.3	41.1	47.0	52.9	58.8	64.6
d [μm]	19	19.7	17.6	15.4	13.5	12.7	11.8

Table 3.4: Separation d of the interference fringes in Fig. 3.18 as a function of the evolution time t_e between the $\frac{\pi}{2}$-pulses.

Visible interference patterns for separations up to 65 μm – approximately the condensate length – could be observed.

In future experiments the Bragg laser setup may be used to investigate the band structure of the optical lattice or in a slightly different approach to act as an inter-band Raman laser, transferring atoms coherently from one Bloch band to another. Since the detunings are on the same order or slightly larger as for spectroscopic use, the two beams can simply be irradiated from the same direction as for the Raman laser.

3.6 Setup for an optical lattice

The intention of this section is to give an idea of the technical issues connected with the implementation of an optical lattice, especially a three-beam optical lattice, at a cold atoms experiment. The physical basis of the generation of periodic potentials with the help of far detuned laser beams will instead be given in the context of Chapter 5 for reasons of continuity. Here the laser system used to derive the lattice beams is presented in detail Furthermore, a technique to eliminate relative phase noise of different laser beams guided through individual optical single-mode fibers will be presented. A well-proven experimental scheme to align the lattice beams is introduced, since it turns out to be non-trivial to achieve a proper adjustment for a triangular lattice. Furthermore methods

[11] Since the acceleration due to the parabolic mean field potential in a Thomas-Fermi BEC exhibits a linear dependence on position, the relative velocity of two arbitrary parts of the condensate depends only on time and their separation, not on the absolute position.

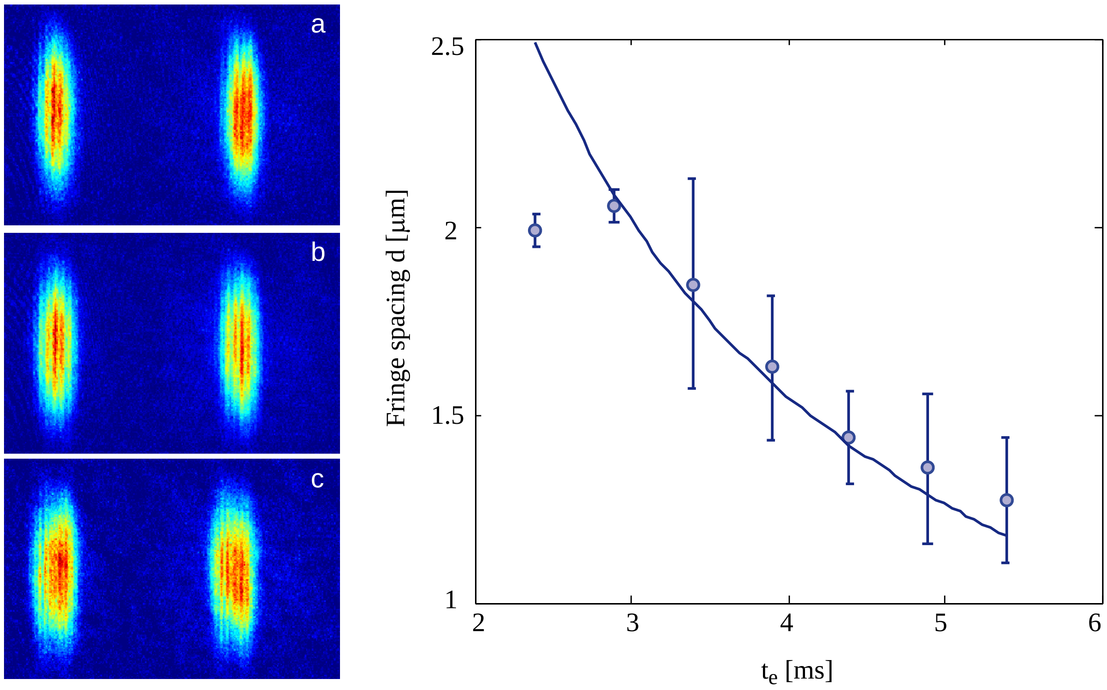

Figure 3.18: Interference patterns resulting from two sequential Bragg $\pi/2$ pulses constituting an interferometer according to Fig. 3.16. The absorption images show typical fringe patterns as observed for evolution times 2.5 ms (a), 3.5 ms (b) and 4.5 ms (c). The graph displays the spacing of the interference fringes determined from absorption images. The data points are plotted along with the theoretical prediction according to Equ. 3.39. The observed agreement is rather good.

to calibrate the lattice depth are briefly sketched. It will be explained how experiments attending to the effect of magnetically-tuned m_F-state changing Bragg scattering can be employed to tackle the indistinct problem of polarization adjustment.

.

3.6.1 A Ti:Sapphire laser system

The demands for a laser system used to create an optical lattice at a BEC experiment include relatively large power, a wavelength that is not too close to the atomic resonance and a narrow line width to ensure a sufficient coherence length. A laser type that may fulfill all of the above requirements is a thoroughly built Titanium-Sapphire laser (Ti:Sa) in the wavelength range of $780-850$ nm. In the following the laser will be presented shortly and it will be shown, how the intensity and frequency-stabilization is implemented.

The laser used for the optical lattice set up is a commercially available Ti:Sa laser (Fa. TekhnoScan Single-frequency Ring Laser model TIS-SF-07) employing an out-of-plane ring resonator. Several wavelength selective elements (1 birefringent filter, 1 thin etalon, 1 thick etalon) together with the positive discrimination of one of the two ring-modes [12] allow for a reliable single-mode operation. The maximum available output power has been determined to be 1.35 W at a wavelength of 830 nm. The laser features an intensity

[12]This is achieved by rotation of the laser polarization through a Faraday rotator and an out-of-plane reflection. Only one of the two otherwise degenerate modes is therefor exactly reproduced after one round trip in the resonator.

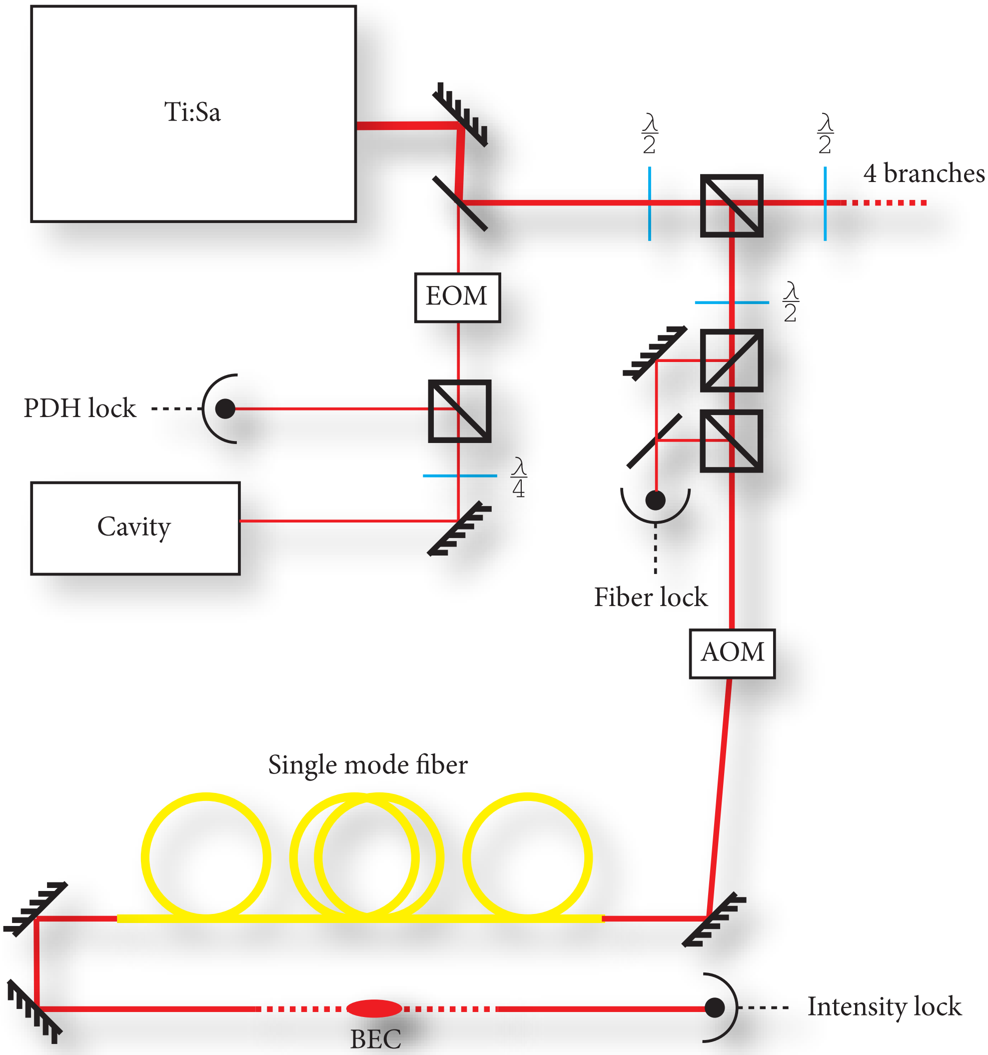

Figure 3.19: Setup of the lasersystem used to generate the optical lattice. A Ti:Saph laser providing up to 1.3 W at $\lambda = 830$ nm is frequency stabilized using a Pound-Drever-Hall lock to a commercially available cavity. The light is split up into four branches, three for the triangular lattice and one for the retro-reflected 1D-lattice. After passing through an AOM used for switching and modulation the laser beams are fiber coupled and guided to the experiment All of them are intensity stabilized using a pure integral servo controller. The three branches employed for the triangular lattice are further phase-stabilized to eliminate the phase noise eventually imprinted in the optical fiber (see Fig. 3.22 for more details.)

---

stabilization relying on a lock-in technique working at 1 kHz. The unavoidable intensity modulation at this frequency has to be kept in mind when designing the final intensity controller, presented later in this section. However, the stability of the dc output power in the locked state is better than 0.5 %. Freely running the line width of the laser can be specified to be several MHz. In order to improve this value to below $\approx$ 100 kHz a Pound-Drever-Hall frequency-stabilization has been set up in the course of this thesis. A very small fraction of the light is split off and send through an electro-optical modulator running at ≈ 30 MHz. The beam is then coupled into a Fabry-Perot cavity (Fa. Coherent) and the reflected light is used as the error signal as usual [140]. All fast deviations from the reference wavelength are controlled by a fast PI-branch of the servo controller actuating a small and fast piezo-mounted mirror inside the Ti:Sa resonator. The maximum travel of this piezo corresponds to a frequency stroke of not more than ≈ 15 MHz. Therefor long term drifts of the laser relative to the external cavity have to be compensated in a different way: the control signal is integrated with a time constant [13] of 3 s and the resulting voltage is fed to the piezo controller of the external cavity.

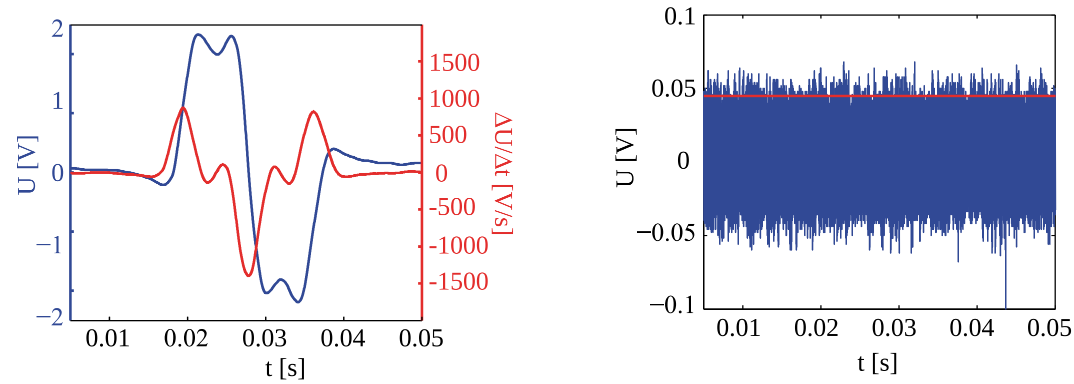

Figure 3.20: (a) PDH signal obtained in scanning mode. The gradient of the signal $\frac{\Delta U_{\mathrm{scan}}}{\Delta t_{\mathrm{scan}}}$ is plotted in red.
(b) Error-signal with activated PDH frequency stabilization. The rms value (red line) of the signal can be taken to estimate the residual line width.

The frequency adjustment range of the external cavity amounts to several GHz - enough to compensate for all drifts occurring in our lab. The line width can be estimated by taking the gradient of the PDH signal in units of volts per free spectral range and plugging in the rms-value of the error signal according to

$$\Gamma_{\mathrm{L}} \approx \left(\frac{\Delta U_{\mathrm{scan}}}{\Delta t_{\mathrm{scan}}} \cdot \frac{\Delta t_{\mathrm{trans}}}{1,5GHz} \cdot \frac{1}{\Delta U_{\mathrm{rms}}} \right)^{-1} . \tag{3.40}$$

t_{trans}, the time equivalent of on free spectral range of the external cavity has been determined to be 800 ms for the measurements presented in Fig. 3.20. The maximum of the gradient is 1.38 V/ms and the rms-voltage can be taken to be 0.045 V. The measured line width in the locked mode could thereby be decreased to ≈ 33 kHz, a value corresponding to a coherence length of several kilometers.
The light coming from the Ti:Sa output is split up into four lattice and one auxiliary beams. As shown in Fig. 3.22 the beams passes an AOM, used to control and switch the intensity and to cancel fiber induced phase-noise. Finally the beams are coupled into 30 m long non-polarization-maintaining single mode fibers and guided to the experiment situated in a neighboring laboratory, where beam shaping telescopes (compare Fig. 3.2a and [141]) directly aim the laser beams onto the BEC without the use of any further optical

[13]Building analog electronics with such high integration constants is actually quite demanding. However, one has to make sure, that for all short-term deviations the laser is locked on the external cavity, and *not* the other way around.

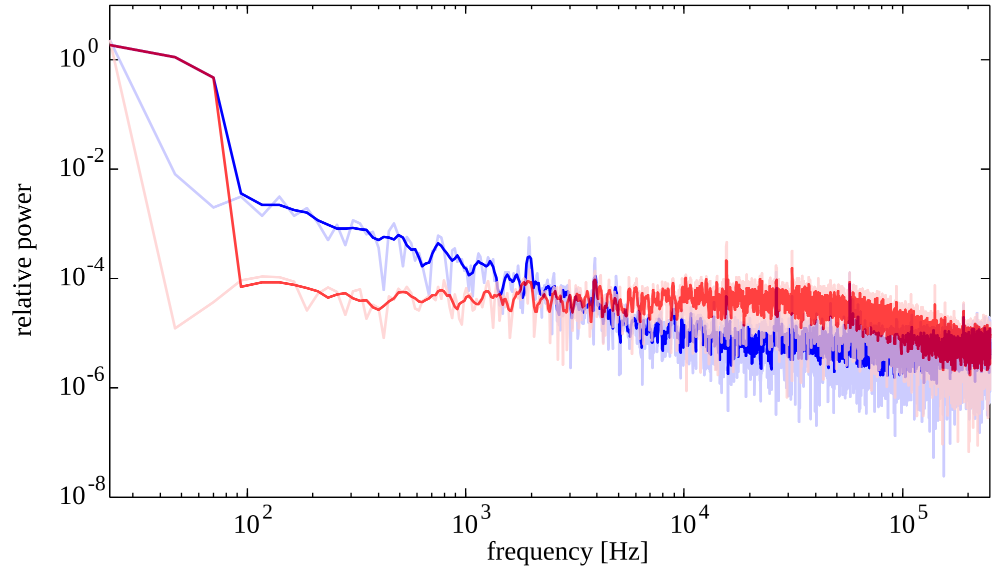

Figure 3.21: Power spectrum of one of the lattice laser beams. The blue curve has been recorded without activated intensity stabilization. The red curve depicts the power spectrum with intensity stabilization. The servo controller is capable of suppressing intensity noise at low frequencies but slightly increases noise beyond frequencies of several kHz, still maintaining a suppression of better than 10^{-4}. Note the double logarithmic scale. The light shaded curves are the original signal recorded with a R&S UPV audio analyzer. The full colored curves have been obtained by averaging over five adjacent bins.

elements. The spot sizes at the position of the atoms have been measured (see Fig. 3.2a) and read $w_0^{1D} = 90\,\mu$m for the 1D lattice, whereas the beams creating the 2D three-beam lattice have waists of $w_0^{2D} = 115\,\mu$m.

3.6.2 Intensity stabilization

The intensity of the lattice beams is conveniently controlled by a pure integral servo controller actuating on rf-mixers used as attenuators in front of the AOMs. The bandwidth ($25 - 30\,$kHz) and dc-accuracy ($\Delta I \leq 50\,\mu$W) of this control circuit is sufficient to control the intensity of an individual lattice beam up to its maximum available level. The power spectrum $\Delta P^2/P^2 = S(\omega)$ (compare Section 5.4) of one of the laser beams measured on a fast photo diode (THORLABS PDA155 - Silicon) employing an audio analyzer (R&S UPV) is shown in Fig. 3.21. The heating rate induced by intensity fluctuations of the lattice laser is proportional to this power spectrum as can be deduced from Equ. 5.40 .[14] A careful analysis of the control circuit and the resulting heating rates has been conducted in cooperation with S. Schnelle and is documented in detail in his diploma thesis [141]. The heating rate observed for the measured power spectrum can be calculated employing Equ. 5.40 and yields a maximum value of $\tau_{\text{heat}} \gtrsim 1\,$s. The corresponding lifetime of the atoms inside the lattice is thus sufficiently long to perform experiments that may last up to 1 s.

[14] A limited bandwidth may drive parametric heating processes in the lattice. However excitation frequencies in the range beyond the measured bandwidth correspond to lattice depth that can not be achieved with our laser power and are therefor safely neglected (see [141] for detailed discussion).

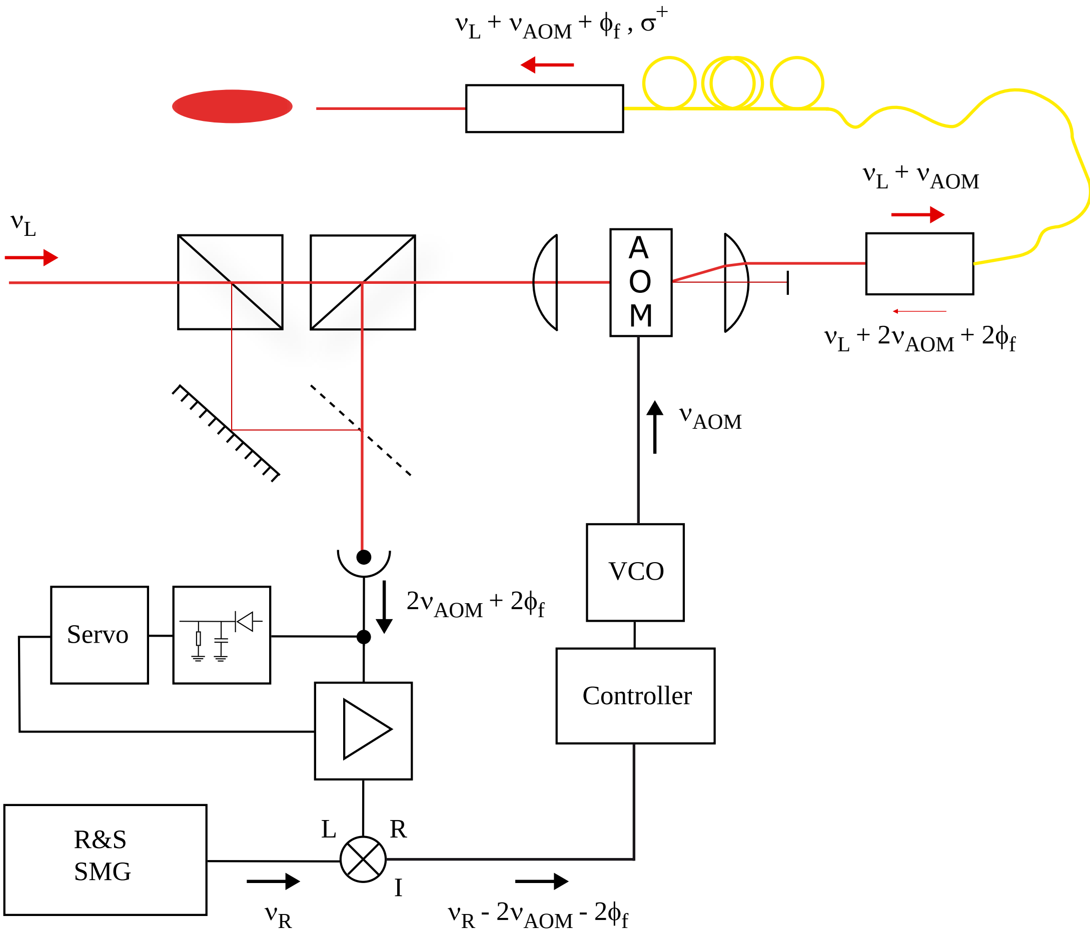

Figure 3.22: Stabilization of the optical path length of a single mode fiber. The phase of the individual laser beams is locked to a reference oscillator (R&S SMG) eliminating any phase jitter imprinted in the optical fiber. Note that *no* additional remote-end components are required for the particular experimental setup developed within this thesis. More details concerning the optical and rf-components used can be found in the text.

3.6.3 Phase noise elimination

Ideally the transmission of an optical signal through an optical fiber will not change the spectral properties of the signal. However temperature fluctuations as well as mechanical vibrations lead to a modulation of the index of refraction n of the fiber core resulting in a change of the optical path length. This on the other hand imprints phase noise on the transmitted light broadening the signal spectrum to several kHz even for fibers as short as a few meters. As will be shown in Chapter 5 fluctuations of the relative phases of the individual laser beams of a three-beam lattice will lead to a global translation of the lattice potential which may result in a parametric heating process. To avoid this heating it is necessary to stabilize the laser beam's relative phases after their transmission through the optical single mode fibers.

The setup to measure and eliminate the phase noise is depicted in Fig. 3.22. The compensation is based on heterodyning probe light that is picked up before the fiber with

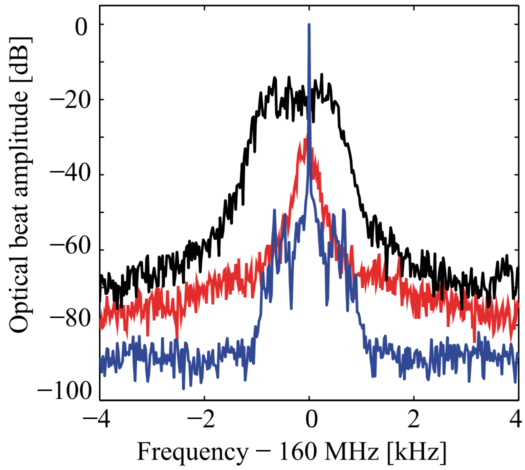

Figure 3.23: Beat note obtained by heterodyning two individually phase-locked fiber-coupled lattice beams. The black line represents the beat signal of two individual unlocked beams that have passed through 30 m long single mode fibers. Phase-locking one of the beams decreases the width of the signal only slightly as expected (red). The blue curve shows the signal of two phase-locked beams. The instantaneous width of the signal decreases to $\Delta\nu \lesssim 1\,\mathrm{Hz}$ as compared to several kHz without stabilization.
The residual rms phase-noise is not larger than $\sqrt{\langle\phi^2\rangle} = 6.8°$.

light that has passed through the fiber and has been reflected back by the plane end of the fiber, therefor revealing the phase modulation Φ_f. A small portion of light with frequency ν_0 is picked up in front of the AOM and directed onto a fast photo detector (HAMAMATSU G4176). The main beam passes through the AOM shifting the frequency of the light by ν_AOM and through the fiber adding a phase noise of Φ_f. At the plane end of the APC-PC fiber 4 % of the light gets reflected back and collects another Φ_f assuming that the modulation of the index of refraction doesn't change during a round trip of the light, which is true for perturbations with frequencies $\nu_{pert} \ll c/(2nL)$. Subsequently the light is again shifted by ν_AOM by the AOM. This light characterized by $\nu_0+2\nu_\mathrm{AOM}+2\Phi_\mathrm{f}$ is now also directed onto the photo detector and generates an optical beat at $2\nu_\mathrm{AOM}+2\Phi_\mathrm{f}$. We compare the phase of this rf-signal with the reference signal of a local oscillator (LO) at ν_ref and use the derived error signal to drive a fast servo loop which controls a voltage controlled oscillator (VCO) feeding the AOM. This optical phase-locked loop (OPPL) ensures that $2\Phi_\mathrm{f}+2\nu_\mathrm{AOM}=\nu_\mathrm{ref}$. The light transmitted through the fiber will consequently have a rigid phase and a frequency of $\nu_0+\nu_{\mathrm{ref}/2}$. It is important to note that the fiber employed in this setup has to have one plane end at the remote side and one angled end at the input side in order to distinguish the light reflected from the front end of the fiber from light reflected from the remote end which exactly traces the incoming beam. In addition the polarization of the light at the end of the fiber has to be circular in order to obtain a linear polarization of the back-reflected beam which is perpendicular to the polarization of the incoming light (see Fig. 3.22). This can be achieved by the use of fiber polarization controllers [142]. Although the setup may look complicated it requires only one interferometer branch in front of every fiber and standard rf equipment as an AOM is required anyways for fast switching and controlling the light intensity. Note in particular that no cumbersome extra optics is required at the experiment end of the fiber which favors our setup over other fiber length stabilization schemes especially for the generation of optical lattices where usually only compact beam shaping telescopes are used to shine the light on the atoms under almost arbitrary angles.

Moreover loading ultra-cold atoms into an optical lattice requires an adiabatic ramp up of the intensities of the lattice beams to avoid heating. This additional requirement complicates the construction of a robust servo loop, since the magnitude of the error signal used for the OPPL will increase over 2 orders of magnitude during the ramping. This problem can be bypassed by implementing an automatic gain control for the rf signal coming from the photo detector. The power of the rf signal is measured using a simple home-made diode square-law detector which yields the error signal for an integral controller. The output of this regulator is fed to a voltage controlled amplifier which keeps the rf power constant at $-10\,\mathrm{dBm}$. This extra servo loop enables the controller to keep the individual laser beams phase-locked over a wide range of intensities ($< 1\,\mathrm{mW} - 1\,\mathrm{W}$). The measured beat signal of two individually phase locked laser beams out-of-loop can be used to determine the quality of the OPPL. Fig. 3.23 shows the beat of two unlocked laser beams under silent laboratory conditions in black, the heterodyne measurement of one locked and one unlocked laser beam is depicted in red and the signal of two locked laser beams in blue respectively. The dramatic decrease of the width of the beat note as compared to two free running beams from $\sigma_{\mathrm{FWHM}} \simeq 2\,\mathrm{kHz}$ down to $\sigma_{\mathrm{FWHM}} \leq 1\,\mathrm{Hz}$ can be easily seen. [15] In order to address the short-term quality of the phase lock more quantitatively, the residual phase offset $\langle\phi^2\rangle$ can be related to the fraction η of the total power contained in the carrier of the spectrum through $\eta = e^{-\langle\phi^2\rangle}$ [143]. A careful integration of the beat spectrum over a wide spectral range gives a value of $\eta = 0.986$ leading to a phase error of $\sqrt{\langle\phi^2\rangle} = 6.8°$.

3.6.4 Adjusting the lattice

A time consuming task demanding for care and patience is the first adjustment of the optical lattice, especially the triangular one.

1D retro-reflected lattice

A standing wave lattice can usually be adjusted in a convenient way by first blocking the retro-reflected beam and imaging the atomic cloud and the laser waist along the axis of propagation of the lattice beam (compare also Section 5.1.1 for details). Great care has to be taken when imaging such a small waist with a CCD camera to avoid destruction of the chip. Even at the smallest laser powers that can be set (limited by the residual leakage rf-power of the AOM-drivers in OFF-position) proper neutral density filters on the order of $-30\,\mathrm{dB}$ should be used to protect the camera from damage. carefully superimposing waist and atomic cloud will yield a reliable starting point for further fine corrections [16]. The final criterion consists in illuminating the atoms in the dipole trap with a very strong lattice beam and trying to eliminate any dipole excitations of the BEC indicating a perfect overlap of the BEC center of mass and the zero of the lattice beams potential. After this first goal is achieved, the retro reflected beam has to be positioned as well. This is conveniently done by re-coupling the laser beam back to the fiber from which it emerged. A beam splitter at the remote end of the fiber allows to separate incoming and outgoing beam and constitutes a very sensitive measure to iteratively superimpose the two waists by adjusting lens position and mirror mounts. In this way the tilt of the retro-reflected beam as well as the exact position of the re-focusing lens can be adjusted with very high precision. The tolerance of the final adjustment amounts to approximately one to two scale divisions of the high precision differential micrometer screws (Fa. Mitotoyo), corresponding to an error in the transverse waist position of $\pm(4-8)\,\mu\mathrm{m}$. The error in the

[15] Note that the minimum width of the beat signal is limited by the maximum resolution of the employed spectrum analyzer R&S FSP of 1 Hz.

[16] Note that chromatic aberration of the imaging optics at the wavelength of the lattice may possibly lead to a tiny shift of the observed and real position of the waist. However this deviation is usually very small.

axial positions of the two waists can not be estimated very well, since the Rayleigh range of the beams with a waist of $w_0 = 90\,\mu$m is fairly large and therefor even a maladjustment on the order of $1-2$ mm cannot be safely excluded. In the end one should of course always check whether the interference pattern obtained by releasing cold atoms that have been loaded in the 1D lattice is as symmetric and strong as possible for a given lattice depth.

2D three-beam lattice

At our experiment it is unfortunately not possible to image the atoms along the directions of the three lattice beams creating the triangular lattice. The convenient method to align the beams described above can therefor not be applied in this case. First of all, because of the large Rayleigh range $z_{\mathrm{R}} \approx 5.1$ mm, it is sufficient to adjust the axial distance between the principle plane of the focusing lens and the position of the atoms to be equal to the lens' focal length within ± 1 mm. This is already quite demanding, since the accessibility at the experiment is limited prohibiting exact measurements of distances and angles. However the effort spent here will pay off, since a later re-adjustment of the waist position is more than cumbersome.
The starting point of the transverse calibration is a rather small portion of atoms in a MOT without pushing beam. An auxiliary fifth fiber connecting the experiment and Ti:Sa lab is used to couple resonant light in the individual lattice beam fibers using FC-APC FC-PC fiber connectors. By gradually decreasing the power of the laser and aiming at the atoms in the MOT, a reasonable starting point for further adjustments can be found. Next one needs to produce BEC in a crossed optical dipole trap and mark the exact position of the trap center from both available detection directions. After this is done, the power of the axial dipole trap is cranked up to a large value to increase the size of the trapped atomic sample. Then one chooses one of the beams – now with the usual lattice detuning–and tries to produce a crossed dipole trap generated by the axial dipole trap and one single lattice beam, hereafter called lattice dipole trap. Since the axial extension of the atom cloud is fairly large, only the vertical direction should be scanned in rather small steps (not more than 2 scale divisions of the Mitotoyo screws at a time are recommended). Usually, at some point one will recover the desired lattice optical dipole trap. Now the horizontal direction may also be adjusted until the lattice dipole trap is exactly at the same position as the crossed dipole trap marker set at the beginning of the procedure. The intensities of the lattice and dipole beams may now be reduced iteratively to obtain a more sensitive measure for the quality of the adjustment. At the lowest possible power (reducing the power even more will lead to an effective potential that does not exhibit a local minimum anymore and is thus not capable of supporting the atoms against gravity) the sensitivity is again on the order of one scale division of the micrometer screws. This procedure does not work for the lattice beam pointing along gravity of course. We have established a different method to obtained an adjustment of equal quality. Bose-Einstein condensates produced in an extremely shallow crossed optical dipole trap are very susceptible to any kind of perturbation. If the vertical lattice beam is not perfectly aimed at the minimum of the potential of the crossed dipole trap, then the atoms will be dragged away horizontally from the point of maximum force. As a result atoms will start to spill out of the trap, which can be observed in absorption images. Only a perfect alignment avoids loss of atoms and can therefor be achieved following this criterion.
Finally, it is a good test for the quality of the alignment to have a look at the position of the crossed dipole trap with a very strong lattice beam impinging on the atoms in addition.

Only if the position as compared to the pure crossed dipole trap does not change at all a good adjustment has been achieved. After the procedure described above has been accomplished for all three lattice beams, one can try to load atoms in the lattice and observe the typical interference pattern after time-of-flight. Usually the observed pattern will already look more or less perfectly symmetric, if the intensities of the beams have been calibrated properly as well (see Section 5.4). As a last step of the calibration, the atoms are driven deep in the Mott-insulating regime (compare Chapter 5 for more details). After a fixed hold-time the lattice depth is reduced to a level corresponding to maximal visibility of the typical interference peaks. The recovered visibility is an extremely sensitive measure for the adjustment of the lattice beams. Re-adjusting the mirror mounts of the beam shaping telescopes by not more than 2 scale divisions will finally yield the best result that can be obtained within the restriction of the described method. Note that a subsequent execution of all of the above steps can barely be accomplished on one day. However it is not always necessary to start from the beginning. It has proven extremely useful to locate a *global* reference point for all adjustments that one can think off. We have chosen the center of mass of the compressed magnetic trap to be this point. Before calibrating the lattice, it is therefor unavoidable to check, whether the dipole trap is correctly adjusted to the point of reference. If this is not strictly considered every time the lattice is adjusted one will end up turning knobs of mirror mounts over and over again, without ever doing experiments.

Polarization adjustment

The adjustment of the polarization is a major issue in order to obtain a well defined lattice structure when working with three-beam lattices as in our experiment. Due to the very compact experimental setup it is not possible to measure and adjust the polarization by conventional means, e.g. using a polarization measuring device. Instead the influence of a misaligned polarization on the atoms themselves has to be employed as a very sensitive measure to properly adjust the lattice. A Zeeman-Bragg resonance described in detail in Section 5.10 which leads to an unwanted population of other m_F-states at low magnetic fields constitutes such a polarization sensitive physical effect that we vastly use for polarization adjustment. Only if circular components of the lattice polarization are *absent*, no transfer to other magnetic states occurs. A wave plate in front of the beam shaping telescopes allows to change the polarization and to eliminate (triangular lattice) or maximize (hexagonal lattice) this effect, thereby yielding a well defined polarization orientation.

Chapter 4

Dynamics of Spinor Bose-Einstein condensates

The physics of single component BEC is based on the assumption that the bosonic particles, constituting the condensate behave as they had no internal structure influencing the physical properties of the BEC in any way. Many properties associated with the *external* degrees of freedom are well understood to date [102, 144]. Spinor Bose-Einstein condensates are characterized by an additional *internal* degree of freedom namely the spin. The order parameter of a spinor condensate consequently takes the form of a vectorial *spinor* rather than a *scalar* as in single component condensates: $\psi \rightarrow \vec{\zeta} = (\zeta_{-F}, \ldots, \zeta_{+F})^T$. The number of components of $\vec{\zeta}$ is given by $2F+1$ in a particular hyperfine manifold. Moreover spinor condensates are set apart from other multi component systems, like mixtures of different isotopes [145] or quasi-spin-1/2 systems composed out of different hyperfine states [49, 146], by a symmetry of the order parameter under rotations. Spinor components transform into one another under a rotation of the coordinate system: The population of the individual m_F-states is not conserved and internal spin mixing dynamics may coherently change the spin-state distribution only constrained by the conservation of the total spin as we will see.
In the beginning of this chapter the physical basics of single spins will be recalled. The well-known two-level physics of spin-1/2 systems will be generalized to particles with spin-1 and spin-2 in order to understand the behavior of ^{87}Rb atoms in a combined static magnetic and rf dressing field. Concluding it will be depicted how this can be understood in terms of a classical spin under the influence of an external torque employing the famous Bloch-sphere picture. Experimental results on Rabi oscillations as well as Ramsey type experiments are presented together with a comparison to theoretical predictions. Subsequently we will turn to interacting spinor condensates and briefly review the mean-field equations of motion followed by the presentation of an analytical solution describing coherent spin mixing dynamics for a particular initial state. Experiments performed with ^{87}Rb atoms in $F = 1$ and $F = 2$ will be shown, demonstrating the occurrence of a spin dynamics resonance as the result of the competition between quadratic Zeeman- and spin dependent interaction energy for the first time. Finally the formation of spin domains induced by spin changing dynamics will shortly be introduced.

The results obtained here contributed significantly to the understanding of spinor condensates in the past couple of years. They have been published in two well-recognized papers appearing in peer-reviewed journals. In [5] Rabi and Ramsey like techniques to manipulate and analyze spinor condensates are presented together with measurements on coherent spin dynamics in $F = 1$ condensates. [4] deals with spin dynamics in $F = 2$ and highlights the occurrence of a resonance effect owing to the competition between quadratic Zeeman effect and spin dependent interaction.

4.1 Single atom spin-1 and spin-2 physics

4.1.1 Theory of single spins in a magnetic field

A single atom with electronic angular momentum J and nuclear spin I in an external magnetic field B_0 well in the Zeeman regime is described by the Hamiltonian (see [147])

$$\mathbf{H}_{\text{HFS}} = A\,\vec{\mathbf{I}}\cdot\vec{\mathbf{J}} - (g_K\mu_K\vec{\mathbf{I}} - g_J\mu_B\vec{\mathbf{J}})\cdot\vec{B} \tag{4.1}$$

where $\vec{\mathbf{I}}$ and $\vec{\mathbf{J}}$ are the angular momentum operators of the nuclear and electronic (including orbital) spin. μ_K and μ_B are the nuclear and Bohr magneton and g_K and g_J the corresponding Landé factors [1].

In the absence of a magnetic field the nuclear spin $\vec{\mathbf{I}}$ and the electronic total spin $\vec{\mathbf{J}}$ couple to the total spin $\vec{\mathbf{F}} = \vec{\mathbf{I}} + \vec{\mathbf{J}}$. The energy levels are simultaneous eigenstates of $\mathbf{I}^2, \mathbf{J}^2, \mathbf{F}^2, \mathbf{F}_z$ with energies $E_{\text{HFS}} = \frac{A}{2}\left((F(F+1) - I(I+1) - J(J+1)\right)$.

This changes in a weak axial magnetic field $\vec{B} = B_0\,\vec{e}_z$, which lifts the degeneracy among the m_F levels and leads to an energy splitting that is given exactly by the Breit-Rabi formula for $J = 1/2$ systems[147]:

$$E\left(F = I \pm \frac{1}{2}, m_F\right) = -\frac{\Delta E_{\text{hfs}}}{2(2I+1)} - m_F g_K\mu_K B_0 \pm \frac{\Delta E_{\text{hfs}}}{2}\sqrt{1 + \frac{4m_F}{2I+1}x + x^2} \tag{4.2}$$

$$\text{with} \quad x = \frac{g_J\mu_B + g_K\mu_K}{\Delta E_0}B_0 \tag{4.3}$$

$\Delta E_{\text{hfs}} \equiv \hbar\omega_{\text{hfs}} = A(I + 1/2)$ is the hyperfine splitting of the two states $F = I \pm \frac{1}{2}$ at zero magnetic field. Expanding the Breit-Rabi result to second order in B_0 yields expressions for the linear and quadratic Zeeman energy respectively. For ^{87}Rb with $I = \frac{3}{2}$ the solutions read

$$E_{\text{LZE}} = m_F\mu_B B_0\left(\pm\frac{g_j}{4} - \frac{(3\pm1)\mu_K}{4\mu_B}g_K\right) \approx \pm\frac{1}{2}m_F\mu_B B_0 \tag{4.4}$$

$$E_{\text{QZE}} = \pm\frac{\mu_B^2 B_0^2}{4\Delta E_{\text{hfs}}}\left(g_j + \frac{\mu_K}{\mu_B}g_K\right)^2\left(1 - \frac{m_F^2}{4}\right) \approx \pm\frac{\mu_B^2 B_0^2}{4\Delta E_0}(4 - m_F^2) \tag{4.5}$$

where $\pm$ refers to the case $F = I \pm \frac{1}{2}$, respectively, i.e. $F = 1$ and $F = 2$. In the last step it has been exploited that $\mu_K \ll \mu_B$. Having found expressions for the linear and quadratic Zeeman energy the Hamiltonian Equ. 4.1 can be rewritten in a more instructive manner:

$$\mathbf{H} \equiv \underbrace{\mathbf{H}_{\text{LZE}} + \mathbf{H}_{\text{QZE}}}_{\mathbf{H}_{\text{ZE}}} + \mathbf{H}_{\text{rf}} = -\hbar p\mathbf{F}_z + \hbar q\mathbf{F}_z^2 - g_F\mu_B\hat{b}\,\cos(\omega t)\,\mathbf{F}_y. \tag{4.6}$$

[1] All four quantities are positive with the sign convention chosen here [103]. The Bohr magneton $\mu_B = \frac{e\hbar}{2m_e c} \approx h \times 1.4\,\text{MHz/G}$ and the nuclear magneton $\mu_K = \frac{e\hbar}{2m_p c} \approx h \times 760\,\text{Hz/G}$ determine the order of magnitude of Zeeman energy shifts. For the electronic ground state of ^{87}Rb , the Landé factor is $g_J \approx 2$ and the corresponding nuclear g factor $g_K \approx 2.75$. Since $\mu_K \ll \mu_B$, the nuclear contribution to the Zeeman effect can be neglected for the purposes of the present work.

where we have defined for now and the rest of this theses $|p| = \frac{1}{2}\frac{\mu_B}{\hbar}B_0$ and $|q| = \frac{p^2}{\omega_{\rm hfs}}$. It turns out that for $F = 2$ ($F = 1$) both p and q are negative (positive). We have explicitly split off a term $\mathbf{H}_{\rm rf}$ which accounts for a small perpendicular time-varying magnetic field as produced by irradiating the atoms with radio frequency. Such a Hamiltonian is well known from nuclear magnetic resonance (NMR) theory and is usually tackled by first going to a *rotating frame* to eliminate the dominating physical effect of *Larmor precession*. The unitary operator for such a rotation around the z-axis is given by

$$\mathbf{T} = e^{-i\omega_0 t\mathbf{F}_z}. \tag{4.7}$$

The transformed Hamiltonian $\tilde{\mathbf{H}}$ in the rotating frame is obtained after some algebra and application of the *rotating wave approximation* (RWA), neglecting all terms at the sum frequency $(\omega + \omega_0)$, which is usually justified for physical phenomena close to atomic resonance.

$$\tilde{\mathbf{H}} = -\hbar(p - \omega_0)\mathbf{F}_z + \hbar q\mathbf{F}_z^2 - \frac{g_F\mu_B\hat{b}}{2}\Big(\cos(\omega - \omega_0 t)\mathbf{F}_y + \sin(\omega - \omega_0 t)\mathbf{F}_x\Big). \tag{4.8}$$

Choosing $\omega_0 = \omega$ is particularly useful when the driving rf field $\hat{b} \neq 0$, since under this choice the last term in $\tilde{\mathbf{H}}$ takes a notably simple form.

In the *rotating frame* the Hamiltonian $\tilde{\mathbf{H}}$ contains no explicit time-dependence, and the temporal evolution of any spinor ζ can readily be obtained following standard quantum mechanics:

$$i\hbar|\dot{\zeta}\rangle = \tilde{\mathbf{H}}|\zeta\rangle \quad \Leftrightarrow \quad |\zeta(t)\rangle = e^{-i\frac{\tilde{\mathbf{H}}}{\hbar}t}|\zeta(0)\rangle. \tag{4.9}$$

One has to keep in mid that $\tilde{\mathbf{H}}$ is a $(2F+1)$-dimensional matrix, so that the exponential has to be calculated numerically using standard linear algebra techniques.

In the easiest conceivable case no rf-field is applied and $\mathbf{H}_{\rm rf}$ is zero. If we neglect the quadratic Zeeman effect for now, the well known physics of *Larmor precession* is obtained, purely driven by the linear Zeeman effect. Recalling that the time evolution of any observable $A \equiv \langle\mathbf{A}\rangle$ is governed by the following equation in the *Heisenberg* picture

$$\langle\dot{\mathbf{A}}\rangle = \frac{i}{\hbar}\langle[\mathbf{H}, \mathbf{A}]\rangle \tag{4.10}$$

we can derive a simple set of equations for the components of $\langle\mathbf{F}\rangle$ using $[\langle\mathbf{F}_x\rangle, \langle\mathbf{F}_y\rangle] = \epsilon_{x,y,z}i\langle\mathbf{F}_z\rangle$

$$\dot{F}_x = +\tilde{p}F_y, \quad \dot{F}_y = -\tilde{p}F_x \quad \text{and} \quad \dot{F}_z = 0. \tag{4.11}$$

describing a rotation around the z axis with the a frequency given be the detuning $|\tilde{p}| = |p - \omega_0|$ with respect to the Larmor frequency $\omega_{\rm L} = |p|$. F_z does not exhibit any time dependence and is a constant of motion. Choosing the frequency of the rf drive to be equal to the Larmor frequency, all components of $\langle\mathbf{F}\rangle$ are stationary. This is the particular reason for switching to the rotating frame: The time evolution takes place at frequencies $|\tilde{p}|$ which usually obey $|\tilde{p}| \ll |p|$.

By taking a finite quadratic Zeeman effect into account, additional time evolution operators appear, which are diagonal in the basis of m_F states and consequently only involve a

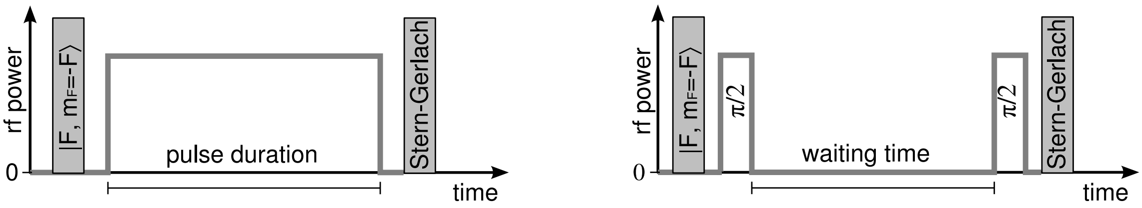

(a) Rabi sequence (b) Ramsey sequence

Figure 4.1: Experimental rf pulse sequence employed for Rabi oscillations and Ramsey type experiments.

phase evolution of the spinor

$$e^{-iqF_z^2 t} \overset{F=1}{=} e^{-iqt}\begin{pmatrix}1 & & \\ & e^{iqt} & \\ & & 1\end{pmatrix} \tag{4.12}$$

$$\overset{F=2}{=} e^{-4iqt}\begin{pmatrix}1 & & & & \\ & e^{3iqt} & & & \\ & & e^{4iqt} & & \\ & & & e^{3iqt} & \\ & & & & 1\end{pmatrix} \tag{4.13}$$

The expectation values of the different spin components for any initial spin state under the influence of the quadratic Zeeman effect can readily be calculated using the above expressions.

In the following some particular configurations of $\mathbf{H}_{\text{rf}}$ will be considered and investigated in more detail. The focus will be mainly on special forms of $\tilde{\mathbf{H}}(t)$ associated with important experimental sequences that are employed throughout this thesis, namely Rabi oscillations and Ramsey type experiments.

Rabi Oscillations

Rf- and microwave driven oscillations are invaluable tools for experimental characterization and preparation (Section 3.5) and moreover may provide insight into the question of spin coherence. Fig. 4.2 shows an example of Rabi oscillations in a $F = 1$ spinor condensate.

Rabi oscillations are a well known phenomena usually familiar to any physicist in the context of two-level systems [148]. Higher spin systems which may exhibit an additional quadratic Zeeman effect – that is absent in spin-1/2 systems – show a similar behavior under the influence of an external rf driving field, although characteristic differences remain. Equ. 4.8 can still be solved analytically as long as we neglect the quadratic Zeeman effect for now. The time evolution of the individual spin components on resonance is given by

$$\dot{F}_x = -\Omega_0 F_z \quad \dot{F}_y = 0 \quad \dot{F}_z = +\Omega_0 F_x. \tag{4.14}$$

The solution to these equations corresponds to a rotation around the y-axis at the Rabi frequency $\Omega_0 = \frac{g_F \mu_B \hat{b}}{2\hbar}$. If we allow for a finite detuning the Hamiltonian can still be

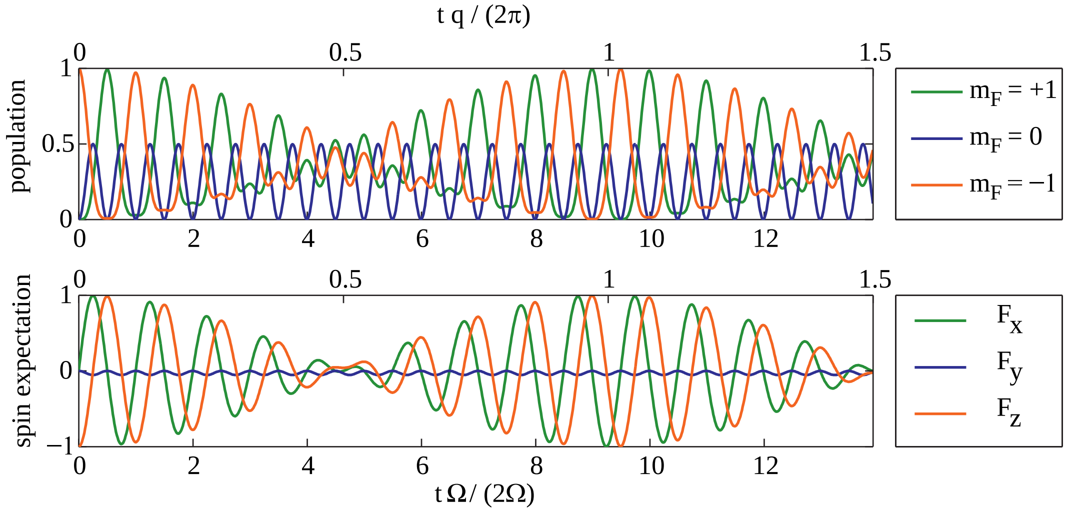

Figure 4.2: Rabi oscillations in $F = 1$ including the quadratic Zeeman effect. The plots have been numerically calculated from RWA solutions of the Schrödinger equation (4.9) with the parameters $\tilde{p} = 0$ and $q \approx 0.11\Omega_0$. Note the double scale of the horizontal axis, showing time in units of $2\pi/q$ as well as $2\pi/\Omega_0$.

---

written in the form of the generator of a rotation

$$\tilde{\mathbf{H}} = -\hbar\Omega\, \vec{n} \cdot \vec{\mathbf{F}} \quad \text{where} \quad |\vec{n}| = 1. \tag{4.15}$$

around a new axis $\vec{n} = \frac{\tilde{p}}{\Omega}\vec{e}_z + \frac{\Omega_0}{\Omega}\vec{e}_y$ with a modified Rabi frequency $\Omega = \sqrt{\tilde{p}^2 + \Omega_0^2}$. Introducing a finite quadratic Zeeman effect lifts the degeneracy of the involved transition energies $\omega_{-1\to 0}$ and $\omega_{0\to +1}$ and introduces a splitting given by q in the simplest case of $F = 1$. As known from classical mechanics the physics of two coupled oscillators is characterized by two frequencies given by the mean $(\omega_{-1\to 0} + \omega_{0\to +1})/2$ and the difference $(\omega_{-1\to 0} - \omega_{0\to +1})/2$ of the individual harmonic frequencies. If the original frequencies differ only a little, a characteristic beat note at the difference frequency will be observed. An exact numerical calculation of the involved physics is shown in Fig. 4.2 and confirms this phenomenological prediction. Starting in $|\zeta(0)\rangle = (0, 0, 1)$ the populations given by $\rho_{+1} = |\zeta_{+1}|^2$ and $\rho_{-1} = |\zeta_{-1}|^2$ oscillate π out of phase at the Rabi frequency while $\rho_0 = |\zeta_0|^2$ oscillates at twice the Rabi frequency. In addition the expectation value of *all* spin components vanishes periodically at a frequency given by the quadratic Zeeman effect. F_z and F_x oscillate $\pi/2$ out of phase as expected from a rotation of $\langle \mathbf{F} \rangle$ around the y-axis, while F_y barely shows oscillations at twice the Rabi frequency induced by the quadratic Zeeman effect.

To experimentally investigate Rabi oscillations we start with a BEC in the astigmatic single waist dipole trap in $|1, -1\rangle$ with a large thermal fraction in order to investigate both, the properties of the condensate as well as the normal fraction. Driving Rabi oscillations in $F = 1$ and $F = 2$ by switching a radio frequency field we observed that the condensed fraction closely resembles the above mentioned characteristics as depicted in Fig. 4.3. The time evolution of the thermal cloud on the contrary is strongly effected by damping processes. Recall that in order to have experimental conditions as reproducible as possible we have employed the line trigger described in Chapter 3. The damping of thermal atoms

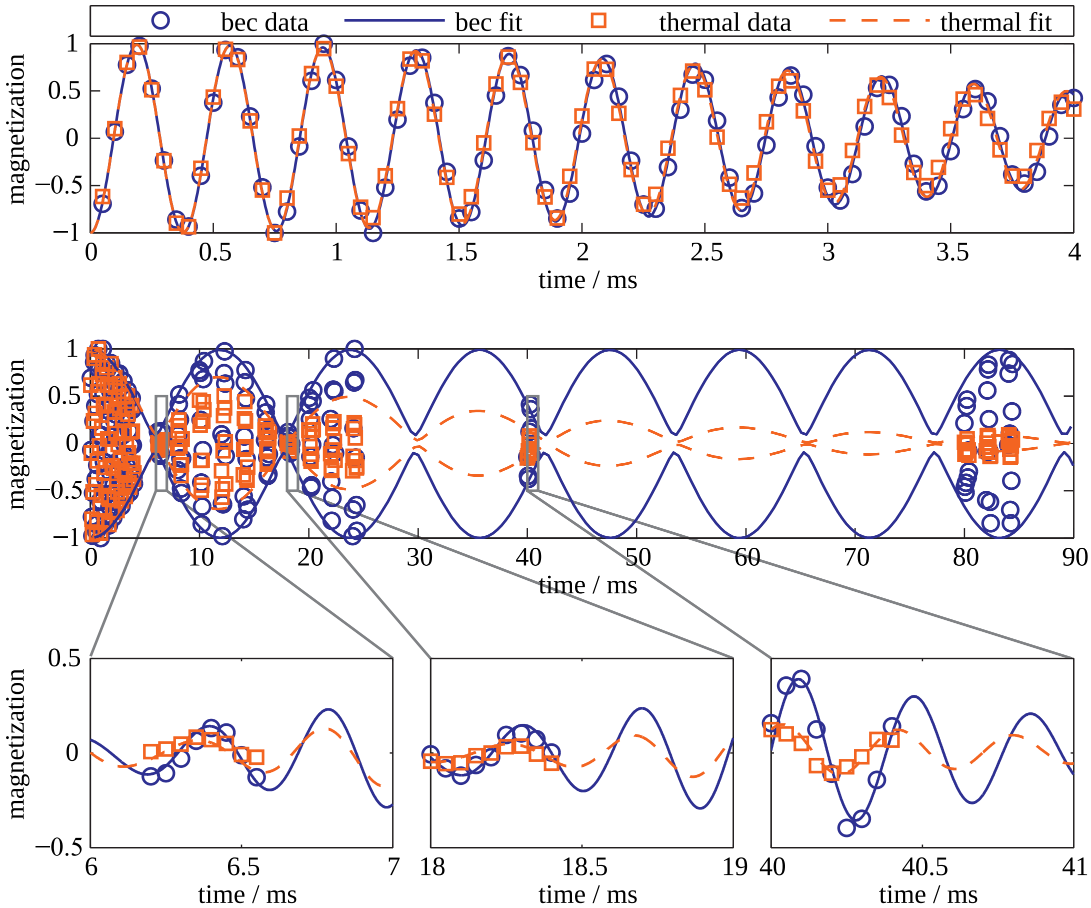

Figure 4.3: Rabi oscillations of a BEC with a significant thermal fraction in $F = 1$. Fits are calculated using a super-operator [71] formalism and include damping for the thermal component. Parameter values obtained from a least-squares fit are Rabi frequency $\Omega_0 = 2\pi \times 5.274\,\text{Hz}$ and detuning $\Delta = -2\pi \times 194\,\text{Hz}$ for the BEC, $\Omega_0 = 2\pi \times 5284\,\text{Hz}$ and $\Delta = -2\pi \times 168\,\text{Hz}$ for the thermal cloud. While the difference in detuning is insignificant in view of the much larger Rabi frequency, the difference in Rabi frequency is in fact noticeable over the observation time of 100 ms (bottom row).

can be understood phenomenologically by regarding the thermal component as a statistical mixture of particles with all different kinds of trajectories and positions, thus being subject to different *local* values of the magnetic field leading to a spatial dependence of the individual detuning [2]. For the condensate however coherent Rabi oscillations could be observed on a time as long as 100 ms. As we will see in the next section, this is in harsh contrast to coherence times extracted from Ramsey experiments. Finally it has to be emphasized, that neither simulations nor experimental results give strong hints on interaction effects which may alter the behavior expected from the simple single atom picture.

[2] We have analyzed this in the framework of the super-operator formalism which is presented in the context of the PhD thesis of Jochen Kronjaeger [71].

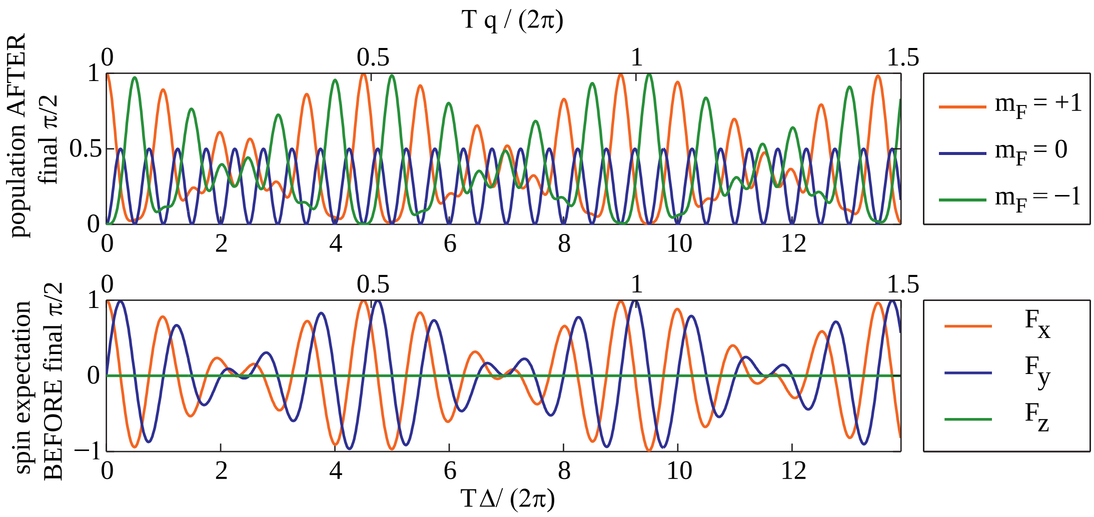

Figure 4.4: Ramsey fringes including quadratic Zeeman effect for $F = 1$, calculated numerically assuming instantaneous $\pi/2$-pulses. Fast oscillations given by the detuning $\Delta \equiv \tilde{p}$ are modulated by the smaller quadratic Zeeman effect $q \approx 0.11\Delta$ leading to a characteristic beat note. Note the double scale of the horizontal axis, showing time in units of $2\pi/q$ as well as $2\pi/\Delta$.

Ramsey experiments

Ramsey spectroscopy has been performed in a ground breaking experiment in 1950 and has been widely used ever since in all fields of physics to probe coherence. The general idea is to prepare a coherent superposition of the particular quantum states involved and to follow the time evolution relative to a local oscillator. Remixing of the superposition state leads to spatial or temporal interference patterns in the original quantum states. The fringe contrast can be taken as a measure for coherence. The specific example of Ramsey spectroscopy in a $S > 1/2$ system consists in a *initializing* $\pi/2$-pulse generating a superposition state $\zeta_{\pi/2} = \exp(i\pi/2\mathbf{F}_y)\zeta_0$ [3]. A subsequent *free evolution* governed by the linear and quadratic Zeeman effect is finally followed by a *read-out* $\pi/2$-pulse leading to the famous interference pattern in the initial states. For the experiments presented hereafter it is essential, that the $\pi/2$-pulses can be taken to act *instantaneously*, which requires, that the pulse time has to be short compared to the timescales imposed through the detuning and the quadratic Zeeman energy $\tilde{p}^{-1}$ and q^{-1} respectively. What can be seen from the simulations in comparison to the Rabi oscillations is, that the role of F_y and F_z have been exchanged. While Rabi oscillations rotate the spin vector around F_y, it starts to rotate around F_z during the free evolution of the Ramsey experiment. The initial $\pi/2$-pulse just rotates the stretched spin state $\langle \mathbf{F}_z \rangle = -1$ by 90° resulting in yet another stretched state orientated along the x-axis $\langle \mathbf{F}_x \rangle = -1$. This state starts to rotate around the z-axis during free evolution and is rotated again by the read-out pulse. As a consequence, measuring $\langle \mathbf{F}_z \rangle$ after the read-out pulse is equivalent to measuring $\langle \mathbf{F}_x \rangle$ before the read-out pulse.

In certain sense, the physics described above can also be seen in the Bloch picture of a classical spin $\vec{s}$ under the influence of an external torque $\vec{\Omega}$ which is an exact analogon

[3] The state $\zeta_{\pi/2}$ will be of great importance later in this chapter to understand the experiments on interacting spinor condensates. Particular properties of this state are explained in more detail there.

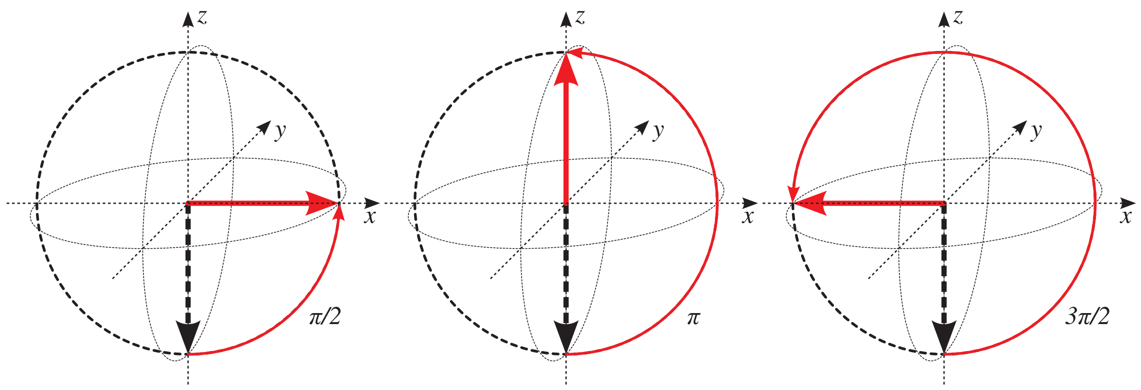

(a) Rabi oscillations (resonant rf drive for time t). From left to right: $F_z(\Omega_0 t = \pi/2) = 0$, $F_z(\Omega_0 t = \pi) = F$, $F_z(\Omega_0 t = 3\pi/2) = 0$.

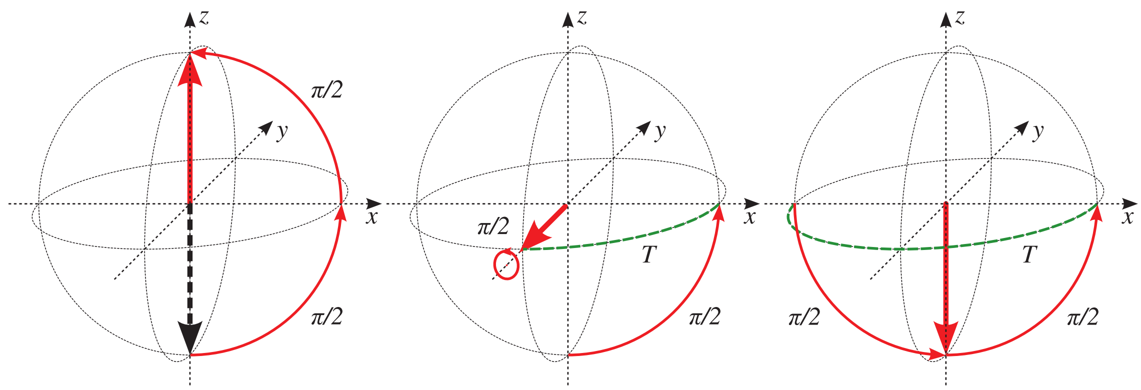

(b) Ramsey fringes (two $\pi/2$-pulses separated by time T, detuned by $\Delta = \omega - \omega_0$). $F_z(\Delta \cdot T = 0) = F$, $F_z(\Delta \cdot T = \pi/2) = 0$, $F_z(\Delta \cdot T = \pi) = -F$.

Figure 4.5: The Bloch sphere: Rabi and Ramsey oscillations in the rotating frame starting in the initial state $F_z = -F$, $F_x = F_y = 0$. Compare to Fig. 4.2 (Rabi) and Fig. 4.4 (Ramsey).

---

in the case of $|s| = 1/2$:

$$\dot{\vec{s}} = -\vec{\Omega} \times \vec{s} \quad \text{with} \quad \vec{\Omega} = \begin{pmatrix} 0 \\ \Omega_0 \cos(\omega t) \\ \omega_0 \end{pmatrix} \quad \text{and} \quad \vec{s} = \begin{pmatrix} \langle\sigma_1\rangle \\ \langle\sigma_2\rangle \\ \langle\sigma_3\rangle \end{pmatrix}. \tag{4.16}$$

Here the σ_i's are the well known Pauli matrices, which moreover represent a complete basis set to describe any possible state in a two level system. As a consequence in a $|s| = 1/2$ system *all* physical states correspond to a vector whose tip lives on the surface of the Bloch sphere. This intuitive and very useful picture can still be maintained in a $|s| > 1/2$ system as long as the quadratic Zeeman effect is neglected. This has been explained above as a rotation around an axis given by $\vec{n} = \frac{\tilde{p}}{\Omega}\vec{e}_z + \frac{\Omega_0}{\Omega}\vec{e}_y$. However the quadratic Zeeman effect leads to characteristic beat nodes where the expectation of *all* three spin components vanishes. Such a state is obviously not compatible with a stretched state whose vector lies on the Bloch sphere. In [71] it is mentioned, how a model equivalent to the Bloch

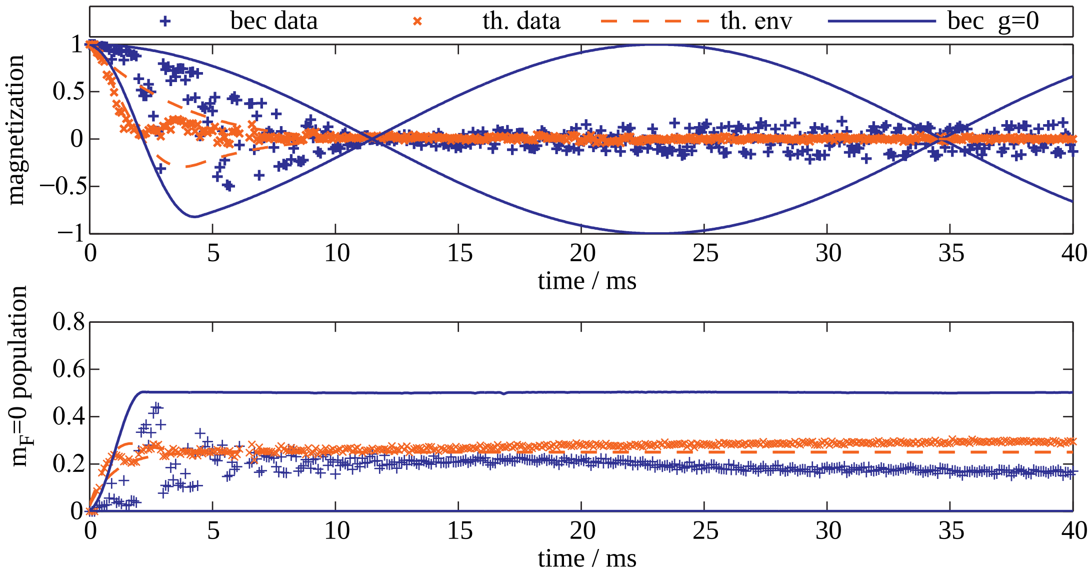

Figure 4.6: Ramsey experiment in $F = 1$. Owing to shot-to-shot fluctuations, pronounced Ramsey fringes cannot be observed. However information can still be extracted from the envelope of all data points. (see text for more details)

---

sphere can be established for arbitrary spin. However, such a model incorporates higher dimensions and lacks the intuitive picture moderated by the Bloch sphere.

The implementation of measurements dedicated to Ramsey spectroscopy is straightforward and has been extensively employed at the Hamburg spinor experiment. Fig. 4.6 shows results of a typical Ramsey experiment. The first interesting observation deduced from the data is the *absence* of nice and pronounced Ramsey fringes that are expected to occur in the magnetization as one varies the evolution time. The main reason for this is that shot-to-shot fluctuations of the Larmor frequency (see Section 3.4) render the traceability of a coherent phase evolution impossible. After a few ms of free evolution time it is only the envelope of the observed data points that allows to extract information on the coherence properties of the system. Repeating the experiment over and over again will produce data points that still fill a certain limited area in the Ramsey graph. Depending on the detuning, this area will be small (Δ small) or more extended (larger Δ). By computing the corresponding envelopes of the maxima with respect to the detuning, an upper limit for the shot-to-shot variation of the underlying detuning can be given. As for the Rabi oscillations, the damping of the normal component is much stronger than for the condensate, although more than an order of magnitude faster than in the Rabi experiment. In principle the damping could be described by Lindblad operators in the framework of the super-operator formalism [149]. A qualitative reason can be given on the basis of the time evolution in the two experiments: While the phase evolution in the Ramsey experiment is linearly affected by fluctuations in the Larmor frequency, the leading term for the time evolution of Rabi oscillations is given by the Rabi frequency. Since the Larmor frequency enters only quadratically in the effective Rabi frequency $\Omega = \sqrt{\omega_0^2 + \Delta^2}$ in terms of the

detuning Δ, Rabi oscillations are expected to be much less affected by small variations of the magnetic field as compared to a Ramsey experiment.
A reason for the damping of the condensate dynamics can be guessed by taking the formation of spin domains into account (see next section). The crucial length scale for the formation of spin patterns is shown to be given by the *spin healing length*. Similar to the healing length introduced in Chapter 2 we can introduce a spin healing length determined by the spin dependent interaction parameter g_1: $\xi_S = \hbar/\sqrt{2mg_1n}$ which is on the order of $\xi_S \approx 4\,\mu$m for typical experimental conditions [4]. The local spin distribution in a spinor condensate will not change over distances smaller than ξ_S The spatial extension of condensates produced in the astigmatic dipole trap is a few times this spin healing length along two of three directions. In principle spin pattern formation along the optical axis of the detection laser could not be observed directly by the employed detection methods. However it could be very well responsible for a spatial dependence of the phase evolution due to magnetic field variations which would be *averaged* through the detection process, reducing the available fringe contrast considerably [5]. As explained in Section 3.4 the residual gradient across the condensate amounts to a relative difference in the Larmor frequencies of at least 20 Hz which would cause a dephasing by π within 25 ms. Comparing this to Fig. 4.6 indicates that this assumption may point in the right direction. As outlined in [71] thermalization effects which lead to a redistribution of atoms between condensate and thermal cloud also contribute to a damping of coherent dynamics and thus reduce the fringe amplitude.
The influence of spin dependent interaction on the dynamics in the Rabi experiments is rather small, which is also confirmed by numerical simulations taking into account the full spin dependent Hamiltonian. Due to the rapidly overtaking decohering processes in the Ramsey experiments it is relatively pointless to try and observe spin dynamics by this experimental approach. The physics of interacting spinor condensates beyond the single particle physics considered so far is presented in the next section. A particularly useful initial state for the observation of *freely* evolving spinor condensates will be introduced, where any influence of spin dependent interaction immediately shows up as population dynamics.

Nevertheless, the experimental techniques of Rabi oscillations and Ramsey experiments represent invaluable tools for characterization of spinor systems and the exploration of technical limitations on the single atom basis. Used for state preparation and magnetic field compensation as already discussed in Chapter 3 they constitute the technical basis for all experiments on spin dynamics of interacting spinor condensates presented in the following.

4.2 Interacting spinor Bose-Einstein condensates

Spinor condensates are distinguished from their scalar counterparts by the introduction of a vectorial order parameter. Despite this fact they are also well described within mean-field theory for most of the purposes considered in this work. This section will give a

[4] In principle a spin healing length associated with every spin dependent interaction term expressed in terms of g_i can be raised as will become clear in the next section. Since the dominating contributions in ^{87}Rb come from g_1 we will stick to the above definition for now.

[5] Spin pattern formation has been observed in various trap geometries at our experiment. Even in spatially tight confined crossed dipole traps, spin domains have been readily observed, justifying the above assumption as a dephasing mechanism.

short introduction to the theoretical treatment of spinor condensates. A more detailed presentation of the underlying theory can be found in [7, 103, 71]. It will be described how the total spin influences the physics of cold collisions among atoms and how ground states can be deduced from these scattering properties. The second part of this section is devoted to experiments with ^{87}Rb spinor BEC in $F = 1$ and $F = 2$ starting from a particular initial state, that exhibits an analytical solution for the otherwise rather complicated problem of spin mixing dynamics. It will be shown how a spin dynamics resonance develops as a result of competition between spin dependent mean-field interaction and quadratic Zeeman effect. Finally the formation of spin patterns in elongated spinor BEC will be briefly presented.

4.2.1 Theoretical description of spinor BEC

The starting point for the following considerations is the mean-field energy functional introduced in Chapter 2.

$$\hat{H} = \int \left(\frac{\hbar^2}{2m} \nabla \hat{\Psi}^\dagger(\vec{r}) \nabla \hat{\Psi}(\vec{r}) \right) d\vec{r} + \frac{1}{2} \int \hat{\Psi}^\dagger(\vec{r}) \hat{\Psi}^\dagger(\vec{r}') V_{\text{int}}(\vec{r} - \vec{r}') \hat{\Psi}(\vec{r}) \hat{\Psi}(\vec{r}') \, d\vec{r} \, d\vec{r}' \tag{4.17}$$

Since the order parameter of a spinor condensate takes the form of a $2F + 1$ component vector, special attention has to be paid to the interaction term. The total spin of two colliding indistinguishable particles can take values according to the rules of angular momentum algebra $|F_1 - F_2| \leq \mathbf{F}_1 + \mathbf{F}_2 \leq |F_1 + F_2|$ together with the constraints on the symmetry of the total wave function imposed by quantum statistics. For s-wave scattering at ultra low energies the spin wave function has to be symmetric for bosonic particles to ensure a symmetric total wave function leading to the constraint $F_{tot} = 0, 2, \ldots, 2F$ for two identical bosons with spin F. The interaction potential $V_{\text{int}}(\mathbf{r} - \mathbf{r}')$ can now be written as a sum over delta potentials for different total spin channels

$$V_{\text{int}}(\vec{r} - \vec{r}') = \delta(\vec{r} - \vec{r}') \frac{4\pi\hbar^2}{m} \sum_{f=0,2,\ldots,2F} a_f \mathbf{P}_f, \tag{4.18}$$

where the $\mathbf{P}_f$ represent projection operators on the individual spin channels with $\sum \mathbf{P}_f = 1$ and the a_f are spin dependent scattering lengths To get a more intuitive form of the interaction potential it is useful to rewrite the $\mathbf{P}_f$'s in terms of products of spin matrices [46, 45, 150] (see Appendix D). The interaction potential then takes the form

$$V_{\text{int}}(\vec{r} - \vec{r}') = \hbar\delta(\vec{r} - \vec{r}')(g_0 + g_1 \vec{\mathbf{F}}_1 \cdot \vec{\mathbf{F}}_2 + \frac{5}{4} g_2 \mathbf{P_0}). \tag{4.19}$$

The g_i's are spin dependent interaction parameters and are determined through

$$F = 1 : g_0 = \frac{4\pi\hbar}{m} \frac{a_0 + 2a_2}{3} \qquad g_1 = \frac{4\pi\hbar}{m} \frac{a_2 - a_0}{3} \qquad \frac{5}{4} g_2 = 0 \tag{4.20}$$

$$F = 2 : g_0 = \frac{4\pi\hbar}{m} \frac{4a_2 + 3a_4}{7} \qquad g_1 = \frac{4\pi\hbar}{m} \frac{a_4 - a_2}{7} \qquad \frac{5}{4} g_2 = \frac{4\pi\hbar}{m} \frac{7a_0 - 10a_2 + 3a_4}{7} \tag{4.21}$$

The term proportional to g_2 only appears for spins $F \geq 2$. The energy functional for a spinor condensate finally takes the form

$$H = \int d^3\vec{r} \sum_{k=-F}^{F} \left[\mathbf{\Psi}_k^*(\vec{r}) \left(-\frac{\hbar^2\nabla^2}{2m} + V_{\text{ext}}(\vec{r}) \right) \mathbf{\Psi}_k(\vec{r}) \right.$$
$$\left. + \frac{\hbar}{2} \left(g_0 n(\vec{r})^2 + g_1 N^2 |\vec{F}(\vec{r})|^2 + g_2 N^2 |S_0(\vec{r})|^2 \right) \right], \quad (4.22)$$

with

$$n(\vec{r}) \equiv \sum_i |\mathbf{\Psi}_i(\vec{r})|^2 \quad (4.23)$$

$$\vec{F} \equiv (F_x, F_y, F_z) \quad \text{and} \quad F_\alpha(\vec{r}) \equiv \frac{1}{N} \sum_{ij} \mathbf{\Psi}_i^*(\vec{r})(F_\alpha)_{ij} \mathbf{\Psi}_j(\vec{r}) \quad (4.24)$$

$$S_0(\vec{r}) \equiv \frac{1}{N}(\mathbf{\Psi}_{-2}\mathbf{\Psi}_2 - \mathbf{\Psi}_{-1}\mathbf{\Psi}_1 + \mathbf{\Psi}_0^2/2). \quad (4.25)$$

$\vec{F}$ and S_0 denote the spin and spin-singlet amplitude per particle. The multi component GPE is derived as usual as the Euler Lagrange equation of motion of the above Hamiltonian. By writing the spinor wave function as a product of two functions one describing the local density and one describing the local spin state $\mathbf{\Psi}_k(\vec{r},t) = \psi(\vec{r},t)\zeta_k(\vec{r},t)$ the multi component GPE can be decomposed into two independent parts and a term coupling the spatial and spin degrees of freedom. An approximation usually applied for spinor condensates, as long as spin domain formation can be neglected is the *single mode approximation* (SMA) which assumes, that all spin states can be described by the same spatial wave function and that no coupling between spin and spatial degrees of freedom exist: $\mathbf{\Psi}_k(\vec{r},t) \stackrel{SMA}{=} \psi(\vec{r}) \cdot \zeta_k(t)$. As evident from this expression the dynamics is governed solely by the spin wave function $\zeta_k(t)$. Under the restriction $g_{1,2} \ll g_0$ the SMA represents a reasonable simplification, which allows for the determination of the spatial part of the wave function by techniques well known from single component condensates (compare Chapter 2). The average density $\langle n \rangle$ [6] is the only connecting factor between spin and spatial GPE. The GPE for the spin part including linear and quadratic Zeeman effect finally reads

$$H_{\text{spin}} = \frac{\hbar}{2} N \langle n \rangle \Big(g_1 \langle \vec{F} \rangle^2 + g_2 |S_0|^2 \Big) + \hbar N \Big(-p \langle F_z \rangle + q \langle F_z^2 \rangle \Big) \quad (4.26)$$

with

$$\langle F_z \rangle \equiv \sum_{ij} \zeta_i^* (F_z)_{ij} \zeta_j \quad (4.27)$$

$$\langle F_z^2 \rangle \equiv \sum_{ijk} \zeta_i^* (F_z)_{ik} (F_z)_{kj} \zeta_j \quad (4.28)$$

$$S_0 \equiv \zeta_{-2}\zeta_2 - \zeta_{-1}\zeta_1 + \zeta_0^2/2 \quad (4.29)$$

[6] For the case of a harmonically trapped BEC in the Thomas Fermi limit $\langle n \rangle = \frac{4}{7} n_0$ where $n_0 = \mu/g_0$ is the peak density in the center of the trap. This relation has been widely used throughout this thesis for the determination of the mean density deduced from spin dynamics measurements

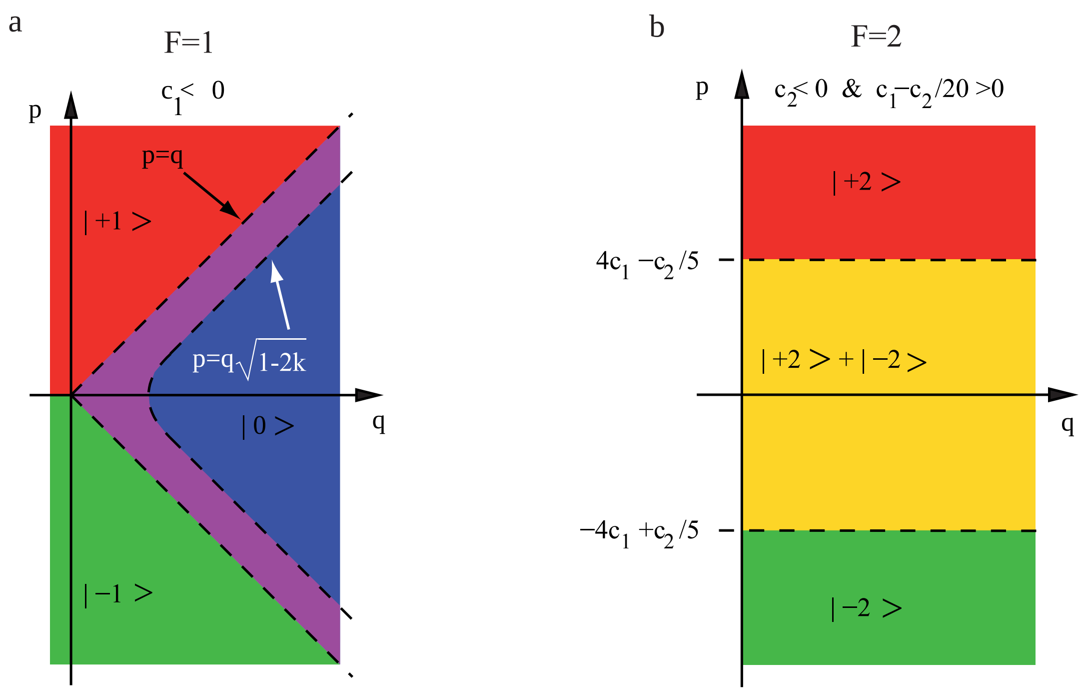

Figure 4.7: Phase diagrams for ^{87}Rb in $F = 1$ and $F = 2$. The q value plotted along the x-direction corresponds to the magnitude of the quadratic Zeeman energy, while the value of p plotted along the y-direction is determined by the linear Zeeman energy and the Lagrange multiplier invoked to account for spin conservation in Equ. 4.26. For the particular initial state $|\zeta_{\pi/2}\rangle$, $\langle \mathbf{F}_z \rangle = 0$ and therefor p vanishes. However residual magnetic field gradients can be taken into account by drawing a vertical line of length $\Delta p = 2R_{\mathrm{BEC}}|\nabla B|$ representing the condensate.
(a) For a *ferromagnetic* $F = 1$ spinor condensate ($g_1 < 0$) the ground state is either a pure m_F-state (red, green and blue area) or a mixture of all three states (purple area) depending on p and q. The dashed lines indicate that the transition takes place gradually across the purple region. Note that any $\langle \mathbf{F}_z \rangle = 0$ system corresponds to a point on the q-axis. For $k = g_1\langle n \rangle/q < 1/2$ the ground state is a pure $m_F = 0$ state.
(b) The anti-ferromagnetic or *polar* ground state of ^{87}Rb in $F = 2$ consists of a homogeneous mixture of $|2, 2\rangle$ and $|2, -2\rangle$ for $\langle \mathbf{F}_z \rangle = 0$.

Note that H_{spin} conserves the norm of the spinor $\sum_k |\zeta_k|^2$, the z-component of the spin $\sum_k m_k|\zeta_k|^2$ as well as the energy. The corresponding equations of motion for the individual spinor components can be found in the Appendix.
The spin healing length $\xi_S = \hbar/\sqrt{2mg_1n}$ already introduced in the last section represents the natural length scale for possible spatial spin structures and is typically two orders of magnitude *larger* than the usual healing length which applies to density variations. By minimizing the energy of the above Hamiltonian the spin vector ζ_{GS} representing the absolute ground state of the system with respect to the different spin depending scattering lengths can be found [45, 42, 46, 150]. In $F = 1$ the ground state at zero magnetic field is obtained easily by inspection of Equ. 4.26. Depending on the sign of g_1 the energy is minimized by either maximizing (negative sign) or minimizing (positive sign) $\langle \vec{F} \rangle$, leading to a *ferromagnetic* or *polar* ground state respectively. Since g_1 has negative sign for ^{87}Rb in $F = 1$ it is *ferromagnetic* with spontaneously broken rotational symmetry. For finite magnetic fields a quantum phase transition to a phase with unbroken symmetry and zero magnetization with all atoms in $m_F = 0$ occurs at $q = 2|g_1| * \langle n \rangle$ [42, 64].

For quantum gases with $F = 2$ an additional cyclic phase can be established, characterized by finite spin singlet amplitude S_0. On the basis of measured values for the s-wave scattering lengths for $F = 2$ [74] and measurements regarding ground state properties performed in our group [59], ^{87}Rb in $F = 2$ is *polar* but very close to the cyclic phase regarding the error bars on the directly measured value for g_2. A summary of theoretical and experimental values of the spin dependent interaction parameter for ^{87}Rb is given in Tab. D.2 in the Appendix.

However in an experiment the absolute ground state can often not be reached dynamically by starting from arbitrary initial states due to spin conservation that has to be incorporated in Equ. 4.26 in terms of a Lagrange multiplier λ, leading to a new effective parameter $p \rightarrow \tilde{p} = p - \lambda$.

4.2.2 Dynamical evolution of a stretched state

The main focus in this work has been on the dynamical evolution of ^{87}Rb spinor condensates in $F = 1$ and $F = 2$. Since the dynamics of the individual spinor components ζ_k depends on their relative phases it is crucial to choose states with a well defined initial phase. In addition it turns out that initial states with a population restricted to a *single* m_F state do not exhibit any temporal evolution according to Equ. D.3 and Equ. D.4. The reason for that is that single m_F states are eigenstates of the Zeeman- *and* the spin dependent mean-field Hamiltonian, and are consequently stationary. Early experiments in ^{23}Na [151, 44, 42, 43] and ^{87}Rb [59, 152, 57, 60] relied on such initial states anyways and where subject to spin dynamics triggered by imperfect initialization or quantum fluctuations. Recently spontaneously triggered spin dynamics in the context of spin domain formation has again attracted attention in the community [65].
For the results presented in this work a different initial state has been chosen in order to overcome the above restrictions. A coherent superposition of *all* m_F states of a given hyperfine manifold can be obtained by the application of a rf $\frac{\pi}{2}$-pulse. This technique has first been applied to quantum gases in the context of quasi spin-1/2 systems [49] and devolved to the field of spinor BEC in the last years [5, 62]. These fully transversely magnetized states are explicitly given by

$$|\zeta_{\pi/2}\rangle \overset{F=1}{=} \begin{pmatrix} \frac{1}{2} & \frac{1}{\sqrt{2}} & \frac{1}{2} \end{pmatrix}^T, \tag{4.30}$$

$$\overset{F=2}{=} \begin{pmatrix} \frac{1}{4} & \frac{1}{2} & \sqrt{\frac{3}{8}} & \frac{1}{2} & \frac{1}{4} \end{pmatrix}^T \tag{4.31}$$

for ^{87}Rb and feature some very convenient properties: The rotated stretched states can be prepared from the magnetically trapped state using a rf $\pi/2$-pulse with very good reproducibility. As a crucial property they have well defined relative phases. $\zeta_{\pi/2}$ is closely related to a classical spin in the well-known Rabi- and Ramsey-experiments and helps to develop an intuitive picture of spin dynamics. In the limit of vanishing interaction, the dynamics induced by the Zeeman effect is strictly limited to the phases of the m_F components, the populations remain constant. Any effect of interactions will become noticeable as population dynamics. At zero magnetic field the fully transversely magnetized states are equivalent to the original stretched state. All stretched states are then stationary due to the symmetry of the interaction Hamiltonian. It is only when a symmetry breaking due to a finite magnetic field occurs that a dynamical evolution will be triggered.
It is useful to write down the Hamiltonian derived in the previous section in matrix form

to get a qualitative understanding of how spin dynamics is driven.

$$\mathbf{H} = 2\hbar g_1 \langle n \rangle \begin{pmatrix} |\zeta_0|^2 & \zeta_0\zeta_{-1}^* & 0 \\ \zeta_0^*\zeta_{-1} & |\zeta_{+1}|^2 + |\zeta_{-1}|^2 & \zeta_0^*\zeta_{+1} \\ 0 & \zeta_0\zeta_{+1}^* & |\zeta_0|^2 \end{pmatrix} + \hbar q \begin{pmatrix} 1 & 0 & 0 \\ 0 & 0 & 0 \\ 0 & 0 & 1 \end{pmatrix} \tag{4.32}$$

$$= 2\hbar g_1 \langle n \rangle \begin{pmatrix} \rho_0 & 0 & 0 \\ 0 & 1-\rho_0 & 0 \\ 0 & 0 & \rho_0 \end{pmatrix} + \hbar q \begin{pmatrix} 1 & 0 & 0 \\ 0 & 0 & 0 \\ 0 & 0 & 1 \end{pmatrix} \tag{4.33}$$

$$+ 2\hbar g_1 \langle n \rangle \sqrt{\frac{\rho_0(1-\rho_0)}{2}} \begin{pmatrix} 0 & e^{-i\theta/2} & 0 \\ e^{i\theta/2} & 0 & e^{i\theta/2} \\ 0 & e^{-i\theta/2} & 0 \end{pmatrix}. \tag{4.34}$$

Note that spin- and energy conservation as well as normalization and global phase invariance reduce the number of independent variables to just two, the population ρ_0 of $m_F = 0$ and a relative phase $\theta \equiv \theta_{+1} + \theta_{-1} - 2\theta_0$[62], where $\zeta_m = \sqrt{\rho_m} e^{i\theta_m}$. If the interaction is small the phase dynamics is mainly governed by the quadratic Zeeman effect leading to a linearly growing relative phase θ which induces an oscillation of the off-diagonal terms at a frequency $\omega = q/\hbar$. This in turn leads to an oscillation of the populations at twice that frequency.

If on the other hand the system is interaction dominated both phase and population will oscillate. A growing $m_F = 0$ population leads to an increasing spin dependent interaction that will overcome the quadratic Zeeman energy and reverses phase dynamics .[7] It is clear that the ratio of $g_1\langle n \rangle / q$ determines at which particular instance this phase reversal will occur. The absence of population dynamics in the limiting cases of zero magnetic field and vanishing interaction further suggests that a competition between quadratic Zeeman energy and spin dependent mean-field interaction is responsible for the phenomenon of spin dynamics. For $F = 1$ an analytic solution of the nonlinear SMA equation of motion Equ. D.3, starting from $\zeta_{\pi/2}$, exists [5] in terms of Jacobi elliptical functions (JEF) [121].

$$\zeta_0(t) = \frac{s}{\sqrt{2}} \left[\frac{(1-k)\,\mathrm{sn}_k(\frac{qt}{2})}{1 - k\,\mathrm{sn}_k^2(\frac{qt}{2})} - \frac{i\,\mathrm{cn}_k(\frac{qt}{2})\,\mathrm{dn}_k(\frac{qt}{2})}{1 + k\,\mathrm{sn}_k^2(\frac{qt}{2})} \right] \tag{4.35a}$$

$$\zeta_\pm(t) = \mp \frac{s\,e^{\pm ipt}}{2} \left[\frac{\mathrm{cn}_k(\frac{qt}{2})\,\mathrm{dn}_k(\frac{qt}{2})}{1 - k\,\mathrm{sn}_k^2(\frac{qt}{2})} - \frac{i(1+k)\,\mathrm{sn}_k(\frac{qt}{2})}{1 + k\,\mathrm{sn}_k^2(\frac{qt}{2})} \right] \tag{4.35b}$$

where $s = \exp(-i(g_1\langle n \rangle - q)t/2)$ is a dynamic global phase. The solution further simplify to

$$|\zeta_0(t)|^2 = (1 - k\,\mathrm{sn}_k^2(qt))/2, \tag{4.36a}$$

$$|\zeta_{\pm1}(t)|^2 = (1 + k\,\mathrm{sn}_k^2(qt))/4, \tag{4.36b}$$

for the experimentally directly accessible spin state populations The occurrence of the parameter $k = g_1\langle n \rangle / q$ in the analytic solution confirms that amplitude and oscillation period of spin dynamics are indeed determined by the ratio of interaction to quadratic Zeeman energy as qualitatively extracted above. Fig. 4.8 illustrates the analytic solution across a wide range of k and in particular the case $k = 1$. The most striking feature

[7] In the next section it will be shown that the particular initial state $\zeta_{\pi/2}$ has vanishing spin-dependent interaction energy.

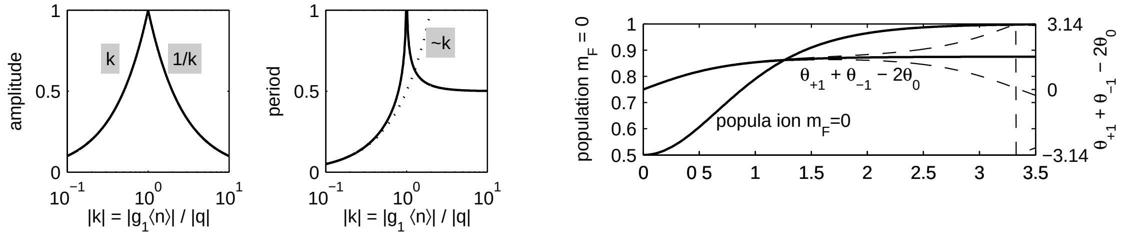

(a) Oscillation period and amplitude for population dynamics, according to the analytic solution (4.36). Note the divergent behavior of the period at $|k| = 1$.

(b) Population and phase dynamics in the vicinity of the resonance $|k| = 1.00 \pm 0.01$, starting from $\zeta_{\pi/2}$.

Figure 4.8: Resonance in $F = 1$ spin dynamics starting from the fully transversely magnetized state according to the analytic solution Equ. 4.36.

---

of the physics described by these equations is a resonance phenomenon around $k \approx 1$ caused by the competition between Zeeman- and interaction-driven phase dynamics and is therefore present in $F = 2$ as well. The JEF in Equ. 4.36 can further be simplified by approximations in two limiting cases:

Zeeman regime ($k \ll 1$) In the Zeeman regime, where the quadratic Zeeman effect dominates over spin dependent interaction the JEF can be approximated by ordinary trigonometric functions $\mathrm{sn}_k(x) \approx \sin(x)$, $\mathrm{cn}_k(x) \approx \cos(x)$, $\mathrm{dn}_k(x) \approx 1$ yielding

$$|\zeta_0(t)|^2 \overset{ZMR}{=} (1 - k\sin^2(qt))/2, \tag{4.37}$$

The amplitude of the oscillation is proportional to k, while the period is simply given by π/q.

Interaction regime ($k \gg 1$) Now the appropriate approximations for the JEF read $\mathrm{sn}_k(x) = \frac{1}{k}\,\mathrm{sn}_{1/k}(kx)$ resulting in population oscillations

$$|\zeta_0(t)|^2 \overset{IAR}{=} (1 - 1/k\sin^2(g_1\langle n\rangle t))/2. \tag{4.38}$$

Now the amplitude scales as $1/k$ and the spin dependent interaction determines the period $\pi/g_1\langle n\rangle$.

The resonance already mentioned above will occur in the intermediate regime where the two energies are on the same order of magnitude. Note that the sign of the spin dependent interaction can be conveniently obtained by determination of the initial direction of spin dynamics as seen from Equ. 4.37. This allows for a straight forward classification of $F = 1$ spinor BEC ground states to be either ferro- or antiferromagnetic. Interestingly the equations of motion for the spinor in $F = 1$ are mathematically equivalent to those of a non-rigid pendulum. Consequently the behavior of amplitude and period of spin dynamics can be directly compared to this classical analogon [61]: The interaction regime corresponds to small amplitude harmonic oscillations of the pendulum. As the amplitude grows, the period gets larger due to non-harmonic contributions to the restoring force. When the angle of deflection reaches π a non-stable equilibrium position is reached and the period goes to infinity. Realizing even larger energy input makes the pendulum rotate around its rotational axis at a smaller and smaller oscillation period.

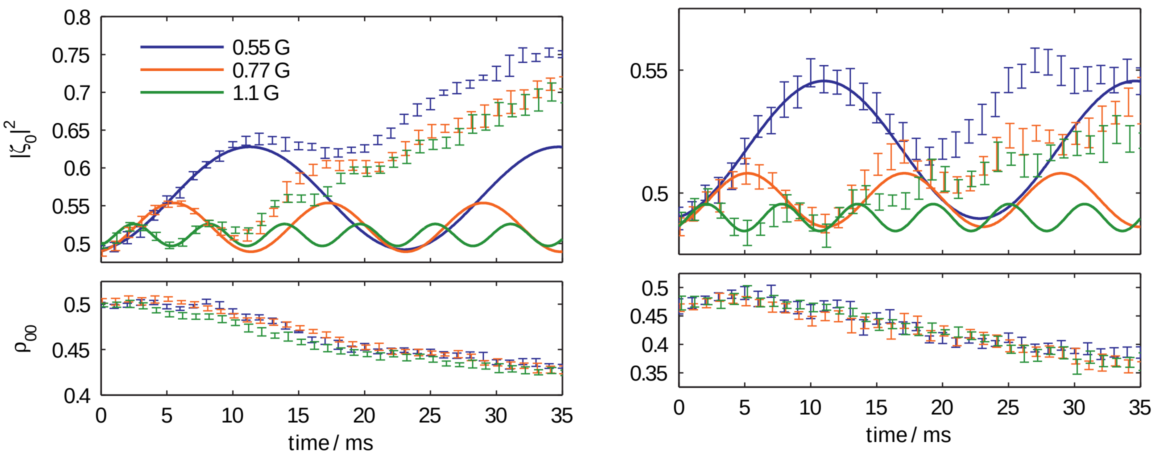

(a) "hot" – 27% cond. fraction ($\approx 3 \times 10^5$ atoms)
From fit: $|g_1\langle n\rangle| \approx 33\,\mathrm{s}^{-1}$, $\langle n\rangle \approx 1.9 \times 10^{14}\,\mathrm{cm}^{-3}$

(b) "cold" – 75% cond. fraction ($\approx 4 \times 10^5$ atoms)
From fit: $|g_1\langle n\rangle| \approx 12\,\mathrm{s}^{-1}$, $\langle n\rangle \approx 0.7 \times 10^{14}\,\mathrm{cm}^{-3}$

Figure 4.9: Population oscillations observed for the condensed fraction (top) demonstrating spin-dependent interaction in ^{87}Rb $F = 1$. In contrast the thermal component (bottom) does not exhibit any oscillatory dynamics. Data points are averaged over several repetitions of the experiment (error bars), theoretical curves (lines) are fits to the data employing the analytic solution Equ. 4.36.

Spin dynamics of a ^{87}Rb $F = 1$ spinor condensate

The experimental procedure for the observation of spin dynamics is very similar to the sequences described in Chapter 3 and the preceding section. After the generation of BEC with up to 3×10^5 particles in the astigmatic dipole trap, the magnetic field is set to the desired value. We than wait for the line trigger (see Section 3.4) to be synchronized to the mains frequency and apply a well calibrated $\pi/2$-pulse to generate the initial state. After a variable evolution time we switch off all confining potentials and image the atoms on a CCD camera after a time-of-flight of 20 ms including Stern-Gerlach separation as described in Section 3.3. The populations of the individual spin states is determined for the condensate fraction and the thermal cloud by fitting a bimodal distribution to the atomic clouds.

The spin dependent interaction term $g_1\langle n\rangle \approx$ in $F = 1$ is rather small, so that all measurements on this hyperfine ground state presented in this thesis are well within the Zeeman regime. Data has been acquired for three different magnetic fields and two different temperatures as shown in Fig. 4.9. A first conclusion that can be drawn from the observed initial growths of the $m_F = 0$ population is the fact that ^{87}Rb in $F = 1$ is *ferromagnetic* as motivated earlier.

In general the observed data is in excellent agreement with the theoretical predictions from mean-field theory for the first 10 ms. Amplitude and period follow the expected correlation $A\,, T \sim 1/B^2$. It can be seen that thermalization effects take over for evolution times larger than $25 - 30$ ms, where the fitted theory starts to deviate considerably from the data points. Unfortunately this renders the observation of oscillations in the interaction regime impossible. Nevertheless by fitting the analytic solution Equ. 4.37 to the data the interaction can be deduced from the obtained amplitude. By averaging over all available data series we find values of $|g_1\langle n\rangle| \approx 12\,\mathrm{s}^{-1}$ and $|g_1\langle n\rangle| \approx 33\,\mathrm{s}^{-1}$ for the cold and hot

samples respectively. This further illustrates that a direct observation of oscillations in the cross-over or interaction regime is viewless under these experimental circumstances and the observed thermalization times. By equating the obtained interaction energies with the quadratic Zeeman energy, a guess concerning the expected magnetic field for the resonance can be found to be $|g_1\langle n\rangle| \approx 12\,\mathrm{s}^{-1} \equiv B = 160\,\mathrm{mG}$ for the cold samples and $|g_1\langle n\rangle| \approx 33\,\mathrm{s}^{-1} \equiv B = 270\,\mathrm{mG}$ for the hot samples. This is well within the reach of our experimental capabilities, highlighting again, that thermalization and *not* inaccessible low magnetic fields inhibit the observation of the spin dynamics resonance.
In Jochen Kronjaeger's PhD thesis [71] a thorough analysis of the involved decohering mechanisms and thermalization effects can be found. It can be stated here that it is not possible so far to unambiguously determine the reason for the strong damping and the qualitative differences of the results for the hot and cold samples. The two most prominent experimental observations concerning thermalization effects are however:

Equipartition The population of the thermal clouds of the individual m_F-states ρ_{mm} where $m = -1,\, 0,\, 1$ tends to $\rho_{mm} = 1/3$. Since the mean kinetic energy per particle at $T \approx 100\,\mathrm{nK}$ clearly overwhelms the quadratic Zeeman energy, equipartition will be favored as the maximum entropy state.

Increasing condensate fraction The condensate fraction in $m_F = 0$ increases over time relative to its initial value while the total $m_F = 0$ population remains fixed. This can be seen in the context of decoherence driven cooling [53] or Bose-Einstein condensation at constant temperature [58], where interactions between thermal and condensed atoms of an initially coherent superposition, induce an evolution towards thermal equilibrium, accompanied by a redistribution of atoms between thermal cloud and condensate.

In conclusion the observation of coherent spin dynamics of ^{87}Rb spinor condensates in $F = 1$ confirms the validity of the SMA mean-field theory developed above. The results of this section have been published in [5]. Similar work has been done in the Georgia Tech group [61], while the Berkley Group developed a non-destructive detection method sensitive to the transverse magnetization at the same time [63]. The understanding of spinor condensates and their dynamics has experienced a crucial boost by the work presented in these three publications.

Observation of a spin dynamics resonance in $F = 2$

The experimental situation for $F = 1$ spinor condensates described above suffers from a awkward ratio of thermalization time to oscillation period in the interaction regime, where consequently coherent oscillations could not be observed. It would be desirable to have a system with an enhanced spin dependent interaction to reduce the time necessary to observe the transition to the interaction regime and eventually detect the predicted resonance. The analogous interaction parameter $|g_1\langle n\rangle|$ for ^{87}Rb in $F = 2$ is approximately an order of magnitude larger than its counterpart in $F = 1$. Nevertheless for $F = 2$ no exact analytical solution exists even for a fully transverse magnetized state. Moreover an additional time evolution determined by the spin singlet amplitude S_0 has to be taken into account when studying spin dynamics in $F = 2$. It turns out that the choice of ^{87}Rb and the initial state $\zeta_{\pi/2}$ is particularly well suited, since it behaves as an *effective* $F = 1$ system to lowest order as we shall see. The equations of motion for $F = 2$ are unfortunately not integrable and no analytic solution exists. However approximate solutions for very large and very small quadratic Zeeman effect can be obtained [4] and give useful insight into the dynamics expected from starting with a fully transversely magnetized state. Deep in the Zeeman regime these solutions read

$$\begin{aligned}|\zeta_0|^2 = \frac{3}{8}\Bigg\{1 &+ \frac{g_1\langle n\rangle}{2q}\left[2\left(1-\cos(2qt)\right)+\frac{1}{2}\left(1-\cos(4qt)\right)\right] \\ &- \frac{g_2\langle n\rangle}{2q}\left[\frac{1}{4}\left(1-\cos(2qt)\right)-\frac{1}{64}\left(1-\cos(8qt)\right)\right]\Bigg\}\end{aligned} \tag{4.39a}$$

$$\begin{aligned}|\zeta_1|^2 = \frac{1}{4}\Bigg\{1 &- \frac{g_1\langle n\rangle}{2q}\left[\frac{3}{4}\left(1-\cos(2qt)\right)-\frac{1}{12}\left(1-\cos(6qt)\right)\right] \\ &+ \frac{g_2\langle n\rangle}{2q}\left[\frac{3}{16}\left(1-\cos(2t)\right)-\frac{1}{48}\left(1-\cos(6qt)\right)\right]\Bigg\}\end{aligned} \tag{4.39b}$$

$$\begin{aligned}|\zeta_2|^2 = \frac{1}{16}\Bigg\{1 &- \frac{g_1\langle n\rangle}{2q}\left[3\left(1-\cos(2qt)\right)+\frac{3}{2}\left(1-\cos(4qt)\right)+\frac{1}{3}\left(1-\cos(6qt)\right)\right] \\ &+ \frac{g_2\langle n\rangle}{2q}\left[\frac{1}{12}\left(1-\cos(6qt)\right)-\frac{3}{64}\left(1-\cos(8qt)\right)\right]\Bigg\}\end{aligned} \tag{4.39c}$$

It can be seen from these equations, that all terms incorporating g_2 have pre-factors that are almost an order of magnitude smaller than those for g_1. Even though $g_2 \approx g_1$ for ^{87}Rb the dynamical evolution of a ^{87}Rb $F = 2$ spinor condensate will thus be governed by oscillatory behavior very similar to $F = 1$ with a fundamental oscillation period π/q and amplitude proportional to k.
On the contrary in the interaction regime as $q \to 0$ the equations of motion are given by

$$|\zeta_0|^2 = \frac{3}{8}\left[1+\frac{q}{2g_1\langle n\rangle}\left(1-\cos(4g_1\langle n\rangle t)\right)\right] \tag{4.40a}$$

$$|\zeta_1|^2 = \frac{1}{4} \tag{4.40b}$$

$$|\zeta_2|^2 = \frac{1}{16}\left[1-\frac{3q}{2g_1\langle n\rangle}\left(1-\cos(4g_1\langle n\rangle t)\right)\right] \tag{4.40c}$$

Approximating the solutions to this order leads to a cancellation of all g_2 terms which can be understood by recalling that $S_0 = 0$ for $\zeta_{\pi/2}$. Again oscillation period $\sim \pi/2g_1\langle n\rangle$ and amplitude $\sim 1/k$ are given by expressions similar to the case $F = 1$.
Fig. 4.10 shows experimental results for spin oscillations in $F = 2$ for various magnetic fields. Similar to $F = 1$, k has been simply varied by changing the magnetic field while keeping the density constant throughout all experimental series [8]. It is clearly visible, that the oscillation amplitude exhibits a maximum at $|k| \approx 1/3$. In the Zeeman regime the amplitude grows like $A \sim 1/q$ as expected from the mean-field solutions while it decreases as $A \sim q$ in the interaction regime. The oscillation period increases as $T \sim \pi/q$ as one

[8] Furthermore this approach ensures equal external trapping for all data sets, since a variation of the density in the dipole trap is always correlated with a change in the trapping frequencies and therefor also the gravitational sag. The harmonic potential is severely distorted for very low trap depths as discussed in detail in Section 3.2. Thus very shallow traps should be avoided as long as comparison with theoretical results obtained in harmonic potentials is desired.

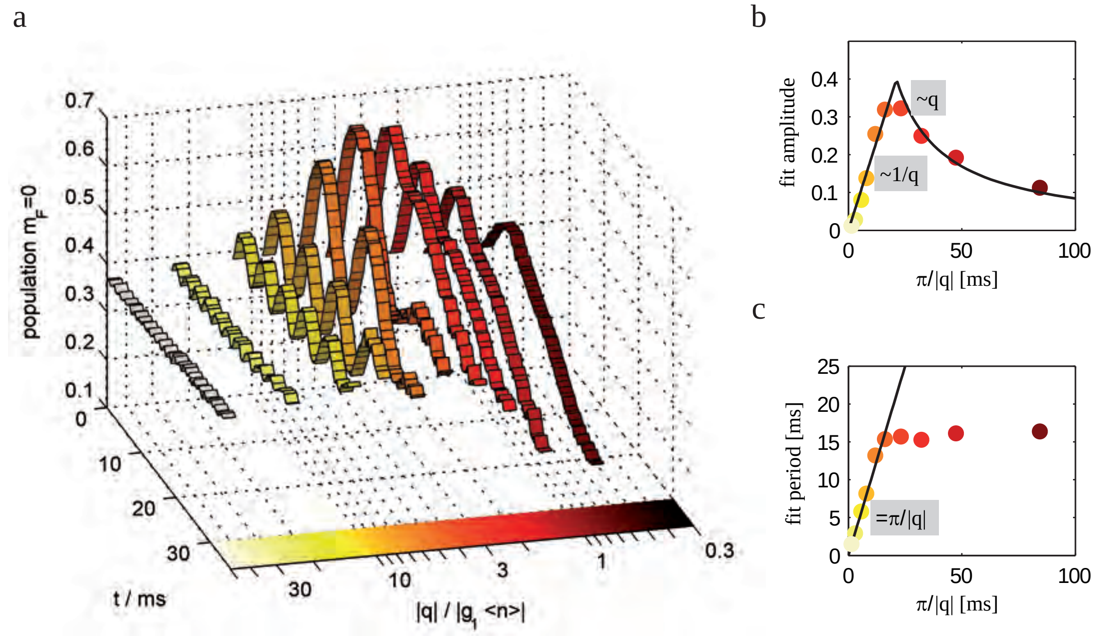

Figure 4.10: (a) Resonance phenomenon in $F = 2$. Plotted are coherent oscillations for different values of $q/(g_1\langle n\rangle)$, where $q \sim B^2$ is the quadratic Zeeman energy and $g_1\langle n\rangle$ the first spin-dependent mean-field energy (processes involving $\Delta m_F = 1$). In this figure, $g_1\langle n\rangle = 47\,\mathrm{s}^{-1}$ (corresponding to a density of $1 \times 10^{14}\,\mathrm{cm}^{-3}$) is used as a reference value, since only the magnetic field has been varied among the different data sets. The mean density has been obtained from SMA theory fits similar to those presented for $F = 1$.
Amplitude (b) and period (c) have been extracted for qualitative comparison with theoretical predictions for $F = 1$ given in Fig. 4.8.

---

approaches resonance from the high field side. In the interaction regime, the period is almost constant as expected. Close to resonance all oscillations are severely damped, so that only one (half) oscillation could be observed for these values of k.
Furthermore a direct observation of the divergence of the oscillation period is inhibited by this damping. Very small deviations from the resonance value lead to large excursion of the resulting dynamics, so that for realistic experimental situations the magnetic field has to be convoluted with an appropriate function taking its finite widths on experimental time scales into account. This will already significantly diminish the divergent behavior at resonance. As outlined in detail in [71] another possible mechanism causing the damping is the formation of spin domains that would of course lead to a breakdown of the single mode approximation.
In the Zeeman regime however the approximate solutions Equ. 4.39 describe the observed physics quite well and justify the effective Spin-1 approach. Fitting the mean-field model to the data shows good agreement for much longer evolution times as compared to measurements performed close to resonance or in the interaction regime.
The experimental results presented above constitute the first evidence for a spin dynamics resonance in ultracold quantum gases. Distinguished as a non-linear *many-body* effect it arises in the mean-field picture and is in contrast to spin dynamics observed for two atoms residing on individual lattice sites in a deep Mott-insulator [72, 74, 73]. Even though based on the same underlying physical processes the resonance phenomenon reported by

the Mainz group is explained by interaction driven Rabi oscillations – linear two-level physics. A possible cross-over between these two regimes is concerned at the end of the next chapter, where spin dynamics in optical lattices of different lattice depth has been investigated.

Formation of spatial spin patterns

All theoretical considerations so far have assumed that spinor Bose-Einstein condensates are very well described within the framework of the single mode approximation. The measurements, especially in $F = 2$, on the other hand give some indications that spin domain formation may have occurred, which would mark the breakdown of the SMA. At the Hamburg spinor experiment various measurements have been performed in $F = 2$ that clearly show that spin domain formation occurs in elongated condensates as well as in almost spherical samples trapped in a crossed dipole trap.
Pattern formation in multi-component BEC was observed first by the MIT group in anti-ferromagnetic ^{23}Na induced by magnetic gradients [52, 54, 50] and is well understood in this context. Quasi spin-1/2 systems of ^{87}Rb in $|1, -1\rangle$ and $|2, 1\rangle$ exhibit spatial structure in terms of state separation [50] and spin waves in the normal component [52] that is explained by demixing dynamics and condensate-normal component interaction respectively. In later experiments structure formation has been observed in ^{87}Rb $F = 2$ [60, 59] and $F = 1$ condensates in the interaction regime [64, 61]. While in the latter case spin domain formation arises naturally as an effect of *spontaneous symmetry breaking* inherent to ferromagnetic systems, the latter can be explained by local density arguments, where the mean-field solutions developed above remain valid in every infinitesimal volume element, leading to a dephasing of different regions of the condensate. None of the mechanisms discussed so far is responsible for the structure formation we have observed in $F = 2$. As described in great detail in [71] and [153] the physical mechanism of *dynamical instability* leads to the formation of spin structures with domain sizes on the order of $2\pi\xi_{\mathrm{S}}$ in very elongated spinor BEC as employed in our experiments. For large magnetic fields spin waves with locally conserved $\langle \mathbf{F}_z \rangle$ occur, while for smaller fields as the influence of the interaction grows spin waves with locally modulated $\langle \mathbf{F}_z \rangle$ are observed. For details concerning the experimental results and methods the reader is referred to Jochen Kronjaeger's PhD thesis [71].

4.3 Future perspectives

The versatile physics that can be investigated with spinor Bose-Einstein condensates holds a large variety of future perspectives. Continuative experiments on structure formation in ferromagnetic and polar condensates may be performed to deepen the understanding in this field of science that extends far beyond the physics of Bose-Einstein condensates. Adding a periodic potential will modify the physics of spinor condensates further. First measurements presented at the end of Chapter 5 promise a rich and complex interplay between spin dependent contact interaction, (spin dependent) tunneling and spin dependent optical potentials. The important role of large dipole moments making quantum gases interact *anisotropically* has already been recognized and the availability of atomic condensates with a large magnetic moment as e.g. ^{52}Cr [67] or the rapid development in the field of heteronuclear ground state molecules [88] will certainly lead to a boost in the field of magnetism in quantum gases again. New developments towards experiments with very small atom numbers promise to achieve such highly non-trivial states as the spin-singlet state in $F = 1$ condensates.

Chapter 5

Spinor Bose Einstein condensates in optical lattices

Since the seminal paper on quantum degenerate atoms in optical lattices by Jaksch *et.al* [78] and the first experimental realization of the quantum phase transition from a superfluid to a Mott-insulating state in a 3D optical lattice by Greiner and colleagues [80] the interest in this new field of research literally exploded as discussed in more detail in the introduction.

The fascinating prospect of investigating strongly correlated systems thus far restricted to nuclear and solid state physics combined with the ultimate experimental control promised by ultracold quantum gases has lead to a vast variety of theoretical proposals concerning this particular physical system. Simulation of solid-sate Hamiltonians in purified systems, quantum computation and the chance to investigate quantum chemical processes with an unprecedented degree of control are only few examples of the fascinating possibilities that open up in this still rapidly expanding field merging somehow atomic and solid state physics.

The underlying thesis contributes to this goal by investigating cold atoms in a triangular optical lattice system for the first time. So far restricted to simple cubic lattice, this work concerns experiments on the superfluid to Mott-insulator transition in this new lattice system. Very first measurements on spin dynamics in the triangular lattice are presented to motivate further work dedicated to quantum magnetism in this particular physical system.

The contents of the underlying chapter is structured as follows: A major part of this PhD thesis has been dedicated to the design and setup of a triangular optical lattice and the realization of experiments within this system. The first part of this chapter will therefor discuss the generation of periodic potentials with interfering laser beams.

After a short reminder of the text book example of a standing wave, an introduction to the crystallography of a two-dimensional three-beam lattice, necessary to understand the formation of the resulting periodic potential of the triangular lattice, will be given. The physics of non-interacting particles in a periodic potential, analogous to solid state physics, is discussed next, since it constitutes the basis of all experiments with cold atoms in optical lattices.

It will be discussed how the lattice depth is calibrated and how the polarization of the beams can be adjusted by investigating Bragg reflection between adjacent m_F-states.

The following part of the underlying chapter motivates and introduces the Bose-Hubbard

model for bosonic atoms. The crucial parameters of an optical lattice – onsite interaction U and tunneling energy J – will be introduced and explicitly calculated. Very first experiments investigating the superfluid-Mott-insulator transition in the triangular lattice arr presented thereafter. In this context the challenge of adiabatic loading of an optical lattice and the formation of Mott-shells is briefly discussed.
Finally measurements on spin changing dynamics, similar to those in Chapter 4, but inside an optical lattice of various depth are presented.

5.1 Generation of periodic potentials for ultracold atoms

5.1.1 The standing wave - textbook physics

The most straightforward way to generate a periodic array of potential wells consists in creating a standing wave by super imposing two laser beams traveling in opposite directions. This is conveniently done by retro-reflecting a Gaussian laser beam with wave vector k_{L} as depicted in Fig. 5.1(a). The potential in the vicinity of the minimal waist ($w(z) \approx w_0$) can be written as

$$I_{\mathrm{1D}}(r,z) = 4 \cdot U_0 e^{-2r^2/w_0^2} \cdot \cos^2(k_{\mathrm{L}} z) \simeq 4 \cdot U_0 \left(1 - \frac{2r^2}{w_0^2}\right) \cdot \cos^2(k_{\mathrm{L}} z), \tag{5.1}$$

where U_0 is given through Equ. 3.3 in the simplest case of large detuning. Note that the potential at the maxima of the standing wave is four times larger than that of a single beam dipole trap. The strength of the lattice potential is usually specified in the natural units of the recoil energy associated with the absorption of one *lattice* photon $E_{\mathrm{r}} = (\hbar k)^2/(2m)$. Sticking to the case of large detuning for simplicity (see Equ. 3.3) the potential strength is given by

$$\frac{V_0}{E_{\mathrm{r}}} = \frac{4U_0}{E_{\mathrm{r}}} = 4 \cdot \frac{3\pi c^2}{2\omega_0^3} \frac{\Gamma}{\Delta} \cdot \frac{2m}{\hbar^2 k^2} \tag{5.2}$$

The periodicity of the generated lattice is described by a reciprocal lattice vector $\mathbf{b} = 2\mathbf{k}_{\mathrm{L}}$. The distance between neighboring lattice sites is consequently $\lambda_{\mathrm{L}}/2$.
A concept that will be very useful for lattices generated by more than two beams can already be derived regarding the example of the 1D lattice. In general the reciprocal lattice vectors of an optical lattice generated by laser beams with wave vectors $\mathbf{k}_{\mathrm{L},i}$ can be written as [82]

$$\mathbf{b}_i = \mathbf{k}_{\mathrm{L},i} - \mathbf{k}_{\mathrm{L},j}. \tag{5.3}$$

A closer look at this equation reveals the similarity to a 2-photon Bragg scattering event as described in Section 3.5.4. In this picture the potential felt by the atoms inside the optical lattice can be regarded as a redistribution of photons among the different lattice beams by virtual absorption and stimulated emission processes. In fact, in solid state physics, constructive interference in X-ray Bragg scattering [154] occurs at incidents fulfilling $\mathbf{k}_{\mathrm{out}} - \mathbf{k}_{\mathrm{in}} = \mathbf{G}$, where $\mathbf{G}$ is any reciprocal lattice vector.
Applying this formalism to the 1D lattice directly gives the correct reciprocal lattice vector

$$\mathbf{b} = \mathbf{k}_{\mathrm{L},2} - \mathbf{k}_{\mathrm{L},1} = k - (-k) = 2k. \tag{5.4}$$

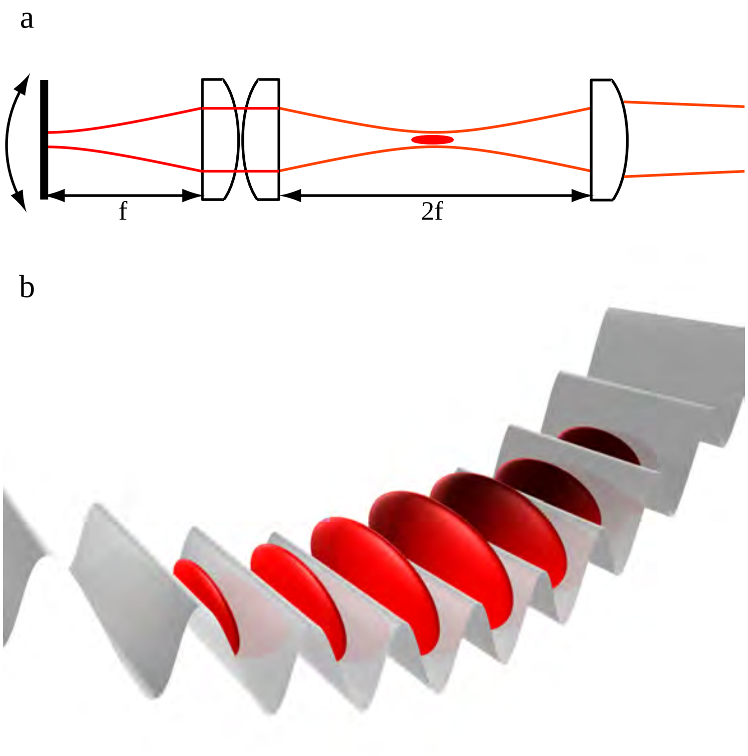

Figure 5.1: (a) Scheme for the setup of a retro-reflected 1D lattice in f-f configuration using achromatic lenses and a mirror. It is crucial to achieve an excellent superposition of the waists of the two counter propagating beams to make the lattice symmetric and minimize offsets. Due to the Gaussian shape of the laser beams an additional harmonic confinement growing with the lattice depth is imposed.
(b) BEC cut into quasi-two dimensional discs by a 1D optical lattice.

A rough estimate of the trapping frequency in a single well of a rather deep standing wave can be obtained by the harmonic approximation leading to

$$\omega_{\mathrm{latt}} = k\sqrt{\frac{2V_0}{m}} = \frac{2E_{\mathrm{r}}}{\hbar}\sqrt{\frac{V_0}{E_{\mathrm{r}}}}. \tag{5.5}$$

Due to the Gaussian shape of the laser beams creating the lattice, an additional global confinement is always added to the system, rendering any realistic lattice configuration *inhomogeneous*. It is thus favorable to use beams of not too small waist size in order to minimize the additional confinement. Moreover for given initial conditions (trapping frequencies of the XDF, temperature, a.s.o.), there will always be one waist size optimizing adiabaticity of the lattice loading process.
A balance between additional external confinement ($\approx \bar{\omega}_{\mathrm{latt}}$) and the repulsive on-site interaction ($\approx U$) has to be achieved in order to keep the Thomas-Fermi radius of the BEC as constant as possible during the lattice ramp-up. If this can be guaranteed the atoms do not need to redistribute to reach the new equilibrium configuration. These constraints will be discussed in more quantitatively later in this chapter. However to anticipate the results, for ^{87}Rb and typical experimental conditions a waist size of $90\,\mu$m $< w_0 < 150\,\mu$m is a rather good choice. The 1D lattice implemented at our experiment has a minimum waist of $w_0^{1D} = 90\,\mu$m, whereas the beams creating the 2D three-beam lattice as described in the next chapter have waists of $w_0^{2D} = 115\,\mu$m.
The trapping frequencies characterizing the additional external confinement can be cast in the harmonic approximation

$$\omega_{\mathrm{harm}} = \sqrt{\frac{4E_{\mathrm{r}}}{mw_0^2}}\sqrt{\frac{V_0}{E_{\mathrm{r}}}}, \tag{5.6}$$

where the variation of the potential along the axial direction z has been neglected. To obtain the overall harmonic trapping frequencies $\omega_{\text{harm}}^{\text{tot}}$, one simply has to add the squares of the individual contributions:

$$\omega_{\text{harm},i}^{\text{tot}} = \sqrt{\omega_{\text{harm},i}^{\text{latt}}{}^2 + \omega_{\text{harm},i}^{\text{XDF}}{}^2}. \tag{5.7}$$

A comparison of the two trapping frequencies reveals that $\bar{\omega}_{\text{harm}}^{\text{tot}} \ll \omega_{\text{latt}}$ indicating that a three dimensional BEC loaded in a 1D standing wave potential will be cut into several pancake-shaped quasi-two dimensional BEC for sufficiently large lattice depth.

5.1.2 Three-beam lattices in two dimensions

Up to now the usual way to create two- or three dimensional optical lattices at ultracold atom experiments has been to simply superimpose three perpendicular standing wave lattices (see e.g. [80]). To avoid any undesired interference between the individual lattice branches, they have been detuned with respect to each other by several tens of Mhz. The resulting lattice potential is square or simple cubic in two and three dimensions respectively. During this thesis a different approach has been made to obtain a two dimensional lattice. The interference pattern of three superimposed *traveling* waves has been employed resulting in a lattice with hexagonal symmetry. It can be stated in general that $D+1$ laser beams are enough to create a periodic potential in D dimensions. Moreover those lattices share some very convenient generic features that will be summarized in the following:

Influence of a fluctuating phase First of all a change in the relative phase of the $D+1$ beams will only result in global shift of the potential. Neither the geometry nor the polarization of the lattice will be influenced. Nevertheless will it be crucial to actively stabilize the lattice beams phases with respect to each other, because a *global shaking* will lead to undesired heating processes. Note that the experimental effort is considerable as compared to a combination of standing waves, where only the coherence length of the laser and the mechanical rigidity of the mirror limit the stiffness of the relative phases [1].

Atomic basis By changing the polarization of the beams, the basis of the underlying lattice in terms of the spatial distribution of the individual potential wells can be changed. The translational symmetries on the other hand remain unchanged and are solely determined by the beam geometry.

In the following we will consider a lattice created by three beams in a plane enclosing angles of 120° as depicted in Fig. 5.2. The corresponding wave vectors of the laser beams read in Cartesian coordinates

$$\mathbf{k}_1 = k_{\mathrm{L}} \left(\quad 0, 0, 1 \quad \right) \tag{5.8}$$

$$\mathbf{k}_{2/3} = k_{\mathrm{L}} \left(\quad \pm\tfrac{\sqrt{3}}{2}, 0, -\tfrac{1}{2} \quad \right) \tag{5.9}$$

[1] The electric field of the laser has to vanish at the surface of the retro reflecting mirror, defining a rigid phase relation between the two beams.

Following the procedure developed in the preceding section, it is straightforward to write down the reciprocal lattice vectors

$$\mathbf{b}_{1/2} = \mathbf{k}_1 - \mathbf{k}_{2/3} = b\Big(\mp \frac{1}{2}, 0, \frac{\sqrt{3}}{2}\Big) \tag{5.10}$$

where a particular symmetric choice has been made and $b = |\mathbf{b}_{1/2}| = \sqrt{3}k_\mathrm{L}$ is the natural unit of the reciprocal lattice. Through the well known relation between reciprocal and direct lattice vectors $\mathbf{a}_i \cdot \mathbf{b}_j = 2\pi\, \delta_{i,j}$ the unit vectors of the direct lattice $\mathbf{a}_i$ are easily found to be

$$\mathbf{a}_{1/2} = a\Big(\mp \frac{\sqrt{3}}{2}, 0, \frac{1}{2}\Big), \tag{5.11}$$

where $a = |\mathbf{a}_{1/2}| = 2/3\,\lambda_\mathrm{L}$ is the periodicity of the direct lattice. While the reciprocal lattice vectors enclose an angle of 60° and are symmetric with respect to $\mathbf{e}_y$, the direct unit vectors obey $\angle(\mathbf{a}_1, \mathbf{a}_2) = 120°$, again symmetric relative to the y-axis. Another useful quantity is the area of the primitive cell that is given by $|\mathbf{a}_1 \times \mathbf{a}_2| = \sqrt{3/4}a^2 = 2/(3\sqrt{3})\,\lambda_\mathrm{L}^2$.

Triangular lattice

So far we did not concern the polarization of the lattice beams at all. Choosing the polarization linear and perpendicular to the plane (π^0) spanned by the lattice beams results in a potential [2].

$$V_{2\mathrm{D}}^{\triangle}(\mathbf{r}) = V_0 \left(\frac{3}{4} + \frac{1}{2} \left(\cos\left(\mathbf{b}_1 \cdot \mathbf{r}\right) + \cos\left(\mathbf{b}_2 \cdot \mathbf{r} + \phi_{12}\right) + \cos\left((\mathbf{b}_1 - \mathbf{b}_2) \cdot \mathbf{r} + \phi_{23}\right)\right)\right). \tag{5.13}$$

The wells are ordered on a triangular pattern as shown in Fig. 5.2(a). This corresponds to a mono atomic basis, where only one potential well per primitive cell is available. The polarization at the minima is purely linear and leads to a *spin-independent* trapping for relatively far detuned laser beams. The number of nearest neighbors in the plane amounts to 6, compared to 4 in a two dimensional square lattice.

A comparison of a single well of the triangular lattice to that of a square lattice at the same lattice depth V_latt reveals the much stronger modulation of the triangular lattice along *all* directions. The influence of neighboring lattice sites on each other is therefor significantly reduced. This will become more evident in Section 5.5 where the transition from a superfluid to a Mott-insulator is investigated.

Hexagonal lattice

If the polarization of the beams is chosen to be in the plane spanned by the lattice beams, the resulting potential will look as shown in Fig. 5.2b. The potential minima are now ordered on a hexagonal lattice.

Moreover the polarization at these minima is purely circular and changes sign between

[2] To be mathematically rigorous the resulting intensity is obtained by adding the fields of the three beams coherently $\mathbf{E}_{2\mathrm{D}}(\mathbf{r}, t) = \sum_i \mathbf{E}_\mathrm{i}(\mathbf{r}, t)$ and averaging its squared modulus over time

$$V_{2\mathrm{D}}^{\triangle}(\mathbf{r}) \sim \frac{1}{T}\int_0^T |\mathbf{E}_{2\mathrm{D}}(\mathbf{r}, t)|^2\, dt \tag{5.12}$$

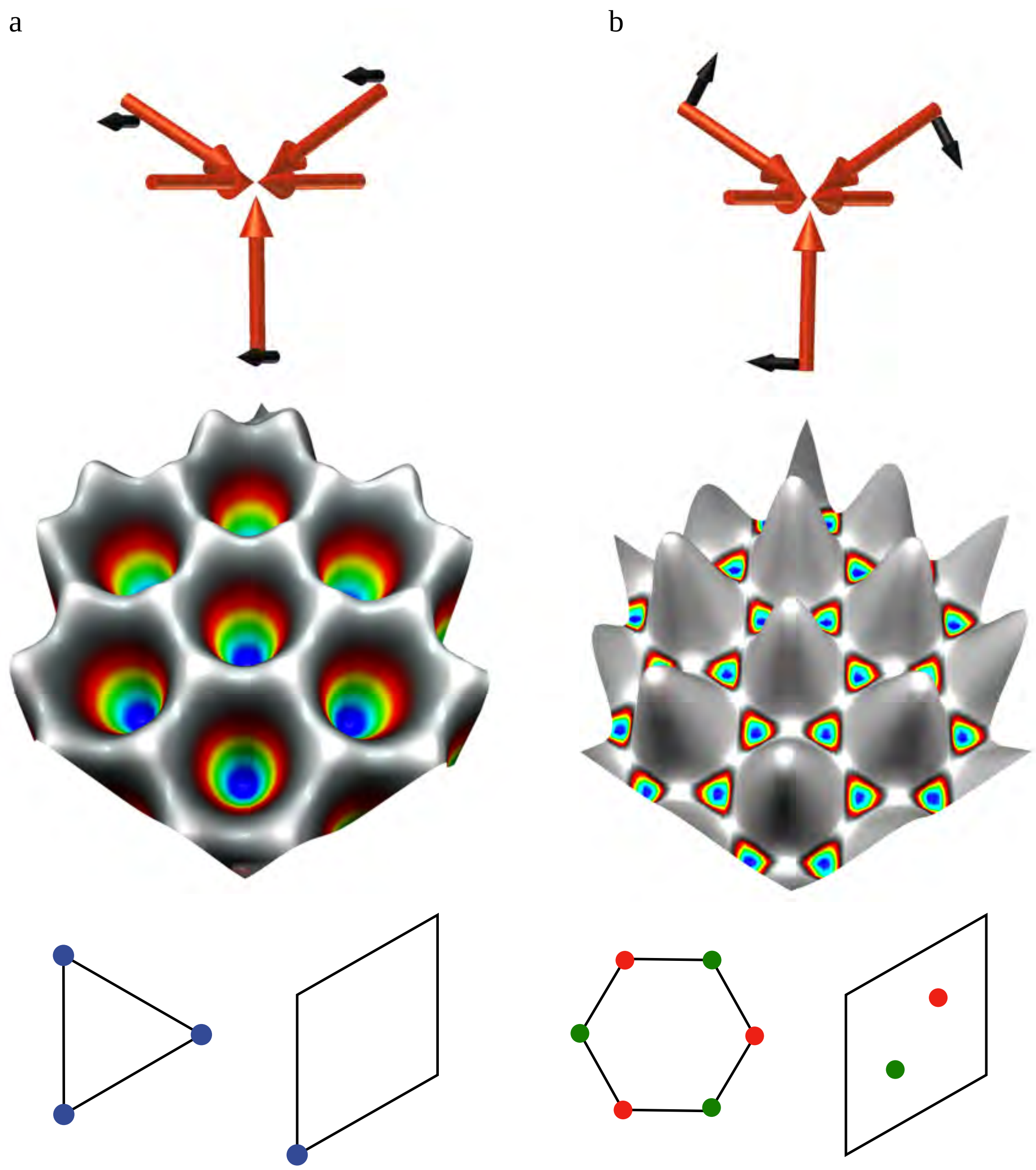

Figure 5.2: (a) The potential wells are ordered in a triangular pattern if the polarization is perpendicular to the lattice plane. The primitive cell contains one atom at $\mathbf{a}^\star = 0$.
(b) If the polarization is rotated in the plane, the potential wells form a hexagonal pattern. The polarization at the potential minima is purely circular and alternating between nearest neighbors. As a result the primitive cell contains an anti-ferromagnetic basis with one σ^+-well at $\mathbf{a}_1^\star = 1/3\,(\mathbf{a}_1 + 2\mathbf{a}_2)$ and a σ^--well at $\mathbf{a}_2^\star = 1/3\,(2\mathbf{a}_1 + \mathbf{a}_2)$.

---

nearest neighbors. For circular polarized light the dipole force is m_F-dependent even for intermediate detunings and thus the hexagonal lattice forms a *spin-dependent* anti-ferromagnetic lattice potential. To get a more quantitative expression for this potential it is convenient to write down the total electric field in the circular basis

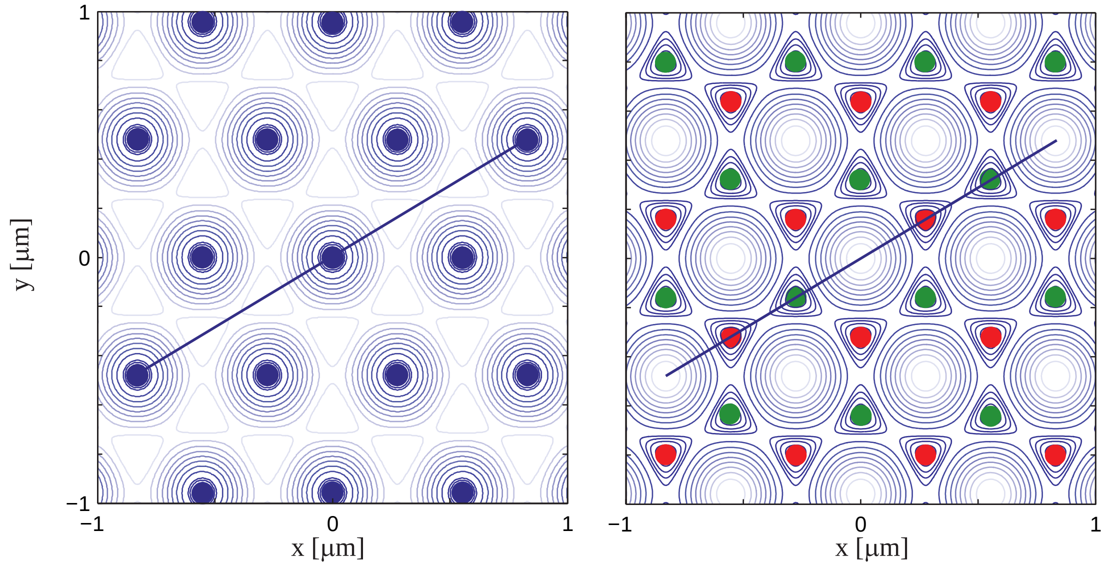

Figure 5.3: Contour plots of the triangular and the hexagonal lattice potential plotted in Fig. 5.2. It is obvious that the hexagonal potential is the *inverse* of the triangular one in a certain sense. The anti-ferromagnetic basis of the hexagonal lattices is indicated by red (σ^+) and green (σ^+) wells. The blue lines mark the direction of the potential cuts presented in Fig. 5.4
.

($\mathbf{e}_+ = 1/\sqrt{2}(\mathbf{e}_x + i\mathbf{e}_y)$, $\mathbf{e}_- = 1/\sqrt{2}(\mathbf{e}_x - i\mathbf{e}_y)$, $\mathbf{e}_z$):

$$E_+ = \frac{E_0}{\sqrt{2}}\left(e^{i\mathbf{k}_1\cdot\mathbf{r}} + je^{i\mathbf{k}_2\cdot\mathbf{r}} + j^2 e^{i\mathbf{k}_3\cdot\mathbf{r}}\right) \tag{5.14}$$

$$E_- = \frac{E_0}{\sqrt{2}}\left(e^{i\mathbf{k}_1\cdot\mathbf{r}} + j^2e^{i\mathbf{k}_2\cdot\mathbf{r}} + j e^{i\mathbf{k}_3\cdot\mathbf{r}}\right), \tag{5.15}$$

where $j = \exp(i4\pi/3)$. The corresponding potential for the two polarizations is thus given by

$$V_+ = \frac{V_0}{8}\left(3 + 2(\cos(\mathbf{b}_1\cdot\mathbf{r} - 2\phi_c) - \cos(\mathbf{b}_2\cdot\mathbf{r} - \phi_c) + \cos((\mathbf{b}_1 - \mathbf{b}_2)\cdot\mathbf{r} - 2\phi_c)\right) \tag{5.16}$$

$$V_- = \frac{V_0}{8}\left(3 + 2(-\cos(\mathbf{b}_1\cdot\mathbf{r} - \phi_c) + \cos(\mathbf{b}_2\cdot\mathbf{r} - 2\phi_c) + \cos((\mathbf{b}_1 - \mathbf{b}_2)\cdot\mathbf{r} + 2\phi_c)\right) \tag{5.17}$$

with the characteristic phase $\phi_c = \pi/3$.
These two expressions clearly emphasize, that the translational symmetry of the underlying sub-lattices is exactly the same as for the triangular lattice. The change in polarization only corresponds to a change of the local basis with respect to the position of the individual potential wells inside a primitive cell.

By finding the maxima of Equ. 5.16 one can easily show that the primitive cell of the hexagonal lattice contains an anti-ferromagnetic basis with one σ^+-well at $\mathbf{a}_1^\star = 1/3\,(\mathbf{a}_1 + 2\mathbf{a}_2)$ and a σ^--well at $\mathbf{a}_2^\star = 1/3\,(2\mathbf{a}_1 + \mathbf{a}_2)$. Disregarding the m_F-dependence as justified for $|F, 0\rangle$ the pure intensity modulation given by the sum of the two terms in Equ. 5.16 can be written as

$$V_{2\mathrm{D}}^{\pm}(\mathbf{r}) = V_0\left(\frac{3}{4} - \frac{1}{4}\left(\cos\left(\mathbf{b}_1\cdot\mathbf{r}\right) + \cos\left(\mathbf{b}_2\cdot\mathbf{r} + \phi_{12}\right) + \cos\left((\mathbf{b}_1 - \mathbf{b}_2)\cdot\mathbf{r} + \phi_{23}\right)\right)\right). \tag{5.18}$$

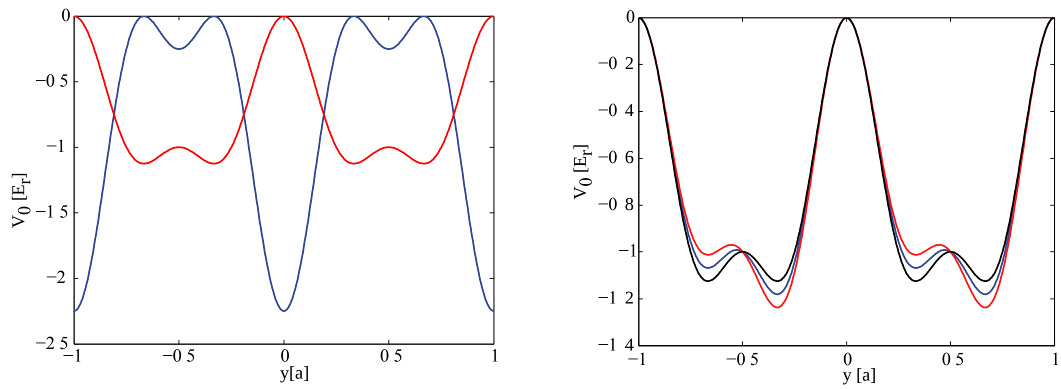

(a) Properties of the triangular and the hexagonal lattice. Note that almost full modulation of the triangular lattice along *all* directions The overall lattice depth of the hexagonal lattice is only half that of the triangular one at the same laser power. Moreover the depth of an individual well amounts to only $1/9V_{\rm latt}$, indicating the need for large laser power.

(b) If the laser detuning is not too large, a multi-level atom will feel a m_F-dependent force in the hexagonal lattice. Shown is the potential strength exerted on atoms in $|F,0\rangle$ (black), $|F,1\rangle$ (blue) and $|F,2\rangle$ (red) confined in a σ^+-well. The opposite is true for negative m_F-values and σ^--wells respectively.

Figure 5.4: Cuts through the potential along the diagonal of the primitive cell.

The hexagonal lattice exhibits a pronounced *channel* structure, with tiny individual lattice sites whose depth relative to the channels is only $1/9V_{\rm 2D}^{\pm}$. All together the laser power required to achieve a trapping at a single potential minimum of the hexagonal lattice equal to one well of the triangular one amounts to $V_0^{\pm} \stackrel{!}{=} 18 \cdot V_0^{\triangle}$. Fig. 5.4 shows a comparison between the triangular and hexagonal lattice along the diagonal of the primitive cell. In addition the potential experienced by different magnetic states in the hexagonal lattice is plotted for a lattice laser wavelength of $\lambda_{\rm L} = 830\,{\rm nm}$. By choosing larger or smaller detunings this difference can be decreases or increased according to Equ. 3.7.

If the polarization of the beams is continuously rotated from *in-plane* to *out-of-plane* the total potential created by the three beams will loose its characteristic periodicity and become a constant offset. This can easily seen by adding Equ. 5.13 and Equ. 5.18 properly weighted corresponding to the current polarization. It is thus *not* possible to load atoms from the triangular lattice into the hexagonal or vice versa. This is further hindered by the fact that the potential minima of the two lattices do not coincide.

Note that trapping atoms in a 2D lattice results in a regular array of quasi-one dimensional tubes. Perpendicular to the lattice plane only the much weaker harmonic confinement acts on the atoms. Inside a single tube different regimes can be realized reaching from 1D Thomas-Fermi configurations to the Tonks Girardeau regime [87].
In order to obtain a three-dimensional periodic confinement we combine the three-beam lattice with a perpendicular standing wave, derived from the same laser but detuned by 160 MHz with respect to the 2D lattice beams to avoid interference of the two different lattices. The two described resulting experimental geometries are presented in Fig. 5.5 together with a cubic lattice at the same wavelength for comparison.

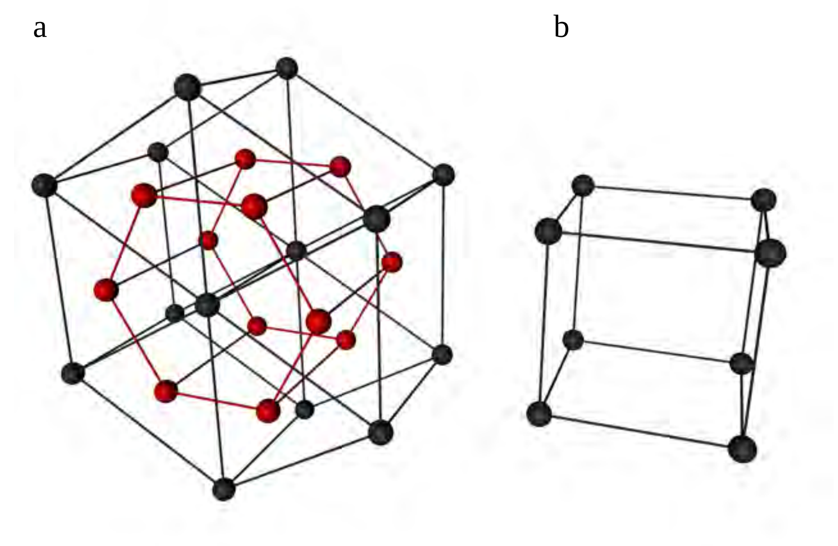

Figure 5.5: Schematic drawings of the 3D lattice structure for the (a) triangular (black), hexagonal (red) and (b) cubic lattice for the same laser wavelength (to scale).

Experimental perspectives

As can be seen from Equ. 5.13 a change in the relative phase of the lattice beams corresponds to a global shift in position. This has already been mentioned in the context of the phase stabilization setup described on Section 3.6.3. In addition to the ability to eliminate any kind of phase noise it is possible to precisely control the individual phases, enabling controlled acceleration (linear frequency sweep) and motion (constant frequency offset) of the lattice. A detuning of 1 Hz corresponds to a velocity of $1\,\mathrm{Hz} \equiv \lambda/s \equiv 0.83\,\mu\mathrm{m/s}$. Velocities on the order of the speed of sound in a BEC $c_\mathrm{s} \approx 1 - 2\,\mathrm{mm/s}$ demand for detunings in the low kHz regime, which can be easily achieved. This feature can be readily employed to perform transport measurements or probe the critical velocity in the lattice (see e.g. [155] and references therein).
By sinusoidally modulating the frequency difference between two beam pairs $\pi/2$ out of phase it is even possible to move the lattice on a circular orbit. Unfortunately this is *not* equivalent to a rotation of the lattice, which would be a highly desirable experimental tool.

Harmonic confinement

As already explained for the case of the 1D lattice the application of the three-beam lattice will also contribute an additional harmonic confinement to the system under investigation. To obtain the corresponding trapping frequencies we will assume the 2D lattice to be in the $x - z$ plane and the standing wave along the y-direction.
Starting with the harmonic approximation for the individual beams

$$V_{\mathrm{2D}}^{\mathrm{harm}}(\mathbf{r}) = \sum_{i=1}^{3} \left(1 - 2\frac{{r_{\perp,i}}^2}{w_0^2} - \frac{{r_{\parallel,i}}^2}{z_\mathrm{R}^2} \right), \tag{5.19}$$

and taking into account the additional factor of 3 occurring because of constructive interference one can derive the following harmonic trapping frequencies for the triangular lattice

$$\omega_y = \frac{1}{\sqrt{2}}\,\omega_{x,z} = \sqrt{\frac{9E_\mathrm{r}}{mw_0^2}}\sqrt{\frac{V_0}{E_\mathrm{r}}}. \tag{5.20}$$

We have neglected the last term in Equ. 5.19. Inclusion of this term will induce a variation of the trapping frequencies due to the spreading of the beams according to

$$\omega_i(x,z) = \omega_{i,0}\sqrt{1 - \frac{3}{2z_\mathrm{R}^2}(x^2+z^2)}. \tag{5.21}$$

Since the Rayleigh range in our experiment is $z_\mathrm{R} = 5\,\mathrm{mm}$ and the extension of typical BEC amounts to $R_\mathrm{BEC} = 15 - 30\,\mu\mathrm{m}$ this variation plays no role in practice. A little bit more important is the variation of the lattice beams intensity perpendicular to the direction of propagation. The value of the intensity will drop from the center of the BEC to its edges by $\approx 5\%$ resulting in an associated decrease of the lattice depth of $\sqrt{5}\%$.
The overall trapping frequencies $\omega_{\mathrm{tot},i}$ are again found by quadratically adding the ω_i's of XDF, 1D lattice and three-beam lattice. The harmonic average is then established through $\bar{\omega} = \sqrt{\prod_i \omega_{\mathrm{tot},i}}$.
It is straightforward to calculate the harmonic trapping frequencies of the lattice since all necessary parameters are known from lattice calibration measurements and careful measurements of the beam waists. It is therefor not necessary to determine the ω's in a separate measurement.

5.2 Single particle in a periodic potential

It is well known that in a non-interacting many body system the challenge of finding the many body eigenfunctions and -values can be reduced to a single particle problem. Diagonalization of the corresponding Hamiltonian yields single-particle eigenstates and -energies. The many-body wave-function is then constructed as a product of single-particle states taking into account the proper symmetrization rules according to the particle's quantum statistics.
As we will see a peculiar property of the energy spectrum in a periodic system is the emergence of energy bands separated by an energy gap as one adds more and more particles to the system. In the following I will briefly summarize how to calculate the band structure of a particle in a periodic potential which is the essence of understanding any kind of physics associated with ultracold atoms confined in optical lattices.
The problem of particles confined in a periodic potential is well known in solid state physics and was originally addressed in terms of electrons moving in a crystal lattice by F. Bloch [154]. It can directly be mapped onto the problem of atoms in optical lattices. In general the Hamiltonian for a periodic system reads

$$\hat{\mathbf{H}}_0 = \frac{\hat{\mathbf{p}}^2}{2m} + V_\mathrm{Latt}(\mathbf{r}) = -\frac{\hbar}{2m}\nabla^2 + V_\mathrm{Latt}(\mathbf{r}) \tag{5.22}$$

where the periodic lattice potential obeys the relation

$$V_\mathrm{Latt}(\mathbf{r}) = V_\mathrm{Latt}(\mathbf{r}+\mathbf{T}), \quad \mathbf{T} = \sum_i n_i \mathbf{a}_i, \quad n_i \,\epsilon\, \mathbf{Z} \tag{5.23}$$

with the basis vectors of the direct lattice $\mathbf{a}_i$. According to Bloch's theorem the eigenstates can be written as [154]

$$\psi_{n,\mathbf{q}}(\mathbf{r}) = u_{n,\mathbf{q}}(\mathbf{r})\, e^{i\mathbf{q}\cdot\mathbf{r}} \tag{5.24}$$

with energy eigenvalues $\hbar\omega^{(n,\mathbf{q})}$.
The Bloch functions $u_{n,\mathbf{q}}$ fulfill the condition $u_{n,\mathbf{q}}(\mathbf{r}) = u_{n,\mathbf{q}}(\mathbf{r}+\mathbf{T})$ and possess the same translational symmetry as the lattice. It will turn out that the quasi-momentum $\mathbf{q}$ is a good quantum number of the physical system and will be used to label eigenfunctions and -values.
Since $\mathbf{q}$ is only uniquely determined up to a reciprocal lattice vector $\mathbf{K}$ it can be restricted to the first Brillouin zone $-1/2\,\mathbf{K} \leq \mathbf{q} \leq +1/2\,\mathbf{K}$. For a given quasi momentum this results in an infinite number of solutions which are consequently labeled by the band index n. Note that every lattice site in the direct lattice corresponds to one possible value for the quasi momentum in the first Brillouin zone. Therefor a lattice consisting of N lattice sites allows for N physically meaningful values for $\mathbf{q}$. The Hamiltonian can be expressed in algebraic form by a plane wave expansion ansatz for the Bloch function $u_{n,\mathbf{q}}(\mathbf{r})$

$$u_{n,\mathbf{q}}(\mathbf{r}) = \frac{1}{\sqrt{N}} \sum_{\mathbf{K}} c_{\mathbf{K}}^{(n,\mathbf{q})}\, e^{-i\mathbf{K}\cdot\mathbf{r}} \tag{5.25}$$

and the potential

$$V_{\text{Latt}}(\mathbf{r}) = \sum_{\mathbf{K}} V_{\mathbf{K}}\, e^{i\mathbf{K}\cdot\mathbf{r}}, \tag{5.26}$$

where the summation runs over all reciprocal lattice vectors $\mathbf{K} = \sum_i n_i \mathbf{b}_i$ and N corresponds to the number of occupied lattice sites. The coefficients $V_{\mathbf{K}}$ are the Fourier transforms of the potential which greatly simplifies the underlying problem in the case of a periodic potential. For a one dimensional sinusoidal potential [3] created by a retro-reflected laser beam as introduced in Section 5.1.1 the coefficients simply read

$$V_{\mathbf{0}} = -\frac{1}{2}\, V_0, \quad V_{\pm\mathbf{b}} = -\frac{1}{4}\, V_0. \tag{5.27}$$

The solution of this problem is well known and can be found e.g. in [156]. Fig. 5.6 shows the energy spectrum for different lattice depth and the corresponding Bloch functions for $\mathbf{q} = 0$ and $\mathbf{q} = 1/2\,\hbar\mathbf{K}$ respectively.

Our interest is focused on the triangular lattice introduced in Section 5.1.2. In the following a brief sketch how to solve for the band structure for this particular 2D system will be given. The triangular lattice is described by a Fourier series with coefficients

$$V_{\mathbf{0}} = -\frac{3}{4}\, V_0 \quad V_{\pm\mathbf{b}_1} = V_{\pm\mathbf{b}_2} = V_{\pm\mathbf{b}_1\mp\mathbf{b}_2} = -\frac{1}{4}\, V_0. \tag{5.28}$$

Substituting 5.24, 5.25 and 5.26 in equation 5.22 yields the algebraic form

$$\left\{ \frac{\hbar^2}{2m}(\mathbf{q}-\mathbf{K})^2 - \hbar\omega^{(n,\mathbf{q})} \right\} c_{\mathbf{K}}^{(n,\mathbf{q})} + \sum_{\mathbf{K}'} V_{\mathbf{K}'-\mathbf{K}}\, c_{\mathbf{K}'}^{(n,\mathbf{q})} = 0. \tag{5.29}$$

[3] Note that the eigenwert problem may also be elegantly addressed in terms of the Mathieu equation [121] in one dimension. Since we are also interested in the solution of the non-separable 2D configuration for the triangular lattice we will adept the more straight forward algebraic method known from solid state physics which is easily extended to higher dimensions.

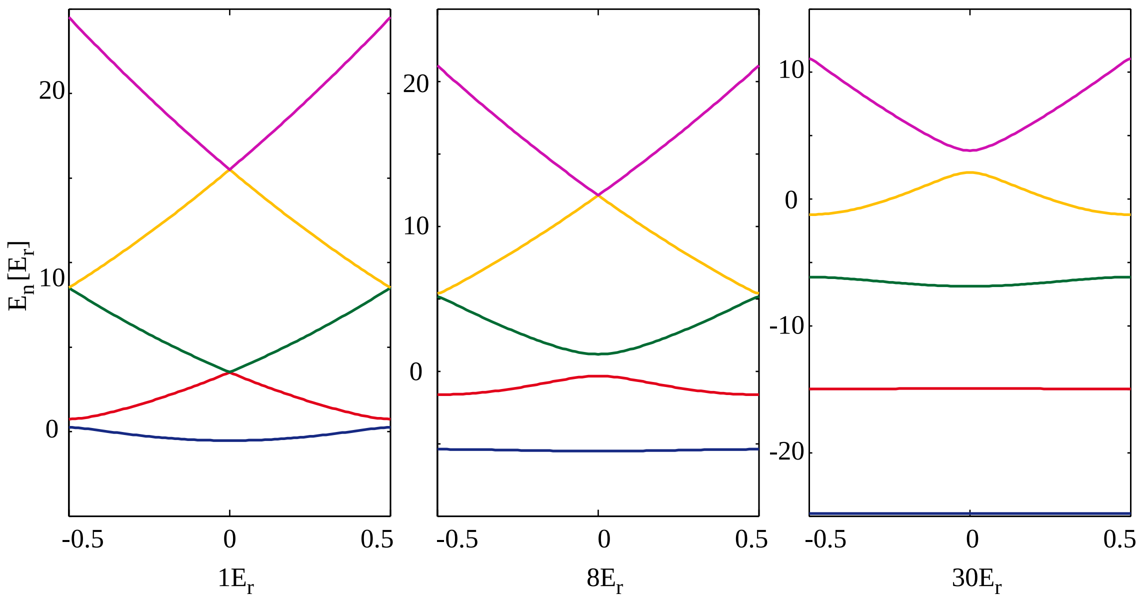

Figure 5.6: The energy spectrum of a particle in a periodic potential for different lattice depth. The emergence of gaps between the different bands for increasing lattice depth is explicit.

For the triangular lattice this can be cast in a normalized dimensionless form using $\tilde{\mathbf{q}} = \mathbf{q}/|\mathbf{b}| = \mathbf{q}/\sqrt{3}k$, $\tilde{\mathbf{K}} = \mathbf{K}/|\mathbf{b}| = \mathbf{K}/\sqrt{3}k$, $\tilde{E}^{(n,\mathbf{q})} = (\hbar\omega^{(n,\mathbf{q})} + 3/4\,V_0)/E_{\text{recoil}}$ and $\tilde{V}_0 = V_0/E_{\text{recoil}}$, where E_{recoil} is the recoil energy $(\hbar k)^2/2m$. The whole problem can now be rewritten in units of the recoil energy:

$$\begin{aligned} & \left\{3(\tilde{\mathbf{q}} - \tilde{\mathbf{K}})^2 - \tilde{E}^{(n,\tilde{\mathbf{q}})}\right\} c_{\tilde{\mathbf{K}}}^{(n,\tilde{\mathbf{q}})} \\ - & \frac{1}{4}\tilde{V}_0 \sum_{\tilde{\mathbf{K}}} \left\{\delta_{\tilde{\mathbf{K}}'-\tilde{\mathbf{K}},\pm\mathbf{b}_1} + \delta_{\tilde{\mathbf{K}}'-\tilde{\mathbf{K}},\pm\mathbf{b}_2} + \delta_{\tilde{\mathbf{K}}'-\tilde{\mathbf{K}},\pm(\mathbf{b}_1-\mathbf{b}_2)}\right\} c_{\tilde{\mathbf{K}}'}^{(n,\tilde{\mathbf{q}})} \\ = & \; 0. \end{aligned} \tag{5.30}$$

Since every reciprocal lattice vector can be decomposed into a sum of primitive vectors $\tilde{\mathbf{K}} = n\hat{\mathbf{b}}_1 + m\hat{\mathbf{b}}_2$ the former equation can be written in a discretized form omitting the tilde

$$\begin{aligned} & \left\{3(\mathbf{q} - \mathbf{K}_{nm})^2 - E^{(n,\mathbf{q})}\right\} c_{nm}^{(n,\mathbf{q})} \\ - & \frac{1}{4}V_0 \sum_{n'm'} \{\delta_{n-n',0}\delta_{|m-m'|,1} + \delta_{|n-n'|,1}\delta_{m-m',0} \\ + & \delta_{n'-n,m-m'}\delta_{|m-m'|,1}\}\, c_{n'm'}^{(n,\tilde{\mathbf{q}})} \\ = & \; 0. \end{aligned} \tag{5.31}$$

Finally to obtain the $E^{(n,\mathbf{q})}$ and $c_{nm}^{(n,\mathbf{q})}$ for the whole Brillouin zone Equ. 5.31 has to be solved for every value of $\mathbf{q} = \gamma\hat{\mathbf{b}}_1 + \delta\hat{\mathbf{b}}_2$ with $-1/2 \leq \gamma, \delta < 1/2$. The kinetic part of the Hamiltonian thus takes the form

$$(\mathbf{q} - \mathbf{K}_{nm})^2 = (\gamma - n)^2 + (\delta - m)^2 + (\gamma - n)(\delta - m) \tag{5.32}$$

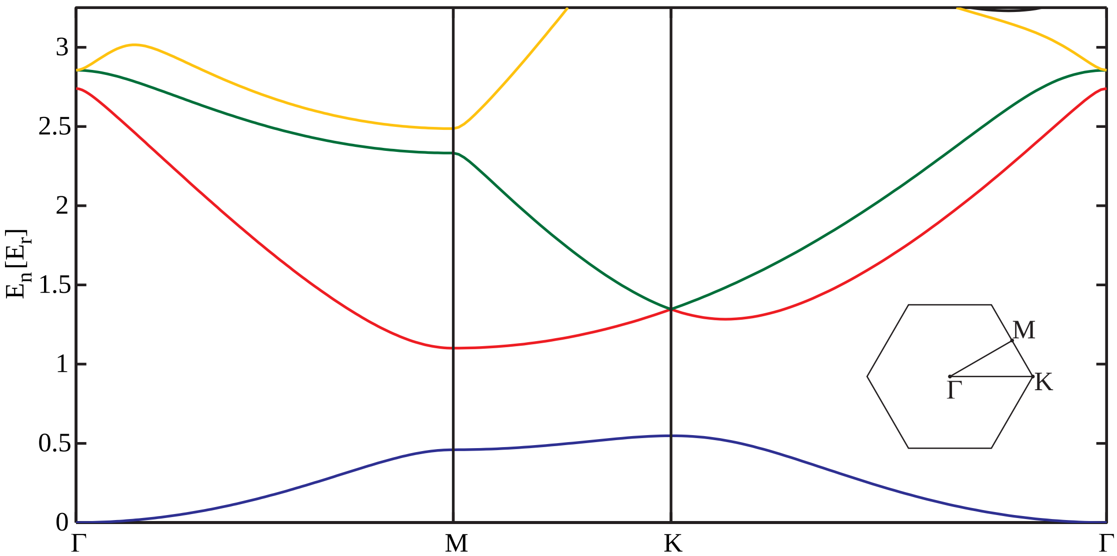

Figure 5.7: Result of a full 2D calculation (Equ. 5.33) of the band structure of the triangular lattice. The dispersion is plotted along lines connecting points in the first Brillouin zone which exhibit high symmetry as indicated in the inset.

---

since $\hat{\mathbf{b}}_1 \cdot \hat{\mathbf{b}}_2 = 1/2$. The resulting equation

$$\begin{aligned} & \left\{3[(\gamma-n)^2+(\delta-m)^2+(\gamma-n)(\delta-m)]-E^{(n,\gamma\delta)}\right\} c_{nm}^{(n,\gamma\delta)} \\ - & \frac{1}{4} V_0 \sum_{n'm'} \{\delta_{n-n',0}\delta_{|m-m'|,1}+\delta_{|n-n'|,1}\delta_{m-m',0} \\ + & \delta_{n'-n,m-m'}\delta_{|m-m'|,1}\}\, c_{n'm'}^{(n,\gamma\delta)} \\ = & \ 0 \end{aligned} \tag{5.33}$$

can be easily solved.

The eigen values obtained from the above calculations correspond to the energies of the individual bands. As an example Fig. 5.7 shows the result of a two dimensional band structure calculation. The energy is plotted versus quasi momentum along directions of high symmetry as indicated in the inset

Due to the low temperatures occurring in BEC experiments the population of higher bands is usually neglected. It turns out, that the physical processes studied in this thesis demand for an incorporation of the lowest Bloch band only. The eigen vectors that drop out of Equ. 5.33 are used to construct the Bloch functions according to Equ. 5.24 and Equ. 5.25. Later in this chapter it will be outlined how the relevant parameters for the Bose-Hubbard (BH) model can be calculated. The Bloch functions are needed to construct basis wave functions (so called Wannier states), which allow to write the underlying energy functional in second quantization leading to the well-known BH Hamiltonian.

5.3 Revealing the momentum distribution

When working with cold atoms in optical lattices, the properties of the reciprocal lattice can be explored in an especially elegant way, If interactions during the expansion

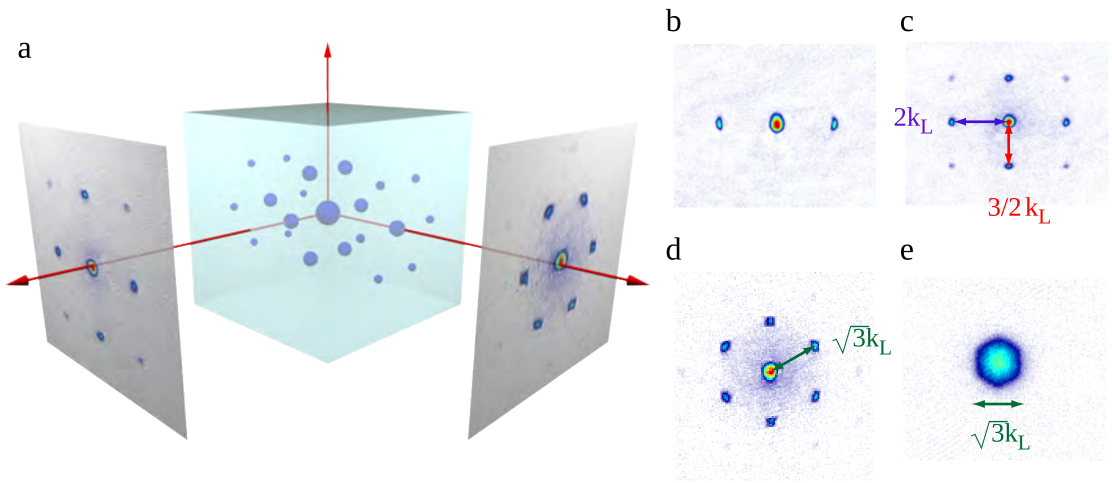

Figure 5.8: TOF images of atoms released from a triangular optical lattice. In (a) a three-dimensional view of the lattice is given, together with projections on the individual imaging directions. The lattice gives rise to interference peaks located at positions $\mathbf{r}$ that are associated with the reciprocal lattice vectors by the relation $\mathbf{r} = \hbar \mathbf{b} t_{\mathrm{TOF}}/m$. A pure 1D lattice is shown in (b), while (c) and (d) emphasize what momenta or projections of momenta are involved in typical images of the triangular 3D lattice. (e) finally shows an image of the first Brillouin zone of the triangular lattice obtained by adiabatic mapping of the quasi momentum on free momentum space.

---

process can be neglected, the density distribution after a sudden switch-off of the lattice potential and a reasonably long time-of-flight ($t_{\mathrm{TOF}} \geq 15 - 25\,\mathrm{ms}$) directly map to the quasi-momentum distribution in the lattice, which exhibits the full symmetry of the reciprocal lattice [157].

The annihilation operator after TOF is related to the annihilation operator in the lattice by the usual time propagation [94]

$$\hat{a}(\mathbf{r}, t) = \sum_j w(\mathbf{r} - \mathbf{R}_j, t)\, e^{i(m/2\hbar t)(\mathbf{r}-\mathbf{R}_j)^2} \hat{a}(\mathbf{R}_j, t = 0). \tag{5.34}$$

Note that we have set $E = (\hbar \mathbf{k})^2/2m$ justified for free expansion and $\mathbf{k} = \mathbf{r}m/\hbar t$ to account for the time of flight. $w(\mathbf{r} - \mathbf{R}_j, t)$ is the Wannier function originally located at a single lattice site after time evolution.
If the TOF is chosen considerably long the observed density can be evaluated according to

$$\langle n(\mathbf{r})\rangle = \langle \Psi_{\mathrm{latt}} | \hat{a}_i^\dagger(\mathbf{r}, t) \hat{a}_j(\mathbf{r}, t) | \Psi_{\mathrm{latt}} \rangle = \left(\frac{m}{\hbar t}\right)^3 \left| \tilde{w}\left(\frac{m\mathbf{r}}{\hbar t}\right)\right|^2 \mathcal{S}\left(\mathbf{k} = \frac{m\mathbf{r}}{\hbar t}\right) \tag{5.35}$$

where $\tilde{w}$ is the Fourier transform of the Wannier function and the structure factor is given by

$$\mathcal{S}(\mathbf{k}) = \sum_{i,j} e^{i\mathbf{k}(\mathbf{r}_i - \mathbf{r}_j)} \langle \Psi_{\mathrm{latt}} | \hat{a}_i^\dagger \hat{a}_j | \Psi_{\mathrm{latt}} \rangle. \tag{5.36}$$

Here Ψ_{latt} is the many-body wave function in the lattice. $\mathcal{S}(\mathbf{k})$ contains all the information related to the periodicity of the reciprocal lattice [158, 159]. Since $\mathcal{S}(\mathbf{k})$ has the form of

a two point correlation function, it is evident that long-range phase coherence will be required to observe sharp peaked features in $n(\mathbf{r})$.
For the simple example of a 1D lattice $\mathcal{S}(\mathbf{k})$ can be evaluated to

$$\mathcal{S}\left(\mathbf{k}=\frac{m\mathbf{r}}{\hbar t}\right) \propto \sum_{i,j=-N}^{N} e^{i\frac{m}{\hbar t}\mathbf{r}(\mathbf{R}_i-\mathbf{R}_j)} = \frac{\sin^2(\pi r N/l)}{\sin^2(\pi r/l)}. \tag{5.37}$$

We have used that the distance between any two lattice sites is a multiple of the lattice spacing $\mathbf{R}_i - \mathbf{R}_j = n \cdot a$. Furthermore we set $a = 2\pi/b$ and introduced $l = \hbar t b/m$. N is the number of lattice sites. For a large three dimensional system ($N \gg 1$) this constitutes a sum of peaks with a width $w \propto l/N$ which will accordingly reduce to a sum of delta peaks in the large N limit resulting in a density distribution

$$\langle n(\mathbf{r})\rangle = \left(\frac{m}{\hbar t}\right)^3 \left|\tilde{w}\left(\frac{m\mathbf{r}}{\hbar t}\right)\right|^2 \sum_{\mathbf{G}} \delta\left(\left[\mathbf{r} - \frac{\hbar t}{m}\mathbf{G}\right]/l\right). \tag{5.38}$$

This observation will be a key stone for the interpretation of the experiments on the superfluid-Mott-insulator transition presented later in this chapter.
For completeness Fig. 5.8(e) shows a picture of the first Brillouin zone of the triangular lattice. This image has been obtained by first populating the first Brillouin zone homogeneously by carefully exciting the atoms. This is necessary since their initial momentum spread is considerably smaller than the extension of the Brillouin zone. Subsequently the lattice potential is ramped down to zero in a time $t_{\mathrm{ramp}} = 5\,\mathrm{ms}$ in order to *adiabatically* map the crystal momentum on free momentum states. This is in contrast to the above described sudden switch off, since this *projects* the quasi momentum in the lattice on free momenta yielding different results.

5.4 Calibration of the lattice depth

An essential prerequisite for experiments is the knowledge of the lattice depth V_0, as introduced in the preceding paragraph.. As already stated earlier the lattice depth is usually given in units of the recoil energy associated with the absorption of one lattice photon $E_r = (\hbar k_{\mathrm{L}})^2/2m$ as $V_0 = sE_{\mathrm{r}}$.
Different methods can be employed in order to experimentally determine the gauging connecting laser intensity and lattice depth. All of them share the idea to calibrate the lattice by working in a 1D lattice generated by only two of the lattice beams and permuting over all possible combinations For the triangular lattice presented above, this implies to work with a total of 3 distinct 1D lattices. Finally the triangular optical potential will only be as symmetric as possible, if the three measured 1D lattice depths are all equal.
The relative population of the interference peaks can be evaluated as a function of the lattice depth s and give a rough calibration [160]. We have tested this method [141] and found the results to be not very reliable.
Another widely used method is the analysis of the diffraction pattern resulting from a very short flashing of the lattice well in the Kapiztka-Dirac regime [161].
Our calibration method relies on the anharmonic parametric excitation of atoms from the first to the third band of the underlying 1D lattice instead [114, 162]. This is achieved by periodically modulating the intensity of the lattice thereby introducing a perturbation to the trapping potential that can be written as

$$H_{\mathrm{pot}}(\vec{r},t) = V_{\mathrm{latt}}(\vec{r})(1+\epsilon(t)), \tag{5.39}$$

where $\epsilon(t)$ describes a small time-dependent perturbation. Assuming a harmonic potential for simplicity one can calculate the transition rate and find that only transitions between in ital and final states with equal parity are non-zero. Moreover the one-sided power spectrum of the perturbation

$$S(\omega) = \frac{2}{\pi} \int_0^T d\tau \cos(\omega\tau) \langle \epsilon(t) \rangle \langle \epsilon(t+\tau) \rangle \tag{5.40}$$

at twice the harmonic frequency enters the result for the effective heating rate

$$\langle \dot{E} \rangle = \frac{2}{\pi} \omega_0^2 S(2\omega_0) \langle E \rangle \tag{5.41}$$

which shows the exponential character of the heating process.
In an anharmonic potential as in an optical lattice, things get more complicated [162], but heating will mainly occur at the frequency difference between the lowest and the *third* band $\omega_{1\to3}$. It is only for very deep lattices that this frequency will approach the value of twice the harmonic value $2\omega_{1\to2}$. Keeping the amplitude of $\epsilon(t)$ tiny assures a negligible excitation to all other bands. A comparison of the measured frequency with band structure calculations allows finally for a precise specification of the lattice depth V_0.
Since the setup for the 2D lattice allows for an active manipulation of the relative phase of two laser beams, another excitation scheme relying on a perturbation

$$H_{\text{pot}}(\vec{r}, t) = V_{\text{latt}}(\vec{r} + \vec{\epsilon}(t)) \tag{5.42}$$

can be realized, since a change in the relative phase corresponds to a global shift in position of the lattice wells. It turns out [114] that the perturbation of the position may induce only parity changing transitions and can therefor by used to probe the energy difference between the two lowest bands $\omega_{1\to2}$ directly. The latter method has only be used occasionally at our experiment, but it can be conveniently employed to cross check ambiguous results obtained by parametric excitation.
By choosing an appropriate amplitude for $\epsilon(t)$ the width of the observed transition can be reduced to a few hundred Hz for resonance frequencies in the range of $30 - 50\,\text{kHz}$.

5.5 Bose-Hubbard model and the transition from a superfluid to a Mott-insulating state

The physics of BEC with reasonably large particle numbers in external traps is well captured within the framework of the nonlinear Gross-Pitavskii equation [102]. Derived as the Euler-Lagrange equation of motion of the many body Hamiltonian in the Bogoliubov approximation it naturally represents a mean-field equation describing the order parameter as outlined in Chapter 2.
Although many fascinating aspects of physics with ultracold atoms have been predicted by the GPE it exhibits one major disadvantage in describing strongly correlated systems. Quantum fluctuations are only concerned as perturbations, which is not the correct treatment for a strongly correlated quantum system where one would expect fluctuations to even dominate the physics, at least in the vicinity of a possible quantum phase transition. Therefor cold atoms in optical lattices are well described by the GPE only for small lattice depth where the superfluid phase still plays an important role and fluctuations stay small. With increasing lattice depth and small occupation numbers per lattice site the

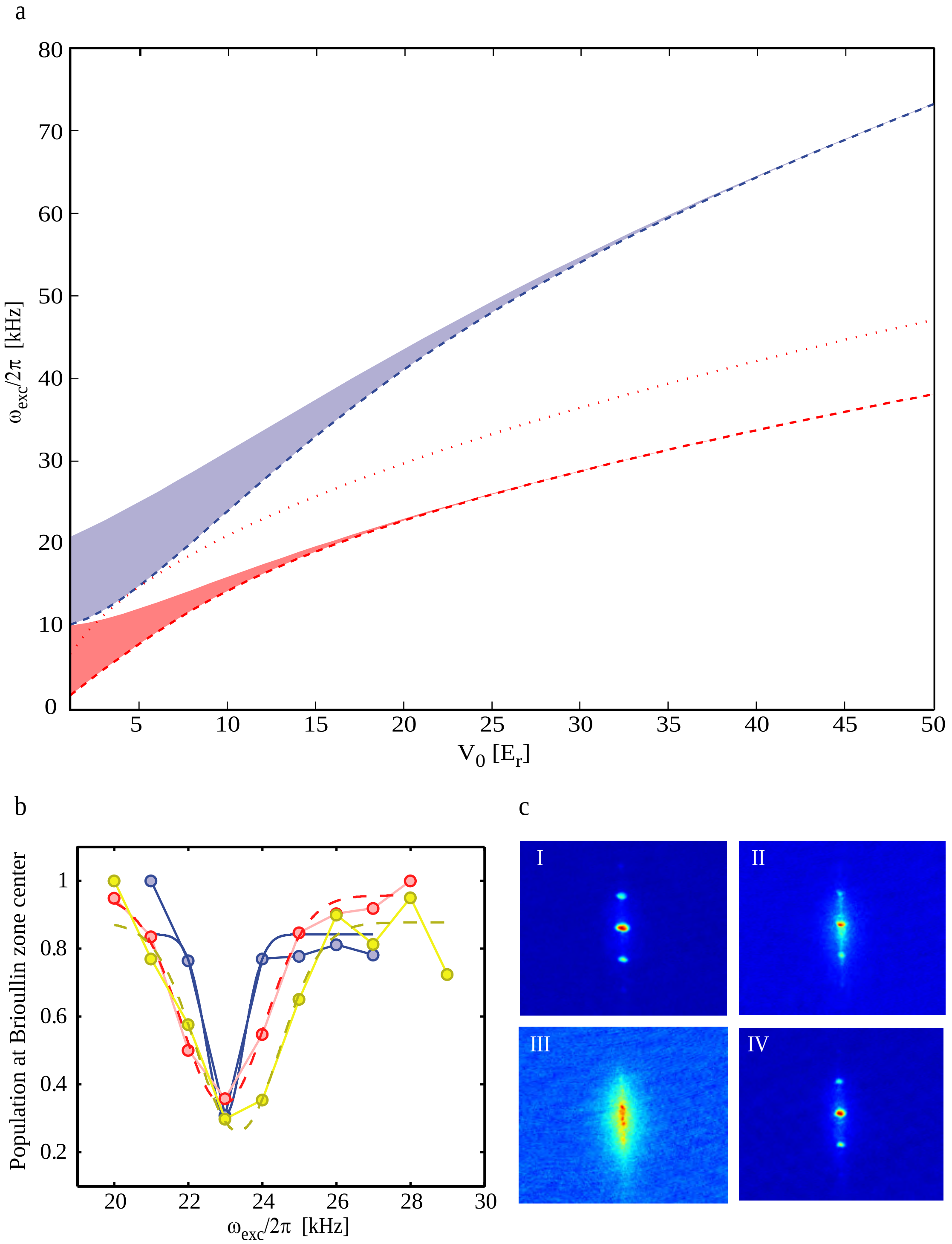

Figure 5.9: (a)Excitation energy to the second band $\omega_{1\rightarrow 2}$ (red) and to the third band $\omega_{1\rightarrow 3}$ (blue). The bandwidths are indicated by the shaded areas and decrease significantly for larger lattice depth. That is the reason why working in deep lattices makes calibration more reliable. (b) Spectra of the three 1D lattices together with fits to the data. The resonance positions coincide to within $1-2\%$. Note that the low lattice depth in this example considerably broadens the resonance. (c) Absorption images indicating the heating caused by the lattice depth modulation below resonance (I) on resonance (II),(III) and above resonance (IV). The measure is the particle number in a small region centered around $\mathbf{q}=0$.

fluctuations grow and non trivial correlations start to build up.
The appropriate choice for the examination of such a system is therefor the Bose-Hubbard (BH) model [79, 78], which has proven very powerful e.g. in the prediction of a quantum phase transition from a superfluid to a Mott-insulating state with increasing lattice depth. In this section the Bose Hubbard Hamiltonian and its constraints and consequences on the underlying physical system will be introduced. A short paragraph will also treat the qualitative behavior of atoms in optical lattices at finite temperatures, a topic that is currently intensively discussed in the community.

5.5.1 The Bose-Hubbard model

To derive the BH Hamiltonian one usually starts with the full Hamiltonian given in second quantization

$$\hat{\mathbf{H}} = \int d\mathbf{r}\hat{\Psi}^\dagger(\mathbf{r})(\hat{\mathbf{H}}_0 + V_{\text{ext}}(\mathbf{r}))\hat{\Psi}(\mathbf{r}) + \frac{1}{2}\int d\mathbf{r}d\mathbf{r}'\hat{\Psi}^\dagger(\mathbf{r}')\hat{\Psi}^\dagger(\mathbf{r})W(\mathbf{r}',\mathbf{r})\hat{\Psi}(\mathbf{r})\hat{\Psi}(\mathbf{r}'). \tag{5.43}$$

It is useful to expand the field operators in a *localized* basis given by the Wannier states at lattice site $\mathbf{a}_i$:

$$\hat{\Psi}(\mathbf{r}) = \sum_i w_n(\mathbf{r} - \mathbf{R}_i)\,\hat{a}_i, \tag{5.44}$$

where $\hat{a}_i$ is the usual annihilation operator and the Wannier states are given by

$$w_n(\mathbf{r} - \mathbf{R}_i) = \frac{1}{\sqrt{N}}\sum_{\mathbf{q}} e^{-i\mathbf{q}\cdot\mathbf{R}_i}\psi_{n,\mathbf{q}}. \tag{5.45}$$

The resulting Hamiltonian now has the BH form

$$\hat{\mathbf{H}} = -J\sum_{\langle i,j\rangle}\hat{a}_i^\dagger\hat{a}_j + \sum_i \epsilon_i\hat{a}_i^\dagger\hat{a}_i + \frac{U}{2}\sum_i \hat{a}_i^\dagger\hat{a}_i^\dagger\hat{a}_i\hat{a}_i \tag{5.46}$$

$$= -J\sum_{\langle i,j\rangle}\hat{a}_i^\dagger\hat{a}_j + \sum_i \epsilon_i\hat{n}_i + \frac{U}{2}\sum_i \hat{n}_i(\hat{n}_i - 1). \tag{5.47}$$

Here $\hat{n}_i$ is the number operator at site i, ϵ_i accounts for the site-dependent local energy and $\langle\cdots\rangle$ denotes summation over nearest neighbors only. The first term representing the kinetic energy is characterized by the tunneling matrix element J, which is given by

$$J = \int d\mathbf{r}\, w_1(\mathbf{r} - \mathbf{R}_i)\hat{\mathbf{H}}_0 w_1(\mathbf{r} - \mathbf{R}_j). \tag{5.48}$$

The third term accounts for the interaction and is proportional to

$$U = g\int d\mathbf{r}\,|w_1(\mathbf{r})|^4. \tag{5.49}$$

The tunneling parameter J is directly connected to the single particle dispersion in the *tight-binding* approximation as

$$\epsilon(\mathbf{q}) = 2J\sum_{\{\mathbf{a}_i\}}\cos(\mathbf{q}\cdot\mathbf{a}_i), \tag{5.50}$$

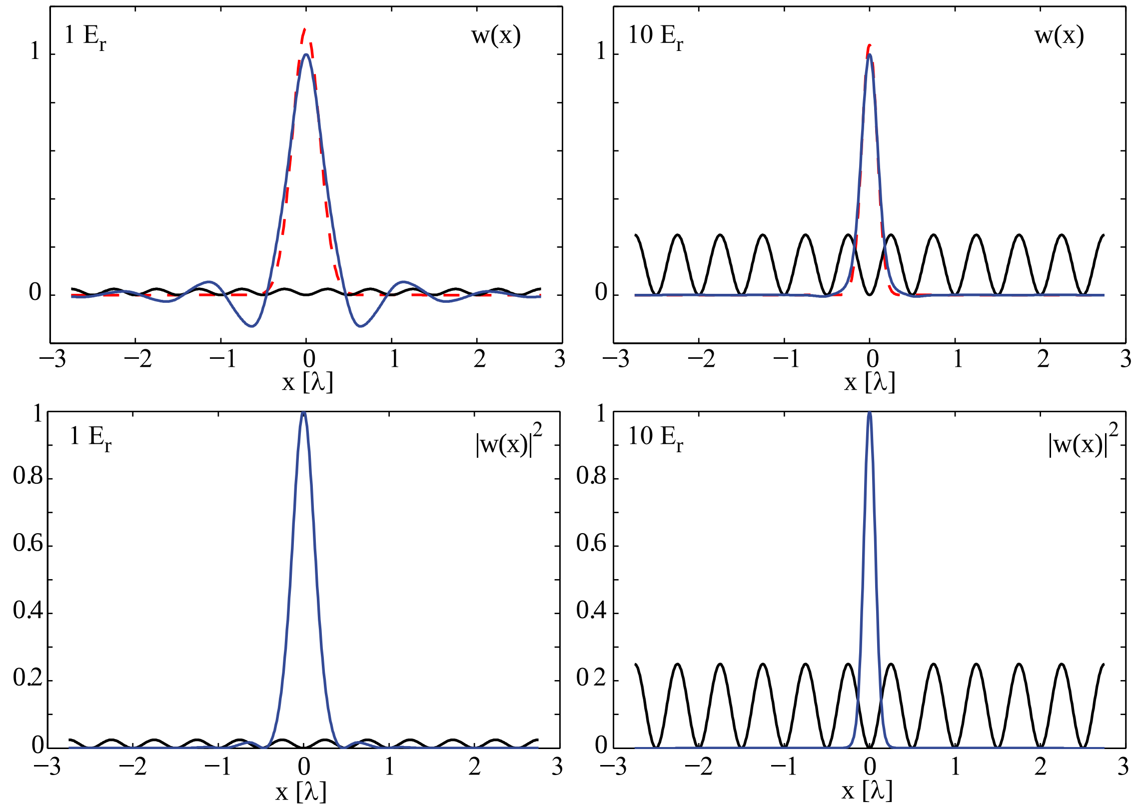

(a) Wannier function (blue) of the lowest Bloch band $w_0(\mathbf{r})$ and its square modulus $|w_0(\mathbf{r})|^2$ for a very shallow (left) and an intermediate (right) lattice potential (black). The Wannier functions become strongly localized as the lattice depth is increased. The comparison with a harmonic oscillator ground state (red) indicates, that the on site interaction is well approximated by employing the simplified Gaussian, while the wave function overlap between neighboring lattice sites entering J is considerable underestimated.

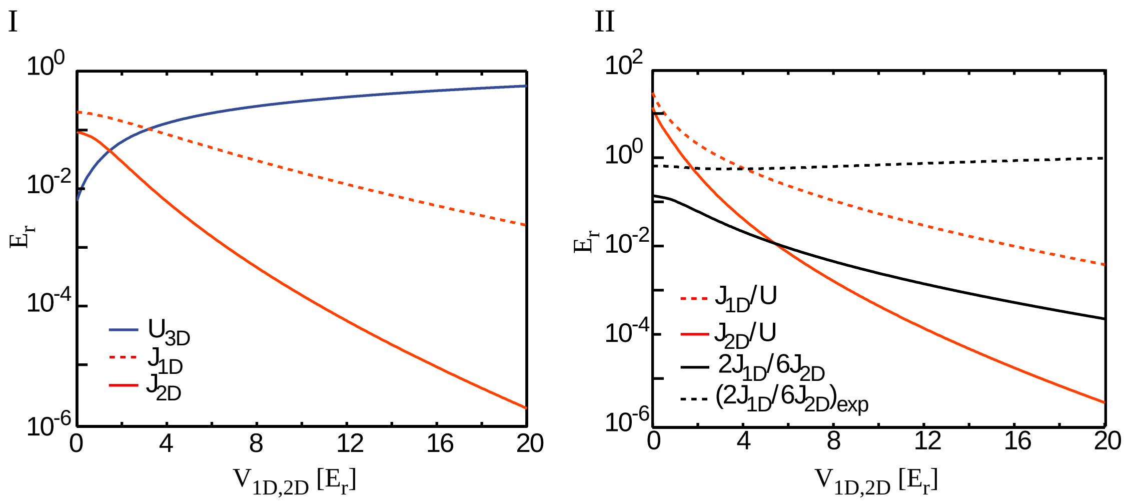

(b) **I** On site interaction U and tunneling energy J for one- and two dimensional lattices The tunneling for the triangular lattice $J_{2D}^{\triangle}$ decreases much faster than for a square lattice and the standing wave along the perpendicular direction $J_{2D}^{\square} = J_{1D}$ for equal lattice depth V_0. Note the logarithmic scale on the ordinate. **II** Comparison of $6J_{2D}^{\triangle}$ and $2J_{1D}$, the two relevant tunneling energies in the combined triangular- standing wave lattice. In an experiment presented later we chose a ratio $2J_{1D}/6J_{2D}^{\triangle}$ such that it is almost constant throughout the probed parameter range (black dashed).

Figure 5.10: Wannier functions and parameters of the Bose Hubbard model

which is a useful approximation for many purposes. Note that also the bandwidth of the lowest Band scales with J [78] like

$$E_0(\mathbf{q} = \mathbf{b}_i/2) - E_0(\mathbf{q} = 0) = 4J. \tag{5.51}$$

To arrive at Equ. 5.46 several approximations have been made in order to simplify the problem:

Temperature and interactions Only the lowest Bloch band has been taken into account. To justify this approximation the excitation energy to the second band has to be much larger than the temperature or any other energy scale in the system: $E_{\text{gap}} \gg k_{\text{B}}T,\, n_iU$.

Localization The tunneling term considers only nearest neighbor contributions. The number of nearest neighbors within the Bose-Hubbard approximation is usually given by z. Moreover it is assumed, that the interaction term is dominated by the on-site contribution. For these assumptions to be true, the Wannier states have to be sufficiently localized. This sets some constraints on the minimum lattice depth, where the BH description remains valid [4].

Interaction potential By writing the interaction as a scalar coupling constant we have assumed that the potential contains no long-range contributions. This is a very good approximation for ultracold atoms, where the s-wave scattering length solely determines the quality of the interaction.

All of the above restrictions are usually met in typical ultracold atom experiments making it a very accurate implementation of the BH model.
The tunneling parameter J and the on-site interaction U can be tuned in the experiment by simply changing the lattice depth. U could also be changed by employing a Feshbach resonance which alters the s-wave scattering lengths a. This is however not done at our experiment.
Unfortunately the BH Hamiltonian Equ. 5.46 is not exactly soluble, but its most prominent features, as the quantum phase transition from a superfluid to a Mott-insulating phase are quite well understood [79].

5.5.2 Ground states and quantum phase transition

To get an idea of how the ground states in the BH model look like it is useful to consider two extreme limits first:

Vanishing interaction In this case $J \gg U$ and the many-body system will behave like a *superfluid* state as in usual BEC establishing long-range phase coherence and characterized by a non-vanishing superfluid fraction. In the Wannier basis this means that every atom will be in a state delocalized over the entire lattice to maximally lower its energy by J per particle and junction. For N bosons and $\{\mathbf{R}_i\}$ being the set containing all lattice sites N_L it can be written as

$$|\Psi_{\text{SF}}\rangle_{U/J\approx 0} = \frac{1}{\sqrt{N!}} \left(\frac{1}{N_L} \sum_{\mathbf{R}_i} \hat{\mathbf{a}}^{\dagger}_{\mathbf{R}_i} \right)^N |0\rangle. \tag{5.52}$$

[4] Note that the much better localization in the triangular lattice compared to a square lattice justifies the BH model for considerably lower lattice depth.

For large numbers of occupied lattice sites and particles $N, N_L \gg 1$ this state becomes practically indistinguishable from a coherent state, manifesting the idea of a state with a well defined macroscopic phase. The number statistics on a single site given by a coherent state is *Poissonian*, which means that the standard deviation at a mean occupation number of $\bar{n}$ is $\sigma = \sqrt{\bar{n}}$. To give an example for the simplest case of $\bar{n} = 1$ the probability of finding more than one particle at a site is 0.27.

Large interaction The opposite case $U \gg J$ leads to totally different ground state. This can be easily understood by looking at the energy cost associated with having more than $\bar{n}$ particles at a given site according to Equ. 5.46. In the model case $\bar{n} = 1$ this energy is simply given by U. Since $U \gg J$ this is unfavorable and will therefor be avoided in the state of lowest energy. As a consequence the ground state in the large interaction limit is given by a product of Fock states at the individual lattice sites.

$$|\Psi_{\mathrm{MI}}\rangle_{U/J\to\infty} = \left(\prod_{\mathbf{R}} \hat{\mathbf{a}}^{\dagger}_{\mathbf{R}}\right)^{N} |0\rangle. \tag{5.53}$$

Note that this *Mott-insulator* (MI) does not exhibit any kind of long-range phase coherence and is characterized by some unique properties as compared to the superfluid (SF) state. Besides the loss of long-range coherence that is associated with a decrease and vanishing of the condensate fraction [163, 164, 85], a gap in the excitation spectrum of order U opens up [78, 80]. Another peculiar feature is the vanishing compressibility in the MI phase characterized by $\partial n/\partial\mu = 0$ [165].

For any $J \neq 0$ the Mott-insulating state will be depleted and eventually at $J \approx U$ the gain in kinetic energy will become of the same order of magnitude as the cost associated with double occupancy. As J grows even more, the atoms will finally be delocalized over the entire lattice and form a superfluid state. This is the qualitative behavior occurring by crossing the Mott-insulator superfluid phase transition. The crossover occurs from a state without phase coherence to a state with a well-defined phase.

The zero temperature phase diagram for a homogeneous system is shown in Fig. 5.11 as a function of J/U. For small values of J/U a series of Mott-insulating lobes is obtained with integer filling $\bar{n} = 1, 2, \ldots$, depending on the particular value of the chemical potential μ/U. As J/U increases the system undergoes a phase transition to the superfluid regime and the condensate fraction n_0/n continuously grows, establishing long-range phase coherence. More details concerning the critical behavior at the phase transition can be found in [79]. The critical value $(U/J)_c$ for the quantum phase transition, defined as the point where the order parameter $\psi \sim n_0/n$ vanishes, can been obtained employing a self-consistent mean-field picture [166] as

$$\eta_c = (U/zJ)_c = 2\bar{n} + 1 + \sqrt{(2\bar{n}+1)^2 - 1} \tag{5.54}$$

where $\bar{n}$ is again the number of atoms per lattice site and z the number of nearest neighbors. For $\bar{n} = 1$ one recovers $\eta_c \approx 5.8$, a result confirmed in [79, 167] and [168]. Large scale Monte-Carlo simulations have obtained slightly different value of $\eta_c = 29.34/z$ with very low uncertainty [169, 170].

A peculiar feature of the homogeneous SF-MI phase transition is the fact, that it occurs only at commensurate filling. This can be understood by assuming an atom number slightly larger than the number of lattice sites $n = 1 + \epsilon$. Increasing the lattice depth

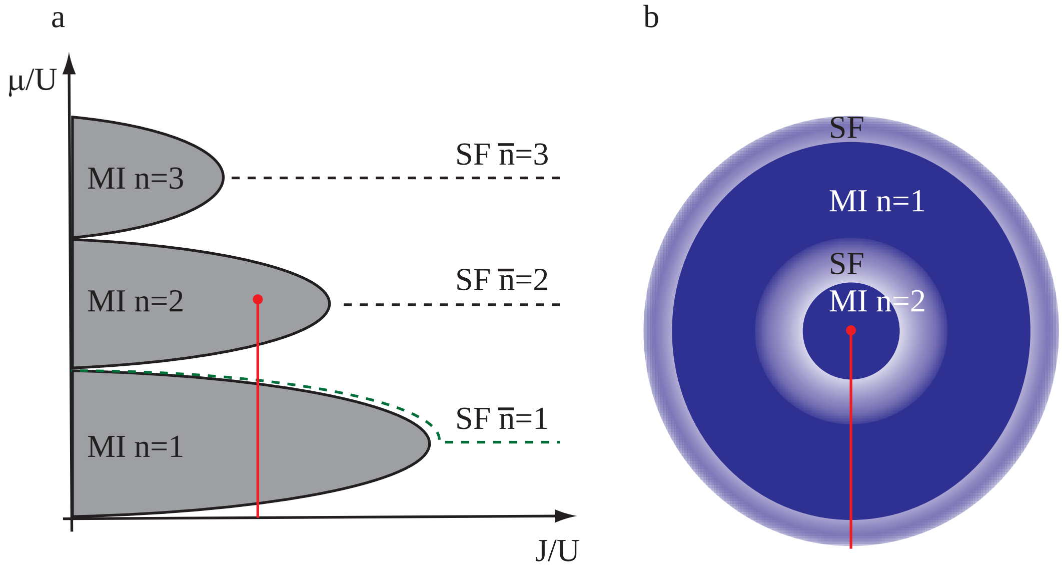

Figure 5.11: (a)Phase Diagram of atoms inside an optical lattice. For low values of J/U the system is in an incompressible Mott phase with integer filling. As J/U grows the atoms undergo a quantum phase transition to a superfluid state. It is important to realize, that real-world experiments work in inhomogeneous systems with fixed μ. This removes the peculiarity of the homogeneous system, where a phase transition only happens at commensurate fillings (green dashed line). Applying the local density approximation (red vertical line) therefor leads to a wedding cake-like structure of alternating Mott- and superfluid shells (b).

---

means going along the green dashed path from right to left in the phase diagram. Obviously for all lattice depth there will always be a finite order parameter ψ associated with atoms that move freely on top of a saturated $\bar{n} = 1$ MI, therefor remaining superfluid.
In a realistic experimental system however, the situation changes due to the inhomogeneity imposed by the additional harmonic confinement. Applying the local density approximation $\mu(\mathbf{r})/U = (\mu - V_{\mathrm{ext}(\mathbf{r})})/U$ one obtains a series of alternating MI shells surrounded by SF regions. Following the vertical line in the phase diagram reveals an example of a MI structure with a central $\bar{n} = 2$ core. It has to be emphasized that the sharp quantum phase transition observed in an homogeneous system with commensurate filling is significantly smoothed in an inhomogeneous system residing in a trap.
Since μ will continuously decrease from the center to the edge of the sample the corresponding critical $(J/U)_c$ will vary accordingly leaving the system in a mixture of various Mott and superfluid regions.
For negligible tunneling $J/U \ll 1$ this predicts the well known "wedding-cake" like density profile [78, 171, 165, 172] which has also been confirmed by Monte-Carlo simulations [169, 159]. The corresponding Mott-shells exhibit radii given by [171, 172]

$$R_n = \sqrt{\frac{2(\mu - nU)}{m\bar{\omega}^2}} \tag{5.55}$$

for harmonic trapping $\bar{\omega}$ (see also Fig. 5.12). The chemical potential has to determined self consistently using the normalization condition $N = \sum_n (4\pi)/(3a^3)(R_{n+1}^3 - R_n^3)$. The former equation can be readily used to estimate the maximum number of atoms per lattice site given particular experimental parameters. This will be of importance later in this chapter, when interpreting and understanding experimental data concerning the SF-MI transition.

5.5.3 The Mott-insulator at finite J

It is quiet instructive to consider the ground state of a system with small but finite J, since it will yield important information on the resulting density distribution as observed in the experiment [108, 158]. Starting with the Fock state of an ideal MI ($J = 0$) it is straightforward to write down the new state employing first order perturbation theory in J/U. Physically this corresponds to the generation of particle-hole excitations in the system, valid for small enough J.

$$
\begin{aligned}
|\mathrm{MI}\rangle^{(1)} &= |\mathrm{MI}_0\rangle^{(0)} + J \sum_{\{|\mathrm{MI}_1\rangle^{(0)}\}} \sum_{\langle i,j\rangle} \frac{{}^{(0)}\langle \mathrm{MI}_0|\hat{a}_i^\dagger \hat{a}_j|\mathrm{MI}_1\rangle^{(0)}}{E_1 - E_0} |\mathrm{MI}_1\rangle^{(0)} \\
&= |\mathrm{MI}_0\rangle^{(0)} + \frac{J}{U} \sum_{\langle i,j\rangle} \hat{a}_i^\dagger \hat{a}_j |\mathrm{MI}_0\rangle^{(0)} \qquad (5.56)
\end{aligned}
$$

Here $|\mathrm{MI}_m\rangle^{(n)}$ represents the nth-order perturbed state in the presence of m particle-hole excitations. Following the considerations from Section 5.3 the calculation of the structure factor $\mathcal{S}$ yields

$$
\begin{aligned}
\mathcal{S}(\mathbf{k}) &= \sum_{i,j} e^{i\mathbf{k}(\mathbf{r}_i - \mathbf{r}_j)} \langle \hat{a}_i^\dagger \hat{a}_j \rangle_{|\mathrm{MI}\rangle^{(1)}} \\
&= \sum_{i,j} n_i \delta_{ij} + \frac{2}{U} \sum_{\langle i,j\rangle} J_{ij} e^{i\mathbf{k}(\mathbf{r}_i - \mathbf{r}_j)} (n_j n_i + n_j) \\
&= n_0 + \frac{4}{U} \sum_{\mathbf{d}} J_{\mathbf{d}} \cos(\mathbf{kd}) n_0 (n_0 + 1) \qquad (5.57)
\end{aligned}
$$

It is obvious from the above equation, that also in the MI regime, features in the density distribution with the periodicity of the reciprocal lattice $2\pi/d$ will appear. This can be explained as follows: the particle-hole pairs depleting the MI-state may delocalize over a few lattice sites thus introducing a finite short-range coherence. The residual visibility of density modulations at reciprocal lattice vectors can be attributed to this short-range coherence [108, 158]. Interestingly this rather simple model accounts for residual visibility in the MI regime fairly well as observed in several experiments [108, 158, 84]. As we will see, the results observed in this thesis can also be well described within this model.

5.5.4 Thermodynamics of cold atoms in optical lattices

All considerations made in this chapter so far have assumed zero temperature. In experiments however BEC is always generated at finite temperatures. This section will briefly outline the consequences on adiabatic loading of cold atoms in optical lattices and the final phase diagram imposed by non-zero temperatures. Despite being a very active field of research, especially theoretical effort in the last years is quiet impressive [171, 173, 174, 175, 176, 177, 172],a conclusive picture has not yet been obtained. Several plausible considerations have been raised, which help to qualitatively understand the changes in finite-T systems. Since it is not possible to easily measure the temperature of

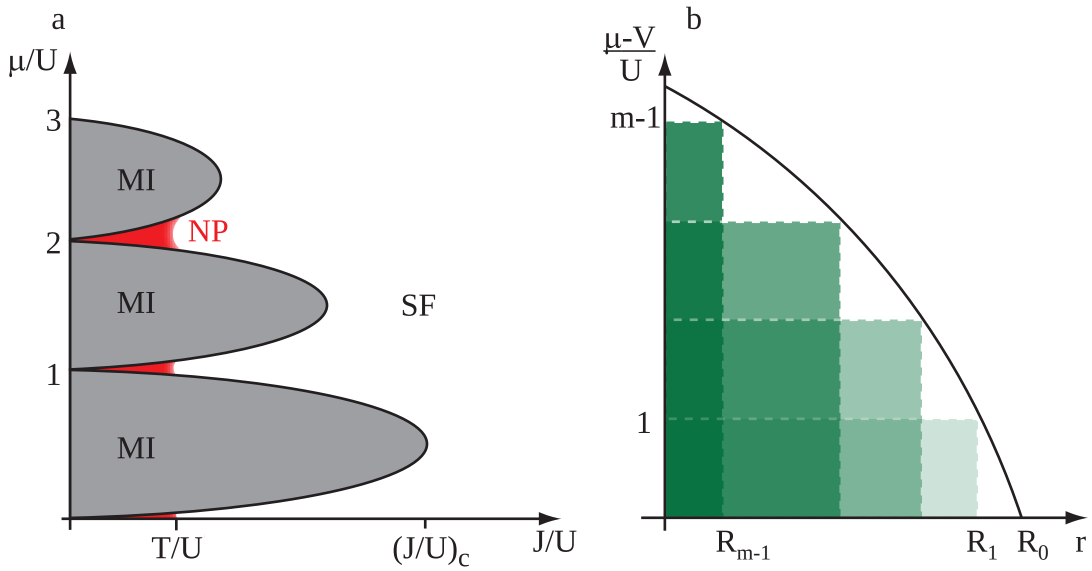

Figure 5.12: (a)Phase diagram at finite temperature. Starting from the right at large $zJ/U > (zJ/U)_c$ the system is superfluid. Crossing the critical point $zJ/U < (zJ/U)_c$ a SF-MI phase transition occurs similar to the $T = 0$ case. For $zJ/U < T/U$ (red area) this phase transition is replaced by a MI-normal phase transition. (b)Mott-shell radii in an inhomogeneous system in the local density approximation.

---

cold atoms in optical lattices on a scale comparable to other energy scales in the system (J, U) it is very useful to investigate the effect of finite T on the observable quantities to interpret experimental results.

The most important thing to realize is, that experiments always work at constant particle number N and constant entropy S rather than constant temperature T. By changing the systems density of states – as is the case by raising a lattice potential – the temperature will have to change as well in order to keep S constant.

For *non-interacting* atoms the density of states in the lowest band grows substantially since it is squeezed around states of very low energy ($\Delta E \approx 4J$) for increasing lattice depth [173]. The entropy can therefor be kept constant at much lower temperatures for deep lattices, if the initial temperature has been low enough to populate only the lowest band. In the tight binding approximation the initial and final temperatures scale as the inverse of the corresponding effective masses $T_\mathrm{f}/T_\mathrm{i} = m_i^\star/m_f^\star$ [173], where the effective mass is obtained from band-structure calculations as $m^\star = (\hbar^{-2}\nabla^2_{\mathbf{q}}\epsilon_{\mathbf{q}}|_{\mathbf{q}=0})$ and grows with increasing lattice depth. If higher bands were populated the opposite effect would occur: since the band gap is proportional to U, which grows for deeper lattices, the temperature has to rise as well to keep S constant. Usually the condition of populating only the lowest band is well fulfilled in experiments (especially our experiment).

At first glance it looks like we have found a promising and powerful cooling mechanism. Unfortunately interaction change this picture drastically. Since interactions broaden the ground band significantly, the cooling power of the above mechanism is severely reduced and eventually reversed for lattice depth corresponding to a MI-state [177, 173]. It turns out that the above mentioned mechanisms important for homogeneous systems are completely ruled out under realistic experimental conditions.

The harmonic trapping in real systems supports the formation of a Mott-shell structure with superfluid rings in between [171, 172]. These rings are much more susceptible to excitations than the Mott-shells themselves. When raising the lattice, the involved adiabatic compression due to the growing harmonic confinement can be identified as the main heating source in the system [177]. As a consequence of these two observations the heating will mainly be restricted to the atoms in the superfluid shells leaving the Mott structure more or less untouched. This is however only true for fairly low temperatures. It has been found that for temperatures $T^\star \geq (0.1-0.2)U$ the Mott-shell structure of an inhomogeneous system completely melts and disappears [171, 176]. Depending on initial and final conditions the heated superfluid atoms will undergo a phase transition to a normal gas. The presence of a lattice significantly reduces the critical temperature $T_c \approx zJ$ for Bose Einstein condensation as compared to its "free" value [176, 178] and it is therefor much more challenging to maintain quantum degeneracy inside a lattice, especially for lattice depth beyond $(J/U)_c$.

Despite at very low temperatures one would therefor expect to have a MI-normal phase transition and a normal-SF phase transition for realistic experimental parameters as depicted in Fig. 5.12.

Concluding it can be mentioned, that without a precise calculation of the entropy for our specific experimental parameters, it can not be safely said, whether cooling or heating occurs in the course of the lattice ramp-up. The initial temperature of our samples is rather low, on the order of less then $0.45T_c = 0.45 \cdot 150\,\mathrm{nK}$. This has to be compared to typical values of U/k_B and zJ/k_B.

Finding strong evidence for the existence of Mott-shells in experiment would set an upper limit on the temperature in the system of $T < T^\star = 0.2 \cdot U/k_\mathrm{B} \approx 20\,\mathrm{nK}$, which marks the melting of the shell structure. This can e.g. be compared to the critical temperature T_c around the SF-MI phase transition which is on the order of $T_c = zJ_{2D}/k_\mathrm{B} \approx 10\,\mathrm{nK}$ for the triangular lattice and decreases exponentially for increasing lattice depths.

It is currently heavily discussed, whether the occurrence of interference peaks in the absorption images can clearly be associated with a large superfluid fraction in the lattice system and whether its disappearance is a criterion for the SF-MI transition. Recent studies of a thermal gas slightly above T_c have shown interference patterns to a certain degree when released from an optical lattice [179, 180]. Moreover these authors found that only a visibility very close to unity can be taken as a clear signature for superfluididty and that already small deviations from unity indicate a purely thermal sample.

Contradictory results show strong evidence that especially for strong harmonic confinement as in our experiment the interference patterns obtained for condensed and thermal atoms are very distinct [164, 157] and can hardly be obscured with each other. Therefor at least a qualitative correlation between a substantial superfluid fraction and the visibility of the interference peaks remains.

In addition the robustness of the visibility against slight changes in the procedure of the determination remains a property of the superfluid regime and is absent for thermal samples.

5.6 Experimental observation of the SF-MI transition of cold atoms in a triangular optical lattice

One of the key properties of cold atoms in optical lattices is the superfluid-Mott insulator transition as extensively discussed above. During this thesis experiments have been performed investigating this phase transition in a combined 3D triangular-standing wave lattice as well as in a two-dimensional system, where the perpendicular degree of freedom has been frozen out using a standing wave at $30\,\mathrm{E_r}$ thus prohibiting any tunneling in this direction. The remaining array of quasi 2D condensates has then been probed by imposing a triangular lattice. To start, it will be briefly sketched how atoms are loaded in the optical lattice adiabatically to minimize any additional heating. Then measurements on the SF-MI phase transition in 3D and 2D are presented and comprehensively analyzed.

5.6.1 Adiabatic loading of the lattice

When a lattice potential is superimposed on a harmonically trapped BEC, several constraints have to be fulfilled in order to adiabatically transfer the atoms from the harmonic trap to the new ground state in the lattice. It is only when adiabaticity can be guaranteed that the considerations of constant entropy make sense. As soon as adiabaticity is violated the system will be heated and excited states will get populated in any case [173]. Two main issues have to be considered when thinking about the relevant time scales for adiabatic loading:

Interactions Interactions between particles are necessary to establish equilibrium in the system. Any change of the underlying potential, aiming to be adiabatic has to be slow compared to the timescale set by interactions $\approx \hbar/\mu$, which amounts to a few ms for realistic experimental parameters

Tunneling As the lattice gets deeper and deeper the ultimate limit for the particles to redistribute in the lattice to find their new equilibrium position is set by the tunneling time $\hbar/J$. For lattice depths associated with the quantum critical point this time is on the order of 10 ms and grows exponentially for deeper lattices.

However the above considerations only suggest a course route since the complex interplay of changing density of states, interaction effects and finite temperature make it hard to precisely predict strict constraints for adiabaticity.

In the course of this work several lattice ramp shapes and times have been tested and analyzed to obtain an optimum loading (see also [181] for similar results). We have loaded atoms in a deep lattice well within the MI regime using different ramps. After a hold time of roughly 50 ms we have ramped down the lattice to a value corresponding to maximum visibility and inspected the recurring interference pattern depending on ramp shape and -time. Best results have been obtained for ramp times $t_{\mathrm{ramp}} \approx 150-200\,\mathrm{ms}$. In particular the value of the visibility does not depend on the exact value of t_{ramp} for such large times. Times shorter than 50 ms considerably degrade the visibility and lead to severe irreversible heating.

Among several tested ramp shapes like linear and exponential the best and most insensitive results have been obtained for a sigmoidal ramp form originally suggested in [182]. This ramp increases slowly in the beginning, rises fast for intermediate lattice depth where μ and J are large and finally slows down again for deep lattices where J is decreasing more

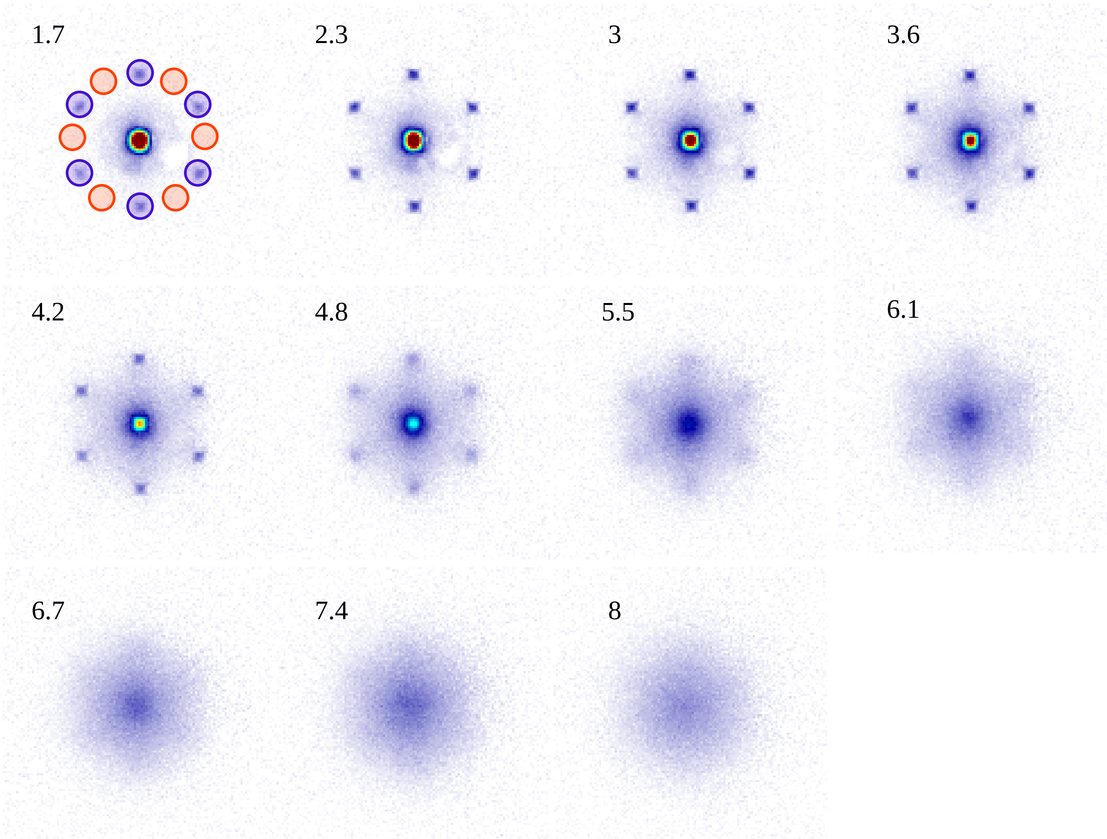

Figure 5.13: Absorption images of atoms released from a triangular optical lattice for various lattice depth given in units of E_r. As the lattice depth is increased the visibility of the interference peaks corresponding to reciprocal lattice vectors starts to decrease. Due to the inhomogeneity of the system a smooth transition is observed rather than a sharp jump in the visibility.

---

and more:

$$V(t) = V_{\text{final}} \frac{1}{1 + e^{-(t^2 - t_w^2)/t_s^2}} \tag{5.58}$$

The characteristic times t_w and t_s determine the shape of the curve and are on the order of $50\,\hbar/J$.

5.6.2 SF-MI transition in an array of 2D condensates

As a first experiment employing the triangular lattice the transition between a superfluid and a Mott insulator has been investigated in great detail. Different experimental measures like the visibility of the interference peaks, the condensate fraction and the width of the central peak, all sensitive to the coherence of the condensate wave function, have been studied to obtain a comprehensive understanding of the SF-MI transition in this new lattice geometry.

Since we have encountered quantitative differences computing the Bose Hubbard parameters J and U compared to a square lattice, we expect differences as compared to results obtained in this geometry [80, 108, 158, 84, 85]. Moreover the number of nearest neighbors in a triangular lattice is $z = 6$ as compared to a 2D square lattice where only 4 nearest

neighbors exist.
The starting point for all experiments described below is a Bose-Einstein condensate in an almost isotropic optical crossed dipole trap, with a harmonic trapping frequency of $\bar{\omega} = 2\pi \times (90 \pm 3)\,\mathrm{s}^{-1}$. The particle number in the condensate is $60000 - 70000$ without any discernible thermal fraction. Together with a critical temperature for Bose-Einstein condensation of $T_c = 150\,\mathrm{nK}$ this yields an estimate for the upper limit of the temperature of $T \lesssim 60\,\mathrm{nK}$.
Since we are especially interested in the physics induced by the triangular lattice we eliminate the influence of the third dimension by creating a stack of quasi two-dimensional disc-shaped condensates by ramping up a 1D lattice over 150 ms to a final depth of $V_0 = 30E_r$. After this step the tunneling along the perpendicular direction $\hbar/J_{1D} \approx 0.5\,\mathrm{s}^{-1}$ is negligible compared to the time needed for the experiment $\tau_{\mathrm{exp}} = 0.17\,\mathrm{s}$. The condition for being two-dimensional $k_{\mathrm{B}}T$, $\mu \ll \hbar\omega_{1D} = \hbar\, 2\pi \cdot 21\,\mathrm{kHz} = k_{\mathrm{B}} \cdot 1\,\mu\mathrm{K}$ is also well fulfilled.
The increased effective coupling $\tilde{g} \approx 2.5 g_0$ leads to a slight expansion of the condensate in all directions [102], whereas the considerably enhanced harmonic confinement $\tilde{\omega} = 1.2\bar{\omega}_0$ tends to compress the sample. After all we end up with ≈ 40 2D system, where the occupation of the central disc amounts to $N_{2D} \approx 4000$. The chemical potential is $\mu = h \cdot 2.7\,\mathrm{kHz} = 133\,\mathrm{nK}$. The determination of the critical temperature for one of the individual 2D systems following the findings of [183] gives a value of $T_c^{2D} = 110\,\mathrm{nK}$ for the central disc. As can be taken from Fig. 5.13 we determine a condensate fraction of 0.43 for very shallow lattices yielding a temperature of 80 nK .[5]
The experimental sequence continues by the smooth ramp-up of the two-dimensional triangular lattice within 150 ms. We hold the atoms for a short time $t_{\mathrm{hold}} = 20\,\mathrm{ms}$ and switch off all confining potential afterwards. The atoms are allowed to expand for a time-of-flight of 21 ms and are subsequently imaged an a CCD camera.
In Fig. 5.13 a series of absorption images for different final lattice depths V_0^{2D} is shown. Every image has been obtained by thoroughly superimposing and adding up to 30 individual images obtained from different experimental runs. Images indicating particle numbers that deviate by more than one standard deviation around the mean particle number of all individual runs are sorted out to reduce a blurring of the phase transition by interaction effects owing to *different* densities. As one can see as the lattice is increased characteristic peaks develop at positions corresponding to reciprocal lattice vectors exhibiting a striking interference pattern. When the lattice depth is increased further and further, the peaks start to smear out and finally for very deep lattices, the pattern has completely disappeared and is replaced by a structure less Gaussian. Note that the range over which the visibility of the peaks decreases is rather large, paying to the inhomogeneity of the system. Different regions of the condensate probe different regions of the phase diagram (compare Fig. 5.11), therefor yielding a smooth cross-over instead of a sudden jump of the visibility.

Visibility

To be more quantitative the visibility can be extracted from the absorption images as indicated in the upper left image in Fig. 5.13. We count the number of atoms corresponding to the position of reciprocal lattice vectors $\mathbf{r} = \hbar t/m\mathbf{b}_i$ (blue circles) N_+ and the number

[5] It should be states here, that the direct determination of the critical temperature in 2D systems in a recent experiment [183] does not agree with theoretical models of BEC in two dimensions. The authors of [183] find considerably lower T_c than predicted. We took their findings into account when *estimating* T_c for our system.

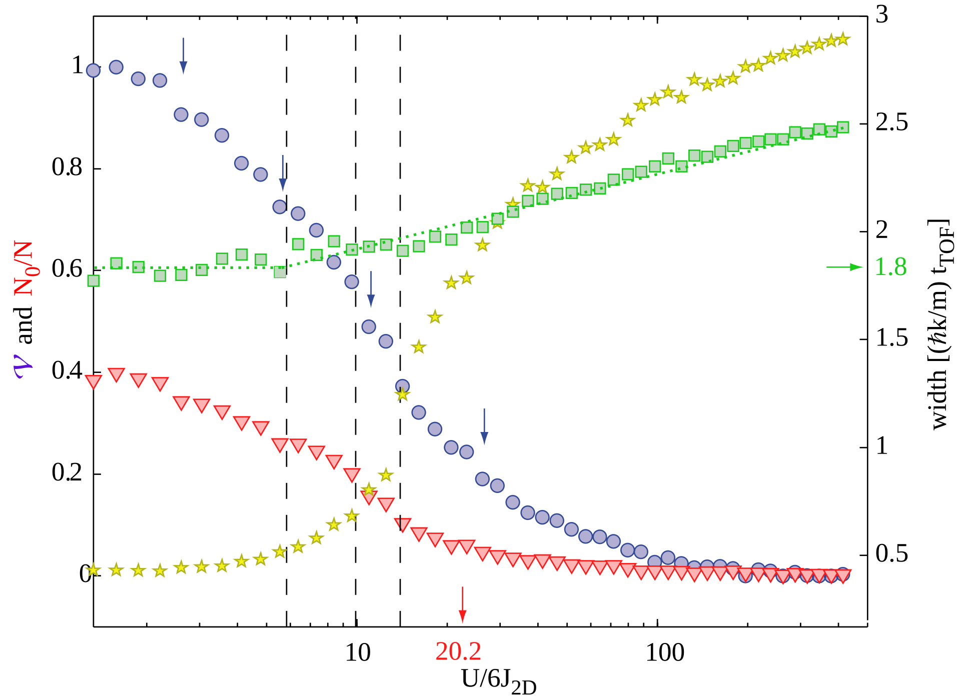

Figure 5.14: Visibility of the interference peaks (blue circles) across the phase transition against U/zJ. Note that the visibility has been renormalized to its maximum value of $\mathcal{V}_{\text{max}} = 0.48$. The visibility already starts to drop around a lattice depth of $3.5 - 4\,\text{E}_\text{r}$. Reproducible kinks marked by blue arrows may indicate the formation of Mott-shells. The condensate fraction (red triangles) decreases as the lattice is ramped to deeper values. Pronounced kinks coinciding with those observed for the visibility are observed. The condensate fraction vanishes more quickly than the visibility ($N_0/N = 0$ indicated by red arrow). The FWHM of the central peak of the momentum distribution (yellow stars) is constant for low lattice depth. Around the phase transition it quickly starts to grow – also exhibiting small but reproducible kinks. The width of the incoherent background is plotted for completeness (green squares). Constant below the phase transition where it is a measure for the temperature (indicated by a green arrow), it starts to increase linearly with respect to U/zJ in the MI regime as expected from Equ. 5.57. Dashed vertical lines indicate the critical values for the transition to a Mott insulating state with $\bar{n} = 1, 2$ and 3 respectively.

---

of atoms at positions at the edge of the Brillouin zone and vanishing structure factor $\mathbf{r} = \hbar t/2m(\mathbf{b}_i + \mathbf{b}_j)$ (red circles) N_-. This is done to account for the non-zero incoherent background density occurring at higher lattice depths. The visibility is than computed following [108]

$$\mathcal{V} = \frac{N_+ - N_-}{N_+ + N_-}. \tag{5.59}$$

The initial visibility is already noticeably smaller than unity, which can be attributed to the finite system size (see Section 5.3), the finite bin size over which the visibility is determined and interaction effects during expansion [157]. In similar experiments in other groups the same tendency has been observed. In our 2D system moreover, discs that are close to the outer edges of the condensate may not exceed the critical particle number for superfluidity and do therefor not contribute significantly to the interference contrast but blur the overall visibility since they cannot be separated prior to detection. The visibility starts to drop around $\eta \equiv U/zJ \approx 3-4$ which corresponds a lattice depth of $V_0 \approx 2.5 - 3E_r$. mean-field calculations [166, 78] for three dimensional systems predict $\eta_c \approx 5.8$ by monitoring the vanishing of the order parameter The only available work that has explicitly been performed on a 2D triangular lattice utilizing the strong coupling approach gives $\eta_c \approx 4.41$ [184]. The authors take the vanishing of the excitation gap as a signature for the phase transition. Large scale quantum Monte-Carlo simulations (QMC) for (non-triangular) 2D systems [169] give values as low as $\eta_c = 2.7$, albeit these authors take as a criterion for the phase transition the onset of the formation of a Mott plateau, while still a large superfluid fraction survives .[6]

Since we work in a highly inhomogeneous system we expect to observe the formation of various Mott-shells and therefor *no* sudden jump in the visibility. Interestingly the QMC value for the formation of a central Mott region with $\bar{n} = 1$ which should at least mark a starting point for the decrease of the visibility coincides with a reproducible step in our experimental data within experimental resolution. On the other hand a total vanishing of the part of the visibility that is attributed to the superfluid fraction (e.g. for not too large η) is not expected before *all* Mott-shells have formed, which is the case at fairly large values of η.

Moreover we observe a whole series of reproducible steps in our visibility curve indicating the formation of more and more Mott-shells. This behavior has already been observed and interpreted in [108, 158]. As a guideline for the reader, the mean-field predictions for vanishing of the order parameter in a homogeneous system with filling $n = 1$, $n = 2$ and $n = 3$ respectively are indicated in Fig. 5.17 as dashed vertical lines. In [165] the Mott-shell structure has been probed directly by measuring the density using magnetic tomography and in [185] spatially resolved high precision spectroscopy has been employed to detect different Mott-shells. Future experiments could include one or the other method to verify the presence of a wedding-cake-like Mott-shell structure in our system.

Using a simple mean-field model already introduced briefly in Section 5.5.2, an estimate can be made of how many Mott-shells will exist based on our experimental parameters and what the maximum occupation per lattice site will be [166, 171]. Assuming that the atoms will occupy a Mott-shell with the number of particles per lattice site fixed by the local chemical potential $\mu(\mathbf{r}) = \mu - V(\mathbf{r})$, the overall normalization condition reduces to a summation over spherical shells with occupation numbers $\bar{n} = 1, \ldots, \bar{n}_{max}$ and inner and outer radii of $R_{\bar{n}}$ and $R_{\bar{n}-1}$ respectively, where the innermost radius is given by $R_{\bar{n}_{max}} = 0$ and the outermost by $R_0 = \sqrt{2\mu/(m\bar{\omega}^2)}$ as can be seen in Fig. 5.12(b). Minimizing the energy $\partial_n E = 0$ in such a system puts the constraint $n = (\mu - V(\mathbf{r}))/U + 1/2$. Since $\bar{n}$ can take only integer values in the MI phase this becomes $n - 1 < (\mu - V(\mathbf{r}))/U < n$. With this condition the radii $R_{\bar{n}}$ of the individual shells are then given by

$$R_{\bar{n}} = \sqrt{\frac{2(\mu - nU)}{m\bar{\omega}^2}}. \tag{5.60}$$

By explicitly writing down the normalization condition for a harmonic external confinement

$$\chi_\mu \equiv \frac{3NV_{\text{cell}}}{4\pi} \left(\frac{m\bar{\omega}^2}{2U}\right)^{3/2} = \sum_{n=0}^{m-1} \left(\frac{\mu}{U} - n\right)^{3/2} \tag{5.61}$$

one can determine the number of particles in each shell and the maximum occupation number $\bar{n}_{max} = m$. A graphical representation of the left hand and right hand side of

[6] The various criteria for the phase transitions are explicitly stated to give the reader an idea of how different the individual approaches are and that they somehow differ considerably already by definition.

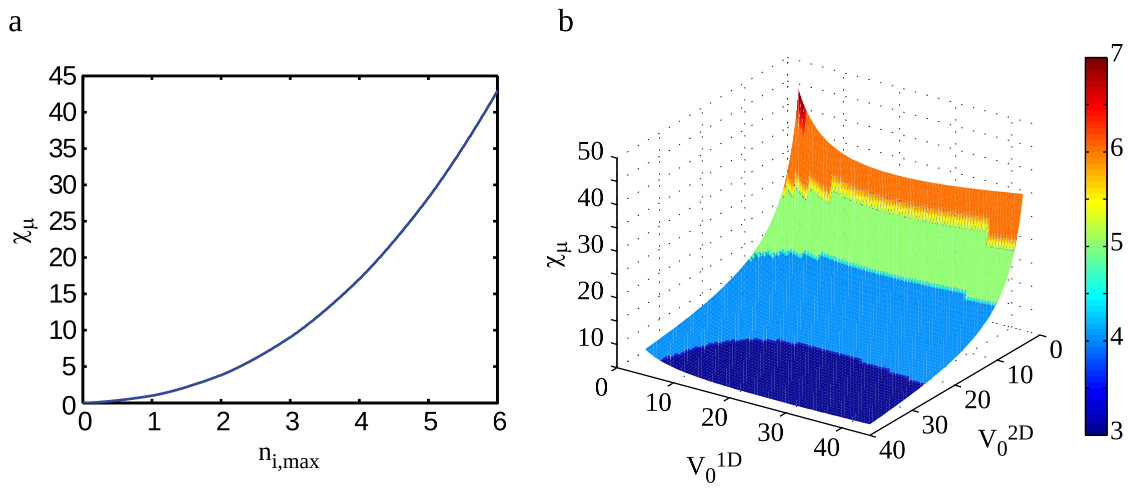

Figure 5.15: Simple model for the determination of a Mott-shell structure taken from [171]. By assuming that all atoms will occupy a Mott-shell according to the local value of the chemical potential $\mu(\mathbf{r}) = \mu - V(\mathbf{r})$, one can calculate the radii of the individual Mott-shells by imposing the normalization condition $\sum_{\text{shells}} n_{\text{shells}} = N$.
(a) Left hand side of Equ. 5.61
(b) Right hand side of Equ. 5.61 for a typical particle number of $N = 7 \cdot 10^4$ and various values for the strength of the 1D and 2D lattice V_{1D} and V_{2D} respectively.

	2D experiment		3D experiment	
site occupation $\bar{n}$	$R_{\bar{n}-1}[10\mu\text{m}]$	$N_{\bar{n}}[10^4]$	$R_{\bar{n}-1}[10\mu\text{m}]$	$N_{\bar{n}}[10^4]$
1	0.98	1.07	0.90	0.84
2	0.87	1.71	0.80	2.27
3	0.76	2.30	0.68	1.87
4	0.61	2.33	0.53	1.73
5	0.43	1.51	0.31	0.59

Table 5.1: Outer radii $R_{\bar{n}-1}$ and corresponding integrated particle numbers $N_{\bar{n}}$ of the individual Mott-shells according to [171]. Data is presented for the MI experiment in 2D (this section) and in 3D (next section). Refer to the text for details.

Equ. 5.61 is given in Fig. 5.15. Note that the value of χ_μ only depends on the experimental parameters in (b), while the results shown in (a) are universal. For the experimental conditions in the 2D experiment presented here, the lattice depths of the 1D and 2D lattice have been $V_{1D} = 30\,\mathrm{E_r}$ and $V_{2D}^{max} = 10.1\,\mathrm{E_r}$ respectively. The corresponding maximum occupation per lattice site is calculated to be $\bar{n}_{max} = 5$.
Interestingly by starting with a strong initial harmonic confinement, the virtual number of particles per lattice site decreases rapidly with increasing lattice depth. This counter intuitive behavior can be understood by taking into account, that the total trapping frequencies depend on the contribution of the lattice only *quadratically* to lowest order. The interaction U on the other hand immediately grows when raising a lattice potential. Thus up to a certain lattice depth, the ratio $\bar{\omega}^2/U$ –and accordingly $\bar{n}_{max}$–drops initially but will finally rise when reaching the regime of very deep lattices. This is a peculiarity owing to our strong initial harmonic confinement and *not* a generic feature of lattice systems.

Tab. 5.1 gives an overview over the estimated radii $R_{\bar{n}-1}$ and integrated particle numbers per shell $N_{\bar{n}}$ for the experimental parameters of the presented measurements. All the above discussion assumes that the temperature in the system is fairly low $T \leq T^{\star} = 0.2U/k_{\mathrm{B}} \approx 20\,\mathrm{nK}$, so that the Mott-shell structure has not completely washed out [176]. Indeed the fact that we see experimental signatures of Mott-shell formation could be employed to estimate an upper limit for the temperature of $T \leq T^{\star}$. This would indeed mean that the sample exhibits significant cooling when loaded in the optical lattice (compare Section 5.5.4).

Condensate fraction

Another useful quantity that can be extracted from the absorption images in Fig. 5.13 is the condensate fraction, by fitting a bimodal distribution to either the central or the interference peaks [164, 85]. The latter method has the advantage to be less susceptible to interaction effects during the expansion process and indeed the condensate fraction measured here is always slightly above the values obtained from the central peak. Consequently all results presented below correspond to parameters extracted from these fits.
After sufficiently long time-of-flight the density distribution consists of sharp interference peaks [157] caused by the condensed atoms which are assumed to exhibit the same parabolic shape as the external harmonic confinement. The other part of the bimodal density distribution is produced by thermal atoms whose distribution has been modeled employing a Gaussian. For small lattice depth this seems reasonable in dependence on a bimodal BEC in a harmonic trap *perturbed* by a periodic potential. For deep lattices the envelope of the density distribution is given by the Fourier transform of the Wannier function $|w(\mathbf{q})|^2$ which is again well approximated by a Gaussian. [7] By fitting the above function the condensate fraction N_0/N as well as a measure of temperature in a shallow lattice can be extracted from the data.
Fig. 5.16 shows examples of column densities and corresponding fits for the central as well as for the satellite peaks for various lattice depth. The width of the condensate peak has been determined and averaged from pictures well in the SF regime. The fitting procedure for larger lattice depth has then been invoked with this width as a constant parameter to ensure better and less forged results.
Plotted in Fig. 5.17 the condensate fraction qualitatively follows the course of the visibility, albeit starting at a lower value of $N_0/N = 0.43$. Especially the number and position of the kinks in the visibility is exactly reproduced and supports the conclusion that these kinks can be attributed to the formation of Mott-shells, since this implies a steep decrease in the superfluid fraction.
A closer look reveals, that besides qualitatively similar, the condensate fraction clearly vanishes before the visibility has dropped to zero. Neglecting very tiny condensate fractions $N_0/N < 0.05$ which could be artifacts of the fitting procedure, we identify a value of $\eta_{cf} \approx 15$. Calculating the critical temperature for Bose Einstein condensation according to $k_{\mathrm{B}}T_c = zJ(\bar{n}_{\max}+1)/2$ [176] yields $T_c \approx 10\,\mathrm{nK}$. This is a rather small value compared to the initial temperatures in the dipole trap ($T_c = 70\,\mathrm{nK}$) and the less reliable value for the individual 2D configurations ($T_c = 80-90\,\mathrm{nK}$).

[7] Thermal atoms confined in a sufficiently deep optical lattice in the tight-binding limit should obey a distribution $\langle n_{\mathbf{q}}\rangle \sim \exp(-\epsilon_{\mathbf{q}}/k_{\mathrm{B}}T) = \exp(2J\sum_{\mathbf{a}_i}\cos(\mathbf{q}\cdot\mathbf{a_i})/k_{\mathrm{B}}T)$. We have tried to fit a corresponding bimodal distribution to the observed data but could not resolve any cosinusoidal modulation. Thus it was not possible to extract temperature data in this way.

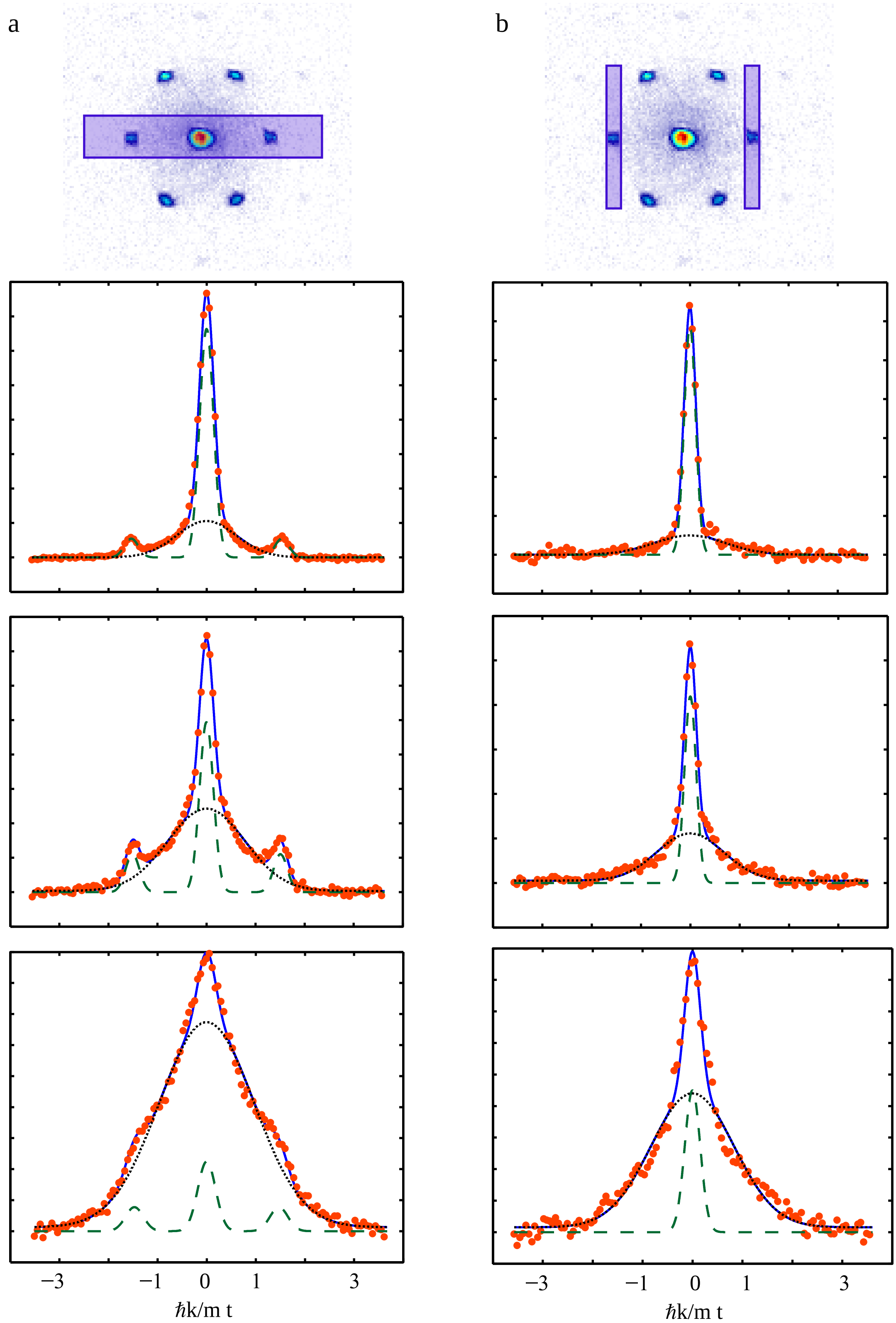

Figure 5.16: Bimodal fits to the peak structure of the absorption images. From top to bottom the lattice depth increases, reaching the critical point in the last row. (a) Fits to column sums of the shaded area corresponding to the central peak (b) Fits to the column sum of the shaded area of all 6 satellite peaks

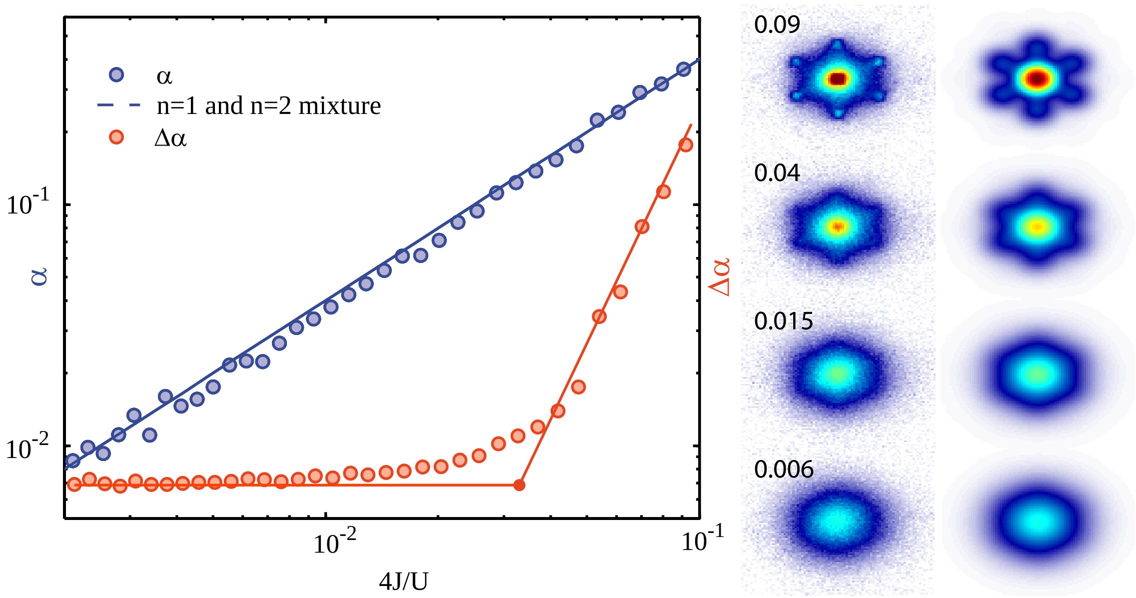

Figure 5.17: First order perturbation coefficients $\alpha = c{\cdot}4J/U$ where c is a free parameter connected to the number of particles per site. The coefficients are obtained from fits to the data shown in Fig. 5.13 as depicted in the right part of the figure for increasing lattice depths. The red circles indicate the error obtained for the fits and exhibit a sharp increase starting at a particular value of $4J/U = 0.035$ indicating the break down of the model. The left column is experimental data, whereas the right column is the theoretical model with the fitted α's as the only free parameter.

Beyond this point no superfluid fraction survives in the system. This also means that the inhomogeneous system is now composed of MI and normal gas layers as outlined in Section 5.5.4. If we take the observed critical temperature for the vanishing of the superfluid fraction as a measure for our temperature we are well below the melting temperature $T^\star \approx 20\,\mathrm{nK}$ indicating that Mott-shells should still be present.

By the observation that the condensate fractions disappears faster than the visibility, we are left with the problem to describe the residual visibility without any superfluid fraction. In Section 5.5.3 we have already developed a perturbative model to account for the residual visibility by short-range coherence induced by particle-hole pairs that distribute over a few lattice sites.

The model distribution has been fitted to our data for large values of η to be well within the regime where the perturbation Ansatz is justified. One free parameter α has been introduced in Equ. 5.57 instead of $4J/U(\bar{n}+1)/2$ to compare the model to the data. Fig. 5.17 shows the results. Two key conclusion can be derived from these observations. First of all the model accounts for the observed visibility surprisingly well as indicated by the theoretical curve, which has been simply obtained by proper weighting of contributions of different Mott-shells by imposing a LDA like approach employing Equ. 5.57.

Secondly the error of the individual fits show a sharp increase at a value of the smallness parameter $4J/U = 0.035$. Corresponding to $\eta = 18$, this coincides with the appearance of the condensate fraction and readily explains why a model *not* taking into account superfluid interference fails to describe the interference pattern for lattice depth smaller than this point.

Experiments performed in systems with only unity occupation have measured the condensate fraction [85] and the critical velocity for superfluidity [155] which should approach zero at the phase transition and find agreement with theory. The results of this experiment confirm, that both visibility and superfluid fraction show a behavior that is compliant with the assumption that both are inherently connected to each other. Residual visibility beyond the critical lattice depth for superfluidity could be described by a model taking into account particle-hole excitations leading to a finite short-range coherence.

Width of the central peak

The FWHM of the central peak in the momentum distribution has also been determined and plotted in Fig. 5.13 as yellow stars. As expected the width is almost constant in the regime where a considerable superfluid fraction survives, since the condensate peak contributes the largest fraction to the overall amplitude of the central peak. It is not before the condensate fraction has almost dropped to zero when the peak width suddenly starts to rise quickly to large values.
Remarkably the kinks observed in visibility and condensate fraction are also visible in the central peak width. It has been predicted [159] and contradicted [169] that the appearance of superfluid shells should lead to the formation of a fine structure of the central peak in terms of an additional small peak in the radial momentum distribution. This peak is expected to show up at momenta $q \approx |b_i|/5$ [159]. We have carefully checked all absorption images, but do not see any hint for additional structure at those momenta. Due to the unavoidable integration along one axis by employing absorption imaging the effect is additionally diminished and would only show up as a tiny shoulder. This could not be confirmed.

Energy scale and temperature

The bimodal fits to the absorption images used to determine the condensate fraction yield some additional information. The width of the incoherent background σ_{th} can be employed to give another estimate for the temperature at rather shallow lattice depth. In Fig. 5.13 the full width has been plotted as green squares in units of the reciprocal lattice vector. The width is approximately constant up to the point where the condensate fraction vanishes and increases linearly beyond that value. Assuming that for very shallow lattices one can estimate the temperature employing the expressions valid in a harmonic trap (see Appendix C)

$$k_{\mathrm{B}}T = \frac{m}{2}\left(\frac{\bar{\omega}^2}{1+\bar{\omega}_i^2 t^2}\sigma_{i,\mathrm{th}}^2\right). \tag{5.62}$$

$\bar{\omega}$ is the geometric average of total harmonic trapping frequency and is independent of the lattice depth to first order for our experimental setup and *shallow* optical lattices. From the extracted value $\sigma \approx 1.9$ in units of $\hbar k_{\mathrm{L}}/m \cdot t_{\mathrm{TOF}}$ for $V_0 \to 0$ a temperature estimate can be deduced according to $T \approx (\hbar^2 k_{\mathrm{L}}^2/4m)\,\sigma^2/k_{\mathrm{B}} = 290\,\mathrm{nK}$. This is not in agreement with the temperature estimates raised earlier in this chapter. Possibly due to the two-dimensional nature of the underlying system a different model has to be employed to correctly model the expansion of a 2D thermal cloud at a given temperature.
The considerations concerning ultracold 2D systems presented in the beginning of this chapter already emphasized well known problems and discrepancies between few experiments and theoretical models. Some of the quasi two-dimensional discs might be non-condensed and obscure the temperature determination even further.

For lattice depth well in the MI regime the width is dominated by incoherent atoms related to quantum fluctuations in the MI regime. It should therefor roughly be given by a convolution of the Fourier transform of the Wannier function $|w(\mathbf{q})|^2$ with the density expectation $\langle n_q \rangle$ given by Equ. 5.57. The expected scaling $\sigma \sim U/zJ$ can be confirmed looking at the corresponding part of the graph.

5.6.3 The SF-MI transition in a 3D system

We have also performed measurements attending to the SF-MI transition in a three dimensional system. To account for the different lattice parameters along the different dimensions of the lattice, we chose a constant factor between the strength of the 2D lattice and the 1D lattice of $V_{1D} = 2.78 \cdot V_{2D}$. As indicated in Fig. 5.10b this leads to an almost constant ratio of one of the corresponding parameters $\eta_{1D} = U/2J_{1D}$ and $\eta_{1D} = U/6J_{2D}$. Since the η's depend on the V's non-linearly the ratio can not be kept completely constant and varies between 0.8 and 1.8. The correct total Bose Hubbard parameter is than calculated according to $\eta = U/(2J_{1D} + 6J_{2D})$. Taking this into account the measurements agree qualitatively with the observations already made in the 2D experiment. Again a reproducible kink structure in the visibility and the width of the central peak is observed as indicated by arrows in Fig. 5.18. The larger initial condensate fraction is due to the fact that we work in a 3D system and further leads to a higher initial visibility of $\mathcal{V} = 0.81$ as compared to the 2D measurements. It has to emphasized, that the visibility has been normalized to this value in Fig. 5.18.
Note that the agreement with the already mentioned mean-field predictions is comparable in quality with the 2D results. The best and most accurate QMC result for the phase transition [170] gives $\eta_c = 3.67$ for this particular experimental configuration .[8] The qualitative agreement is evident. Again since an abrupt jump in all relevant parameters is not expected in inhomogeneous systems a rigorous check of these values can barely be achieved with a harmonically trapped system, especially at large harmonic confinement, because of the inherently connected large number of Mott-shells.
Since the long standing goal in the design phase of this experimental setup was the investigation of spinor condensates in optical lattices of various depth, it is unavoidable to start with a BEC in an optical dipole trap from the scratch. Trapping frequencies as low as $\bar{\omega} = 2\pi \times 10\,\mathrm{Hz}$ as achieved in some experiments starting in magnetic traps are not realizable using optical dipole traps relying on laser that can be afforded in usual cold atoms laboratories.
Concluding the superfluid to Mott-insulator transition has been investigated in a two-dimensional triangular lattice and in a three-dimensional periodic potential generated by the combination of a triangular lattice and a standing wave perpendicular to that lattice. A comparison of the results obtained by investigating different experimental parameters that are theoretically expected to change across the phase transition, allows to draw a concurrent and conclusive picture of the SF-MI transition in a triangular lattice. The main difference to the results obtained in the well explored cubic lattice is, that the phase transition occurs at much smaller values of the lattice depth as low as $V_{\mathrm{latt}} \approx 3.5 - 4\,\mathrm{E_r}$. This is consistent with the Bose-Hubbard model, since the crucial parameters U, z and J differ significantly from the corresponding values obtained for cubic lattices.
Reproducible kink-like features in various experimental parameters suggest the existence of

[8] Note however that these calculations have not been performed on a triangular lattice. We have scaled the result by taking into account our number of nearest neighbors z.

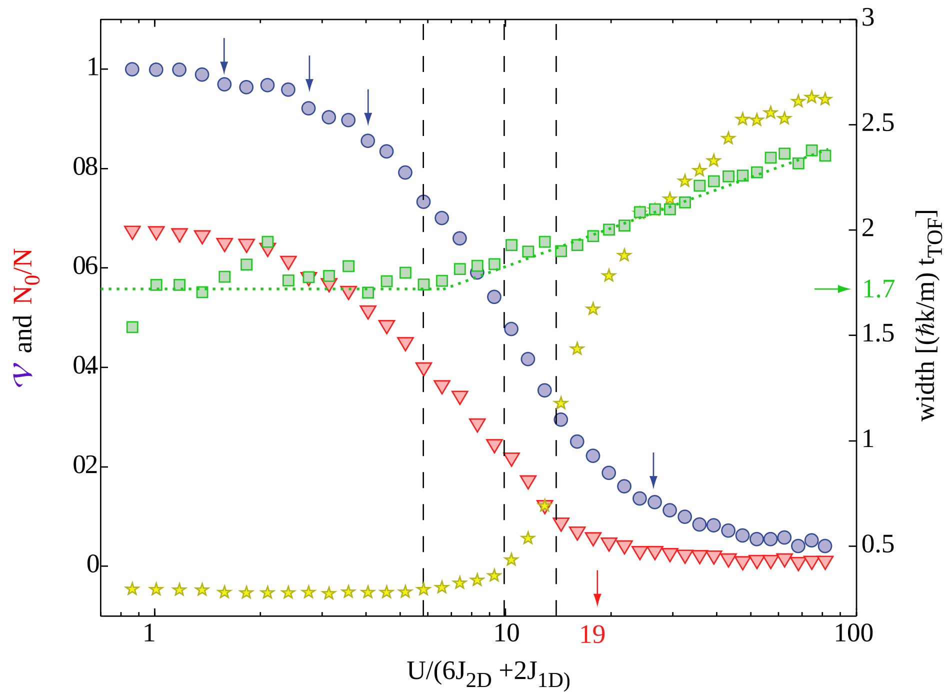

Figure 5.18: Visibility of the interference peaks across the phase transition against $U/(2J_{1D} + 6J_{2D})$. Note that the visibility has been normalized to its maximum value of $\mathcal{V} = 0.81$. The visibility starts to drop around a lattice depth of $3.5 - 4\,\mathrm{E_r}$ Reproducible kinks may indicate the formation of Mott-shells. The condensate fraction (red triangles) decreases as the lattice is ramped to deeper values. Pronounced kinks coinciding with those observed for the visibility can be distinguished. The FWHM of the central peak of the momentum distribution (yellow stars) is constant for low lattice depth. Around the phase transition it quickly starts to grow – also exhibiting small but reproducible kinks. The width of the incoherent background is plotted for completeness (green squares). Constant below the phase transition where it is a measure for the temperature, it starts to increase linearly with respect to U/zJ in the MI regime as expected from Equ. 5.57. Dashed vertical lines indicate the critical values for the transition to a Mott insulating state with $\bar{n} = 1, 2$ and 3 respectively.

several Mott-shells which is further supported by the large degree of inhomogeneity present in our system. The residual visibility of the interference pattern could be explained within the framework of a pertubative approach based on a slightly modified perfect Mott insulator.

The ability to enter the Mott insulating regime reversibly as demonstrated here constitutes the basis for future experiments attending to e.g. novel ground states, quantum information protocols or the investigation of quantum magnetism in optical lattices.

5.7 The hexagonal lattice

In the course this work most experiments have been performed in the triangular lattice, mainly due to the reasons stated in Section 5.1.2 that the laser power at equal laser detuning required to reach quantum criticality is 18 times larger than for the triangular lattice. With the non-achromatic polarization optics that is used in the experiments at

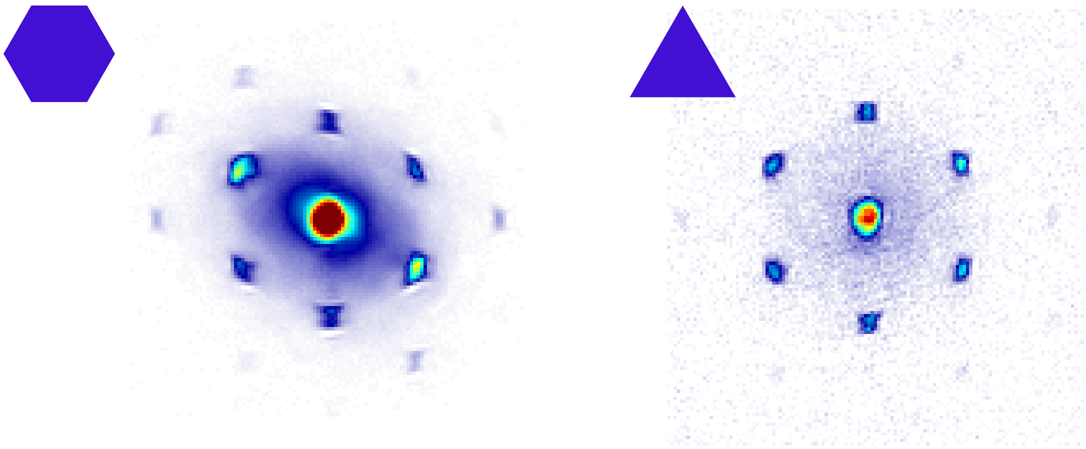

Figure 5.19: Comparison of absorption images obtain by releasing ultracold atoms either from a hexagonal (left) or triangular (right) lattice.

---

the time of these experiments it is neither possible to deliver these high laser powers nor is it possible to go to significantly smaller detunings to reduce the required power. Nevertheless attempts have been made to load atoms in the hexagonal lattice and to study the resulting density distribution after time of flight. Typical results are shown in Fig. 5.19. The patterns look very similar, what is expected by recalling, that the hexagonal lattice potential is somehow the 'negative' of the triangular lattice. In conventional optics it is well known from Babinet's principle that the expected interference pattern of two complementary diffracting objects is identical except for the overall forward beam intensity. Applying the theorem to our particular physical system yields the same interference pattern for both lattices, as long as the atoms are *not* localized in the tiny individual minima of the hexagonal lattice. From a quantum optics point of view it can be understood by keeping in mind that the involved reciprocal lattice vectors are exactly the same. Since interference peaks appear only at positions corresponding to reciprocal lattice vectors, it is clear that no principally new interference peaks will appear It is only when the atoms are well localized in individual minima of the hexagonal lattice, when one expects slight changes in the interference pattern. This can be seen by looking at the structure factor known from solid state physics that is expected to differ due to the different basis sets $\mathcal{B}_\triangle = \{0, 0\}$ and $\mathcal{B}_\square = \{1/3(2\mathbf{a}_1 + \mathbf{a}_2), 1/3(\mathbf{a}_1 + 2\mathbf{a}_2)\}$ of the two lattices:

$$\begin{aligned} \mathcal{S}_\triangle &= 1 \,\text{for all}\, (h, k), & (5.63) \\ \mathcal{S}_\square &= 2\cos\left(\frac{2\pi}{3}(h-k)\right) & (5.64) \\ &= 1 \,\text{for}\, (h,k) = \{1, 0\} \\ &= 2 \,\text{for}\, (h,k) = \{1, 1\} \\ &= 1 \,\text{for}\, (h,k) = \{1, \bar{1}\}. \end{aligned}$$

Since the scattering amplitude is proportional to $|\mathcal{S}|^2$ it is clearly seen that the relative amplitude of the second order peaks in the absorption images should be four times stronger in the hexagonal lattice as compared to the triangular lattice.
By looking at the individual interference peaks in Fig. 5.19 another striking observation can be made: Two of the six first order peaks are clearly more pronounced than the four others. We assign this to a residual misalignment of either the beams or their polarization. If the one of the beam pairs would contain a non-negligible amount of π^0 polarization, the corresponding two diffraction peaks should be explicitly stronger than the others. This effect dominates any possible detection of enhanced second order scattering and will definitely have to be suppressed in future experiments in order to clearly identify the hexagonal lattice.
Finally it should be stated, that the lattice depth associated with the images in Fig. 5.19 corresponds to the maximum available laser power at that time. Obviously no sign of a SF-MI transition is observed. To enter this regime it will be indispensable to go to larger laser power or – more realistic – smaller detunings. Since the required potential strength has to be 18 times larger than for an equivalent triangular lattice, serious problems concerning additional harmonic confinement and spontaneous scattering have to be expected.

5.8 Observation of noise correlations in a triangular lattice

So far we have analyzed the atoms by absorption imaging and extraction of parameters related to *first* order coherence properties. Especially in the MI-state a structure-less Gaussian density distribution is observed, as the result of an incoherent sum of all single particle wave function. Predictions concerning ordering or coherence properties are therefor not possible by simply analyzing the density $n_{\mathbf{r}}$. To obtain a more complete understanding of strongly correlated systems like cold atoms in optical lattices it is desirable to have access to higher order correlation functions. The fact that quantum fluctuations in many observables, e.g. the visibility or the momentum distribution after release from the trap contain information about correlations in the initial quantum state, is at the heart of the noise correlation technique proposed in [90, 91, 92, 93] and realized in bosonic [94] and fermionic systems [95, 96]. Noise correlation analysis is capable of detecting spatial ordering, e.g. ferromagnetically ordered states or spin waves to name a few prominent examples. Since the density distribution after time of flight represents and only represents the in-trap momentum distribution when interactions do not significantly modify the free expansion process, it is crucial that these constraints are met for noise correlation measurements. According to the experiment originally performed by Hanburry-Brown and Twiss [186, 187] the experimentally obtained density-density correlation function

$$\mathcal{C}(\mathbf{d}) = \frac{\int \langle n(\mathbf{r}+\mathbf{d}/2) \cdot n(\mathbf{r}-\mathbf{d}/2\rangle d^2\mathbf{r}}{\int \langle n(\mathbf{r}+\mathbf{d}/2)\rangle\langle(\mathbf{r}-\mathbf{d}/2\rangle d^2\mathbf{r}} \tag{5.65}$$

is characterized by the interference of different detection paths in a multi-detector array. Note that $\langle n(\mathbf{r})\rangle$ denotes the *average* of the atomic density averaged over many experimental realizations. In an ideal experiment the joint detection probability for atoms released from an optical lattice for two detectors separated by $\mathbf{d}$ will be sinusoidally modulated with a periodicity given by $l = (\hbar t|\mathbf{b}|)/(m)$. However for this assumption to be true some experimental constraints will have to be fulfilled to ensure that the dominating source of noise in the experiment is really the fluctuation in the atom number and not technical or

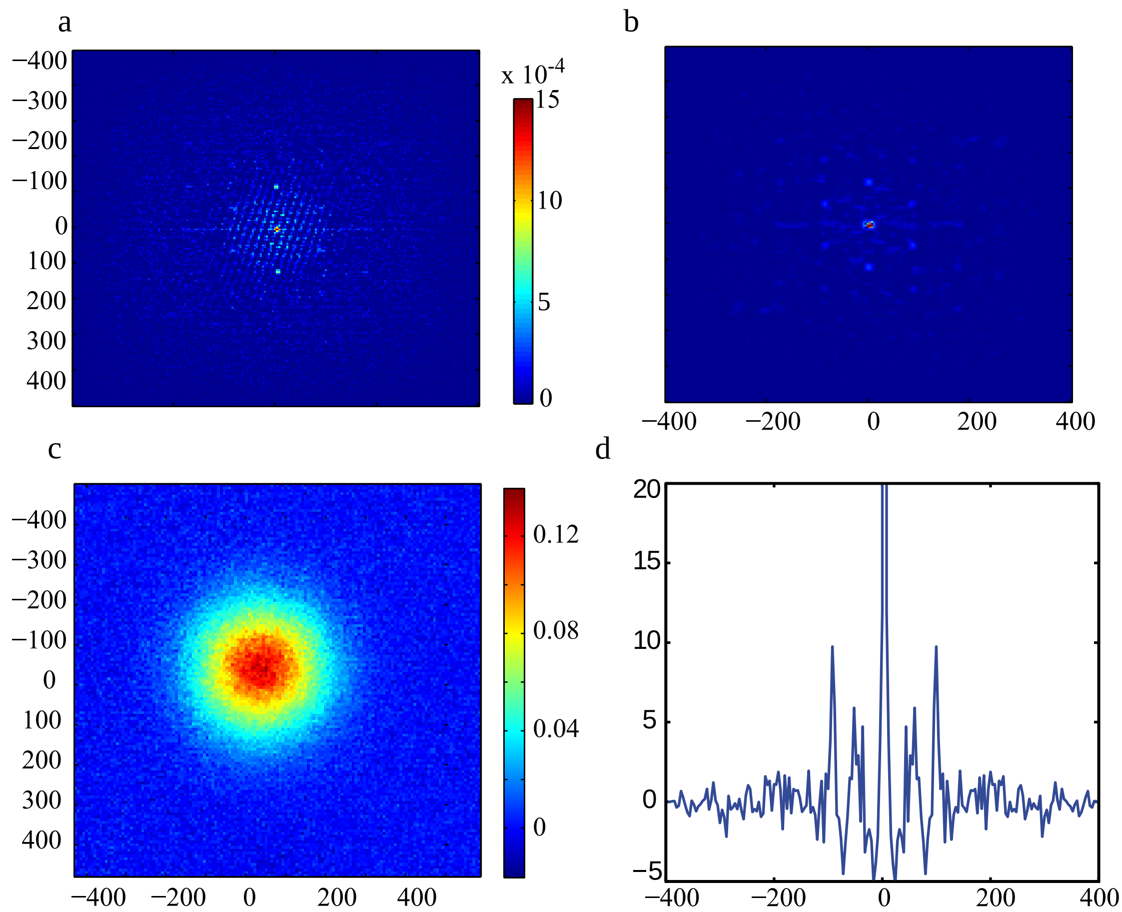

Figure 5.20: (a) Noise correlations obtained from averaging over 50 individual realizations of the same MI experiment. Peaks at the positions of reciprocal lattice vectors are visible. (b) The results of (a) have been filtered to emphasize the peak structure. (c) Corresponding mean density of the analyzed imaged. (d) Cut through (a) revealing the amplitude of the noise correlation.

---

photon shot-noise. Above a critical photon number of [90]

$$p > p_c = \frac{e^{2n_{\mathcal{OD}}}\langle N_\square \rangle}{\varepsilon n_{\mathcal{OD}}^2} \tag{5.66}$$

the atom shot-noise will overwhelm the photon noise and it should in principle be possible to observe correlations. Here $n_{\mathcal{OD}}$ is the optical density of the atomic cloud, $\langle N_\square \rangle$ the average number of particles per pixel and ε the detection efficiency of the CCD camera. The above expression exhibits a maximum at $n_{\mathcal{OD}} = 0.5$, which gives a good estimate for the particular choice of particle number and time-of-flight in the experiment.
A rigorous calculation of the second order correlation function $g^2(\mathbf{r}_1, \mathbf{r}_2)$ of the MI-state (see e.g. [188]) yields the following expression for the density-density correlation function.

$$\mathcal{C}(\mathbf{d}) = 1 + \frac{\bar{n}}{N} \sum_{\mathbf{G}} \delta\left(\left[\mathbf{r} - \frac{\hbar t}{m}\mathbf{G}\right]/l\right), \tag{5.67}$$

which confirms the above considerations. In the framework of the Diploma thesis of S. Dörscher a very extensive analysis of noise correlation and the associated computational tools has been performed at the spinor BEC experiment. Details concerning the exact determination of the above correlation function employing fast Fourier transformation can be found in his thesis. In a first proof of principle experiment we have observed noise correlations in the triangular lattice deep in the MI regime. The density correlations have been computed using a set of $\approx 50-70$ absorption images. Fig. 5.20 shows the averaged density together with the noise correlation according to Equ. 5.65. Clearly peaks situated at the position of reciprocal lattice vectors are visible. In Equ. 5.65(b) the resulting image has been filtered using an adaptive filter (MATLAB instruction `wiener2`), which pronounces the correlation peaks relative to the residual noise.
Future experiments could possibly include the detection of magnetically ordered states in the triangular and especially the hexagonal lattice. Here noise correlation spectroscopy represents an especially elegant way to pin down an experimental measure that is hard to reveal by other detection methods.

5.9 Spin dynamics in a triangular optical lattice

In the framework of this dissertation measurements of spin dynamics in lattices of different depth and at different magnetic fields have been performed in order to gain insight into the physics of magnetic systems in periodic potentials. In principle one would expect a crossover from mean-field regime spin dynamics as described in Chapter 4 to few particle spin oscillations isolated at individual lattice sites. The latter has been investigated and presented in three publications by the Mainz group [72, 74, 73]. They mainly focused on the physics of two particles at a single lattice site and found that coherent oscillations between two two-particle states $\psi_i = |0,0\rangle \leftrightarrow \psi_f = |-1,1\rangle$ occur that can be readily explained within the framework of a Rabi-like model. For atoms with $F = 1$ in an optical lattice the effective Rabi frequency is composed out of a coupling strength $\Omega_{if} \propto g_1 \int |w(\mathbf{r})|^4 \, d\mathbf{r}$ given by the spin-dependent interaction between the two states and a detuning $\delta = \delta_0 + \delta(B^2)$. δ is given by a part proportional to the quadratic Zeeman shift $\delta(B^2)$ and an offset term determined by the difference in interaction energy of the initial and final state $\delta_0 \propto g_1/2$. The authors of this work started with BEC in a magnetic trap with small trapping frequencies which was switched off after the deep MI regime had been reached. Thereby small occupation numbers n_i could be achieved but measurements were limited to the deep MI regime.
The ability of investigating spin dynamics at arbitrary lattice depths is associated with an overall spin *independent* trapping potential from the beginning. We have performed such measurements starting in an almost isotropic crossed optical dipole trap. Spin dynamics of ^{87}Rb BEC in $F = 1$ has been observed in the superfluid regime, close to the phase transition from superfluid to Mott-insulator and deep in the Mott-insulating regime inside a triangular optical lattice. In addition the magnetic field has been varied as a parameter to investigate the behavior of oscillation amplitude and period. In the language of mean-field spinor physics developed in Chapter 4 experiments corresponding to a whole variety of different k values have been performed. We have checked whether the observed dynamical behavior for the individual parameter sets can be described in terms of mean-field physics with a renormalized spin-dependent interaction $|g_1|\langle n_{\mathrm{norm}}\rangle$ or within a few-particle model or none of them.

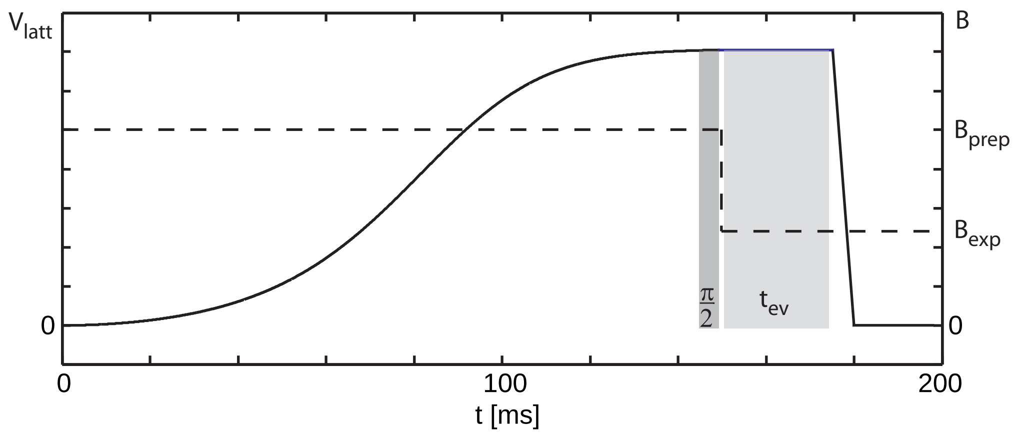

Figure 5.21: Essential part of the experimental cycle for the measurements on spin dynamics in optical lattices. After a smooth ramp-up the initial state is prepared at a certain magnetic field employing a rf $\pi/2$-pulse of 0.5 ms duration. Subsequently the magnetic field is switched to the desired final value and the atoms are allowed to evolve for a variable time t_{evo}. After that the lattice potential is ramped down fast within 5 ms in order to obtain absorption images that are optically dilute enough to unambiguously determine the particle numbers in the individual m_F-states.

5.9.1 Experimental sequence

The experimental procedure for the presented results is as follows. After preparation of BEC in $|1,-1\rangle$ with particle numbers of $N \approx 10^5$ with no discernible thermal fraction, we load the atoms in a three-dimensional optical lattice consisting of a 2D triangular lattice and a perpendicular 1D standing wave. The individual lattice depths have been adapted to yield equal U/zJ for the different spatial directions. After the final lattice depth has been reached, we let the system relax to equilibrium for 5 ms before we apply a $\pi/2$-pulse to prepare the well-known initial state $|\zeta_{\pi/2}\rangle$. At very low magnetic fields technical limitations of the rf amplifier circuit render the initial state preparation by the aforementioned method impossible. To circumvent this problem we prepare the initial state at a magnetic field large enough to guarantee a reliable and reproducible initial configuration. Necessarily the magnetic field has to be switched to the desired final value, which is done abruptly. We have checked that the quantization axis is well defined throughout and after the switching and that no zero crossings of the magnetic offset field are induced, which would shuffle the populations of the different m_F-states in an unpredictable way. We then hold the atoms for a variable evolution time to allow spin dynamics to take place. In order to have atomic samples which are *not* optically thick after time-of-flight, we quickly ramp down the lattice within 5 ms following the end of the evolution time to obtain atomic clouds that allow for a reliable and unambiguous atom number determination. Finally all trapping potentials are switched off and after 21 ms of time-of-flight including Stern-Gerlach separation the atoms are imaged with resonant light.

5.9.2 Below the phase transition: modified mean-field physics?

The obtained results can be analyzed in two different ways: First it is interesting to see how amplitude and frequency of spin dynamics at a given magnetic field change when the atoms are loaded in an optical lattice. Secondly the question whether the observed

experimental regime	XDF	superfluid	SF-MI crossover	MI
$\bar{n}_{\mathrm{norm}}$ [10^{12} cm^{-3}]	1.112	3.025	3.933	6.919

Table 5.2: Average normalized densities $\bar{n}_{\mathrm{norm}} = \bar{n}/N_{\mathrm{tot}}^{2/5}$ in lattices of different depth as employed for the spin dynamics measurements. n_{norm} has been obtained in a Thomas-Fermi approximation of the Bose-Hubbard model assuming Poissonian statistics as justified for a superfluid state (see text for more details).

---

dynamics can still be described by the analytical solution

$$|\zeta_0(t)|^2 = (1 - k\,\mathrm{sn}_k^2(qt))/2, \tag{5.68a}$$

$$|\zeta_{\pm1}(t)|^2 = (1 + k\,\mathrm{sn}_k^2(qt))/4, \tag{5.68b}$$

at least as long as a superfluid order parameter exists, can be approached by fitting the model to the data and check the agreement. In the superfluid regime the addition of a periodic potential should mainly show up in terms of an increased effective spin-dependent coupling owing to an increased mean density. The resulting effective k will determine frequency and amplitude of spin dynamics within this simple model. However different additional effects e.g. caused by reduced mobility or an increased thermalization rate might lead to deviations from this behavior and the data is carefully analyzed whether any indications for those deviations can be found and whether they can be attributed to a specific physical process.

To estimate atomic densities in the different lattice regimes we have employed a Thomas-Fermi-like approximation of the Bose-Hubbard model for the superfluid regime and the regime close to the SF-MI phase transition [156]. By assuming that the system is still well described by a superfluid order parameter ψ, the solution of the Bose-Hubbard model can be recast in a simple form, neglecting the kinetic energy term proportional to J (Thomas-Fermi approximation) which makes the energy diagonal in the basis of individual lattice sites i:

$$E_i \simeq \epsilon_i|\psi|^2 + \frac{U}{2}|\psi|^4 = \epsilon_i\bar{n}_i + \frac{U}{2}\bar{n}_i^2. \tag{5.69}$$

The single site chemical potential $\mu = \partial E_i/\partial n_i$ has to be replaced by its LDA value $\mu_i = \mu - \epsilon_i$ in an inhomogeneous system. If the external potential varies slowly on a length scale given by the lattice spacing this can be approximated by $\mu(\mathbf{r}) = \mu - V(\mathbf{r})$. Imposing the normalization condition $N = \int n(\mathbf{r})\,d\mathbf{r}$ finally leads to an expression for the chemical potential

$$\mu = \left(\frac{15}{16}\frac{V_{\mathrm{cell}} m^{3/2} N U \bar{\omega}^3}{\sqrt{2}\pi}\right)^{2/5}, \tag{5.70}$$

which allows to determine the density according to $n(\mathbf{r}) = (\mu - V(\mathbf{r}))/g_0$ and the Thomas-Fermi average density $\langle n\rangle = 4/7\, n(0)$ in analogy to harmonically trapped BEC. The corresponding densities are calculated by taking into account the particular harmonic trapping frequencies $\bar{\omega}$ and onsite interaction matrix elements U and are summarized in Tab. 5.2. To arrive at the average density the tabulated value has to be multiplied by $N^{2/5}$ where N is the total particle number of the individual experimental run.

Fig. 5.22 shows spin dynamics measurements in a crossed dipole trap ($\eta = 0$), in the superfluid regime ($\eta = 1.45$) and in the vicinity of the SF-MI phase transition ($\eta = 8.9$)

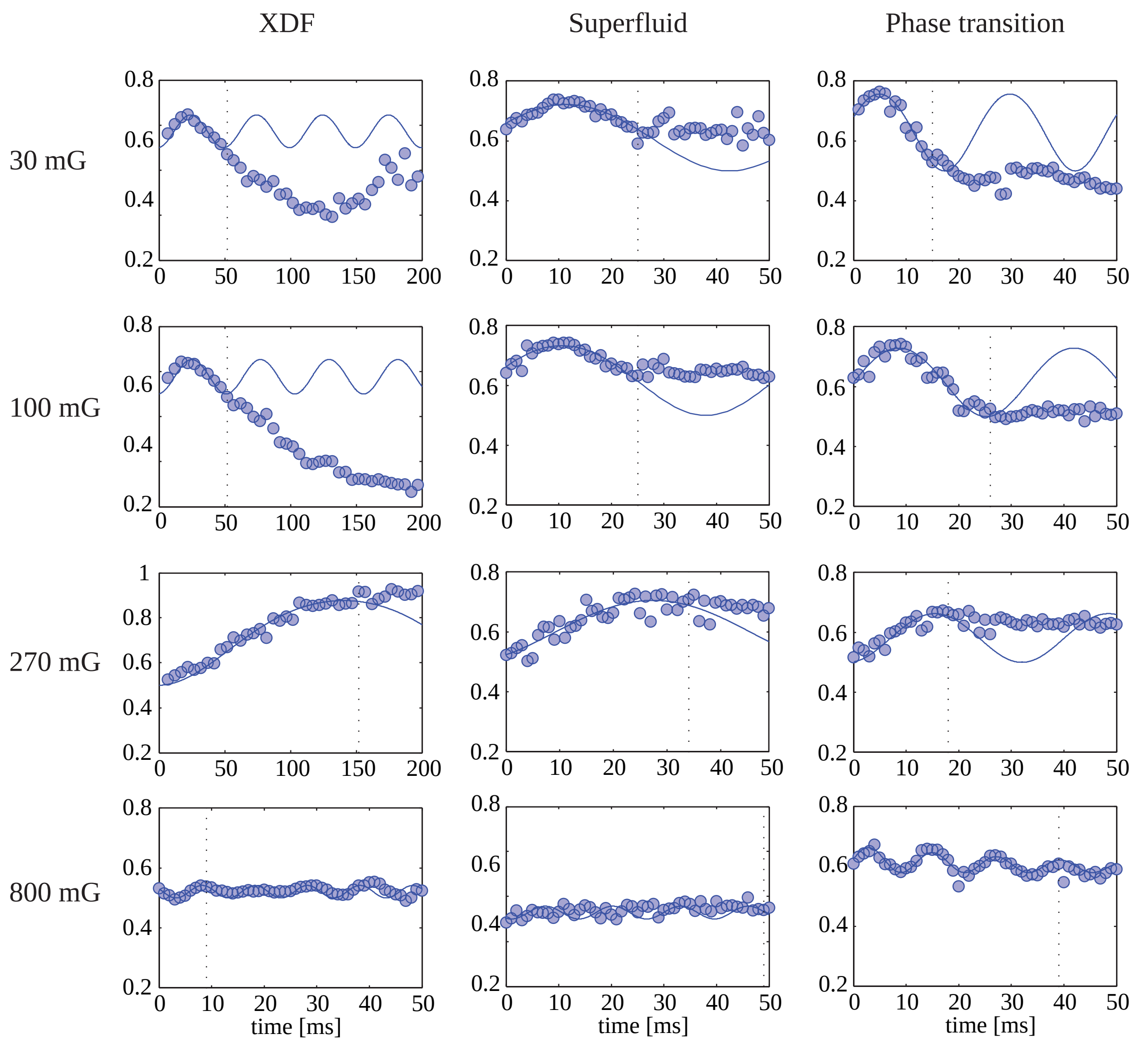

Figure 5.22: Spin dynamics of a ^{87}Rb $F = 1$ spinor condensate in optical lattices of various depth starting in $|\zeta_{\pi/2}\rangle$. The individual graphs show the time evolution of the population in the $m_F = 0$ state ρ_0. Data is presented along with fits (solid lines) to determine oscillation amplitude and period. The dotted vertical lines indicate the time up to which the fits have been performed. While the left column shows measurements performed in a crossed dipole trap, the column in the middle displays results obtained in an optical lattice corresponding to the superfluid regime ($\eta = 1.45$). In the right column finally spin dynamics in the vicinity of the SF-MI phase transition is presented ($\eta = 8.9$). The magnetic field increases from top to bottom.

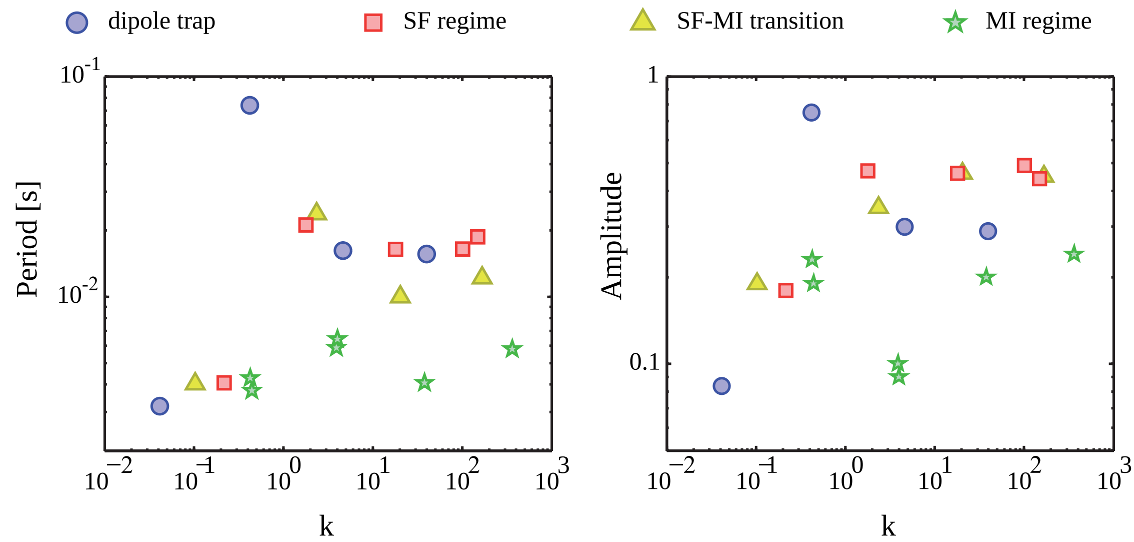

Figure 5.23: Spin dynamics at various lattice depths: oscillation amplitude and period. The individual k-values have been calculated employing measured trapping frequencies and particle numbers (see Tab. 5.2). Amplitude A and period $2\pi/B$ have been deduced from fits to the data according to $\rho_0 = (1 - A\sin^2(B\cdot(t+C)))/2$. Comparison with the corresponding predictions of the analytic solution Equ. 5.68 given in Fig. 4.8 reveals qualitative agreement for the measurements performed at lattice depths below the deep MI regime (see text for more details).

---

at various magnetic fields. The time evolution of the $m_F = 0$ population has been fitted with a function $\rho_0 = (1 - A\sin^2(B\cdot(t+C)))/2$ to extract the oscillation amplitude A and period $2\pi/B$.

We have tried to fit the analytic solution Equ. 5.68 to the data as well but this does not give convenient results for the measurements performed at 30 and 100 mG for *all* lattice depths that have been investigated. A similar phenomenon has already been observed for spin dynamics in $F = 2$ presented in Chapter 4. The fits of the analytic solution to the data assume that the single mode approximation can safely be applied. *No* effects of spatial structuring are taken into account, since the population of the individual m_F-states is integrated over the whole condensate. In Chapter 4 it was found that for larger magnetic fields or smaller k the SMA analytic solution fits much better to the data than in the opposite case. This very fact is also true for the results obtained in the optical lattice at 270 and 800 mG, where Equ. 5.68 gives reasonable results.

A comparison of the k-value extracted from fits of the analytic solution with the k-value obtained by calculating $k = g_1\langle n\rangle/q$ directly, employing the observed total particle numbers according to Tab. 5.2, shows reasonable agreement with deviations $|k_{\mathrm{fit}} - k_{\mathrm{calc}}/k_{\mathrm{calc}}| \leq 0.2$ for most of the data sets recorded at magnetic fields of 270 and 800 mG. The measurements at a magnetic field of 100 mG show qualitative agreement regarding the oscillation period but the amplitude is systematically underestimated by the analytical model. Finally at 30 mG neither the observed oscillation period nor the amplitude is in accordance with the SMA mean-field solution.

The individual images of the data series at small k corresponding to 30 and 100 mG show strong local effects especially at low lattice depths and in the XDF which clearly indicate the breakdown of the single mode approximation. Note however that the largest spin dynamics amplitude occurs if the SMA remains valid. Spatially dependent oscillation fre-

quencies can therefor *not* account for the *larger* amplitudes observed in our experiments. Furthermore for evolution times beyond 50 ms the low magnetic field samples evolve towards spin mixtures with $\rho_0 < 1/2$ that are *not* governed by the mean-field solution at all.
Additional unknown effects might be responsible for this evolution, possibly including thermalization or a component demixing of $|1,1\rangle$ and $|1,-1\rangle$ which would inhibit a reconversion to $|1,0\rangle$. ρ_0 would consequently take very small values after a reasonable evolution time. Phase separation of $|1,1\rangle$ and $|1,-1\rangle$ starts to play a role as soon as the linear Zeeman energy associated with the residual magnetic field gradient across the condensate $\Delta p = 2R_{\mathrm{BEC}}|\nabla B|$ overwhelms the quadratic Zeeman energy q.
As shown in Section 3.4 the quality of the gradient compensation is usually on the order of $|\nabla B| \leq 0.2\,\mathrm{mG/mm}$. For typical spatial extensions of the condensate of $R_{\mathrm{BEC}} \simeq 10\,\mu\mathrm{m}$ the maximum difference amounts to $\Delta p/2\pi$ of a few Hz. Comparing this to the quadratic Zeeman energy at $B = 100\,\mathrm{mG}$ of $q/2\pi \simeq 0.7\,\mathrm{Hz}$ indicates that component separation might indeed be the reason for the long term evolution towards states with a very small ρ_0 that is observed for all data series performed at 100 mG and especially at 30 mG.
For deeper lattices the effect is slightly suppressed which might be explained by the reduced mobility owing to the significantly reduced tunneling times $t_{\mathrm{t}} = \hbar/J_{\mathrm{tot}}$. The tunneling time increases from 1.8 ms in the superfluid regime to 6.7 ms close to the phase transition and finally to 400 ms in the deep MI regime where tunneling is completely negligible.
However clear indications for these mechanisms can not be deduced from the data, although component separation of $|1,1\rangle$ and $|1,-1\rangle$ can be observed in *some* of the absorption images mainly those recorded in the XDF and the superfluid regime. At larger magnetic field this effect can not be observed within our optical resolution and sensitivity concerning particle number determination.

On the other hand thermalization leads to a rapid decohering of the *thermal* atoms followed by an equipartition among the individual thermal clouds of different magnetic states as already described in Section 4.2.1. As a result the atom number in the $m_F = 0$ thermal cloud decreases, which is maintained by condensation of excess atoms. The condensate fraction ρ_0 consequently grows. Since large effort has been taken to work at very low temperatures, strong thermalization effects are not expected. The absence of a growth of ρ_0 indicates that thermalization is not responsible for the observed long term evolution of the low-B samples. Note however that condensate and thermal fraction have only been determined separately for the XDF measurements while the particle numbers obtained for the other three regimes are *total* atom numbers.
Fig. 5.23 shows oscillation amplitudes and periods extracted from the fits to the data as presented in Fig. 5.22. Excluding the measurements at 30 mG a qualitative agreement of the course of the oscillation period as compared to the predictions of the mean-field solution is observed. The similarity of the results at 30 and 100 mG are not explained within the analytic solution. It could be an indication for an additional physical process that dominates "free" spin dynamics at very low B-fields. The currently available data sets do not allow to further specify any possible processes.

In conclusion the observed spin dynamics of ^{87}Rb in $F = 1$ in an optical lattice shows qualitative agreement with the mean-field solution raised in Chapter 4, as long as the lattice is shallow enough to maintain a significant superfluid fraction. The differences in the results at different lattice depths can mainly be reduced to an effective spin-dependent

	$N = 6 \cdot 10^4$		$N = 8 \cdot 10^4$		$N = 12 \cdot 10^4$	
site occupation $\bar{n}$	$R_{\bar{n}-1}[10\mu\text{m}]$	$N_{\bar{n}}[10^4]$	$R_{\bar{n}-1}[10\mu\text{m}]$	$N_{\bar{n}}[10^4]$	$R_{\bar{n}-1}[10\mu\text{m}]$	$N_{\bar{n}}[10^4]$
1	0.94	1.29	1.00	1.39	1.10	1.54
2	0.79	2.09	0.86	2.33	0.97	2.69
3	0.60	2.13	0.70	2.65	0.83	3.32
4	0.32	0.49	0.47	1.62	0.65	3.20
5	-	-	-	-	0.40	1.24

Table 5.3: Integrated particle numbers $N_{\bar{n}}$ of the individual Mott-shells according to [171]. Data is presented for the spin dynamics experiments in the deep MI regime for different total particle Numbers.

interaction $g_1\langle n_{\text{norm}}\rangle$. Especially at low magnetic fields local effects complicate the analysis of spin dynamics at all lattice depths and inhibit an accurate quantitative comparison.

5.9.3 Spin dynamics in the MI regime

The character of the observed spin dynamics changes in the deep MI regime. The aforementioned approximations assumed for the measurements below the critical point seem not plausible anymore if we go to a sample of isolated, localized few-atom systems. The system consists of Mott-shells with different occupation numbers which will exhibit spin changing dynamics with a frequency and amplitude that is among others determined by the particular number of particles per lattice site.

Averaging the density over all Mott-shells to arrive at an effective overall k does not seem to be a very promising starting point in order to describe the resulting spin dynamics. It appears much more plausible that the overall population dynamics will be a superposition of the contributions from different Mott-shells weighted with the relative particle number in the individual shell.

It remains true that the spin-dependent coupling takes a renormalized form $\tilde{g}_1 = g_1 \cdot \int |w_0(\mathbf{r})|^4\, d\mathbf{r}$, where $w_0(\mathbf{r})$ denotes the Wannier function for a particular lattice depth. Even though interaction effects tend to broaden the single site wave function for occupations $n_i > 1$ and thus lower the density as compared to the non-interacting value $\langle n_{\text{NI}}\rangle = n_i \cdot \int |w(\mathbf{r})|^4\, d\mathbf{r}$, the former expression still constitutes a reasonable approximation to the exact density. The corrections to the density due to interaction effects are on the order of $\Delta n = 1/(1+0.01n_i)$ [189]. To obtain the weighting factors we have employed the zero-tunneling Mott-shell model from [171] already introduced in the context of the SF-MI transition. Tab. 5.3 lists the atom numbers per Mott-shell for the range of total particle numbers observed in our experiments.

The measurements are presented in Fig. 5.24 and clearly show conceptional differences to the results in shallower lattices. Moreover it is evident that coherent oscillations as observed in [72] cannot be traced for more than half a period or sometimes one complete period. As recently shown in the group of Prof. D. Pfannkuche [190] the amplitude behavior for few-atom spin dynamics at a single lattice site exhibits a resonant phenomenon similar to the mean-field results for the initial state $|\zeta_{\pi/2}\rangle$. This resonance should be determined by $k_{\text{MI}}^{n_i} = 1$ where $k_{\text{MI}}^{n_i} = q/(2n_i - 1)\tilde{g}_1$ is the critical parameter for spin dynamics involving n_i atoms. Regarding our measurements this behavior can *not* be confirmed.

We observe almost equal amplitudes of the initial oscillation for all magnetic fields except at 270 mG where the amplitude is smallest in contrast to the results for shallower lattices.

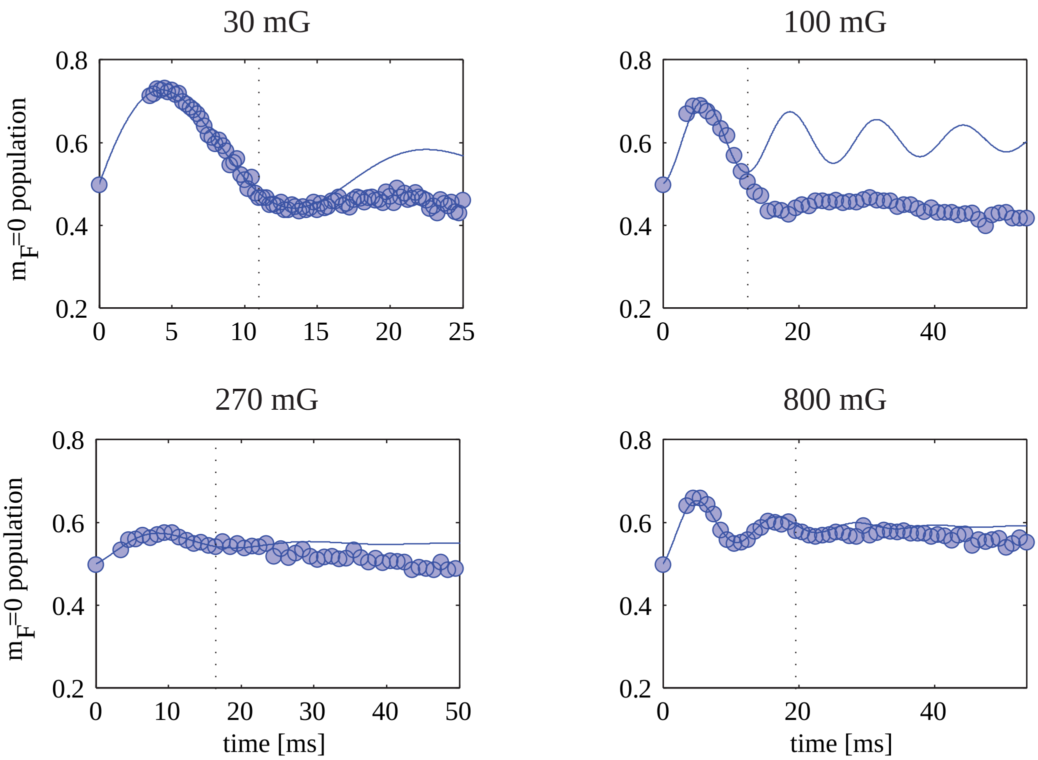

Figure 5.24: Experimental results for spin dynamics in the deep MI regime corresponding to $\eta = 1.3 \cdot 10^3$.

Starting in $|\zeta_{\pi/2}\rangle$ the maximum amplitude in the few-atom model is limited to 0.125 for two atoms on resonance. For higher particle numbers and off-resonant $k_{\text{MI}}^{n_i}$ this value is further reduced [190]. The initial oscillation amplitude in our experiments clearly exceeds this value.
The frequency spectrum of spin dynamics in the few-atom model for $n_i \geq 3$ is characterized by a primary oscillation frequency $\omega \sim q$ and a beat note at approximately $2\tilde{g}_1$ for large magnetic fields. The latter is in harsh contrast to the mean-field predictions. As a striking result the period of the beat note is the same for all particle numbers n_i for $k_{\text{MI}}^{n_i} \gg 1$. Thus it should in principle be possible to observe this beat note in an inhomogeneous system regardless of the many different onsite occupation numbers present.
For our experimental parameters a beat note frequency of $2\pi \cdot 2\tilde{g}_1 = 2\pi \cdot 13\,\text{Hz}$ would be expected, which means that the first zero in ρ_0 is expected after 40 ms. For the measurements at $B = 800\,\text{mG}$ the decrease of the oscillation amplitude is on the same order of magnitude as this value. However, since we are not able to observe a recurrence of the full or even partial amplitude it can not be argued that this causes the decrease of the amplitude or if simply thermalization or decoherence lead to the observed decrease.

Concluding it can be stated that non of the models discussed in this section is capable to describe the observed amplitudes correctly. The quality of the data will have to be improved significantly in future experiments to compare it to the theoretical prediction in more detail. Mott-shell resolved detection of spin dynamics would circumvent the intrinsic inhomogeneity if the system in a certain way and allow for an observation of spin dynamics for a single occupation n_i. The experimental sequence should also be refined and the final ramp-down of the lattice should by avoided at least for the MI measurements. An unpredictable dynamical evolution may take place during that time, obscuring the dynamics that occurs in the deep lattice.

5.10 A Zeeman-Bragg resonance - polarization effects

The adjustment of the polarization of the three lattice beams creating the triangular lattice constitutes a serious problem, since measuring devices can not be used at the experiment, simply because there is not enough room to place them somewhere in the optical path. On the other hand it is crucial to make sure to have very clean polarizations to avoid any kind of Zeeman induced optical pumping to other m_F-states. This is especially important when studying phenomena related to spin changing dynamics inside the lattice at very low magnetic fields.

We have studied this Zeeman-Bragg effect for very low magnetic fields at our experiment. A significant transfer of atoms - coherent Rabi oscillations on a short time scale could be observed - occurs only when the energy associated with the the Bragg-like momentum transfer from two lattice beams matches the energy difference between the two m_F-states given by the linear Zeeman effect.

Furthermore to undergo a m_F-state changing Bragg transition angular momentum has to be transferred to the atom. It is thus only possible, if the polarization of the two beams is *not* equal. Another important difference to conventional Bragg scattering is the fact, that the process is *not* sensitive to the sign of the momentum transfer, since the energy needed to fulfill energy conservation is provided by the Zeeman energy and not by the detuning between the two beams as usual. This detuning is in fact always zero inside the lattice, which prohibits any real two-photon transitions when the polarization is perfectly adjusted.

Recalling the angle dependent momentum transfer mediated by a 2-photon Bragg process

$$\Delta p_\phi = 2\hbar k_\mathrm{L} \cdot \sin\left(\frac{\phi}{2}\right), \tag{5.71}$$

the corresponding free-particle energy transferred by either two beams of the triangular lattice is easily calculated as $E_\mathrm{free} = \Delta p_\phi^2/2m = (10.0 \pm 0.4)\,\mathrm{kHz}$, where a pessimistic estimate for the accuracy of the angle adjustment of $\Delta\phi = \pm 2°$ has been made [9]. Naturally the transferred momentum corresponds to a reciprocal lattice vector of the triangular lattice.

It is straight forward to calculate the Zeeman energy that is freed by making a transition with $\Delta m_F = +1$:

$$\Delta E_\mathrm{ZM} = \mu_\mathrm{B} g_F |B_\mathrm{off}|. \tag{5.72}$$

For a first-order Bragg process we expect therefor a resonance at a magnetic field on the order of 15 mG. This is in fact a small value that demands for a very precise control of the magnetic field (compare Section 3.4).

Fig. 5.25 provides a schematic representation of the first and second order Zeeman-Bragg processes as observed in our experiment. The magnetic field in Fig. 5.25 is chosen to be resonant with the second order process, where a 4-photon transition with the corresponding energy transfer $2E_\mathrm{free}$ transfers the atoms from $|-1, p = 0\rangle$ to $|+1, p = 2\Delta p_\phi\rangle$. Note that

[9] The angles enclosed by the beams can be deduced from the reciprocal lattice vectors determined through absorption images.

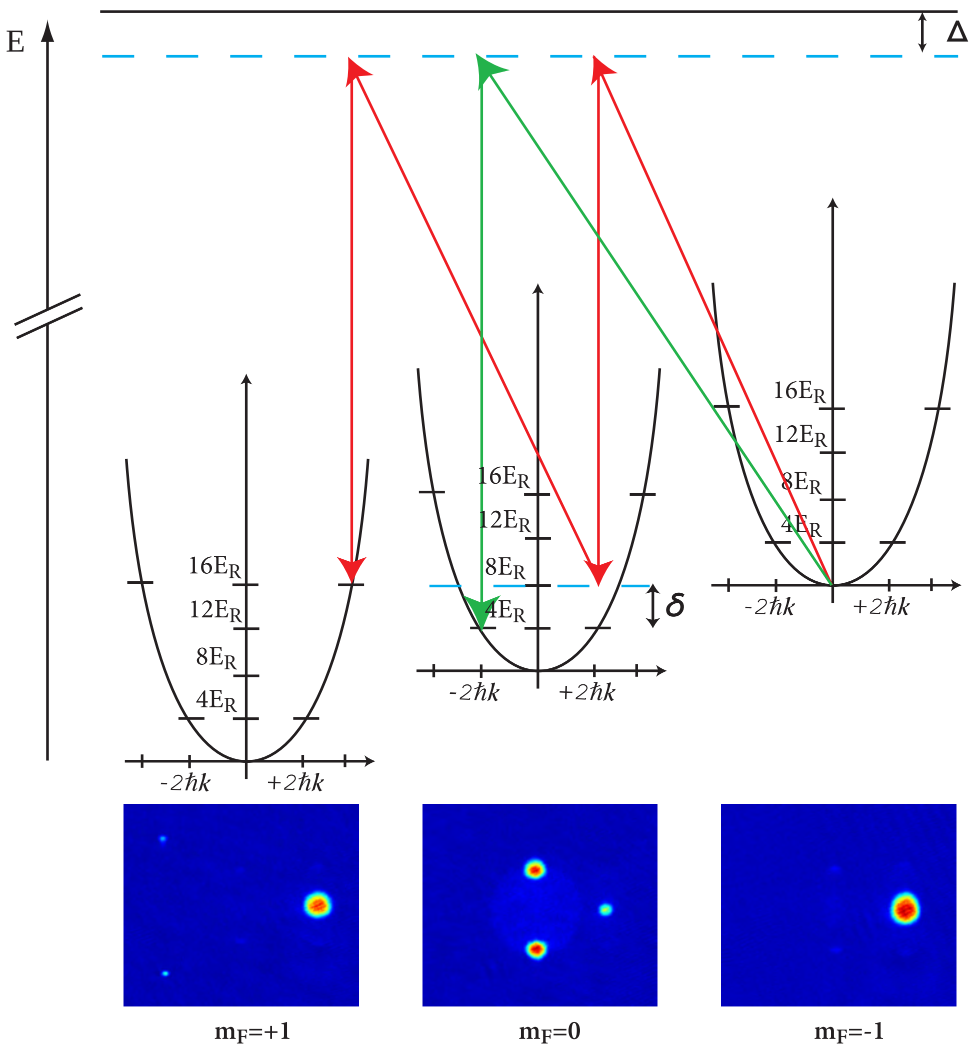

Figure 5.25: Momentum-energy scheme for first- and second-order Zeeman-Bragg processes. The linear Zeeman effect provides the energy necessary to fulfill energy and momentum conservation according to the systems dispersion $\omega\Delta p$. Exemplary absorption images are displayed showing atoms in $|m_F = -1, p = 0\rangle$, $|m_F = 0, \Delta p_\phi\rangle$ and $|m_F = +1, 2\Delta p_\phi\rangle$ (see text for more details).

---

only two beams of the triangular lattice have been employed for all results presented in this section. Their polarizations have been chosen to be π for one beam and $1/\sqrt{2}(\sigma^+ + \sigma^-)$ (linear in the plane spanned by the lattice beams) for the other. The resulting optical potential does *not* show any periodic structure in harsh contrast to the usual lattice geometry. However, if not perfectly aligned the triangular lattice with small in-plane polarization components exhibits exactly the same m_F changing transitions at low magnetic field. This renders the investigation of spin changing dynamics almost impossible and even more severely leads to strong heating that destroys any quantum degeneracy.
Note that the process involving $\Delta m_F = 2$ from $|1, -1\rangle$ to $|1, +1\rangle$ which would be expected for two beams with $1/\sqrt{2}(\sigma^+ + \sigma^-)$ polarization and $\Delta E_{\mathrm{ZM}} = 2 \cdot 30\,\mathrm{mG}$ is not allowed for this particular experimental situation, as can be seen by coherently adding up the transition strength according to Equ. 3.34. We have checked this and did not find any

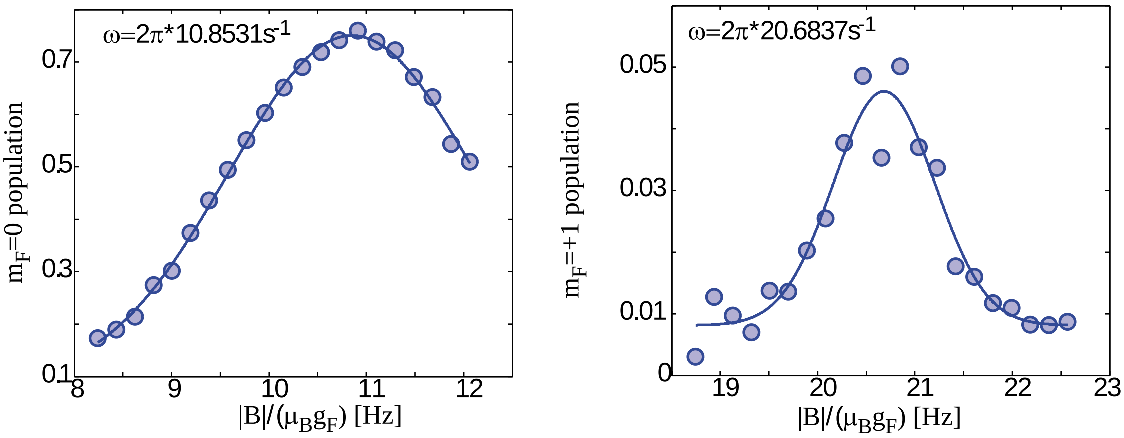

Figure 5.26: Measurements of the Zeeman-Bragg resonances for first-order $|m_F = -1, p = 0\rangle \rightarrow |m_F = 0, \Delta p_\phi\rangle$ and second-order processes $|m_F = -1, p = 0\rangle \rightarrow |m_F = 0, 2\Delta p_\phi\rangle$. The magnetic field $B_{\rm off}$ has been varied and short $(\Omega_0\tau < 1)$ Bragg pulses have been applied to the system.

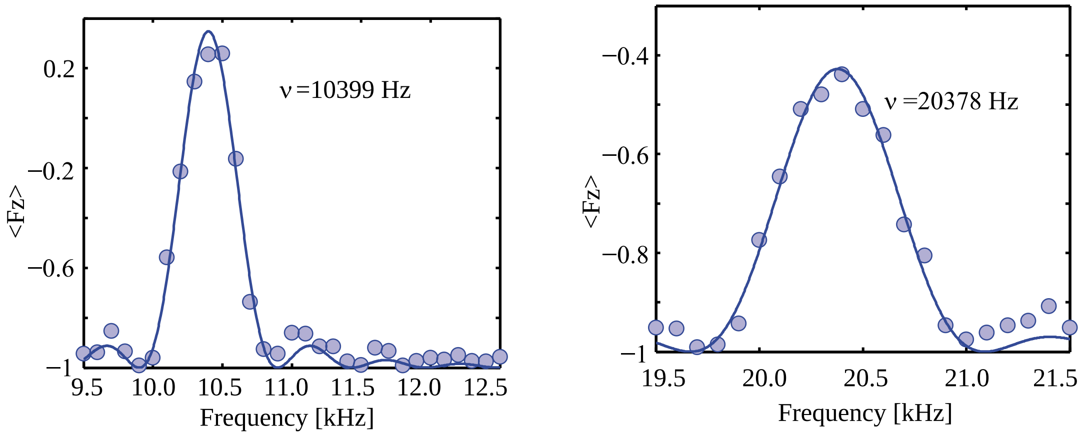

(a) Calibration at the value of the first resonance.

(b) Calibration around the value of the second resonance.

Figure 5.27: Magnetic field calibration at very low fields. The rf-amplifier and- antenna usually employed at our experiment do not work properly anymore at such low frequencies. Instead, the current through offset field coils has been modulated at the corresponding frequencies.

---

detectable transfer of population confirming the theoretically expected vanishing of the two-photon transition

We have measured the transfer to the first- and second-order Bragg states in dependence on the magnetic field $B_{\rm off}$. Bose-Einstein condensates of $N \approx 80000$ particles are prepared in a crossed optical dipole trap with $\bar{\omega} = 2\pi \times 90\,{\rm s}^{-1}$. in $|F = 1, m_F = -1\rangle$. Subsequently the atoms are exposed to a Bragg pulse of $t_{\rm Bragg} = 1\,{\rm ms}$ duration with a power of $P = 90\,{\rm mW}$ in each beam at a wavelength of 830 nm. Directly after the pulse all trapping potentials are switched off and the atoms are imaged after a TOF including Stern-Gerlach separation.
The results of these experiments are shown in Fig. 5.26 and clearly demonstrate the resonant character of the underlying physics. The energies associated with the observed

resonances are $E_{1st} = h \cdot 10.85\,\text{kHz}$ and $E_{2nd} = h \cdot 20.68\,\text{kHz}$. Besides the uncertainty of the exact angle $\Delta\phi = 2° \hat{=} 0.4\,\text{kHz}$ and a possible maximum error in the gauging of the magnetic field of $\Delta B = \pm 1\,\text{mG} \hat{=} 0.7\,\text{kHz}$ (see Fig. 5.27) a systematic shift to an energy larger than the free particle dispersion law, which would correspond to energies of $E_{1st} = h \cdot 10.01\,\text{kHz}$ and $E_{2nd} = h \cdot 20.02\,\text{kHz}$, is observed.
Since the atoms are in a harmonic trap rather than being free and non-interacting, a first step towards the explanation of this shift is the inclusion of first-order Bogoliubov theory. Applying the local density approximation to account for the inhomogeneity of the trapped system yields the famous dispersion law [102]

$$\epsilon(\vec{r}, \vec{q}) = \sqrt{\frac{\hbar^2 q^2}{2m}\left(\frac{\hbar^2 q^2}{2m} + gn(\vec{r})\right)}. \tag{5.73}$$

Moreover two-photon scattering events in cold gases probe the imaginary part of the response function, which is strongly connected to the dynamic structure factor. A rigorous calculation [102] finally results in an expression for the shift of the expected resonance peak relative to the free case for a Thomas-Fermi condensate

$$\Delta\omega_{\text{peak}} = \frac{2}{3}\frac{\mu}{\hbar}. \tag{5.74}$$

Plugging in our experimental values to obtain μ, we arrive at a shift of $\Delta\omega_{\text{peak}} = 2\pi \cdot (950 \pm 120)\,\text{s}^{-1}$. This is in qualitative agreement with the measured deviations from ω_{free} which amount to $\Delta\omega^{\text{exp}}_{\text{peak},1st} = 2\pi \cdot 885\,\text{Hz}$ and $\Delta\omega^{\text{exp}}_{\text{peak},2nd} = 2\pi \cdot 680\,\text{Hz}$. To nail down this effect measurements for different atomic densities and/or different angles between the beams could be employed. This is however far beyond the scope of this work, although the Zeeman-Bragg effect has been observed for the first time in our experiment to our best knowledge.
So far we did only employ this effect to calibrate the polarization of the three-beam lattice. Future experiments involving the hexagonal lattice might need to investigate the Zeeman-Bragg effect or related physical phenomena in much more detail.
Finally Fig. 5.28 shows coherent Rabi oscillations between $|m_F = -1, p = 0\rangle \to |m_F = 0, \Delta p_\phi\rangle$. The observed Rabi frequency $\Omega_{\text{exp}} = 2\pi \cdot 1.99\,\text{kHz}$ is in good agreement with the theoretical value $\Omega_{\text{theo}} = 2\pi \cdot 3.29\,\text{kHz}$ obtained by solving Equ. 3.34 explicitly and taking into account the large uncertainty in the determination of the exact intensity at the position of the atoms. This is due to the fact that neither the exact waist size $w(z)$ at the position of the atoms nor the intensity can be appropriated to better than $20 - 30\%$.

5.11 Conclusion and Outlook

In conclusion the physics of ultracold ^{87}Rb atoms in a triangular optical lattice has been investigated. An appropriate experimental upgrade of the apparatus has been designed and implemented that allows for the generation of a triangular as well as a spin-dependent hexagonal lattice. Measurements on the superfluid-Mott insulator transition in a three-dimensional optical lattice composed out of a triangular lattice and a perpendicular standing wave have been performed. Moreover this quantum phase transition has been studied in detail in a quasi two-dimensional system exhibiting a triangular symmetry for the first time. The additional spatial dimension has been frozen out using a very tight one-dimensional lattice.

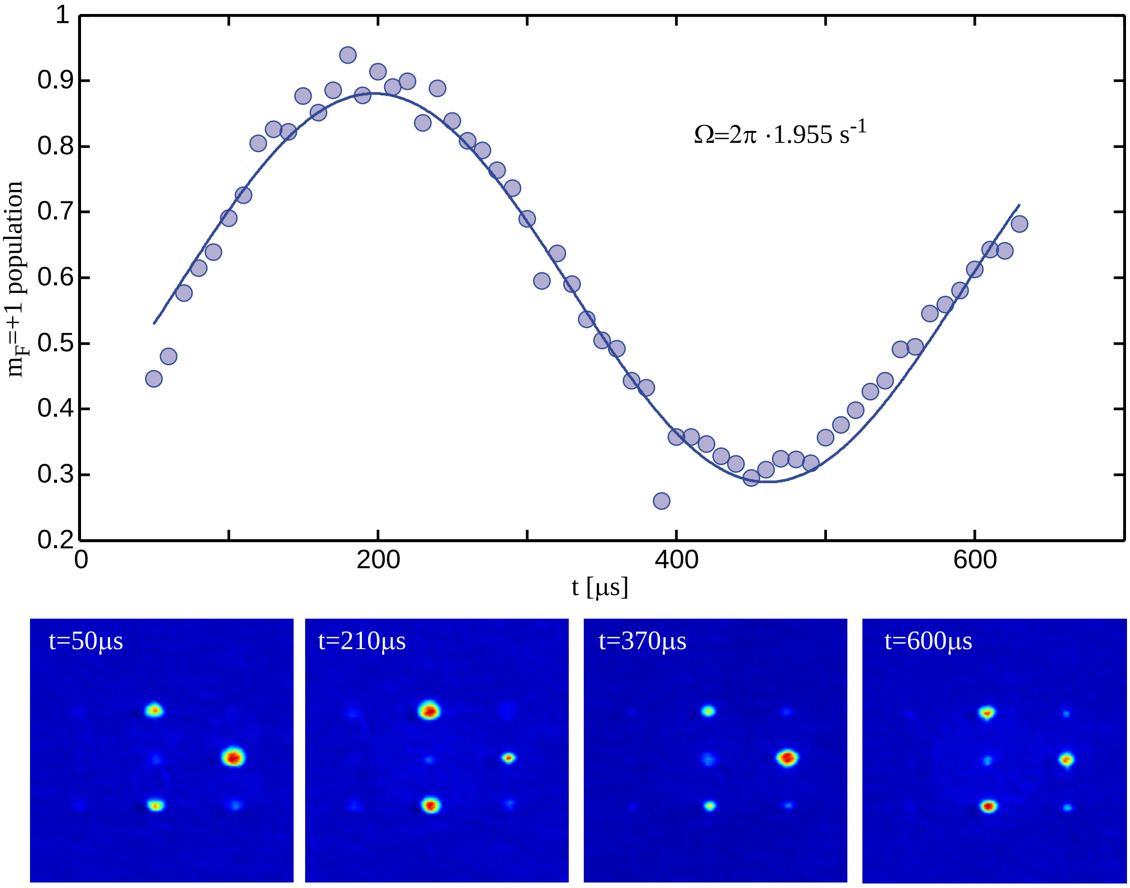

Figure 5.28: Fraction of atoms in the $|m_F = 0, \Delta p_\phi\rangle$ as a function of time. A nice sinusoidal oscillation is observed. Exemplary absorption images are presented for comparison. Paying to the large harmonic confinement, the coherence time is only on the order of few ms. For longer observation times the atoms are heated and begin to spill out of the trap.

Visibility as well as the condensate fraction and the width of the interference peaks have been analyzed in detail to develop a concise understanding of the physics in our highly inhomogeneous system. Proof-of-principle measurements attending to noise-correlation spectroscopy have been conducted promising further studies of magnetically ordered or frustrated phases in future experiments.

Spin dynamics of ^{87}Rb in $F = 1$ in lattices of variable depth has been studied and it was shown that qualitatively the change of oscillation period and amplitude can still be explained within a mean-field description with an effective coupling constant. Albeit additional interesting but unexplained effects appear that require further investigation. Measurements performed in the Mott insulating regime suffer from the large degree of inhomogeneity present in our experiments.

Future experiments will aim at a selective detection of sites with a given occupancy thus hopefully enabling us to consecutively study spin-dynamics of two, three, four, ... atoms. The investigation of the hexagonal lattice by further improving the optical power of the lattice laser or reducing the detuning holds fascinating prospects concerning the initialization of anti-ferromagnetically ordered phases or the suppression of spin dynamics by spin selective tunneling processes.

The interplay of magnetic contact interaction and permanent and optically induced dipole-dipole interaction together with a spin-dependent lattice potential moreover promises a whole wealth of new and fascinating physical effects.

Chapter 6

Oscillations and interactions of dark and dark-bright matter-wave solitons

As described in detail in the introduction, Solitons are distinguished as wave packet like objects that do not change their shape and propagate with a constant velocity in homogeneous systems. A detailed balance between dispersion induced spreading and a focusing or defocusing mediated by a non-linear interaction stabilizes the soliton as it propagates through a well suited non-linear medium. Bose-Einstein condensates that can be described within the framework of the Schrödinger equation exhibiting a cubic non-linearity represent an especially well suited system to investigate solitons.
In this chapter experiments on dark and dark-bright solitons in elongated Bose-Einstein condensates are presented. Due to spectacular long life times oscillations as well as collisions of different types of solitons could be observed for the very first time in the framework of this thesis. After an introductory theoretical derivation of the most important physical properties of dark and dark-bright solitons it will be explained how solitary excitations can be generated in a BEC employing a high resolution optical phase imprinting method. We will then turn to experimental results regarding the oscillation of a dark soliton in a harmonically trapped elongated BEC, showing good agreement with theoretical predictions. Collisions of two dark solitons will be presented subsequently. Both phenomena have been observed within this dissertation for the first time, enabled by unsurpassed long lifetimes of the produced dark solitons as long as several seconds.
The last part of this chapter is devoted to the physics of dark-bright solitons in a multi-component ^{87}Rb BEC, where the density notch of a dark soliton in $|1,0\rangle$ is filled with atoms in another hyperfine state $|2,0\rangle$. Interestingly strongly populated dark-bright solitons initially propagate in the direction opposite to unperturbed dark solitons. Moreover the oscillation period of dark-bright solitons is dramatically extended as compared to dark solitons as will be shown.

The results presented here have been published in two articles appearing in peer-reviewed journals. In [3] oscillations of dark and dark-bright solitons in elongated BEC are discussed, whereas [2] reports on collisions of two dark solitons in a condensate.

6.1 Theoretical prerequisites for the understanding of solitons

The theoretical prerequisites for understanding the physics of dark- and dark-bright solitons include the cross over from 3D to quasi 1D BEC. It turns out that dark solitons are only dynamically stable if the excitation of transverse modes of the condensate is strongly suppressed as will be discussed in more detail during this section. The wave function of solitary solutions of the single- and multi component one-dimensional GPE will be presented and the equation of motion of a soliton in an externally trapped BEC is given. It will be discussed which decay mechanisms tend to decrease the life time of the soliton and how these mechanisms are avoided in our experiments. Finally the theoretical findings concerning interaction of solitons will be presented shortly in view of the various collision experiments that have been conducted within this thesis.

6.1.1 Quasi-1D condensates

If a BEC is confined in a strongly anisotropic trap $\omega_\perp \gg \omega_z$ the dimensionality of the system may undergo a transition from three-dimensional to quasi one-dimensional if the energy associated with transverse trapping is much larger than the chemical potential $\gamma := \hbar\omega_\perp / g_0\langle n\rangle \ll 1$. [1] It is thus useful to derive an effective one-dimensional GPE for condensates that fulfill the above restriction. The wave function for such a system can be written as the product of an arbitrary longitudinal function and the ground state wave function of the harmonic potential in the transverse direction $\psi(\mathbf{r}) = \psi(z) \cdot \phi(\mathbf{r}_\perp)$. Substituting this into Equ. 2.7 the 3D GPE can be reduced to an effectively one-dimensional equation:

$$i\hbar\frac{\partial}{\partial t}\psi(z,t) = -\frac{\hbar^2}{2m}\frac{\partial^2}{\partial z^2}\psi(z,t) + V_{\text{ext}}(z,t) + g_{1\text{D}}|\psi(z,t)|^2\psi(z,t). \tag{6.1}$$

The one-dimensional coupling constant is given by $g_{1\text{D}} = 2\hbar\omega_\perp a = g_0/(2\pi a_{\text{HO}}^2)$, where a_{HO} is the harmonic oscillator length and a the s-wave scattering length determining interatomic interaction. The 1D density $n_{1\text{D}}(z,t) = |\psi(z,t)|^2$ is connected to its 3D counterpart by

$$n_{1\text{D}}(z,t) = n(\mathbf{r}_\perp = 0, z, t)\, \pi a_{\text{HO}}^2 \tag{6.2}$$

For tight harmonic trapping the effective density is found by *transverse averaging* leading to $\bar{n}(z,t) = 1/2\, n(\mathbf{r}_\perp = 0, z, t)$. [2] Other important properties of the condensate are also affected by this transverse averaging. The healing length and speed of sound in a quasi one-dimensional BEC have to be replaced by

$$\bar{\xi}(z,t) = \sqrt{2}\xi(\mathbf{r}_\perp = 0, z, t) \quad \text{and} \quad \bar{c}_s = \frac{1}{\sqrt{2}}c_s(\mathbf{r}_\perp = 0, z, t) \tag{6.3}$$

respectively, as compared to their corresponding values in a 3D system. This will be important since healing length and speed of sound are fundamental measures determining

[1] Throughout literature various definitions can be found, deciding whether a BEC can be described within the one-dimensional limit. One of the most established is characterized by the parameter $\gamma' := (\omega_z/\omega_\perp)Na/a_{\text{HO}}$. Only if $\gamma' \ll 1$ can a BEC be regarded to behave one-dimensional.

[2] In the opposite limit of an elongated 3D Thomas-Fermi BEC the (hydro-dynamic) transverse averaging results in a factor of 1/2 for the mean density as well [191]. This result has been confirmed experimentally [192]

the basic properties of solitons.
The density distribution of an axially harmonically trapped condensate in the Thomas-Fermi limit is simply given by

$$n_{1\mathrm{D}}(z) = n_{1\mathrm{D},0} \cdot \max\left(1 - \frac{z^2}{R_z^2}, 0\right) \tag{6.4}$$

where $n_{1\mathrm{D},0} = n(\mathbf{r}=0)\,\pi a_{\mathrm{HO}}^2 = \mu/g_{1\mathrm{D}}$. The Thomas-Fermi radius R_z is given as usual by $R_z = \sqrt{2\mu/m\omega_z^2}$. The mean density is evaluated to $\langle n_{1\mathrm{D}}\rangle = 4/5\, n_{1\mathrm{D},0}$. In our system the two different criteria for being one-dimensional introduced above typically take values of $\gamma \approx 4$ and $\gamma' \approx 13$. They are both far away from being much smaller than one.
As we will see the solitons generated in our experiments are nevertheless highly stable and behave almost as if they were strictly one-dimensional.

Dimensionless GPE

Following [27] it is very useful to rewrite the GPE in a dimensionless form as will become clear especially in the case of a multi-component BEC. By introduction of new dimensionless variables for energy $E' = E/(\hbar\omega_\perp)$, length $x' = x/\sqrt{\hbar/(m\omega_\perp)}$ and wave function $\psi_i' = \psi_i\sqrt{g_{ii}/(\hbar\omega_\perp)}$ where g_{ij} are intra- and inter-species interaction parameters the dimensionless form of Equ. 6.1 is given by

$$i\frac{\partial}{\partial t'}\psi' = \left(\frac{1}{2}\frac{\partial^2}{\partial x'^2} + V' + |\psi'|^2\right)\psi' \tag{6.5}$$

Having found the necessary expressions for quasi one-dimensional condensates we can now commence and investigate solitary solutions of the corresponding GPE.

6.1.2 Dark solitons in Bose-Einstein condensates

Homogeneous system

The solitary solutions of Equ. 6.1 can be divided into two fundamentally different classes, depending on the nature of the atomic interaction basically given by the s-wave scattering length a. For attractive interactions ($a < 0$) *bright* solitons are a solution to Equ. 6.1 [13, 22, 23, 26]. Characterized as a non-spreading wave packet they constitute the ground state of the underlying system and are only stable up to a critical particle number N_c above which the condensate is liable to an interaction induced collapse [193].
In the course of this thesis solitons in ^{87}Rb Bose-Einstein condensates which interact repulsively ($a > 0$) have been investigated. The soliton solutions for repulsive interaction are called *dark* solitons and manifest as a depression in the local density of the condensate accompanied by a certain phase slip that is acquired when passing the nodal plane of the soliton. As a solution to Equ. 6.1 the wave function of a dark soliton at position q propagating along z with a velocity $\dot{q}$ can be written as [194, 195]

$$\psi_D(z,t) = \sqrt{n_{1\mathrm{D},0}}\left\{i\frac{\dot{q}}{\bar{c}_s} + \sqrt{1-\frac{\dot{q}^2}{\bar{c}_s^2}}\,\tanh\left[\kappa\left(z-q(t)\right)\right]\right\}e^{-ign_0t/\hbar}. \tag{6.6}$$

We recall from Chapter 2 that the speed of sound in a quasi-1D condensate is given by $\bar{c}_s = \sqrt{n_0 g/2m}$ and n_0 is the peak density of the condensate. The inverse size of

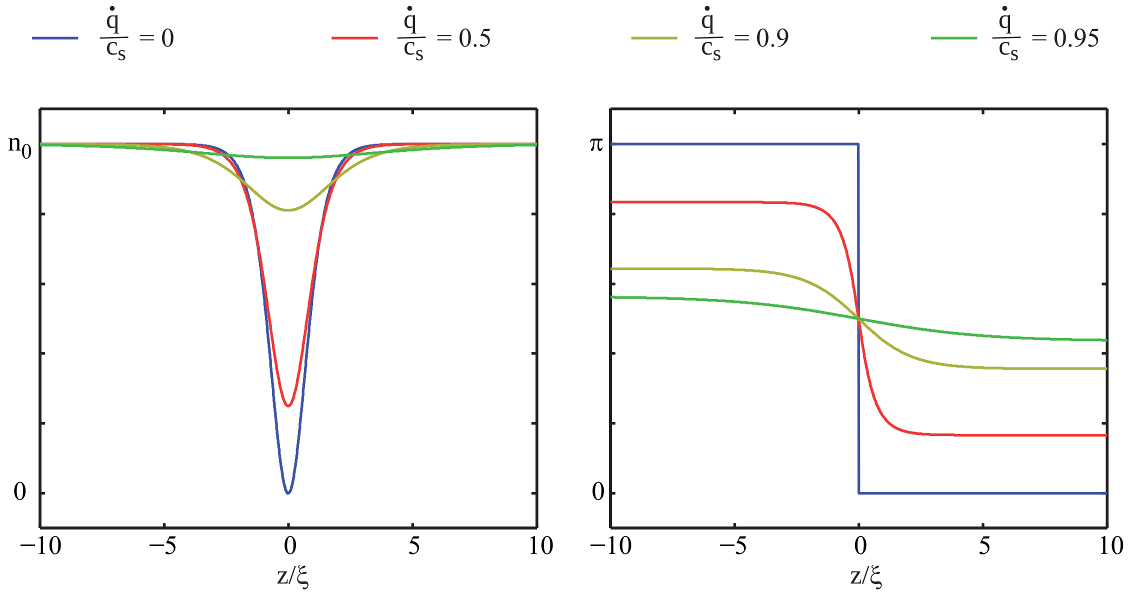

Figure 6.1: Density (left) and phase (right) distribution of dark solitons for different velocities in units of the speed of sound. Note that length is given in units of the healing length $\bar{\xi}$.

the soliton κ is determined by the healing length $\bar{\xi} = \hbar/m\bar{c}_s$ and the soliton speed $\dot{q}$ through $\kappa = \bar{\xi}^{-1} \times \sqrt{1-(\dot{q}/\bar{c}_s)^2}$. The phase and density distributions of a dark soliton are schematically shown in Fig. 6.1. As depicted, the phase only shows significant changes in the vicinity of the nodal plane of the soliton and is constant elsewhere.

Crossing the nodal plane of the soliton, the wave function accumulates a specific phase slip between 0 and π depending on the depth and speed of the dark soliton related by $n_s/n_{1\mathrm{D},0} = 1-(\dot{q}/\bar{c}_s)^2 = \sin^2(\Delta\phi/2)$ where n_s denotes the missing density at the position of the soliton and $\Delta\phi = \phi(z \to -\infty, t) - \phi(z \to \infty, t)$. A phase jump of $\Delta\phi = \pi$ corresponds to a fully modulated soliton with zero velocity representing the only time independent soliton solution of the GPE. This particular solution is sometimes called *black* soliton as opposed to other dark solitons named *gray* solitons in this context which are not fully modulated.

The explicit form of the solution Equ. 6.6 is often found in literature concerning only dark solitons.

With regard to the experiments on *dark-bright* solitons it is however very instructive to state an alternative notation, which can directly be assigned to the solution for dark-bright solitons [39]. Accordingly the wave function of a dark soliton can also be expressed as

$$\psi_D(z,t) = \sqrt{n_{1\mathrm{D},0}}\left\{ i\sin(\alpha) + \cos(\alpha)\,\tanh\left[\kappa\,(z-q(t))\right]\right\} e^{-ign_0t/\hbar}. \tag{6.7}$$

with the supplementary definitions

$$\begin{aligned} \kappa &= \bar{\xi}^{-1}\cos(\alpha) \\ \dot{q} &= \frac{\hbar\kappa}{m}\tan(\alpha) \\ &= \bar{c}_s\sin(\alpha). \end{aligned}$$

The velocity angle $-\pi/2 \leq \alpha \leq \pi/2$ parametrizes the solution Equ. 6.7 and unambiguously determines depth, width and speed of the soliton. Similar conclusions as those drawn from Equ. 6.7 remain true for dark-bright solitons, with the modification that another parameter, the number of particles in the bright component, enters the expressions for κ and $\dot{q}$.

Following [20] it is straight forward to calculate the energy of the dark soliton according to

$$E_{\mathrm{DS}} = \int \left(-\frac{\hbar^2}{2m} \psi_D^\star \frac{\partial^2}{\partial z^2} \psi_D + \frac{1}{2} g_0 (|\psi_D|^2 - n_{1\mathrm{D},0})^2 \right) dz. \tag{6.8}$$

The contribution of the homogeneous background without soliton n_0 has been subtracted in order to guarantee convergence of the integral. The result obtained from the above expression reads

$$E_{\mathrm{DS}} = \frac{4}{3} g_0 n_{1\mathrm{D},0}^2 \bar{\xi} \cos^3(\alpha) = \frac{2}{3} M_{\mathrm{DS}} \, (\bar{c}_s^2 - \dot{q}^2), \tag{6.9}$$

where the mass of the dark soliton is given by $M_{\mathrm{DS}} = m \, n_{1\mathrm{D},0} \, 2\bar{\xi} \cos(\alpha)$ and corresponds to the mass of the atoms that have been pushed aside by the dark soliton. [3] In this sense a dark soliton can be regarded as a "hole" similar to the definition of e^+ charge carriers used in solid state physics. Interestingly the energy of the soliton decreases with increasing velocity and smoothly disappears as $\dot{q} \to c_s$. Because of the above peculiar properties a *negative* mass is frequently assigned to dark solitons in literature.

Inhomogeneous systems: Equation of motion

Concluding the preceding section it has to be emphasized again that in a homogeneous system a soliton propagates at a constant velocity without any change of its amplitude or width. This situation changes when one studies dark solitons in a Bose-Einstein condensate which is usually externally trapped and thus naturally constitutes an *inhomogeneous* system, where the atomic density decreases smoothly from its maximum value n_0 to zero at the edges of the condensate. The dynamics of dark solitons in inhomogeneous BEC has been vastly investigated theoretically. Analytical [27, 28, 29, 30] as well as numerical approaches [31, 32] agree with each other concerning the results for dark soliton dynamics in a trapped BEC. The most striking outcome is that a dark soliton is subject to the following equation of motion just like a classical particle.

$$m\ddot{q}(t) = -\frac{1}{2} \frac{\partial V(z)}{\partial z}. \tag{6.10}$$

A beautiful derivation of the equation of motion in the framework of the local density approximation substituting the speed of sound by its local value $\bar{c}_s \to \bar{c}_s(z)$ in Equ. 6.9 can be found in [29]. The ratio of the negative soliton mass to the likewise negative TF density potential of the BEC $-M_{\mathrm{DS}}/-V_{\mathrm{TF}}(z)$ is precisely twice the ratio of atomic mass to external potential $m/V(z)$. Therefore the soliton behaves like a classical particle with mass $-2m$ in a potential $-V(z)$. If $V(z)$ is a harmonic potential, the soliton will consequently oscillate at a frequency given by $\Omega = \omega_z/\sqrt{2}$. Note that the soliton does not change its *depth* while it oscillates in the condensate. The turning points of the oscillation are hence determined by the condition that the remaining condensate density

[3] In literature one often finds the definition $E_{\mathrm{DS}} = \frac{1}{3} M'_{\mathrm{DS}} \, (\bar{c}_s^2 - \dot{q}^2)^{3/2}$ where $M'_{\mathrm{DS}} = 4m \, n_{1\mathrm{D},0} \bar{\xi}$. This is mathematically beautiful since the mass does not depend on the velocity. However M'_{DS} does not correspond to the real mass of the soliton.

vanishes: $n_{1\mathrm{D},0}(Z) = n_s$. Extracting the turning points thus provides a useful check for the results obtained for the soliton depth n_s and the initial soliton speed $\dot{q}(t = 0)$ directly obtained from the absorption images as described in more detail later. Since oscillation frequencies can be determined with very high accuracy the observation of a soliton oscillation should provide an unambiguous test of the theoretical prediction and a confirmation of this paradigm of particle-wave dualism: A matter wave composed out of microscopic particles behaves like a mesoscopic classical particle again. The above results have been obtained in strictly one dimensional systems at zero temperature. Few theoretical work addressed configurations where the criterion for being one-dimensional is not strictly fulfilled [196] and found slight deviations towards *higher* values for the expected oscillation frequency.

6.1.3 Dark-bright solitons in multi-component condensates

In multi-component Bose-Einstein condensates the possibility of establishing *vectorial* solitons exists: A dark soliton in one component of the BEC hereafter denoted by ψ_d may be "filled" with a bright soliton being composed out of atoms in another component ψ_b. The bright soliton is trapped in the co-propagating dark soliton and is stable despite of the *defocusing* properties of the non-linear medium. In the context of this thesis the two components are represented by two different hyperfine states of ^{87}Rb namely $|1, 0\rangle$ and $|2, 0\rangle$. States which are not liable to the linear Zeeman effect have been chosen to avoid any disturbance of the preparation process or the dynamics by residual magnetic stray fields. The dimensionless coupled GPE for this particular system read [39]

$$i\dot{\psi}_\mathrm{d} = -\frac{1}{2}\psi''_\mathrm{d} + \left(V_\mathrm{d} + |\psi_\mathrm{d}|^2 + g_\mathrm{d}|\psi_\mathrm{b}|^2 - \mu\right)\psi_\mathrm{d} \tag{6.11}$$

$$i\dot{\psi}_\mathrm{b} = -\frac{1}{2}\psi''_\mathrm{b} + \left(V_\mathrm{b} + |\psi_\mathrm{b}|^2 + g_\mathrm{b}|\psi_\mathrm{d}|^2 - \mu - \Delta\right)\psi_\mathrm{b}. \tag{6.12}$$

where ψ_d and ψ_b are the wave function of the dark and bright component respectively, the V_i being external potentials and $\mu_\mathrm{b} = \mu$ and $\mu_\mathrm{d} = \mu + \Delta$ are the chemical potentials. The intra-species interaction parameters g_{ii} are normalized to unity, whereas the inter-species interaction parameters g_{ij} are very close to unity in the case of ^{87}Rb . The corresponding soliton solutions can be written as

$$\psi_\mathrm{d}(z, t) = i\sqrt{n_{1\mathrm{D}}}\sin\alpha + \sqrt{n_{1\mathrm{D}}}\cos\alpha\tanh\{\kappa(z - q(t))\} \tag{6.13}$$

$$\psi_\mathrm{b}(z, t) = \sqrt{\frac{N'_\mathrm{b}\kappa}{2}}\, e^{i\phi}\, e^{i\Omega_\mathrm{b}t}\, e^{i\,z\kappa\tan\alpha}\,\mathrm{sech}\{\kappa(z - q(t))\}. \tag{6.14}$$

N'_b is the rescaled number of particles in the bright component. The phase factor in ψ_b is relevant only for collisions of two or more dark-bright solitons which are only covered qualitatively. $\kappa = \sqrt{n_{1\mathrm{D}}\cos^2\alpha + (N'_\mathrm{b}/4)^2} - N'_\mathrm{b}/4$ is the inverse length of the dark-bright soliton which is clearly expanded by the Thomas-Fermi-like repulsion of the bright component as compared to the unperturbed dark soliton (see Fig. 6.2). Rewriting this expression in SI units yields

$$\kappa\,\bar{\xi} = \sqrt{\cos^2\alpha + \left(\frac{N_\mathrm{b}}{4n_{1\mathrm{D}}\,\bar{\xi}}\right)^2} - \frac{N_\mathrm{b}}{4n_{1\mathrm{D}}\,\bar{\xi}}. \tag{6.15}$$

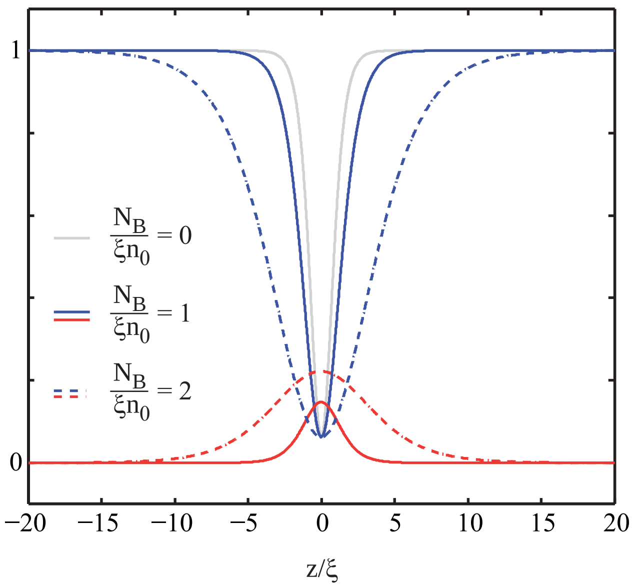

Figure 6.2: Density distribution of dark-bright solitons for different filling factors $N_\mathrm{B}/(n_0\bar{\xi})$ and $\cos(\alpha) = 0.25$. The density of $|1,0\rangle$ is plotted in blue whereas the red curves depict the density of $|2,0\rangle$. A dark soliton ($N_\mathrm{B} = 0$) is plotted for comparison in light blue. Note that length is given in units of the healing length $\bar{\xi}$.

For the experimental parameters of the dark-bright soliton experiments we obtain $\kappa^{-1} = 6.7\,\mu$m from the above expression. The velocity of the dark-bright soliton is given by an expression formally identical to that of a dark soliton.

$$\dot{q} = \frac{\hbar\kappa}{m}\tan(\alpha) \tag{6.16}$$

The frequency shift of the bright relative to the dark soliton is given by

$$\hbar\Omega = \frac{\hbar^2\kappa^2}{2m}(1 - \tan^2\alpha) - \Delta \tag{6.17}$$

and is composed out of the excess kinetic energy of the dark soliton $E_\mathrm{d}^\mathrm{kin} = \hbar^2\kappa^2/2m\,\tan^2\alpha$, the binding energy of the bright soliton in the well formed by the dark soliton $E_\mathrm{b}^\mathrm{pot} = -\hbar^2\kappa^2/2m$ and the difference in the two chemical potentials $\mu_\mathrm{b} - \mu_\mathrm{d} = \Delta$.

Equation of motion for a dark-bright soliton

Following [39] the equation of motion of a dark bright soliton can be derived from the free energy of the dark-bright soliton and reads

$$m\ddot{q}(t) = -\frac{1}{2}\frac{\partial V_d(z)}{\partial z} - \frac{1}{2}\frac{1}{\sqrt{1+\left(\frac{4\bar{\xi}n_{1\mathrm{D},0}}{N_\mathrm{b}}\right)^2}}\frac{\partial(V_d(z) - 2V_b(z))}{\partial z}, \tag{6.18}$$

where $V_{d,b}(z)$ denote the external potential felt by the individual components. If the particle number in the bright component is large enough $N_\mathrm{b} \gg 4\bar{\xi}n_{1\mathrm{D},0}$ this equation can be simplified to

$$m\ddot{q}(t) = -\frac{1}{4}\left(\frac{4\bar{\xi}n_{1\mathrm{D},0}}{N_\mathrm{b}}\right)^2\frac{\partial V_d(z)}{\partial z} + \left(1 - \frac{1}{2}\left(\frac{4\bar{\xi}n_{1\mathrm{D},0}}{N_\mathrm{b}}\right)^2\right)\frac{\partial(V_b(z) - V_d(z))}{\partial z}. \tag{6.19}$$

For the present experiments the difference in the dipole potentials for the individual hyperfine states $(V_b - V_d)/V_d$ is exceedingly small so that the second term in Equ. 6.19 can

safely be neglected for typical values of $4\bar{\xi}n_{1\mathrm{D},0}/N_{\mathrm{b}}$.
The resulting equation of motion

$$m\ddot{q}(t) = -\frac{1}{4}\left(\frac{4\bar{\xi}n_{1\mathrm{D},0}}{N_{\mathrm{b}}}\right)^2 \frac{\partial V_d(z)}{\partial z} \tag{6.20}$$

is solved by an oscillatory behavior of $q(t)$ with a frequency given by

$$\Omega_{\mathrm{DB}} = \frac{\omega_z}{2}\,\alpha(Z)\,\frac{4\bar{\xi}n_{1\mathrm{D},0}}{N_{\mathrm{b}}}. \tag{6.21}$$

$\alpha(Z)$ is an amplitude dependent factor that can easily be determined numerically for a particular choice of $V_d(z)$. Note that even for a harmonic trapping potential α depends on the oscillation amplitude and renders Equ. 6.21 a non-linear equation of motion. It can be seen that for large particle numbers in the bright component $N_{\mathrm{b}} \gg 4\bar{\xi}n_{1\mathrm{D},0}$ the motion of the dark-bright soliton is drastically slowed down as compared to a dark soliton.

6.1.4 Stability of solitons in Bose-Einstein condensates

The stability of solitons and especially dark solitons in Bose-Einstein condensates strongly depends on the dimensionality and the temperature of the system. In the past decade the theoretical effort to explore the stability of dark solitons in BEC has been tremendous Dimensional [33, 34, 35, 36, 37] as well as thermodynamic [34, 37, 38, 32] stability analysis has been performed.

Strictly speaking a dark soliton is only stable in pure 1D BEC without any small-scale fluctuations of the non-linear interaction. However as long as the available energy in the Bose-Einstein condensate $\mu = g_0 n_0$ is much smaller than the energy associated with transverse trapping $\hbar\omega_\perp$ *no* transverse modes can be excited and the condensate remains in its transverse ground state for all times. In this case the BEC can be treated as being quasi one-dimensional and solitons should be perfectly stable at zero temperature. If the above restriction is relaxed, the transversely varying density leads to a speed of sound that depends on the transverse coordinate. As a result the nodal plane of the soliton will start to bend and eventually decay into vortex-antivortex pairs [37, 36], a process known as *transverse dynamical instability* or *snake instability* which has been observed in [12, 21]. The time-scale for this decay has been found to be on the order of the inverse of the transverse trapping frequency $\omega_\perp$ [37]. These authors report moreover that *black* solitons are stable in Bose-Einstein condensates where $g_0 n_0/\hbar\omega_\perp \lesssim 2.5$.

In the context of a transversely varying density the condition of being one-dimensional can be reformulated as the requirement that the soliton length be much larger than the transverse extension of the condensate: the wavelength of transverse excitations destabilizing the soliton must be larger than the soliton width in order to have a recognizable effect [37]. For tight transverse trapping the transverse extension of the condensate is approximately given by the harmonic oscillator ground state leading to the expression $a_{\mathrm{HO}}/2\bar{\xi} \ll 1$ as the criterion for dynamical stability. As soon as the above parameter exceeds unity transverse instabilities arise and lead to a fast decay of the soliton. Note that faster solitons have a larger width according to Equ. 6.6 and are therefor stable in less restricted geometries as compared to deep and slow solitons. Especially dark-bright solitons which are broadened to many healing lengths in the case of large filling should hence be much less susceptible to transverse instability and exhibit drastically longer lifetimes [39].

Solitons are collectively excited states of the condensate which means that their energy is always larger than that of the corresponding ground state condensate without a soliton. Since solitons do not carry any topological charge they can in principle be transferred to the ground state by any kind of dissipative processes as opposed to vortices where the topological charge prohibits dissipation and drastically increases the lifetime. At finite temperature a soliton can interact with excitations in the thermal cloud [35, 37, 34]. The energy transfer mediated by those scattering events can be regarded as a friction force that leads to an acceleration of the dark soliton owing to its *negative* kinetic energy (see Equ. 6.9). The soliton will ultimately be accelerated until it approaches the speed of sound, where it disappears. The timescale for this decay to take place does depend on temperature in a very delicate fashion ($\tau \sim T^{-4}$ [34]), so that long soliton lifetimes should be an unambiguous indication for very low temperatures. An alternative picture for dissipative dynamics of dark solitons in trapped BEC can be drawn invoking the physical process of sound emission by a soliton [38, 32]. A moving soliton emits sound that will be reabsorbed when the soliton is trapped in a harmonic potential. This periodic energy exchange between phonons and soliton is however disturbed when thermal atoms interact dissipatively with sound modes. The loss of energy leads to an acceleration of the soliton which will finally disappear.

6.1.5 Collisions of solitons

The collisions of solitons are in the focus of interest since the first numerical simulations of the Korteweg-deVries equation fifty years ago had shown that solitons emerge from collisions with one another without any change in shape thus retaining their identities far away from the collision vertex [15]. The only effect of the interaction being a small shift in the space-time trajectories of the individual solitons [15, 194]. It has to be emphasized that the presence of two soliton-like structures within a finite nonlinear system is highly nontrivial, since in general a superposition of two solutions does *not* constitute a solution itself. While the interaction of bright solitons depends on their relative phase and is attractive for $\Delta\phi = 0$ and repulsive for $\Delta\phi = \pi$ dark solitons are believed to *always* repel each other [197, 198]. This has explicitly been demonstrated experimentally for solitons in non-linear optical media in the temporal [199] as well as in the spatial domain [200]. It is only in non-local non-linear media that the interaction can even be tuned to attraction [197].

Numerical simulations [15, 201] and analytic calculations [202, 203, 204] have shown a positive shift after the collision. This can be understood qualitatively by the following considerations: when the solitons approach each other the residual density decreases which reduces the velocity of the individual solitons and thus leads to a *positive* shift of the space-time trajectory which is regarded as mutual repulsion by the authors of [203].

These authors further describe two different regimes for the head-on collision of two dark solitons.

Gray collisions are realized if the combined amplitude of the two solitons never exceeds the available density during the collision. The phase gradients of the two solitons, pointing in opposite directions, simply add up whilst the interaction and far away from the collision vortex the only measurable effect is a shift in the space-time trajectories.

Black collisions are distinguished by a vanishing density at some instant of the collision. The individual density minima "touch the ground" at some point and do not move anymore. Simultaneously the phase gradients steepen more and more and flip from π to $-\pi$ or vise versa depending on the direction of propagation. After a certain (short) time the available phase slip is redistributed among the solitons and they start to move again. Although it looks as if the solitons had never passed through each other, they retain their identity asymptotically far away from the collision point and it appears as if they had passed through each other only inducing tiny shifts in the individual space-time trajectories.

The above findings could also be identified by a detailed investigation of the results of simulations addressing the head-on collisions of two dark solitons, performed in our group [201].

6.2 Generation of solitons in a BEC

The engineering of soliton states in elongated Bose-Einstein condensates at the Hamburg spinor experiment has been achieved employing an optical phase imprinting method that has already been applied successfully in few former experiments [134, 11, 12]. Other methods to generate dark solitons in BEC by combined phase and density engineering which would yield a modified condensate closer to the soliton solution have been proposed [205, 204], but have not been considered here. The authors of [206] generated dark solitons by sweeping a penetrable barrier through a Bose-Einstein condensate but could not achieve the generation of single well-controlled solitons. In the MIT group solitons were produced by merging two BEC on an atom chip [207]. However this method of soliton generation does not seem feasible to control individual solitons either. Experimental ease and reproducibility distinguish the phase imprinting method and make it the method of choice at our experiment.
The generation of dark-bright solitons at our experiment has been achieved using a spatially selective Raman-Rabi oscillation technique developed in our group. At JILA dark-bright solitons in a spherical trap and their decay has been investigated [21]. Here dark-bright solitons had been produced by a microwave transfer between two hyperfine states tuned to resonance by a spatially varying dipole potential generated via a scanned laser focus.

The experiments attending to solitons presented here rely on a versatile Raman-laser system used in conjunction with a high resolution SLM set up, both described in Chapter 3. This section provides an overview how quasi-one dimensional condensates are produced and what their characteristic parameters are. More importantly the experimental procedures necessary to prepare dark and dark-bright solitons will be presented.

6.2.1 Engineering of super cold elongated BEC

The experiments on dark and dark-bright solitons presented in the following have been performed in the elongated crossed dipole trap (EXDT) introduced in Section 3.2. Recalling the trapping frequencies $\omega_{x,y,z} = 2\pi \times (85, 133, 5.9)\,\mathrm{rad\,s^{-1}}$ one obtains an aspect ratio of approximately 20 .[4] The atoms residing in state $|1, -1\rangle$ are loaded into the EXDT and

[4] In Section 3.2 the symmetry axis of the experiment has been termed "x-axis" and the direction of gravity "z-axis". In this chapter however the "z-axis" is the symmetry axis, while the x- and y-direction

evaporated over 16 s by lowering the optical power of the trap using a bipartite linear ramp. We reduce the power of the trap as much as possible to achieve the lowest temperatures in our condensates. We have searched for signatures of phase fluctuations as an indication of finite temperature effects and have optimized the loading procedure to suppress them as much as possible. Finally no visible signs of finite temperature were observed in our experiments. Neither a detectable thermal cloud nor interference effects caused by phase fluctuations after long time-of-flight could be monitored. Note that the low trap depths provides a powerful continuous evaporation throughout the whole experimental sequence: all atoms that gain a certain amount of energy due to any heating processes are immediately spilled out of the trap. This leads to a small additional atom loss but ensures very low temperatures. Anyway, the $1/e$ lifetimes of our condensates exceed 10 s easily, which is sufficient for all experiments presented here.
Typical atom numbers for the soliton experiments are in the range of $4-7\cdot 10^4$ resulting in peak densities on the order of $n_0 = 5-6\cdot 10^{13}\,\mathrm{cm}^{-3}$. The one-dimensional speed of sound and healing length in those BEC read $\bar{c}_s \simeq 1\,\mathrm{mm/s}$ and $\bar{\xi} \simeq 0.8\,\mu\mathrm{m}$ respectively. The chemical potential for typical experimental parameters as given above can be calculated to be $\mu = k_\mathrm{B}\cdot 20\,\mathrm{nK}$.

6.2.2 Generating dark solitons

Since a dark soliton is characterized by a certain phase slip according to Equ. 6.6 it is obvious to try and generate a dark soliton by imprinting a phase slip across a region of the BEC that is on the order of the healing length $\bar{\xi}$. For typical experimental parameters the healing length takes values of $\bar{\xi} \simeq 700-800\,\mathrm{nm}$ which poses a serious challenge for the imaging system employed for the phase imprinting process. We use a moderately detuned laser beam ($8\,\mathrm{GHz} \leq \Delta \leq 30\,\mathrm{GHz}$) and image a sharp edge generated with the SLM onto the BEC using a high resolution optical system. The unmasked part of the condensate will be subject to a phase evolution caused by the dipole potential of the laser beam (see Equ. 3.6) according to

$$\psi(z,t) = \psi(z,0)\, e^{-i/\hbar\, U_\mathrm{dip}(z)\, t_\mathrm{pulse}}. \tag{6.22}$$

If the pulse time t_pulse is chosen appropriately a phase difference of $\phi = U_\mathrm{dip}(z)/\hbar\; t_\mathrm{pulse} \approx \pi$ is imprinted. To avoid a simultaneous disturbance of the local density, the pulse time has to be short compared to the correlation time of the condensate $\tau_\mathrm{corr} = \bar{\xi}/\bar{c}_s = 700\,\mu\mathrm{s}$. For the experiments presented in this thesis $t_\mathrm{pulse} = 40\,\mu\mathrm{s}$ has been chosen. The theoretically expected laser intensity required to generate a phase slip of π during this time is $I \approx 1\,\mathrm{mW/cm^2}$ when employing π-polarized light. We expand the phase imprinting beam to a diameter of $d \approx 2\,\mathrm{cm}$. The maximum available laser power amounts to $4-5\,\mathrm{mW}$ behind the optical fiber which results in an intensity of $I = 1-2\,\mathrm{mW/cm^2}$ in qualitative agreement with the theoretical value.

By employing SLM structures with an arbitrary number of steps a corresponding number of solitons can be generated. Choosing a more gradually shaped edge results in a shallower and faster soliton as compared to an edge as steep and sharp as possible. As will be explained in more detail in the corresponding section, the investigation of collisions of solitons are based on preparation schemes relying on the above mentioned extended experimental possibilities that are provided by our high resolution SLM system. Moreover the integrated Rabi frequency of the preparation pulse can be varied to alter the initial

are frozen out due to the tight transverse confinement.

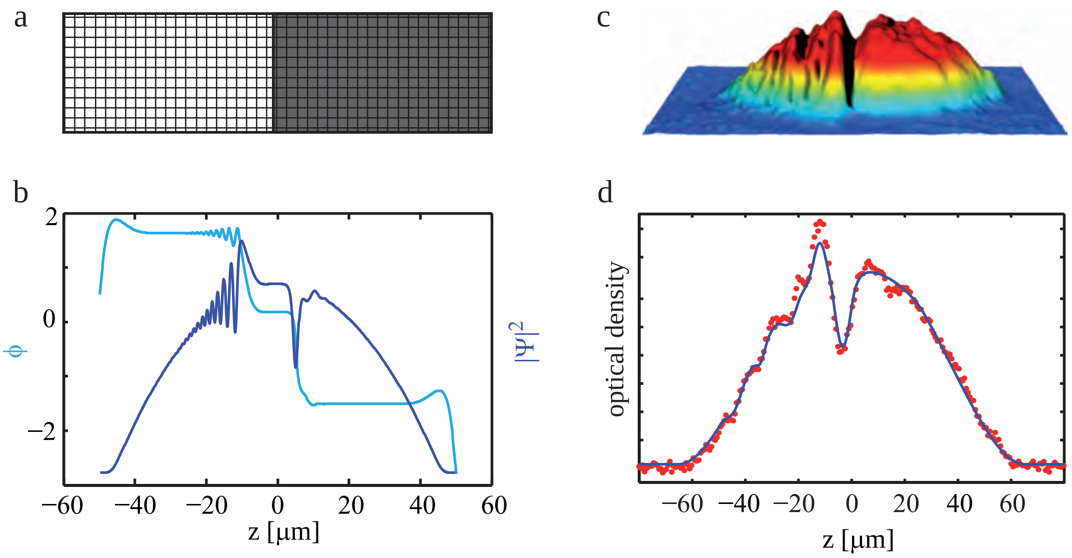

Figure 6.3: Generation of dark solitons employing the phase imprinting method.
(a) Simple sharp edge generated with a SLM which is imaged onto the BEC.
(b) Simulation of the phase imprinting process. Density (blue) and phase (light blue) of the BEC are shown 5 ms after the imprinting. The dark soliton propagating to the right and the density wave propagating in the opposite direction can clearly be identified (taken from [201]).
(c) Absorption image of a BEC 3 ms after phase imprinting.
(d) Column sum of (c) together with a fit to the data points. Soliton and density wave show a remarkable agreement with the results of the simulations in (b).

phase slip, which also influences the soliton parameters as well as the number of solitons [204].

The imprinted phase gradient will lead to a certain *local* velocity field given by $v_{\rm SF} = \hbar/m\,\partial_z\phi$ [204] that has been mapped directly using Bragg spectroscopy [137]. As already mentioned a dark soliton can be regarded as a hole rather than a particle and hence moves in the direction opposite to the superfluid flow of the condensate. Hence dark solitons generated by the phase imprinting method using red detuned light will always propagate towards the non-illuminated part of the condensate. An advantage of the choice of red detuning is that the identification of the dark soliton is not hindered by any other possible structures which might be generated by the illumination of the condensate .[5] The velocity field can also be interpreted as a local potential gradient transferring momentum to the condensate thus assisting the formation of a density minimum. The timescale for the formation of the dark soliton is given by $\tau_{\rm DS} \approx \tau_{\rm corr}\, l_e/\bar{\xi}$. The size of the imprinted edge l_e plays a dominant role not only for the time needed to form the soliton but also for the maximum depth that can be achieved by the phase-imprinting method [204]. The authors of [204] have performed numerical simulations of the 1D GPE which show that it is not possible to generate a perfect dark soliton employing the phase imprinting method. A significant portion of the phase gradient ($\sim \phi/2$) will always be carried away by a density wave – characterized by an increased density – in the direction opposite to the dark

[5] A possible origin of such additional structure of the condensate might be phase fluctuations owing to an inhomogeneous illumination of the condensate. After time-of-flight those phase fluctuations will evolve into density modulations that could possibly be confused with a dark soliton.

soliton. This density wave propagates approximately at the speed of sound $\bar{c}_s$. Due to repulsive interaction and dispersion the density wave will be damped quickly. The dark soliton on the other hand self-stabilizes and propagates without any further decay in the ideal case of strict one-dimensionality and zero temperature. Imprinting phase slips larger than π will eventually lead to slightly deeper solitons and moreover to the emergence of multiple solitons. All of these results have been confirmed by simulations of the 1D GPE using the *split operator method* performed in our group by E.-M. Richter [201].
We have chosen the pulse length to generate dark solitons as slow and therefor deep and stable as possible. Fig. 6.3(c) shows a BEC 3 ms after the phase imprinting pulse. The dark soliton is easily recognized as a deep and form stable local minimum in the condensate density. The accompanying density wave is also clearly visible shortly after the preparation. For larger evolution times the density wave is quickly damped and disappears after approximately 50 ms in typical experiments. The particular phase slip employed for the dark soliton experiments presented later seems to be larger than π since comparison to simulations suggest that the soliton depths we measure are not compatible with $\phi \leq \pi$. This suggestion is further supported by the emergence of a second smaller soliton that propagates ahead of the deep primary soliton because of its larger velocity .[6]

6.2.3 Filling the notch: creation of dark-bright solitons

The generation of dark-bright solitons is a little bit more tricky than just imprinting a phase slip across a Bose-Einstein condensate. The crucial ingredient for the generation of those multi-component structures is the ability to transfer population in between two different internal states *spatially resolved.* The Raman-laser system together with the SLM set up introduced in Chapter 3 represent ideal tools for such a local population transfer. The experimental protocol we have employed to generate dark-bright solitons relies on the fact that during a Rabi-oscillation the *population* ($|\psi|^2$) oscillates at twice the frequency of the wave function (ψ). In other words, during a full 2π-cycle of population oscillation, the wave function acquires a phase of π. Mathematically the preparation process is described by the Hamiltonian

$$\mathbf{H}_{\text{prep}} = \frac{\hbar}{2} \begin{pmatrix} \frac{1}{2}\sum_i \frac{\Omega^2_{\text{d},\,i}}{\Delta_i} & \Omega \\ -\Omega & \frac{1}{2}\sum_i \frac{\Omega^2_{\text{b},\,i}}{\Delta_i} \end{pmatrix} \tag{6.23}$$

The off-diagonal elements lead to a population oscillation between the two involved states $\psi_{\text{d}} = |1, 0\rangle$ and $\psi_{\text{b}} = |2, 0\rangle$ at the frequency $\Omega = \Omega_1\Omega_2/2\Delta$ (see Section 3.5.2). The effect of the diagonal elements can be divided into to main effects:

Differential light shift The light shift produced by the involved laser beams is different for the two involved states. This is due to the different detunings of the two lasers with respect to the two hyperfine states. Note that the different number of available excited states as well as the difference in the Clebsch-Gordon coefficients are exactly canceled due to symmetry reasons [109] and do *not* lead to a differential light shift. As a consequence the resonance frequency is shifted away from the bare hyperfine splitting. As already stated in Chapter 3 this shift is typically on the order of 10 kHz in our experiments.

[6] The phase difference between the two parts of the condensate could have been determined using matter wave interferometer schemes as introduced in Chapter 3. This has been done by the authors of [12] who found that phase slips of $\phi \approx 1.5\,\pi$ lead to the best results concerning soliton depth and stability.

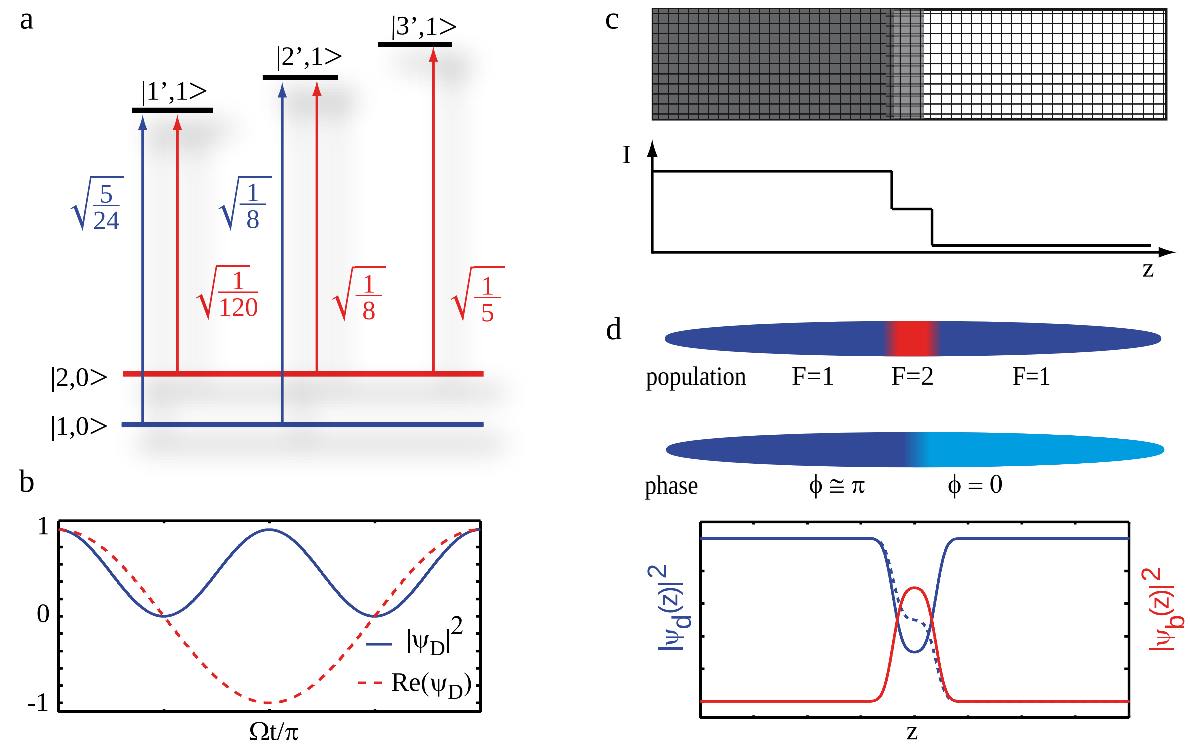

Figure 6.4: Basic principle of the generation of dark-bright solitons.
(a) Λ-system for the two-photon Raman transition connecting the two hyperfine ground states $|1,0\rangle$ and $|2,0\rangle$.
(b) Schematic representation of the population $|\psi|^2$ (full line) and the wave function $\psi = \sqrt{n} \cdot \exp i\phi$ (dashed line) of the dark component during a Rabi cycle.
(c) The pattern generated on the SLM consists of an edge with an intermediate step corresponding to *half* the maximum intensity I_0. The width of the intermediate step is typically chosen to be on the order of $10 - 15\,\text{px} \simeq 6 - 9\,\mu\text{m}$.
(d) Density (full line) and phase distribution (dashed line) after the application of a 2π Rabi-Raman pulse. The SLM pattern has been convoluted with an Airy-disc corresponding to the optical resolution. While the population in the fully exposed part of the condensate doesn't change effectively a phase-slip of π is acquired in the dark component $|1,0\rangle$. At the position of the intermediate step an effective π-pulse transferred the population to the upper hyperfine state $|2,0\rangle$.

Phase evolution Since the number of available excited states for *single* photon processes is larger than the corresponding number of excited states involved in the Λ-process an additional phase evolution owing to the coupling to these states occurs. This is mainly important for the dark component where the overall phase slip determines the parameters of the resulting dark soliton. By changing the Rabi frequencies of the individual Raman beams Ω_1 and Ω_2 independently but keeping the product $\sqrt{\Omega_1 \Omega_2}$ constant the phase slip can be varied without changing the number of atoms in the bright component.

In [208] the temporal evolution of a two component BEC irradiated by two Raman laser beams in the context of soliton generation is analyzed in detail. Including mean-field interaction effects the full Hamiltonian of the two-component BEC is solved. However for our purposes it is sufficient to understand the single atom Hamiltonian Equ. 6.23 qualitatively

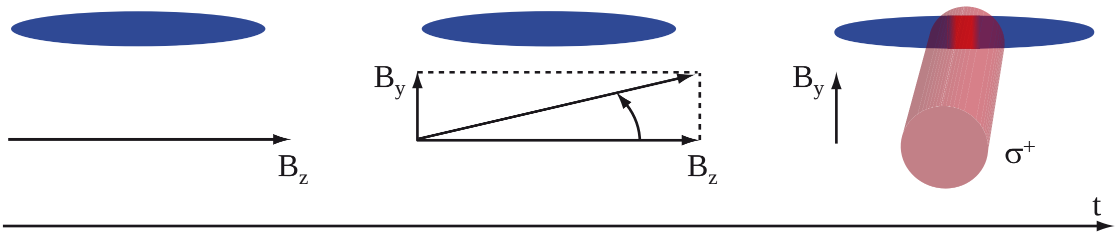

Figure 6.5: Rotation of the quantization axis. In order to obtain a non-zero Raman coupling between $|1,0\rangle$ and $|2,0\rangle$ the quantization axis has to be rotated by 90° into the direction of the Raman beams prior to the application of the Raman pulse (See text for more details.).

in order to find suitable values for the relevant experimental parameters.
The Raman coupling of the two specific ^{87}Rb hyperfine ground states $|1,0\rangle$ and $|2,0\rangle$ is afflicted with some difficulties. π-polarized light cannot be employed owing to the lack of shared excited states. Light which is linearly polarized perpendicular to the quantization axis can be decomposed into equal portions of σ^+ and σ^- polarized light. In this case the individual paths interfere destructively and no Raman coupling occurs. The same is true for any combination of the above cases. In order to achieve a non-zero coupling the quantization axis has to be rotated in the direction of propagation of the two Raman beams prior to the application of the Raman pulse (see Fig. 6.5). Moreover a quarter wave plate is inserted in the optical path between the last beam splitter cube and the imaging optics to obtain pure σ^+-polarization. Two non-vanishing contributions to the Raman transfer remain in this way, $|1,0\rangle \leftrightarrow |1',1\rangle \leftrightarrow |2,0\rangle$ and $|1,0\rangle \leftrightarrow |2',1\rangle \leftrightarrow |2,0\rangle$, where the latter is three times stronger. The resulting two-photon Rabi frequencies obtained in this particular experimental geometry are on the order of $10-25\,$kHz. The highest values are achieved for near optimum adjustment of Raman-laser system, imaging optics and SLM optics. For all measurements concerning dark-bright solitons presented in this thesis a 2π-Raman-Rabi preparation pulse of $40\,\mu$s duration has been employed.

The particular method we have employed to generate dark-bright solitons is based on imaging of a step-like pattern depicted in Fig. 6.4 onto the BEC. We apply a 2π Raman pulse to one half of the condensate which leaves the population effectively unchanged but leads to a phase difference of π as compared to the masked part of the condensate. In a small region around the edge of the mask $l \approx \bar{\xi}$ only half the maximum intensity is felt by the atoms resulting in a transfer of atoms to $|2,0\rangle$. In practice the portion of transferred atoms can be controlled by employing a step-like pattern rather than a simple edge. The size of the intermediate step is typically chosen to be on the order of $8-10\,\mu$m. By varying the width of the step the number of particles transferred to the bright component can be adjusted. It can be seen from Fig. 6.16 that indeed a dark-bright vector soliton emerges from this preparation process. Note that the depth of the dark-bright soliton is given by the parameter α introduced in Section 6.1.3 and is basically not affected by the number of atoms in the bright component, which modifies only the width and speed of the vector soliton. The shape and magnitude of the phase slip determine the depth of the dark-bright soliton just as for a unperturbed dark soliton. However the underlying preparation method does not allow to vary shape and magnitude of the phase step and bright component particle number totally independent from each other: The wider the step, the shallower the phase gradient which makes the dark soliton shallower and less visible. The parameters employed for the experiments presented here correspond to the deepest and most long-lived vector solitons that we were able to produce.

6.3 Oscillations and collisions of dark solitons

Up to date few experiments have produced dark solitons [11, 12, 21] in Bose-Einstein condensates which were all prone to dimensional as well as thermodynamic instabilities. While experiments in geometries close to spherical observed a bending of the soliton plane [12] and eventually the decay into vortex-antivortex pairs [21] experiments in more elongated geometries suffered from too high temperatures [11] and were consequently not able to conduct more elaborate experiments such as the observation of oscillations or collisions of dark solitons. In the framework of this thesis dark solitons with unrivaled lifetimes could be produced in ultracold BEC. We have been able to track the oscillation of a dark soliton in a trapped BEC for the very first time and moreover studied the collision of two dark solitons. During the writing of this thesis the Heidelberg group was able to produce long lived solitons and observed oscillations of dark solitons and modifications of these oscillations by interactions of two dark solitons and dimensionality effects [40]. Preceding the section describing the experimental results, two short paragraphs on data analysis and the dynamics of the envelope of the condensate, crucial to normalize the data, are presented.

6.3.1 Extraction of soliton parameters from TOF images

The experimental data presented in this chapter has been obtained from time-of-flight images. After the generation of the solitons and a variable evolution time, the trapping potentials have been switched off and the atomic cloud was allowed to freely expand for a time of 11.5 ms. The soliton size $l_s \approx \bar{\xi} \approx 0.8\,\mu$m in the trap is beyond optical resolution and thus a sufficiently long time-of-flight is indispensable to obtain reliable and clear results for the soliton parameters that are extracted by fitting a model density distribution to the images as described in the following.
For the detection of dark-bright solitons the double exposure method introduced in Section 3.3 has been employed to image both components in one single shot. Recall that the maximum optical density in the dark-bright images is limited to one half inherent to this particular detection method, which lowers the quality of the images as compared to single exposure images used for the dark soliton experiments. However the correlation between the dark and bright component can be directly determined in this way and allows for an unambiguous interpretation of the data.

Data fitting

The program used to analyze the soliton images has been created in the framework of S. Dörschers Diploma thesis [188] and constitutes a powerful tool to quickly obtain all information desired from the experimental data. To extract the parameters of the solitons from TOF images we have fitted a two-dimensional model function to the data, composed out of an envelope function and several modulations to account for solitons, density waves

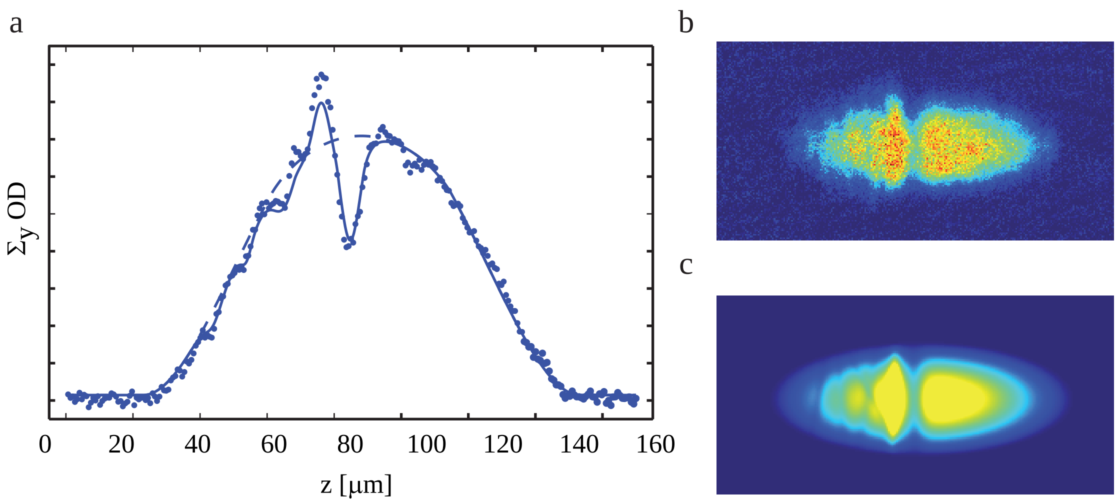

Figure 6.6: Exemplary fit to the data for dark soliton experiments.
(a) Column sum of the optical density together with the resulting fit function Equ. 6.24. The dashed curve is the envelope according to Equ. 6.26.
(b) Absorption image
(c) Two-dimensional plot of Equ. 6.24 fitted to the data in (a).

---

or other excitations:

$$n_d(y,z) = n_E(y,z) \cdot \left[1 + \sum_{i=1}^{K_d} \sigma_i^{(d)}\, h_i^{(d)}\, \mathrm{sech}^2\left(\frac{z - z_{0,i}^{(d)}}{w_i^{(d)}}\right)\right] \tag{6.24}$$

$$n_b(y,z) = n_E(y + \Delta y_E, z) \cdot \left[\sum_{i=1}^{K_b} \sigma_i^{(b)}\, h_i^{(b)}\, \mathrm{sech}^2\left(\frac{z - z_{0,i}^{(b)}}{w_i^{(b)}}\right)\right], \tag{6.25}$$

where $K_{d,b}$ is the number of structures in every component, $\sigma_i^{(d,b)} = \pm 1$, $h_i^{(d,b)}$, $w_i^{(d,b)}$ and $z_{0,i}^{(d,b)}$ are the sign, amplitude, width and position of the individual dips and peaks. The envelope of the BEC in the Thomas-Fermi approximation integrated along the line of sight is given by

$$n_E(y,z) = n_0 \left(1 - \left(\frac{y - y_E}{R_y}\right)^2 - \left(\frac{z - z_E}{R_z}\right)^2\right)^{3/2}. \tag{6.26}$$

n_0 is the central density, y_E, z_E denote the position of the envelope while the R_i give the Thomas-Fermi radii along the corresponding direction. Alternatively the fit is allowed to account for a cut-off in the optical density which enhances the quality of the results especially for the amplitude of the dark solitons $h_i^{(d)}$ and the central density n_0 of the envelope. However the cut-off value is best determined directly from the absorption images and than set as a constant to optimize the fitting routine. As an additional computational option the soliton plane can be allowed to enclose an arbitrary angle with the long axis of the condensate. However most of the data sets have been fitted with the angle of the soliton plane fixed and perpendicular to that axis. The dark soliton has been chosen per hand for the space-time plots as the most prominent density depression among the fitted structures. Examples of fits in the case of purely dark solitons and dark-bright solitons

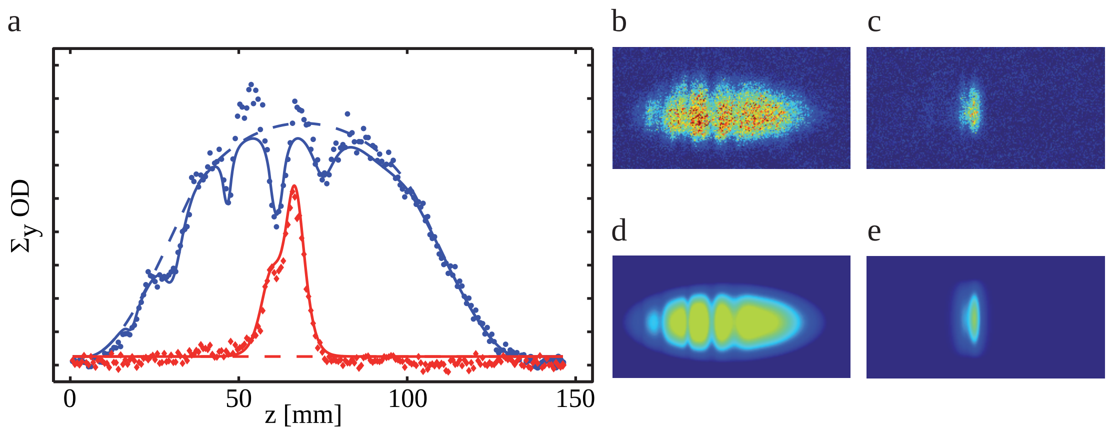

Figure 6.7: Exemplary fit to the data for dark soliton experiments.
(a) Column sum of the optical density of the dark (blue) and bright (red) component together with the resulting fit function Equ. 6.24 and Equ. 6.25. The dashed curve is the envelope according to Equ. 6.26.
(b,c) Absorption images of the dark and bright component
(d,e) Two-dimensional plot of Equ. 6.24 and Equ. 6.25 fitted to the data in (b) and (c) respectively.

---

are given in Fig. 6.6 and Fig. 6.7 respectively. More details concerning data analysis of the soliton experiments can be found in S. Dörschers Diploma thesis [188].

Envelope of the condensate

By imprinting a phase or transferring population by the aforementioned preparation methods does not only generate soliton structures but also drives several other excitations of the condensate. The most prominent examples being small amplitude dipole oscillation of the whole condensate as well as the *breathing mode* quadrupole oscillation of the shape of the condensate (see Fig. 6.8). We have determined the dipole and quadrupole oscillation parameters to normalize the soliton position the the center of mass of the condensate and to the width of the envelope $z \to (z - z_0)/2R_z$. Checking the frequencies provides a nice consistency check of the obtained condensate parameters and trapping frequencies. As found in [27] the motion of the center of mass of the condensate and the propagation of the soliton should basically decouple and not influence each other. The influence of the quadrupole oscillation leading to an oscillatory modulation of the density and therefor the soliton parameters is unclear and has thus far not been considered theoretically to our knowledge. Normalizing the soliton position to the instantaneous width of the condensate gives however reasonable results and has thus been performed without a rigid theoretical justification.
The observed trapping frequencies for the dark and dark-bright experiments read $\omega_z = 2\pi \cdot (6.8 \pm 0.5)\,\mathrm{s}^{-1}$ and $\omega_z = 2\pi \cdot (6.6 \pm 0.3)\,\mathrm{s}^{-1}$ respectively. This is contradicted by an independent measurement of the axial trapping frequency for the same experimental parameters yielding $\omega_z = 2\pi \cdot (5.86 \pm 0.02)\,\mathrm{s}^{-1}$. It remains unclear whether this inconsistency is due to slightly different experimental parameters or if the presence of a whole variety of excitations leads to a slight modification of the oscillation frequency. The frequencies of the observed quadrupole oscillations $\omega_{QP}^{\mathrm{d}} = 2\pi \cdot (10.8 \pm 0.1)\,\mathrm{s}^{-1}$ and $\omega_{QP}^{\mathrm{db}} = 2\pi \cdot (10.4 \pm 0.1)\,\mathrm{s}^{-1}$ on the other hand are in excellent agreement with the the-

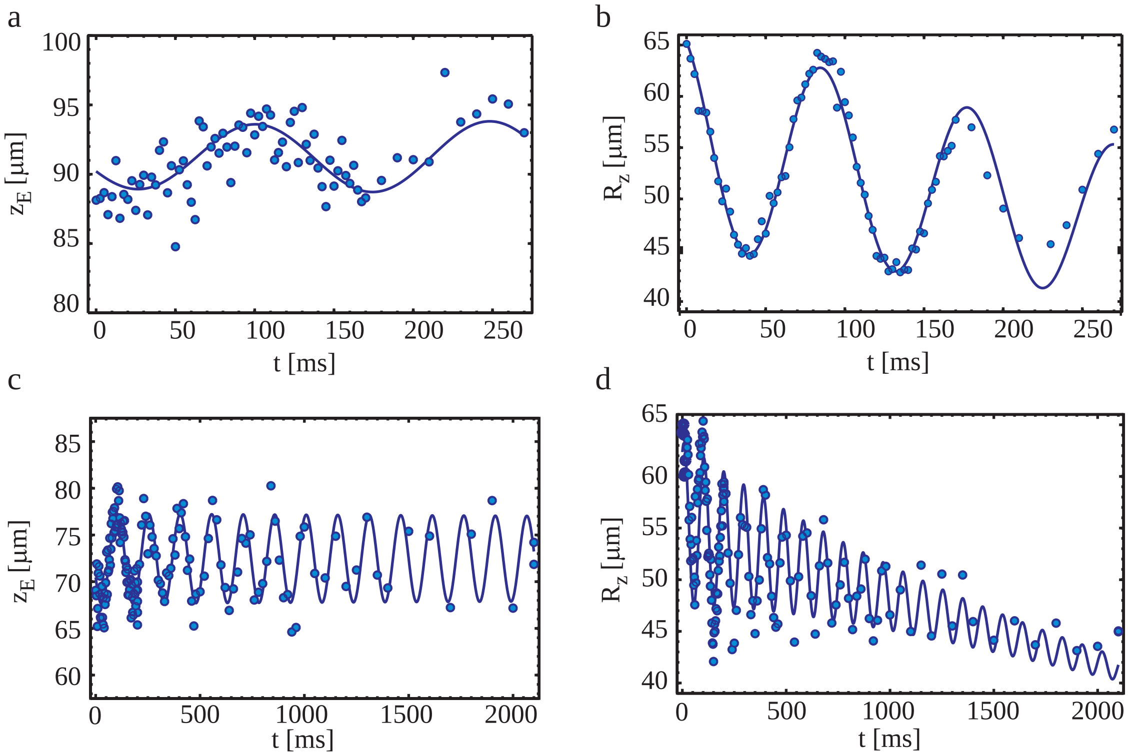

Figure 6.8: Center of mass (left column) and shape oscillations (right column) of the condensate as observed for the experiments and dark (first row) and dark-bright solitons (second row).

---

oretical prediction of $\omega_{QP} = \sqrt{5/2}\,\omega_z$. Note that the initial direction of propagation of the whole condensate is towards the attractive potential mediated by the red detuned phase imprinting laser as expected. The amplitude of the dark-bright dipole oscillation is approximately twice that of the dark soliton experiments. This is in agreement with the approximately twice as large integrated Rabi frequency for the preparation process. The occurrence of shape oscillation does not come as a big surprise since the phase imprinting method imparts momentum to the condensate spatially resolved and therefor locally disturbs the density distribution.

Particle number

The particle numbers have been determined from fits to the absorption images and give reasonable agreement with other methods to determine the density or particle number (e.g. spin dynamics) only for the fits employing a cut-off of the optical density. The particle numbers determined in this way are plotted in Fig. 6.9 for the experiments on dark (left) and dark-bright (right) solitons. While for large evolution times the decay of the dark component is well described by a decreasing exponential, the loss of particles is significantly higher for a short time after the preparation. This might be a combined effect of three-body losses which diminish dramatically with decreasing density (see e.g. [7]) and losses induced by the preparation process.
The decay of the bright component on the other hand is well described by an exponential decay for all times with a time constant of $\tau = (1.5 \pm 2)\,$s, significantly shorter than the corresponding lifetime ($t \leq 150\,$ms) of $\tau = (2.8{\pm}3)\,$s obtained for the dark component. The

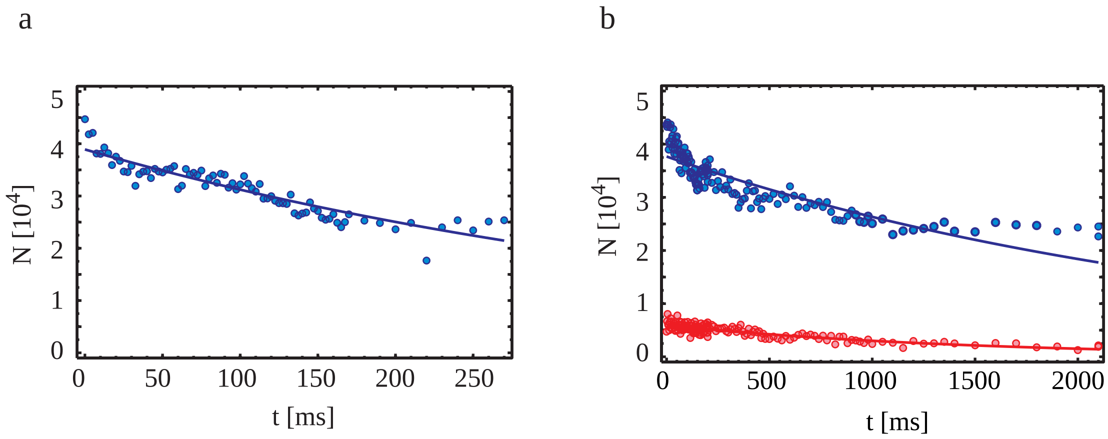

Figure 6.9: Lifetimes of dark and bright component for the soliton experiments.
(a) Dark soliton experiments. The lifetime amounts to $\tau = (0.45 \pm 0.04)\,$s.
(b) Dark-bright soliton experiments. The dark component (blue) shows increased losses during the first 250 ms (compare (a)) The average lifetime is calculated as $\tau = (2.8 \pm 3)\,$s much greater than for the dark soliton experiments. The lifetime of the bright component (red) is $\tau = (1.5 \pm 2)\,$s and seems to be the limiting factor for the lifetime of dark-bright solitons.

lifetime measured for the dark soliton experiments is significantly shorter $\tau = (0.45 \pm 0.04)\,$s owing to the fact that it has been determined in the regime where the initial strong losses still play a dominant role. One can calculate the mean density in the bright component in a simplified model according to $\langle n_\mathrm{b} \rangle = 2N_\mathrm{b}\kappa/(\pi R_x R_y) = 4.8 \cdot 10^{13}\,\mathrm{cm}^{-3}$, where the R_i are the Thomas-Fermi radii in the transverse direction fulfilling $1/2m\omega_i^2 R_i^2 = \mu$. With the above lifetime the two-body loss rate is obtained through $\tau^{-1} = G \cdot \langle n \rangle$ and reads $G = 1.39 \cdot 10^{-14}\,\mathrm{cm}^3\mathrm{s}^{-1}$. By comparing this to a two-body loss rate obtained in [7] for $|2,0\rangle$ $G = 10.2 \cdot 10^{-14}\,\mathrm{cm}^3\mathrm{s}^{-1}$ we find a value that is eight times smaller. However in [7] spin selective detection lead to a fast decay of $|2,0\rangle$ due to spin dynamics distributing the upper hyperfine population among all states $|2, m_F\rangle$. In the dark-bright soliton experiments *no* spin selective detection has been performed. We thus measure the total $F = 2$ population which could be very roughly accounted for by dividing the decay rate from [7] by a factor of $2F + 1 = 5$ resulting in a value that is only slightly but significantly above the decay rate observed here.

6.3.2 Oscillations

The time evolution of a dark soliton created by the aforementioned phase imprinting method is shown in Fig. 6.10. Soliton positions have been determined using the above mentioned data fitting procedure. We were able to detect nearly pure dark solitons after times as long as 5 s in single experimental realizations, surpassing lifetimes of dark solitons in any former experimental realization by more than a factor of 200. Fluctuations in the soliton position due to small preparation errors however prevent the observation of soliton dynamics for evolution times $\tau_\mathrm{evol} \gg 250\,$ms. The extraordinary long lifetimes facilitate the first observation of an oscillation of a dark soliton in a trapped BEC. The soliton clearly propagates axially along the condensate with an initial velocity of $\dot{q} = 0.56\,\mathrm{mm/s} = 0.56\,\bar{c}_s$ indicating a relative soliton depth of $n_s = 0.68\,n_0$.
The occurrence of a second small soliton can be extracted from the experimental data as

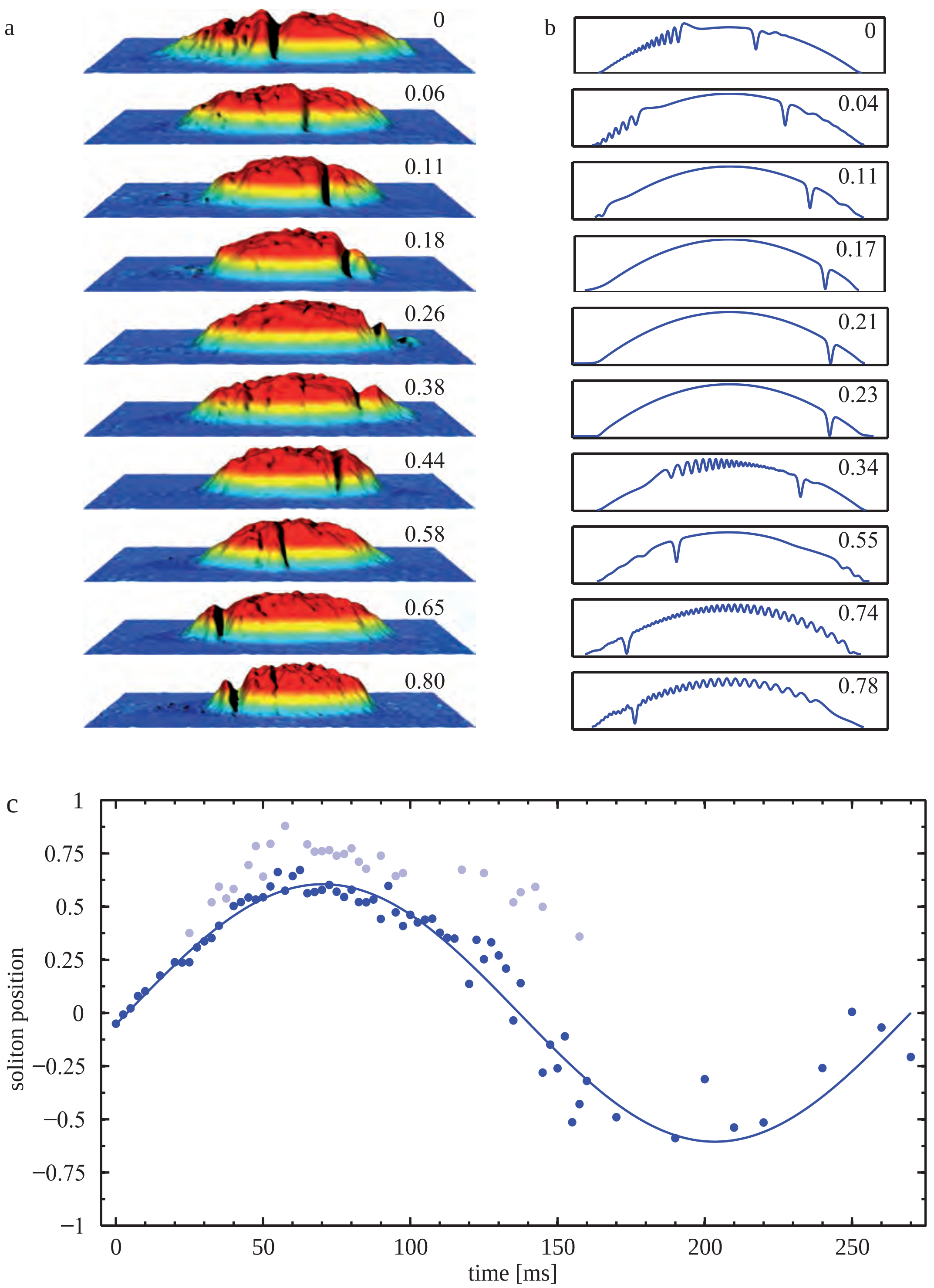

Figure 6.10: Oscillation of a dark solitons in a BEC. (a) Absorption images showing a dark soliton propagating in a trapped Bose-Einstein condensate. The evolution time is given in units of the oscillation period $2\pi/\Omega$.
(b) Numerical simulations of the 1D GPE featuring our experimental parameters using the *split operator method* (taken from [201]).
(c) Extracted soliton position normalized to the instantaneous width of the condensate (dark blue circles). A sinusoidal fit to determine the oscillation parameters is shown in addition (full curve). The light blue dots denote the position of a second tiny soliton that is generated through the phase imprinting process.

well as from the simulations as shown in Fig. 6.10. This is expected theoretically from the method of phase imprinting (see also Section 6.2.2). Due to its larger velocity the shallower second soliton separates clearly from the primary soliton in the vicinity of the turning points of the oscillation, because it has a significantly larger oscillation amplitude. The visibility of the secondary soliton is further enhanced here compared to the bulk of the BEC because the optical density has dropped to reasonably low values in the wings of the BEC.

An oscillation frequency of $\Omega = 2\pi \times (3.8 \pm 0.1)\,\mathrm{Hz}$ has been recorded for the primary soliton and could be followed for more than one period. Caused by the shallowness of our dipole trap the atoms experience the full Gaussian potential of the elongated crossed beam trap introduced in Section 3.2. The Gaussian potential is less steep than harmonic leading to a larger amplitude-dependent oscillation period for the soliton. A calculation of the soliton oscillation frequency solving equation Equ. 6.10 for a Gaussian potential created by a laser beam with a waist of $117\,\mu\mathrm{m}$ and taking the observed soliton amplitude of $Z_s = 33\,\mu\mathrm{m}$ as an initial value yields an oscillation frequency of $\Omega = 2\pi \times 3.95\,\mathrm{Hz}$. This is in good agreement with our experimental data. The validity of this model has been checked further by calculating the frequency for shallower, faster solitons that show a larger oscillation amplitude. The calculated values agree with the experimental data for small to intermediate oscillation amplitudes. The oscillation period of large amplitude oscillations as observed for the secondary solitons mentioned above agree qualitatively but show significant deviations towards even larger periods. Furthermore, as already mentioned the observed amplitude allows for a consistency check of the soliton depth. At the turning point of the soliton motion Z_s the constant soliton depth equals the Thomas-Fermi density $n_{\mathrm{TF}}(Z_s)$ of the condensate and interrupts the superfluid flow of atoms. At this point the soliton starts to move in the opposite direction. Given the measured initial speed of the soliton and the observed density distribution of the condensate Z_s can be calculated to be $36\,\mu\mathrm{m}$ and is in very good agreement with the directly measured value. Note that the depth of the soliton is the only measure that can hardly be determined directly since the absorption images are partly optically thick which makes it very difficult to reliably fit the amplitude of the model function to the data.

The density wave that is always created when employing the phase imprinting method is also clearly identified in Fig. 6.10 and travels in the opposite direction at a velocity equal to the speed of sound (compare Section 6.2.2). The density waves die out after approximately 50 ms leaving an almost flat BEC with only one or two soliton excitations. Calculating the dimensionality parameter $\gamma = n_0 g/\hbar\omega_\perp = 3.7$ and comparing this value to the critical ratio γ_c given by Muryshev *et al.* [37] we find the dark soliton to be right on the edge of the region of dynamical stability from Fig. 6.11. This is confirmed regarding the observed soliton lifetimes. It might be possible that owing to initial instabilities the soliton is accelerated until it reaches a velocity corresponding to a parameter regime of transverse dynamical stability. The velocity of the soliton increases slightly from one zero crossing to the other. The initial velocity of $\dot{q}_0 = 0.56\,\bar{c}_s$ increases to $\dot{q} = 0.77\,\bar{c}_s$ during the first zero crossing, which indicates that dissipative processes tend to accelerate the soliton. Note however that the scatter of the data points in the vicinity of the first zero crossing used to perform a linear fit may lead to an overestimation of the return velocity in this particular case as can be deduced from Fig. 6.10.

The crucial feature to the observed long lifetimes of dark solitons seems to be the very low temperature of our samples. The critical temperature for Bose-Einstein condensation for our experimental parameters is $(67 \pm 5)\,\mathrm{nK}$. Estimating that a thermal fraction of at least

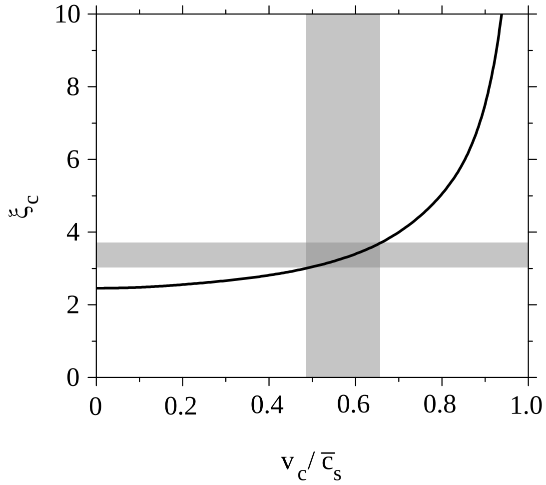

Figure 6.11: Stability diagram for dark solitons. Critical parameter ξ_c obtained from numerical calculations performed by Muryshev and coworkers [37]. The parameter regime beneath the curve corresponds to dynamically stable dark solitons. The gray shaded area represents a typical combination of soliton speed and ξ as found in the experiments presented here. The finite width of the shaded area indicates experimental scatter and statistical uncertainty of the experimentally obtained initial velocity (horizontal width) and atomic density (vertical width).

10% could have been detected in absorption imaging – which was not the case – an upper limit for the temperature of $T \leq 0.5\,T_c = 30\,\mathrm{nK}$ can be given which is on the order of the chemical potential μ. We assume a significantly smaller temperature, since temperatures of $T \approx 0.2\,T_c$ would already have considerably limited the solitons lifetime [32], which has not been observed in our experiment.

6.3.3 Collisions

As the next step to further investigate the physics of dark solitons in Bose-Einstein condensates we have generated more than one soliton in order to study their collisional properties. This has been achieved by imaging an appropriate SLM pattern onto the BEC depicted and explained in Fig. 6.12. Note that the number of solitons created can be varied, as can their individual depths, initial positions and directions of movement be chosen over a wide range of parameters by tailoring the nearly arbitrarily shapeable light field potentials acting on the BEC. In the experiment presented here two solitons with slightly different depths are generated in such a way that they propagate to opposite sides of the condensate, are reflected there, approach one another and eventually collide in the center of the trap. This approach is advantageous for various reasons

Identification The observed oscillation frequency when first propagating "independently" is used to identify the density modulation as dark solitons with characteristic oscillation frequencies $\Omega = \omega_z/\sqrt{2}$

Determination of the amplitude As explained above the residual density of the solitons can only be determined with a large uncertainty. Instead the amplitude of their oscillation, which directly depends on the depth n_s, is used to tag the individual solitons. The oscillation amplitudes can be measured prior to the first collision.

Signal-to-noise Density waves and other excitations originating from the imperfect imprinting method will be dampened during the pre-collision time, leaving two well-characterized dark solitons on an almost uniform background.

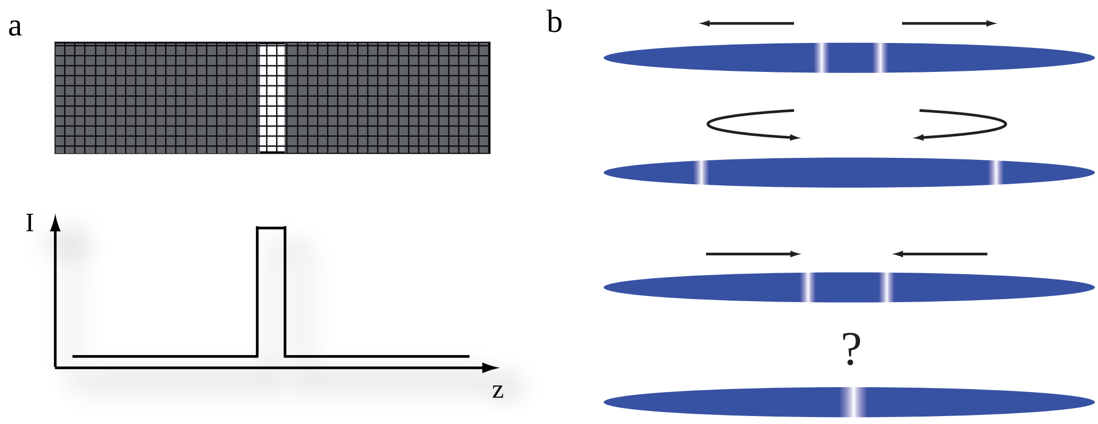

Figure 6.12: Experimental scheme for the investigation of dark soliton collisions. A small stripe-like region of the condensate is illuminated with far red detuned laser light. In this way the solitons travel to the outer ends of the condensate first, which allows additional excitation in the condensate to be damped prior to the collision. The solitons oscillate back and approach each other close to the center of mass of the condensate eventually colliding with each other.

A time series of the axial optical density of the BEC is shown in Fig. 6.13. As can be clearly inferred, the two initial solitons propagate to opposite edges of the condensate, are reflected and then pass through one another. No mutual interaction of the solitons can be detected and appears that they emerge unscathed from the collision.
Two density waves carrying away the excess phase gradient can be observed as well during the first 25 ms. The corresponding space-time plot of the extracted soliton positions is used to determine the oscillation frequencies to be $\Omega_1 = 2\pi \cdot 3.5\,\mathrm{Hz}$ and $\Omega_2 = 2\pi \cdot 3.8\,\mathrm{Hz}$. The deviation from the theoretical value $\Omega = \omega_z/\sqrt{2}$ can be explained by the anharmonicity of the trap as shown above. The relative oscillation amplitudes of $Z_1 = 0.55$ and $Z_2 = 0.60$ correspond to relative depths n_s/n_0 of the dip of 0.74 and 0.69 prior to the collision for soliton 1 and 2, respectively. The scatter is due to shot-to-shot fluctuations, e.g. of the atom number and power of the phase-imprinting laser. Furthermore, the acceleration-instability due to thermal collisions is also temperature-dependent [32, 34, 37] and may fluctuate from shot-to-shot as well. The scatter increases with evolution time and, together with a decrease in contrast, renders a precise and reproducible determination of the soliton position impossible for evolution times larger than 200 ms. By comparison of the oscillation amplitudes before and after the collision, it is more likely that the solitons pass through one another and retain their characteristics. We employed a fit to the data assuming a “reflection” during collision, but find a much weaker agreement. This strongly favors a behavior of “passing” through each other instead of being reflected as sometimes discussed in the context of soliton physics. Recall that the individual identity of solitons as quasi-particles breaks down if they are very close to one another. The authors of [203] state that momentum transfer can occur during the collision of two dark solitons. With this in mind the color coding of Fig. 6.13 is too simple minded, but it emphasizes the fact that for long times after the collision, the observed states propagate like two solitons that are unperturbed by one another. The observed lifetimes are about the same as for the single soliton experiments, which excludes any dominating dissipation mechanism originating from the interaction of dark solitons via sound emission and re-absorption [38].
Numerical simulations of the 1D-GPE performed by E.-M. Richter [201] show an excellent

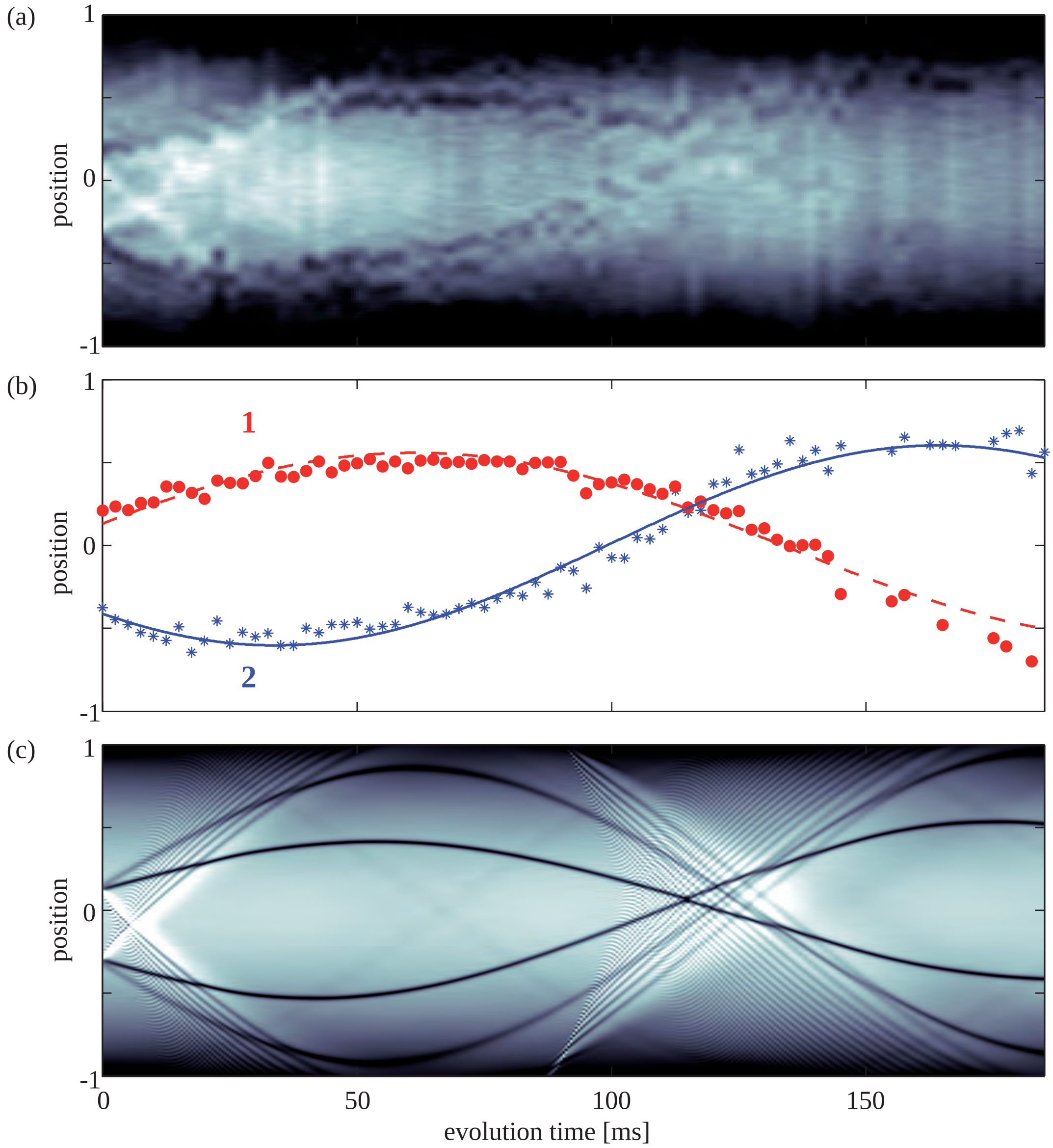

Figure 6.13: Collision of two dark solitons. Analogously to the oscillation of dark solitons positions are normalized to the condensate extension and center of mass to correct for quadrupole and dipole oscillations.
(a) Density plot of the condensate. Each column represents the optical density of the elongated condensate integrated along the transverse direction. The density depressions of the dark solitons as well as the increased density of the density waves are clearly visible. The evolution time increases along the positive x-direction. The propagation of the solitons has been tracked every 2.5 ms.
(b) Sinusoidal fits to the extracted soliton positions are shown together with the data points. Note that the choice of asymmetric starting points of the two solitons results in different depths and therefore allows for the *identification* of the solitons as 1 (colored red, deeper, smaller oscillation amplitude) and 2 (colored blue, shallower, larger oscillation amplitude) (see text for details). The error bars in both time and position are well within the marks.
(c) Results of numerical simulation of the 1D-GPE [201] adapted to our parameters. Additional smaller solitons, only faintly visible in (a), can also be observed similar to the oscillation experiment Fig. 6.10.

agreement with the experimental data. The simulations take into account the independently determined experimental parameters (trapping potential and particle number) and fully incorporate the phase imprinting method through a time evolution, thus showing all the generic features of the experiment except for finite temperature effects, like damping. A possible position shift due to the interaction has been investigated in many theoretical works and with different methods. Given our experimental parameters, a positive shift of $\Delta x \approx 0.015\,\mu$m (with respect to the unperturbed trajectory of a single soliton) is predicted analytically [203]. A shift of $\Delta x = 0.51\,\mu$m can be retrieved from an alternative analytic model [202, 204]. Both of these shifts are way smaller than the optical resolution of our imaging system and cannot be resolved.

In a second series of experiments we have studied the collisional behavior of two dark solitons of different amplitude traveling in the same direction. The shallower and thus faster soliton starts ahead of the deeper and slower soliton. Because of its smaller amplitude it exhibits a larger oscillation amplitude and period. After the reflection at the end of the condensate one expects, that the faster soliton will "overtake" the slower soliton at some point. We call this experiment the *chase* scenario. Like for the head-on collisions above residual excitation of the condensate are significantly damped prior to the soliton interaction which ensures a better visibility of the collision process. The observations we have made in our experiment are quite remarkable: After being reflected at the end of the condensate the two solitons approach each other, seem to merge and develop into one very deep and *standing* soliton. We have observed almost black solitons generated in this manner with lifetimes as large as 5 s as shown in Fig. 6.15.

The solitons start approximately $20\,\mu$m apart from each other, the fast advancing soliton with an initial speed of $\dot{q}_0^{\rm s} = 0.7\,\bar{c}_s$ and the slower soliton travelling at $\dot{q}_0^{\rm f} = 0.62\,\bar{c}_s$. These values would correspond to depths of $n_s^{\rm f}/n_0 = 0.51$ and $n_s^{\rm s}/n_0 = 0.61$ respectively. The associated phase slips across the nodal planes of the solitons read $\Delta\phi^{\rm f} = 0.34\pi$ and $\Delta\phi^{\rm s} = 0.42\pi$ for the fast and slow soliton respectively. Adding up the two phase slips results in $\Delta\phi = 0.75\pi$ which would correspond to an almost black soliton with an amplitude of $n_s/n_0 = 0.93$ and a velocity of only $\dot{q} = 0.27\,\bar{c}_s$. This is something close to an almost fully modulated soliton that does rarely move at all – just what we observe in our experiment. However to further support the merging scenario more detailed measurements would be required. Note that theoretical predictions do *not* include something like merging of two dark solitons but rather predict an almost unperturbed propagation of the individual solitons after the interaction just characterized by a certain phase acquired during the collision.

6.4 Dark-bright solitons in multi-component BEC

After the investigation of the physics of dark solitons in elongated BEC we now turn to the more exotic entities that are dark-bright solitons. We have created those two-component solitons using the Raman-Rabi method introduced above. The experimental parameters for the experiment are the same as for the dark solitons. A time series of the propagation of such a dark-bright soliton is shown in Fig. 6.16. After a short time of flight of 9 ms the atoms are first exposed to a light pulse resonant only with $|F = 2\rangle$. After another 2 ms the $|F = 1\rangle$ atoms are subsequently imaged. The dynamics of the dark-bright soliton could be followed for more than 2 s as seen in Fig. 6.16. The correlation in the position of the dark and bright soliton is remarkable and strongly supports the idea of a joint vectorial soliton structure. The mask pattern used in the experiment described here resulted in a

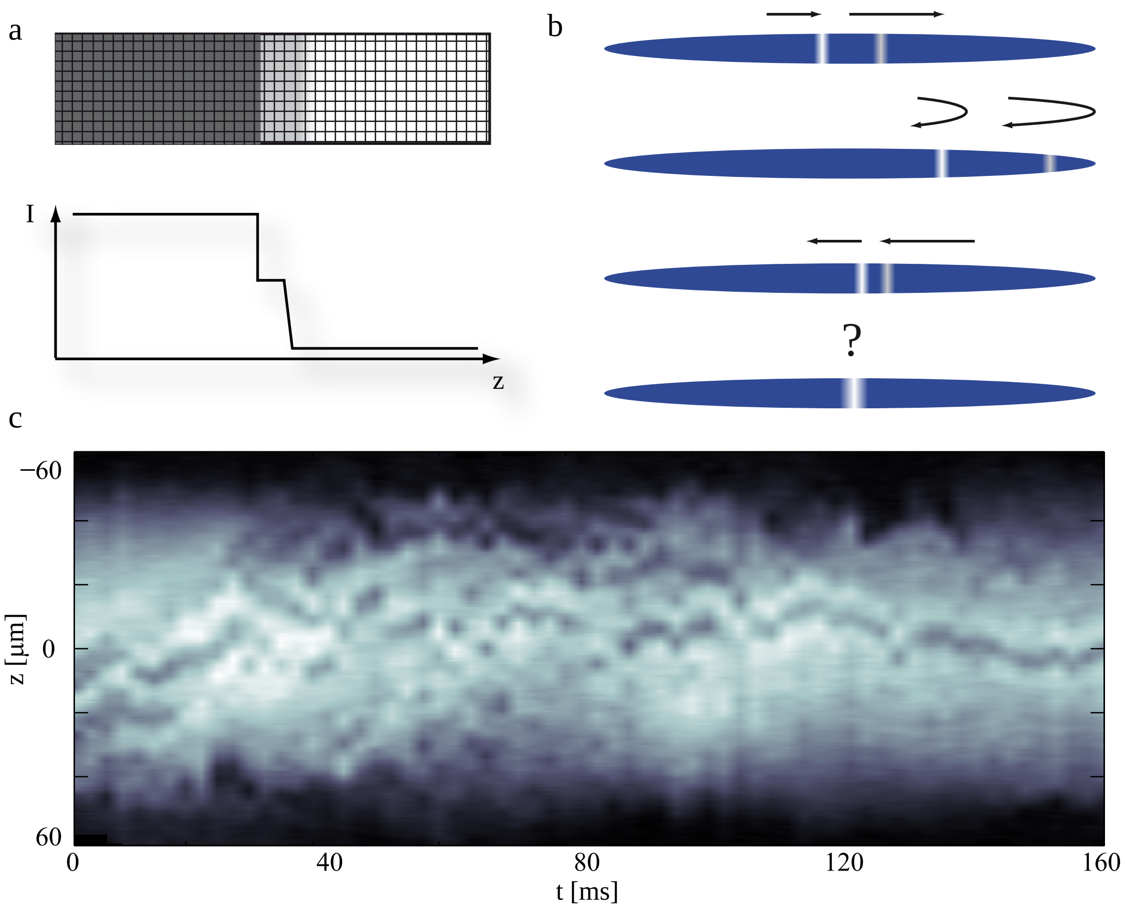

Figure 6.14: Chase scenario for two dark solitons. Two dark solitons are generated that travel in the same direction at different velocities. After a quarter oscillation period they reverse their direction of propagation and travel in the opposite direction where the fast soliton will eventually overtake its slower counterpart.
(a) Intensity profile used to generate two solitons at different velocities. To generate a faster soliton less phase feed is applied over a larger region.
(b) Schematic representation of the *chase* scenario of a fast (gray) and a slow (white) soliton.
(c) Density plots of the condensate density similar to Fig. 6.13. While it can not be deduced what exactly happens during the collision, it is clearly seen that for long evolution times a single very deep soliton that does hardly move at all is formed. Note that we have observed structures similar to the last 45 ms of the graph for evolution times up to 5 s!

---

bright component population $N_B = 0.11 N_{\mathrm{tot}}$, where N_{tot} is the total number of atoms. The initial velocity of the dark-bright soliton can be obtained from a fit to the first 200 ms and gives $\dot{q}_0^{\mathrm{db}} = 0.14\,\bar{c}_s$ which is much smaller than the velocities of any dark solitons that we have produced and only a small fraction of the speed of sound underlining its solitary nature. The return velocity after half an oscillation period reads $\dot{q}_0^{\mathrm{db}} = 0.17\,\bar{c}_s$ and is only slightly larger indicating the robustness of the dark-bright soliton.
Interestingly the initial direction of propagation of the dark-bright soliton is in the opposite direction as compared to the dark soliton experiments. The reason for that is that the momentum transfer on the bright atoms in the filling dominates over the momentum transfer on the residual dark atoms beneath the density dip of the dark soliton. The dark-bright soliton thus moves in the direction of the physical momentum transfer as opposed to

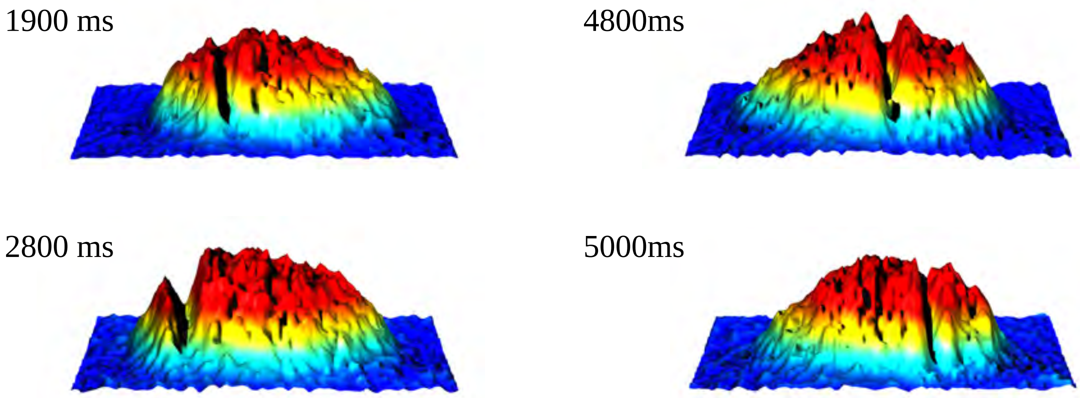

Figure 6.15: Examples of extremely longlived dark solitons. The dark solitons shown here have been observed in the course of measurements attending to the *chase* scenario (see text). After the solitons have interacted only one very pronounced soliton remains in the condensate. For single experimental realizations, lifetimes of up to 5 s could be observed surpassing any former experiments by more than a factor of 100.

---

a pure dark soliton which moves in the direction opposite to the superfluid flow of atoms. We observe an oscillation of the dark-bright soliton with a frequency of $\Omega_{\rm db} = 2\pi \times (0.90 \pm 0.02)\,{\rm Hz} = 0.24 \times \Omega$, much smaller than the frequency of the corresponding dark soliton. To our knowledge that is the first measurement of *coherent dynamical* properties of vectorial solitons in Bose-Einstein condensates. Evaluating the expression for the oscillation frequency according to Equ. 6.21 demands for the determination of the bright particle number parameter $N_{\rm B}/(4n_0\bar{\xi})$. The one-dimensional density n_0 can be calculated by integrating over the transverse degrees of freedom within the 3D Thomas-Fermi limit resulting in $n_0 = (15/16)\,N/R_z$. With a particle number of $N = 5.2 \cdot 10^4$ and a mean condensate radius of $R_z = 56\,\mu$m we calculate $4N_{\rm B}R_z/(15N\bar{\xi}) = 2.4$. Plugging in this value results in an oscillation period of $\Omega_{\rm DB} = 2\pi \cdot 0.94\,{\rm Hz}$ which is in excellent agreement with the measured value. Since the oscillation amplitude is solely determined by the depth of the dark soliton given by the parameter α according to $|\sin(\alpha)| = Z/R_z = 0.68$ we can check the above value for the bright particle number parameter employing Equ. 6.15 which connects α, $\dot{q}$ and $N_{\rm b}$ and yields $N_{\rm B}/(4n_0\bar{\xi}) = 1.85$ in reasonable agreement with the directly measured value.

The extraordinary long lifetime of the dark-bright solitons $\tau \gtrsim 2\,{\rm s}$ seems to be an impressive confirmation of the theoretical prediction that a larger soliton size drastically reduces scattering of excitations leading to enhanced stability [39]. Indeed the limiting factor seems to be the lifetime of the bright component which has been measured to be $\tau = (1.5 \pm 0.2)\,{\rm s}$. For times larger than this the soliton has already significantly reduced its size, which makes it more liable to excitations and decay as explained above. Moreover, differing fundamentally from the physics of dark solitons, the oscillation period depends on the number of particles in the bright soliton and is therefor directly affected by errors in preparation. Hence the scatter of the soliton position for these larger evolution times is also strongly increased which renders a reliable tracking of the soliton dynamics impossible beyond times larger than $2 - 2.5\,{\rm s}$.

Another interesting feature that can be extracted from this measurement is the interaction of a dark soliton and a density wave with the much slower dark-bright soliton. Owing

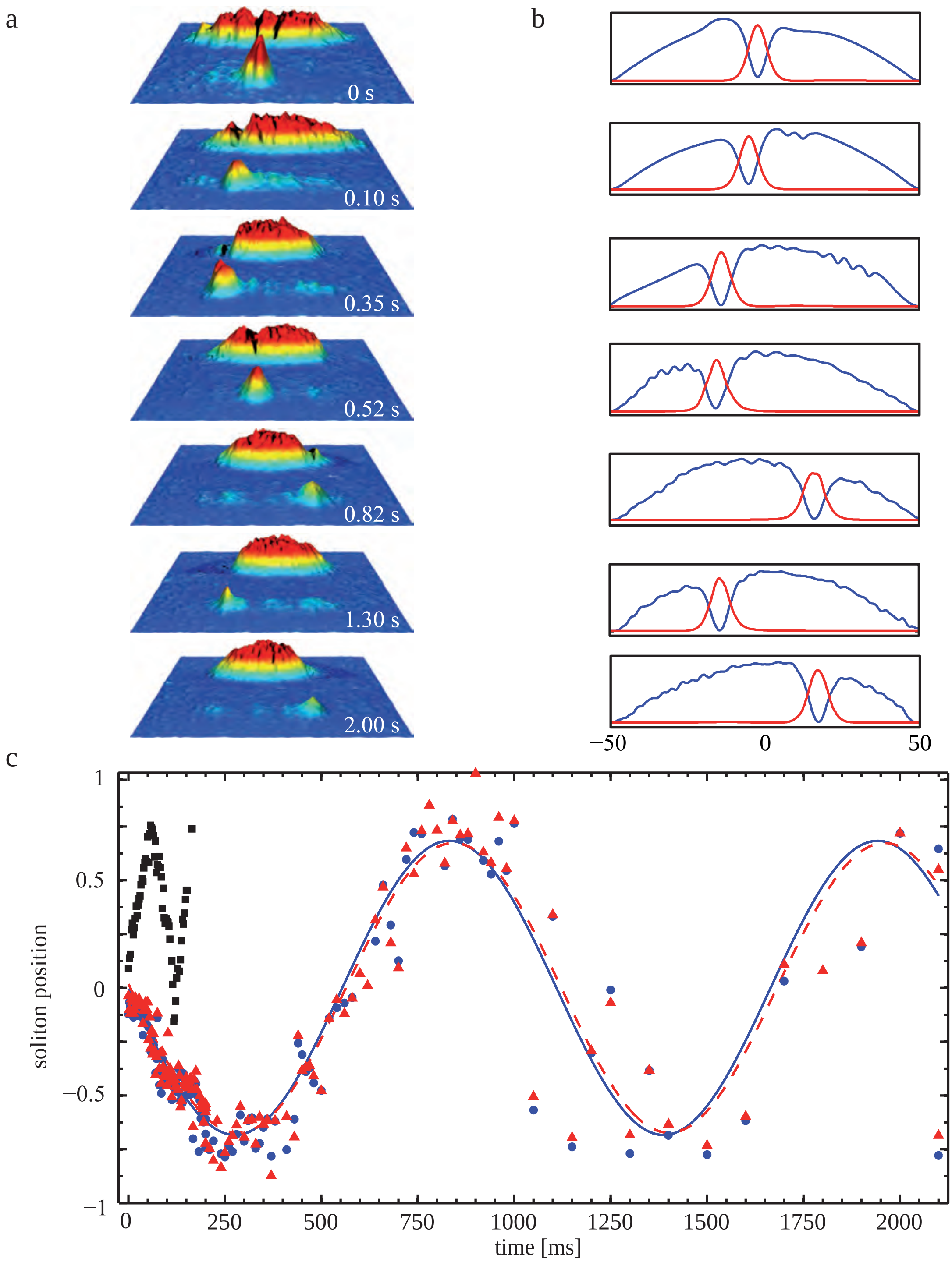

Figure 6.16: Oscillation of a dark-bright soliton in a two-component BEC (a) Absorption images showing a dark soliton in $|1,0\rangle$ (back) and a bright soliton (front) in $|2,0\rangle$ co-propagating in a trapped two-component Bose-Einstein condensate. The evolution time is given in seconds.
(b) Numerical simulations of the two-component 1D GPE where our preparation process has been fully implemented (taken from [201]).
(c) Extracted positions of dark (blue circles) and bright (red triangles) soliton normalized to the instantaneous width of the condensate. Sinusoidal fits to determine the oscillation parameters are shown in addition (full and dashed curve). The correlation between the two solitons is remarkable supporting the idea of a dark-bright soliton. The black squares denote the position of a second dark soliton that is generated through the specific preparation process and interacts with the dark-bright soliton around $t \approx 100\,\text{ms}$.

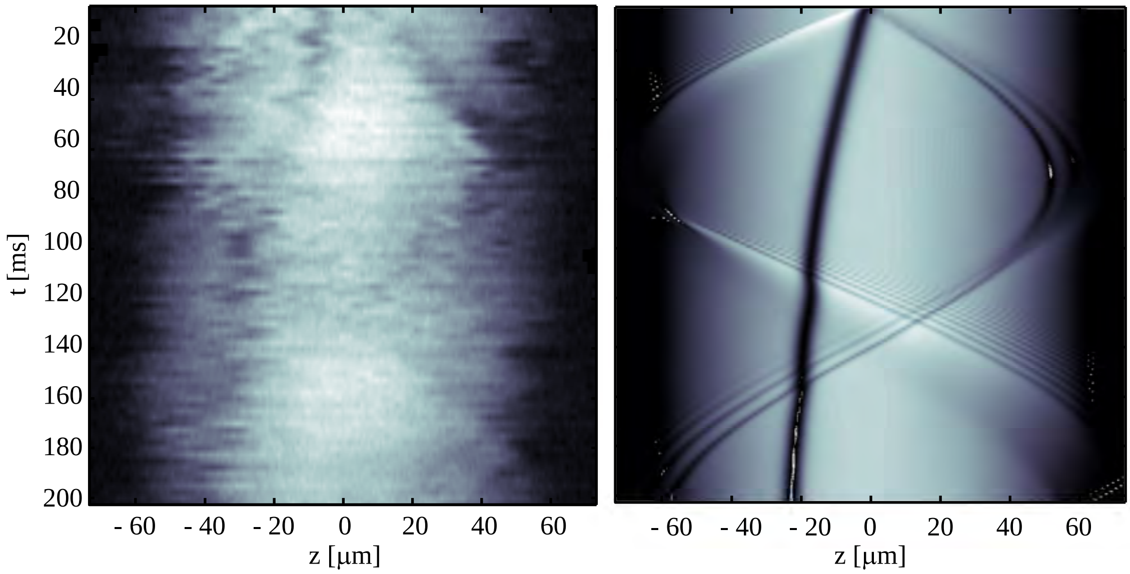

Figure 6.17: Interaction of a dark and a dark-bright soliton. The images show experimental results (left) and theoretical simulations (right) of the dark component for the first 200 ms of Fig. 6.16. The images are obtained by summing up the optical density along the transverse direction, resulting in a "one-dimensional" density distribution along the horizontal direction. Every row corresponds to one experimental run at an advancing evolution time. Both images clearly show that a density wave and a dark soliton are generated in addition to the dark-bright soliton. The different structures pass through each other without any unambiguous influence on each other as if they were transparent. Density wave as well as dark soliton have already undergone considerable damping prior to the interaction, which renders their detection for such long times rather difficult.

---

to the method of initial state preparation, an extra dark soliton is always generated in addition to the dark-bright soliton, as is also confirmed by numerical simulations [201]. As shown in Fig. 6.17 the dark soliton propagates in the *opposite* direction as compared to the dark-bright one without any discernible filling. The soliton oscillates in the trapped BEC with almost the same parameters as a dark soliton in an unperturbed experiment. Velocities of initially $\dot{q}_0 = (0.5 \pm 0.2)\bar{c}_s$ and $(\dot{q}_{1^{st}} = (0.8 \pm 0.3)\bar{c}_s$ after the first reflection have been determined. The oscillation amplitude is $Z = 0.65 R_z$ corresponding to a depth of $n_s/n_0 = 0.58$ while the oscillation frequency amounts to $\Omega = 2\pi \cdot (4.1 \pm 0.2)\,\text{Hz}$. After 120 ms it thus approaches the position of the dark-bright soliton which has only moved very little due to its much smaller oscillation frequency. Picking the most pronounced density depressions from the individual images and identifying them with a dark soliton it seems that the dark soliton is reflected off the dark-bright one comparable to a hard-wall reflection and moves back (compare the first 200 ms in Fig. 6.16). This would be in harsh contradiction to theoretical work [39] that investigated interaction of dark and dark-bright solitons and found *no* indication of reflection.

A detailed investigation of the density plots of the experiment and E.-M. Richter's numerical simulations of the coupled 1D GPE suggests another scenario: Both an additional dark soliton as well as a density wave are generated together with the dark-bright soliton. Since the density wave and the dark-bright soliton propagate into the region of the condensate that has been illuminated and therefor exhibits additional excitations it can hardly be tracked as long as it is in that part of the condensate ($t \leq 140\,\text{ms}$). The simulations show however that the dark soliton and the density wave pass through each other and through the dark-bright soliton after a time that coincides with the time of the pretended reflection. Comparing data and simulations it is more likely that the latter scenario takes place as compared to the reflection picture favored in the first place. For an unambiguous confirmation of the theoretical prediction further measurements would be required to enhance the resolution and statistics of the images.

6.4.1 Collisions of two dark-bright solitons

Collisions of dark-bright solitons have been studied in the course of this dissertation only marginally despite the whole wealth of interesting physical effects that are expected to occur. Theoretical calculations [39] predict that the interaction of dark-bright solitons can get more complex than the interaction of dark solitons. In particular particle exchange between the two bright solitons as well as a dependence of the collisional properties on the relative phases of the involved bright solitons are expected.
Experimentally it has proven rather difficult to prepare two dark-bright solitons and at the same time *not* to excite the condensate so much that dissipative processes are still negligible. We produced two counter propagating dark-bright solitons by imaging a slit similar to the dark soliton head-on collision experiments onto the condensate and performing the Raman-Rabi preparation technique (compare Fig. 6.12). Density plots of the dark and bright component obtained from the experiment and the simulations are shown in Fig. 6.18. Two dark bright solitons are generated and propagate to opposite ends of the condensate first. It can be deduced from the picture that two dark solitons are also created which likewise travel to the edges of the condensate. The dark solitons oscillate back after approximately 120 ms and interestingly they trap a tiny fraction of the bright component as is seen in the density plot of the bright component and in the simulations. The dark solitons associated with the main bright solitons can hardly be distinguished at all for longer evolution times. It seems as if the bright solitons existed without having their stabilizing dark counterpart. In principle this is not possible in a repulsive BEC and the associated dark solitons will accordingly be very shallow. However the bright solitons oscillate in the condensate and collide at a time $t_{\text{coll}} \approx 400 - 500\,\text{ms}$. The quality of the data is unfortunately not good enough to unambiguously follow the collision and identify the scattering products for long times after the interaction. Albeit these first results promise interesting physical effects and motivate further investigation of the collisions of dark-bright solitons. Above all the prerequisites for these future experiments are even more stable experimental conditions.

6.5 Outlook

The observations on dark and dark-bright solitons presented in this chapter open up the way for a whole variety of new experiments attending to those highly interesting collective excitations. With lifetimes of up to several seconds complex experiments with various oscillation or collisions seem to be within experimental reach now. Possible future experiments include the interaction of more than two dark solitons or the interaction of a dark soliton with an arbitrary shapeable potential barrier. As a paradigm of quantum mechanics reflection and transmission through this barrier could be investigated. By trapping the soliton and the emitted sound waves in potentials of different shape the dissipative dynamics of solitons could be studied in more detail in order to explore the temperature

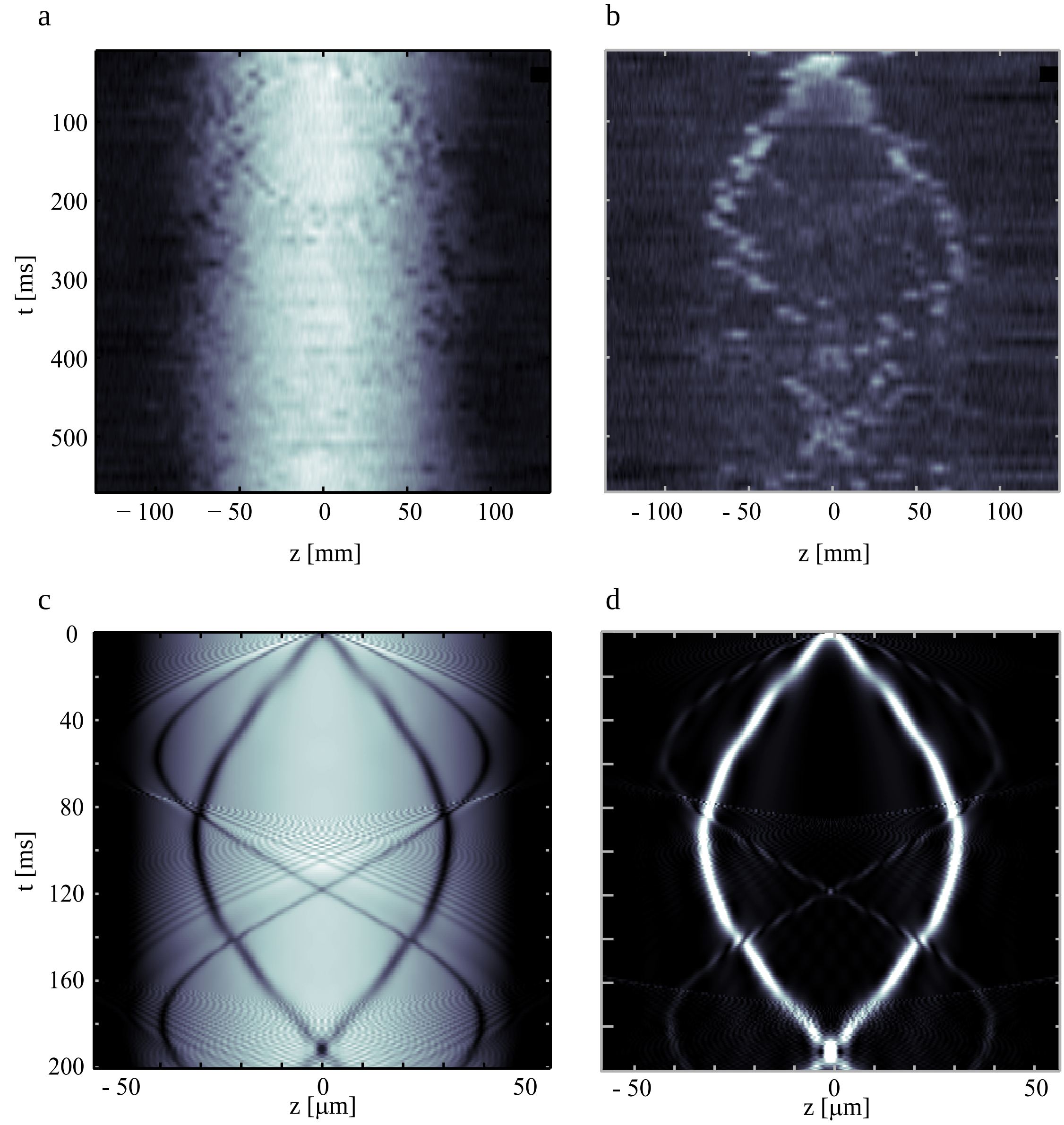

Figure 6.18: Interaction of two dark-bright solitons. The images show experimental results for the dark (left) and bright (right) component respectively. The images are obtained analogously to Fig. 6.17.

---

dependence or the influence of dimensionality in a controlled way. Collisions of dark-bright solitons with suitably engineered fillings and phases could make important contributions to the understanding of solitary structures and constitute a serious test for theoretical models. The dependence of the oscillation frequency on the bright particle number could be tested to name an example. A next step towards even better experimental conditions has already been taken by the implementation of an actively stabilized optical table which ensures that the dipole trap is always perpendicular to gravity and no gravitational sag effects draw the BEC to either side which introduced a considerable scatter of the experimental results. Finally numerous theoretical proposals have dealt with spinor solitons (see e.g. [209]), similar to dark-bright solitons but involving states from the same hyperfine manifold. Since we have an experimental setup specialized to the investigation of spinor condensates numerous experiments are conceivable attending to this idea.

Appendix A

^{87}Rb **data**

The author has decided to provide the reader with all necessary information about ^{87}Rb to follow or reconstruct the findings presented in this thesis. Most of the values found below have been taken from the ^{87}Rb *line data* [109]. The values found here have been employed for all calculations throughout this thesis that involve any ^{87}Rb data.

Table A.1: Fundamental physical constants (taken from 1998 CODATA [6])

speed of light	c	$2,99792458 \times 10^{8}$ m s^{-1} (exact)
Permeability of vacuum	μ_0	$4\pi \times 10^{-7}$ N $\cdot$ A^{-2} (exact)
Permittivity of vacuum	ϵ_0	$\mu_0^{-1} c^{-2}$ (exact)
		$8,854187817 \cdots \times 10^{-12}$ F $\cdot$ m^{-1}
Planck's constant	h	$6.62606876(52) \times 10^{-34}$ J $\cdot$ s
		$4.1356627(16) \times 10^{-15}$ eV $\cdot$ s
Electron charge	e	$1,602176462(63) \times 10^{-19}$ C
Bohr magneton	μ_B	$9.27400899(37) \times 10^{-24}$ J $\cdot$ T^{-1}
		$h \cdot 1,399624624(56)$ MHz $\cdot$ G^{-1}
Atomic mass unit	u	$1,66053873(13) \times 10^{-27}$ kg
Electron mass	m$_e$	$5,485799110(12) \times 10^{-4}$ u
		$9,10938188(72) \times 10^{-31}$ kg
Bohr radius	a_B	$0,5291772083(19) \times 10^{-10}$ m
Boltzmann's constant	k$_B$	$1,3806503(24) \times 10^{-23}$ J $\cdot$ K^{-1}

Table A.2: ^{87}Rb physical properties (taken from [7] and references therein)

Atomic number	Z	37
Total nucleons	Z+N	87
relative natural abundance	$\eta(^{87}Rb)$	$27,83(2)\%$
Nuclear lifetime	τ_n	4.88×10^{10}years
Atomic mass	m	$1,44316060(11) \times 10^{-25}$ kg
Density at $25°C$	ρ_m	$1.53\ \mathrm{g \cdot cm^{-3}}$
Melting point	T_M	39.31 °C
Boiling point	T_B	688 °C
Specific heat capacity	c_p	$0,363\ \mathrm{J \cdot g^{-1} \cdot K^{-1}}$
Molar heat capacity	C_p	$31,060\ \mathrm{J \cdot mol^{-1} \cdot K^{-1}}$
Vapor pressure at $25°C$	P_v	4.0×10^{-7} mbar
Nuclear spin	I	3/2
Ionization limit	E_I	$4,1771270(2)$ eV
Zeeman shift of the clock transition	$\Delta\omega_{clock} \cdot B^{-2}$	$2\pi \cdot 575,15\ \mathrm{Hz \cdot G^{-2}}$
s-wave scattering length F=1	a_0	$110,0 \pm 4,0\, a_B$
	a_2	$107,0 \pm 4,0\, a_B$
s-wave scattering length F=2	a_0	$89,4 \pm 3.0\, a_B$
	a_2	$94,5 \pm 3,0\, a_B$
	a_4	$106,0 \pm 4,0\, a_B$
Elastic two-body collisions	Γ_{el}	$32 a_0 n \sqrt{\pi k_B T/m}$
		$1,4 \times 10^{-11} \frac{n}{[cm^{-3}]} (\frac{T}{[\mu K]})^{0,5}$
Inelastic two-body collisions F=2,m_F=2	G_{dip}	$10^{-14}\ \mathrm{cm^3 \cdot s^{-1}}$
Three-body collisions F=2,m_F=2	L_{3k}^{BEC}	$1,8 \times 10^{-29}\ \mathrm{cm^6 \cdot s^{-1}}$
Inelastic two-body collisions F=1, m_F=-1	G_{dip}	$< 1,6 \times 10^{-16}\ \mathrm{cm^3 \cdot s^{-1}}$
Three-body collisions F=1, m_F=-1	L_{3k}^{BEC}	$5,8 \times 10^{-30}\ \mathrm{cm^6 \cdot s^{-1}}$

Table A.3: ^{87}Rb $D_2(5^2S_{1/2} \rightarrow 5^2P_{3/2})$
transition optical properties

Frequency	ω_0	$2\pi \cdot 384,2279818773(55)$ THz
Wavelength (Vacuum)	λ	$780,246291629(11)$ nm
Wave Number (Vacuum)	$\mathrm{k}_L \cdot (2\pi)^{-1}$	$12816,46591247(18)\ \mathrm{cm}^{-1}$
Lifetime	τ	$26,24(4)$ ns
Natural line width (FWHM)	Γ	$2\pi \cdot 6.065(9)$ MHz
Recoil velocity	v_r	$5,8845\ \mathrm{mm} \cdot \mathrm{s}^{-1}$
Recoil energy	ω_r	$2\pi \cdot 3,7709$ kHz
Recoil temperature	T_r	$361,95$ nK
Doppler shift ($v_{\mathrm{atom}} = v_r$)=	$\Delta\omega_d(v_{atom} = v_r)$	$2\pi \cdot 7,5418$ kHz
Doppler temperature	T_D	$146\,\mu$K
Saturation intensity ($F = 2 \rightarrow F = 3$)	I_{sat}	$3,576(4)\ \mathrm{mW} \cdot \mathrm{cm}^{-2}$
Saturation intensity ($m_F = \pm 2 \rightarrow m'_F = \pm 3$)	I_{sat}	$1,669(2)\ \mathrm{mW} \cdot \mathrm{cm}^{-2}$
Reduced transition dipole matrix element	$\langle J = 1/2 \Vert e\mathbf{r} \Vert J' = 3/2 \rangle$	$3.584 \cdot 10^{-29}\ \mathrm{C} \cdot \mathrm{m}$

Table A.4: ^{87}Rb $D_1(5^2S_{1/2} \rightarrow 5^2P_{1/2})$
transition optical properties

Frequency	ω_0	$2\pi \cdot 377,1074635(4)$ THz
Wavelength (Vacuum)	λ	$794,9788509(8)$ nm
Wave Number (Vacuum)	$\mathrm{k}_L \cdot (2\pi)^{-1}$	$12578,950985(13)\ \mathrm{cm}^{-1}$
Lifetime	τ	$27,70(4)$ ns
Natural line width (FWHM)	Γ	$2\pi \cdot 5.746(8)$ MHz
Recoil velocity	v_r	$5,7754\ \mathrm{mm} \cdot \mathrm{s}^{-1}$
Recoil energy	ω_r	$2\pi \cdot 3,6325$ kHz
Recoil temperature	T_r	$348,66$ nK
Doppler shift ($v_{\mathrm{atom}} = v_r$)	$\Delta\omega_d(v_{atom} = v_r)$	$2\pi \cdot 7,2649$ kHz
Doppler temperature	T_D	$138\,\mu$K
Reduced transition dipole matrix element	$\langle J = 1/2 \Vert e\mathbf{r} \Vert J' = 1/2 \rangle$	$2.537 \cdot 10^{-29}\ \mathrm{C} \cdot \mathrm{m}$

Appendix B

Atom-light interaction in the two-level picture

It is sometimes more convenient to reformulate the expressions derived for the dipole potential in Section 3.2 in terms of Rabi frequencies familiar from the textbook example of a two level atom. Starting with the general equation Equ. 3.5

$$U_{\mathrm{dip}}(\mathbf{r}) = 3\pi c^2 \left(\sum \frac{|c_{CG,i}|^2}{\omega_{0,i}^3} \frac{2\Gamma_i \Delta_i}{\Gamma_i^2 + 4\Delta_i^2} \right) I(\mathbf{r}) \tag{B.1}$$

we arrive at the expression ($\Delta_i \gg \Gamma_i$)

$$U_{\mathrm{dip}}(\mathbf{r}) = \frac{\hbar}{4} \sum_i \frac{\Omega_i^2}{\Delta_i} \tag{B.2}$$

in terms of the Rabi frequencies of the individual transitions

$$\begin{aligned} \Omega_i(\mathbf{r}) &= \frac{6\pi c^2 \Gamma_i}{\hbar w_{0,\,i}^3} \cdot I(\mathbf{r}) && \text{(B.3)} \\ &= \frac{E_0}{\hbar} \langle F_f, m_{F,\,f} | e\mathbf{r} | F_i, m_{F,\,i} \rangle && \text{(B.4)} \\ &= \sqrt{\frac{2I}{\hbar^2 c \epsilon_0}} \langle J_i \| e\mathbf{r} \| J_f \rangle \sum_{F_f, \mathcal{P}} c_{CG}(F_i, m_{F,\,i}, \mathcal{P}; F_f, m_{F,\,f}). && \text{(B.5)} \end{aligned}$$

We take advantage of this particular form in Chapter 6 when the preparation of dark-bright soliton is considered.

Appendix C

Determination of ensemble parameters

C.1 Bimodal density distribution of a partly condensed Bose gas

Atom-photon interaction

The rate at which mono chromatic light is scattered by one atom is given by $\Gamma_{sc} = \tilde{\Gamma}_{sc} \times I$ with

$$\tilde{\Gamma}_{sc} = \frac{\gamma}{2I_{sat}} \frac{1}{\left[1 + 4\left(\frac{\delta}{\gamma}\right)^2 + \left(\frac{\bar{I}}{I_{sat}}\right)\right]} \quad , \tag{C.1}$$

where $\bar{I}$ is the average intensity along the optical axis and $I_{sat} = (\hbar\omega^3\gamma)/(12\pi c^2)$ is the saturation intensity. The scattering rate of photons incident on the area A with a rate $R_{ph} = I\,A/(\hbar\omega_0)$ can be calculated along the infinitesimal distance Δy using the expression $\Gamma_{ph} = \tilde{\Gamma}_{sc} I n(y) A \Delta y$; where $n(y)$ is a three-dimensional density. The attenuation of the intensity by the atomic sample is therefor given by

$$\frac{d}{dy} I(y) = -\tilde{\Gamma}_{sc}\,\hbar\omega_0 n(y)\,I(y) \tag{C.2}$$

exhibiting the solution

$$\ln I_A - \ln I_0 = -\tilde{\Gamma}_{sc}\hbar\omega_0 \int dy\, n(y) \quad , \tag{C.3}$$

where I_A is the detected intensity. By definition $N^{\text{atoms}} = A \int dy\, n(y)$ and using the expression for the saturation intensity we arrive at the number of atoms per CCD pixel:

$$N^{\text{atoms}} = -\frac{A\omega_0^2\,\alpha}{6\pi c^2} \left(1 + 4\left(\frac{\delta}{\gamma}\right)^2 + \frac{\bar{I}}{I_{sat}}\right) \ln\left(\frac{N_A}{N_R}\right) \quad , \tag{C.4}$$

α is a factor which depends on the relative orientation of the quantization axis and the optical axis of the detection. For the most prominent experimental examples α has been determined using a rate equation in [103] and is only states here without comment.

perpendicular and linear Detection light that is incident perpendicular to the quantization axis defined by the magnetic field and linearly polarized $\pi^{\perp} = \pi^0$ leads to $\alpha = 0.55$.

perpendicular and circular If the light is circular polarized coming from the same direction $\sigma^{+\perp} = 1/2\,\sigma^+ - 1/\sqrt{2}\,\pi^0 + 1/2\,\sigma^-$, $\alpha = 0.47$.

parallel and linear If the light propagates along the quantization axis and is linear polarized $\pi^{\|} = 1/\sqrt{2}(\sigma^+ + \sigma^-)$ the detection coefficient amounts to $\alpha = 0.5$.

parallel and circular Finally right handed circular polarization with respect to the quantization axis σ^+ drives the cycling transition after a few scattering events and will lead $\alpha \approx 1$ for typical detection parameters ($t_{\mathrm{det}} = 40\,\mu$s, $I/I_{sat} = 0.2$, $N_{sc} \approx 300$).

Bimodal distribution

Absorption images of Bose-Einstein condensates usually contain signatures of the condensed and normal fraction. To extract the relevant parameters from the images, a bimodal distribution is fitted to the column density which accounts for the Thomas-Fermi parabolic part of the condensate and a much broader Gaussian like background following Bose statistics [102, 117]:

$$n_{tot}^{TOF}(\vec{r}) = n_{th,0}\, g_{3/2}\left(z \exp\left[\sum_{i=1}^{3} \frac{(x-x_i)^2}{\sigma_{i,th}^2}\right]\right) + n_{c,0} \max\left(1 - \sum_{i=1}^{3} \frac{(x-x_i)^2}{\sigma_{i,c}^2}, 0\right). \quad \text{(C.5)}$$

z is the fugacity $\exp(-\mu/k_{\mathrm{B}}T)$ and $g_j(z) = \sum z^i/i^j$ the Bose function [102]. The most important ensemble parameters are among position and width of the individual clouds the total particle number in the condensate and the thermal cloud, the condensate fraction and the temperature. They are given by the fit parameters of the latter equation through:

$$N_c = \frac{2\pi}{5} n_{c,0}^{2D}\, \sigma_{x,c}\, \sigma_{y,c} \quad \text{(C.6)}$$

$$N_{th} = g_3(1)\, \pi n_{th,0}^{2D}\, \sigma_{x,th}\, \sigma_{y,th} \quad \text{(C.7)}$$

$$\mathrm{F} = \frac{N_c}{N_c + N_{th}} \quad \text{(C.8)}$$

$$T = \frac{m}{2k_B}\left(\frac{\omega_i^2}{1+\omega_i^2 t^2}\sigma_{i,th}^2\right), \quad i \in \{x,y\} \quad \text{with } t : \mathrm{time-of-flight}. \quad \text{(C.9)}$$

Appendix D

Supplementary mathematical material for Spinor condensates

D.1 Representation of Projection operators

One explicit representation of the projection operators $\mathbf{P}_f$ in terms of products of spins is given by

$$F=1:\ \mathbf{P}_0=\frac{1}{3}(1-\vec{\mathbf{F}}_1\cdot\vec{\mathbf{F}}_2)\qquad \mathbf{P}_2=\frac{1}{3}(2+\vec{\mathbf{F}}_1\cdot\vec{\mathbf{F}}_2), \tag{D.1}$$

$$F=2:\ \mathbf{P}_2=\frac{1}{7}(4-\vec{\mathbf{F}}_1\cdot\vec{\mathbf{F}}_2-10\mathbf{P}_0)\qquad \mathbf{P}_4=\frac{1}{7}(3+\vec{\mathbf{F}}_1\cdot\vec{\mathbf{F}}_2+3\mathbf{P}_0). \tag{D.2}$$

D.2 Equations of motion for spinor condensates

For completeness the equations of motion [210] for the individual components of the spinor $\zeta$are cited here for reference (also compare [62] (F=1) and [211] (F=2)).

Spin equations of motion for $F=1$

$$\left.\begin{aligned} i\dot{\zeta}_{+1} &= g_1\langle n\rangle\left[+F_z\zeta_{+1}+A_1\zeta_0\right]+(-p+q)\zeta_{+1}\\ i\dot{\zeta}_{0} &= g_1\langle n\rangle\left[A_1^*\zeta_{+1}+A_1\zeta_{-1}\right]\\ i\dot{\zeta}_{-1} &= g_1\langle n\rangle\left[-F_z\zeta_{-1}+A_1^*\zeta_0\right]+(+p+q)\zeta_{-1}\end{aligned}\right\}F=1 \tag{D.3}$$

Spin equations of motion for $F = 2$

$$\left.\begin{aligned}
i\dot{\zeta}_{+2} &= \frac{g_1\langle n\rangle}{2}\left[+4F_z\zeta_{+2} + 2A_2\zeta_{+1}\right] + \frac{g_2\langle n\rangle}{2}S_0\zeta^*_{-2} + (-2p+4q)\zeta_{+2} \\
i\dot{\zeta}_{+1} &= \frac{g_1\langle n\rangle}{2}\left[+2F_z\zeta_{+1} + \sqrt{6}A_2\zeta_0 + 2A^*_2\zeta_{+2}\right] - \frac{g_2\langle n\rangle}{2}S_0\zeta^*_{-1} + (-p+q)\zeta_{+1} \\
i\dot{\zeta}_0 &= \frac{g_1\langle n\rangle}{2}\left[\sqrt{6}(A_2\zeta_{-1} + A^*_2\zeta_{+1})\right] + \frac{g_2\langle n\rangle}{2}S_0\zeta^*_0 \\
i\dot{\zeta}_{-1} &= \frac{g_1\langle n\rangle}{2}\left[-2F_z\zeta_{-1} + \sqrt{6}A^*_2\zeta_0 + 2A_2\zeta_{-2}\right] - \frac{g_2\langle n\rangle}{2}S_0\zeta^*_{+1} + (+p+q)\zeta_{-1} \\
i\dot{\zeta}_{-2} &= \frac{g_1\langle n\rangle}{2}\left[-4F_z\zeta_{-2} + 2A^*_2\zeta_{-1}\right] + \frac{g_2\langle n\rangle}{2}S_0\zeta^*_{+2} + (+2p+4q)\zeta_{-2}
\end{aligned}\right\} F = 2 \tag{D.4}$$

For reasons of readability $|A_F|^2 = \langle F_x\rangle^2 + \langle F_y\rangle^2$:

$$A_2 = 2(\zeta_{+2}\zeta^*_{+1} + \zeta^*_{-2}\zeta_{-1}) + \sqrt{6}(\zeta_{+1}\zeta^*_0 + \zeta^*_{-1}\zeta_0) \tag{D.5}$$
$$A_1 = 2(\zeta_{+1}\zeta^*_0 + \zeta^*_{-1}\zeta_0) \tag{D.6}$$

has been introduced.

D.3 Spin dependent scattering lengths and interaction parameter for ^{87}Rb

Table D.1: Theoretical results for scattering lengths and measured differences[74].

predicted scattering lengths	$F=1$	$F=2$
a_0/a_B	101.78 ± 0.2	87.93 ± 0.2
a_2/a_B	100.40 ± 0.1	91.28 ± 0.2
a_4/a_B	—	98.98 ± 0.2

measured differences	$F=1$	$F=2$
$(a_2 - a_0)/a_B$	-1.07 ± 0.09	3.51 ± 0.54
$(a_4 - a_2)/a_B$	—	6.95 ± 0.35

Table D.2: Calculated and measured coupling parameters, cited from [74]. g_2 is hard to determine: as the authors of [74] note, depending on details of the fitting procedure, even the sign of g_2 may change. $g_2 \equiv 4c_2$ when comparing values to [74].

predicted and measured coupling parameters	measured		predicted	
	$F=1$	$F=2$	$F=1$	$F=2$
$g_1/(4\pi a_B\hbar/m)$	-0.36 ± 0.04	$+0.99 \pm 0.06$	-0.46	$+1.10$
$g_2/(4\pi a_B\hbar/m)$	—	-2.12 ± 2.32	—	-0.20
$g_0/(4\pi a_B\hbar/m)$	—	—	100.86	94.58
$4\pi a_B\hbar/m = 2\pi \times 7.73 \times 10^{-14}\,\mathrm{Hz\,cm^3}$				

Bibliography

[1] C. Becker, P. Soltan-Panahi, S. Dörscher, J. Kronjäger, K. Bongs, and K. Sengstock. Mott-insulator transition in a triangular optical lattice. *to be transmitted to Phys. Rev. Lett.*

[2] S. Stellmer, C. Becker, P. Soltan-Panahi, E. M. Richter, S. Dörscher, M. Baumert, J. Kronjäger, K. Bongs, and K. Sengstock. Collisions of dark solitons in elongated bose-einstein condensates. *Phys. Rev. Lett.*, 101:202020, 2008.

[3] C. Becker, S. Stellmer, P. Soltan-Panahi, S. Dörscher, M. Baumert, E. M. Richter, J. Kronjäger, K. Bongs, and K. Sengstock. Oscillations and interactions of dark and dark-bright solitons in bose-einstein condensates. *Nature Physics*, 4:496 –501, 2008.

[4] J. Kronjäger, C. Becker, P. Navez, K. Bongs, and K. Sengstock. Magnetically Tuned Spin Dynamics Resonance. *Phys. Rev. Lett*, 97:110404, 2006.

[5] J. Kronjäger, C. Becker, M. Brinkmann, R. Walser, P. Navez, K. Bongs, and K. Sengstock. Evolution of a spinor condensate: coherent dynamics, dephasing and revivals. *Phys. Rev. A*, 72:063619, 2005.

[6] P. J. Mohr and B. N. Taylor. Codata recommended values of the fundamental physical constants: 1998. *Rev. Mod. Phys.*, 72:351, 2000.

[7] H. Schmaljohann. *Spindynamik in Bose-Einstein Kondensaten*. PhD thesis, Universität Hamburg, 2004.

[8] K. B. Davis, M. O. Mewes, M. R. Andrews, N. J. van Druten, D. S. Durfee, D. M. Kurn, and W. Ketterle. Bose-Einstein Condensation in a Gas of Sodium Atoms. *Phys. Rev. Lett.*, 75:3969, 1995.

[9] M. H. Anderson, J. R. Ensher, M. R. Matthews, C. E. Wieman, and E. A. Cornell. Observation of Bose-Einstein Condensation in a Dilute Atomic Vapor. *Science*, 269:198–201, 1995.

[10] K. W. Madison, F. Chevy, W. Wohlleben, and J. Dalibard. Vortex Formation in a Stirred Bose-Einstein Condensate. *Phys. Rev. Lett.*, 84:806, 2000.

[11] S. Burger, K. Bongs, S. Dettmer, W. Ertmer, and K. Sengstock. Dark Solitons in Bose-Einstein Condensates. *Phys. Rev. Lett.*, 83:5198 – 5201, 1999.

[12] J. Denschlag, J. E. Simsarian, D. L. Feder, C. W. Clark, L. A. Collins, J. Cubizolles, L. Deng, E. W. Hagley, K. Helmerson, W. P. Reinhardt, S. L. Rolston, B. I. Schneider, and W. W. Phillips. Generating Solitons by Phase Engeneering of a Bose-Einstein Condensate. *Science*, 287:97 –101, 2000.

[13] K. E. Strecker, G. B. Partridge, A. G. Truscott, and R. G. Hulet. Formation and propagation of matter-wave soliton trains. *Nature*, 417:150, 2002.

[14] J. Scott-Russell. Report on Waves. *Proc. Roy. Soc. Edinburgh*, page 319, 1849.

[15] N. J. Zabusky and M. D. Kruskal. Interaction Of “Solitons” In A Collisionless Plasma And The Recurrence Of Initial States. *Phys. Rev. Lett.*, 15(6):240, 1967.

[16] N.J. Zabusky. Soliton and bound states of the time-independent schrödinger equation. *Phys. Rev.*, 168(1):124, 1968.

[17] A. R. Osborne and T. L. Burch. Internal Solitons in the Andaman Sea. *Science*, 208:451 – 460, 1980.

[18] Z. Sinkalaa. Soliton/exciton transport in proteins. *J. Theor. Biology*, 241:919 –927, 2006.

[19] E. Guendelman and I. Shilon. Gravitational trapping near domain walls and stable solitons. *Phys. Rev. D*, 76:025021, 2007.

[20] Y. S. Kivshar and B. Luther-Davies. Dark optical solitons: physics and applications. *Physics Reports*, 298:81 –197, 1997.

[21] B. Anderson et al. Watching Dark Solitons Decay into Vortex Rings in a Bose-Einstein Condensate. *Phys. Rev. Lett.*, 86(14):2926–2929, 2001.

[22] L. Khaykovich, F. Schreck, G. Ferrari, T. Bourdel, J. Cubizolles, L. D. Carr, Y. Castin, and C. Salomon. Formation of a Matter-Wave Bright Soliton. *Science*, 296:1290 –1293, 2002.

[23] S.L. Cornish, S.T. Thompson, and C.E. Wieman. Formation of Bright Matter-Wave Solitons during the Collapse of Attractive Bose-Einstein Condensates. *Phys. Rev. Lett*, 96:170401, 2006.

[24] B. Eiermann et al. Dispersion Managment for Atomic Matter Waves. *Phys. Rev. Lett.*, 91:060402, 2003.

[25] B. Eiermann et al. Bright Bose-Einstein Gap Solitons of Atoms with Repulsive Interaction. *Phys. Rev. Lett.*, 92:230401, 2004.

[26] L. Salasnich, A. Parola, and L. Reatto. Condensate bright solitons under transverse confinement. *Phys. Rev. A*, 66(4):043603, Oct 2002.

[27] Th. Busch and J.R. Anglin. Motion of Dark Solitons in Trapped Bose-Einstein Condensates. *Phys. Rev. Lett*, 84(11):2298–2301, 2000.

[28] V. A. Brazhnyi and V. V. Konotop. Evolution of a dark soliton in a parabolic potential: Application to Bose-Einstein condensates. *Phys. Rev. A*, 68(4):043613, Oct 2003.

[29] V. V. Konotop and L. Pitaevskii. Landau Dynamics of a Grey Soliton in a Trapped Condensate. *Phys. Rev. Lett.*, 93(24):240403, Dec 2004.

[30] D. E. Pelinovsky, D. J. Frantzeskakis, and P. G. Kevrekidis. Oscillations of dark solitons in trapped Bose-Einstein condensates. *Physical Review E (Statistical, Nonlinear, and Soft Matter Physics)*, 72(1):016615, 2005.

[31] G. Theocharis, P. Schmelcher, M. K. Oberthaler, P. G. Kevrekidis, and D. J. Frantzeskakis. Lagrangian approach to the dynamics of dark matter-wave solitons. *Physical Review A (Atomic, Molecular, and Optical Physics)*, 72(2):023609, 2005.

[32] B. Jackson, N. P. Proukakis, and C. F. Barenghi. Dark-soliton dynamics in bose-einstein condensates at finite temperature. *Phys. Rev. A*, 75(5):051601, 2007.

[33] B. Jackson, G. M. Kavoulakis, and C. J. Pethick. Solitary waves in clouds of Bose-Einstein condensed atoms. *Phys. Rev. A*, 58(3):2417–2422, 1998.

[34] P. O. Fedichev, A. E. Muryshev, and G. V. Shlyapnikov. Dissipative dynamics of a kink state in a bose-condensed gas. *Phys. Rev. A*, 60(4):3220–3224, 1999.

[35] A. Muryshev and G. V. van Linden van den Heuvell, H. B.and Shlyapnikov. Stability of standing matter waves in a trap. *Phys. Rev. A*, 60(4):R2665–R2668, 1999.

[36] D. L. Feder, M. S. Pindzola, L. A. Collins, B. I. Schneider, and C. W. Clark. Dark-soliton states of Bose-Einstein condensates in anisotropi traps. *Phys. Rev. A*, 62:053606, 2000.

[37] A. Muryshev, G. V. Shlyapnikov, W. Ertmer, K. Sengstock, and M. Lewenstein. Dynamics of Dark Solitons in Elongated Bose-Einstein Condensates. *Phys. Rev. Lett.*, 89(11):110401, 2002.

[38] N.G. Parker, N. P. Proukakis, M. Leadbeater, and C.S. Adams. Soliton-Sound Interactions in Quasi-One-Dimensional Bose-Einstein Condensates. *Phys. Rev. Lett.*, 90(22):220401, 2003.

[39] Th. Busch and J.R. Anglin. Dark-bright solitons in inhomogeneous bose-einstein condensates. *Phys. Rev. Lett*, 87(1):010401, 2001.

[40] A. Weller, J. P. Ronzheimer, C. Gross, J. Esteve, M. K. Oberthaler, D. J. Frantzeskakis, G. Theocharis, , and P. G. Kevrekidis. Experimental Observation of Oscillating and Interacting Matter Wave Dark Solitons. *Phys. Rev. Lett.*, 101:130401, 2008.

[41] D. M. Stamper-Kurn, M. R. Andrews, A. P. Chikkatur, S. Inouye, H.-J. Miesner, J. Stenger, and W. Ketterle. Optical confinement of a Bose-Einstein condensate. *Phys. Rev. Lett.*, 80:2027, 1998.

[42] J. Stenger, S. Inouye, D. M. Stamper-Kurn, H.-J. Miesner, A. P. Chikkatur, and W. Ketterle. Spin domains in ground-state Bose-Einstein condensates. *Nature*, 396:345, 1998.

[43] H.-J. Miesner, D. M. Stamper-Kurn, J. Stenger, S. Inouye, A. P. Chikkatur, and W. Ketterle. Observation of metastable states in spinor Bose-Einstein condensates. *Phys. Rev. Lett.*, 82:2228, 1999.

[44] D. M. Stamper-Kurn, H.-J. Miesner, A. P. Chikkatur, S. Inouye, J. Stenger, and W. Ketterle. Quantum Tunneling across Spin Domains in a Bose-Einstein Condensate. *Phys. Rev. Lett.*, 83(4):661, 1999.

[45] Tin-Lun Ho. Spinor Bose condensates in optical traps. *Phys. Rev. Lett.*, 81(4):742, 1998.

[46] T. Ohmi and K. Machida. Bose-Einstein condensation with internal degrees of freedom in alkali gases. *J. Phys. Soc. Jap.*, 67:1822–1825, 1998.

[47] C. K. Law, H. Pu, and N. P. Bigelow. Quantum Spins Mixing in Spinor Bose-Einstein Condensates. *Phys. Rev. Lett.*, 81(24):5257–5261, Dec 1998.

[48] M. R. Matthews, D. S. Hall, D. S. Jin, J. R. Ensher, C. E. Wieman, E. A. Cornell, F. Dalfovo, C. Minniti, and S. Stringari. Dynamical Response of a Bose-Einstein Condensate to a Discontinuous Change in Internal State. *Phys. Rev. Lett.*, 81(2):243–247, Jul 1998.

[49] D. S. Hall, M. R. Matthews, J. R. Ensher, C. E. Wieman, and E. A. Cornell. Dynamics of component separation in a binary mixture of Bose-Einstein condensates. *Phys. Rev. Lett.*, 81:1539, 1998.

[50] H. J. Lewandowski, D. M. Harber, D. L. Whitaker, and E. A. Cornell. Observation of anomalous spin-state segregation in a trapped ultracold vapor. *Phys. Rev. Lett.*, 88:070403, 2002.

[51] M. R. Matthews, B. P. Anderson, P. C. Haljan, D. S. Hall, M. J. Holland, J. E. Williams, C. E. Wieman, and E. A. Cornell. Watching a superfluid untwist itself: Recurrence of rabi oscillations in a Bose-Einstein condensate. *Phys. Rev. Lett*, 83:3358, 1999.

[52] J. M. McGuirk, H. J. Lewandowski, D. M. Harber, T. Nikuni, J. E. Williams, and E. A. Cornell. Spatial resolution of spin waves in an ultracold gas. *Phys. Rev. Lett.*, 89:090402, 2002.

[53] H. J. Lewandowski, J. M. McGuirk, D. M. Harber, and E. A. Cornell. Decoherence-driven cooling of a degenerate spinor Bose gas. *Phys. Rev. Lett.*, 91:240404, 2003.

[54] J. M. McGuirk, D. M. Harber, H. J. Lewandowski, and E. A. Cornell. Normal-superfluid interaction dynamics in a spinor Bose gas. *Phys. Rev. Lett.*, 91:150402, 2003.

[55] D. M. Harber, H. J. Lewandowski, J. M. McGuirk, and E. A. Cornell. Effect of cold collisions on spin coherence and resonance shifts in a magnetically trapped ultracold gas. *Phys. Rev. A*, 66:053616, 2002.

[56] V. Schweikhard, I. Coddington, P. Engels, S. Tung, and E. A. Cornell. Vortex-lattice dynamics in rotating spinor Bose-Einstein Condensates. *Phys. Rev. Lett.*, 93:210403, 2004.

[57] M.-S. Chang, C. D. Hamleyand M. D. Barrett, J. A. Sauer, K. M. Fortier, W. Zhang, L. You, and M. S. Chapman. Observation of Spinor Dynamics in Optically Trapped 87Rb Bose-Einstein Condensates. *Phys. Rev. Lett.*, 92:140403, 2004.

[58] M. Erhard, H. Schmaljohann, J. Kronjäger, K. Bongs, and K. Sengstock. Bose-einstein condensation at constant temperature. *Phys. Rev. A*, 70:031602(R), 2004.

[59] H. Schmaljohann, M. Erhard, J. Kronjäger, M. Kottke, S. van Staa, L. Cacciapuoti, J. J. Arlt, K. Bongs, and K. Sengstock. Dynamics of $F = 2$ spinor Bose-Einstein condensates. *Phys. Rev. Lett.*, 92:040402, 2004.

[60] T. Kuwamoto, K. Araki, T. Eno, and T. Hirano. Magnetic field dependence of the dynamics of ^{87}Rb spin-2 Bose-Einstein condensates. *Phys. Rev. A*, 69:063604, 2004.

[61] M.-S. Chang, Q. Qin, W. Zhang, L. You, and M. S. Chapman. Coherent spinor dynamics in a spin-1 Bose condensate. *Nature Physics*, 1:111, 2005.

[62] W. Zhang, D. L. Zhou, M.-S. Chang, M.-S. Chapman, and L.You. Coherent spin mixing dynamics in a spin-1 atomic condensate. *Phys. Rev. A*, 72:013602, 2005.

[63] J. M. Higbie, L. E. Sadler, S. Inouye, A. P. Chikkatur, S. R. Leslie, K. L. Moore, V. Savalli, and D. M. Stamper-Kurn. Direct Nondestructive Imaging of Magnetization in a Spin-1 Bose-Einstein Gas. *Phys. Rev. Lett.*, 95:050401, 2005.

[64] L. E. Sadler, J. M. Higbie, S. R. Leslie, M. Vengalattore, and D. M. Stamper-Kurn. Spontaneous symmetry breaking in a quenched ferromagnetic spinor Bose-Einstein condensate. *Nature*, 443:312, 2006.

[65] M. Vengalattored, S. R. Laslie, J. Guzman, and D. M. Stamper-Kurn. Spontaneously Modulated Spin Textures in a Dipolar Spinor Bose-Einstein Condensate. *Phys. Rev. Lett.*, 100:170403, 2008.

[66] L. Santos, G. V. Shlyapnikov, P. Zoller, and M. Lewenstein. Bose-einstein condensation in trapped dipolar gases. *Phys. Rev. Lett.*, 85(9):1791–1794, Aug 2000.

[67] A. Griesmaier, J. Werner, S. Hensler, J. Stuhler, and T. Pfau. Bose-Einstein Condensation of Chromium. *Phys. Rev. Lett.*, 94:160401, 2005.

[68] J. Stuhler, A. Griesmaier, 1 M. Fattori T. Koch, T. Pfau, S. Giovanazzi, P. Pedri, and L. Santos. Observation of Dipole-Dipole Interaction in a Degenerate Quantum gas. *Phys. Rev. Lett.*, 95:150406, 2005.

[69] Axel Griesmaier, Jürgen Stuhler, Tobias Koch, Marco Fattori, Tilman Pfau, and Stefano Giovanazzi. Comparing Contact and Dipolar Interactions in a Bose-Einstein Condensate. *Physical Review Letters*, 97(25):250402, 2006.

[70] T. Koch, T. Lahaye, J. Metz, B. Frölich, and A. Griesmaierand T. Pfau. Stabilization of a purely dipolar quantum gas against collapse. *Nature Physics*, 4:218–222, 2008.

[71] J. Kronjäger. *Coherent Dynamics of Spinor Bose-Einstein Condensates.* PhD thesis, Universität Hamburg, 2007.

[72] A. Widera, F. Gerbier, S. Fölling, T. Gericke, O. Mandel, and I. Bloch. Coherent collisional spin dynamics in optical lattices. *Phys. Rev. Lett.*, 95:190405, 2005.

[73] F. Gerbier, A. Widera, S. Fölling, O. Mandel, and I. Bloch. Resonant control of spin dynamics in ultracold quantum gases by microwave dressing. *Phys. Rev. A*, 73:041602, 2006.

[74] A. Widera, F. Gerbier, S. Fölling, T. Gericke, O. Mandel, and I. Bloch. Precision measurement of spin-dependent interaction strengths for spin-1 and spin-2 ^{87}Rb atoms. *New Journal of Physics*, 8:152, 2006.

[75] A. Hemmerich and T. W. Hänsch. Two-dimensional atomic crystal bound by light. *Phys. Rev. Lett.*, 70:410, 1993.

[76] P. Verkerk, B. Lounis, C. Salomon, C. Cohen-Tannoudji, J.-Y. Courtois, and G. Grynberg. Dynamics and spatial order of cold cesium atoms in a periodic optical potential. *Phys. Rev. Lett.*, 68:3861, 1992.

[77] C. C. Bradley, C. A. Sackett, J. J. Tollett, and R. G. Hulet. Evidence of Bose-Einstein Condensation in an Atomic Gas with Attractive Interactions. *Phys. Rev. Lett.*, 75:1687, 1995.

[78] D. Jaksch, C. Bruder, J. I. Cirac, C. W. Gardiner, and P. Zoller. Cold Bosonic Atoms in Optical Lattices. *Phys. Rev. Lett.*, 81:3108–3111, 1998.

[79] M. P. A. Fisher, P. B. Weichman, G. Grinstein, and D. S. Fisher. Boson localization and the superfluid-insulator transition. *Phys. Rev. B*, 40:546–570, 1989.

[80] M. Greiner, O. Mandel, T. Esslinger, T. W. Hänsch, and I. Bloch. Quantum phase transition from a superfluid to a Mott insulator in a gas of ultracold atoms. *Nature*, 415:39–44, 2002.

[81] M. Lewenstein, A. Sanpera, V. Ahufinger, B. Damski, A. Sen, and U. Sen. Ultracold atomic gases in optical lattices: mimicking condensed matter physics and beyond. *Advances in Physics*, 56:243–379, 2007.

[82] K. I. Petsas, A. B. Coates, and G. Grynberg. Crystallography of optical lattices. *Phys. Rev. A*, 50:5173–5189, 1994.

[83] T. Calarco, U. Dorner, P. S. Julienne, C. J. Williams, and P. Zoller. Quantum computations with atoms in optical lattices: Marker qubits and molecular interactions. *Phys. Rev. A*, 70:012306, 2004.

[84] I. B. Spielman, W. D. Phillips, and J. V. Porto. Mott-insulator Transition in a Two-Dimensional Atomic Bose Gas. *Phys. Rev. Lett.*, 98:080404, 2007.

[85] I. B. Spielman, W. D. Phillips, and J. V. Porto. Condenstate Fraction in a 2d Bose Gas Measured across the Mott-Insulator Transition. *Phys. Rev. Lett.*, 100:120402, 2008.

[86] T. Stöferle, H. Moritz, C. Schori, M. Köhl, and T. Esslinger. Transition from a Strongly Interacting 1D Superfluid to a Mott Insulator. *Phys. Rev. Lett.*, 92:130403, 2004.

[87] B. Paredes, A. Widera, V. Murg, O. Mandel, S. Fölling, I. Cirac, G V. Shlyapnikov, T. W. Hänsch, and I. Bloch. Tonks-girardeau gas of ultracold atoms in an optical lattice. *Nature*, 429:281, 2004.

[88] J. J. Zirbel, K.-K. Ni, S. Ospelkaus, T. L. Nicholson, M. L. Olsen, P. S. Julienne, C. E. Wieman, J. Ye, and D. S. Jin. Heteronuclear molecules in an optical dipole trap. *Physical Review A (Atomic, Molecular, and Optical Physics)*, 78(1):013416, 2008.

[89] C. Ospelkaus, S. Ospelkaus, L. Humbert, P. Ernst, K. Sengstock, and K. Bongs. Ultracold Heteronuclear Molecules in a 3d Optical Lattice. *Physical Review Letters*, 97(12):120402, 2006.

[90] E. Altman, E. Demler, and M. D. Lukin. Probing many-body states of ultracold atoms via noise correlations. *Phys. Rev. A*, 70:013603, 2004.

[91] L.-M. Dua. Detecting Correlation Functions of Ultracold Atoms through Fourier Sampling of Time-of-Flight Images. *Phys. Rev. Lett.*, 96:103201, 2006.

[92] V. Gritsev, E. Altman, E. Demler, and A. Polkovnikov. Full quantum distribution of contrast in interference experiments between interacting one-dimensional Bose liquids. *Nature Physics*, 2:705–709, 2006.

[93] C. Zhang, V. W. Scarola, and S. Das Sarma. Probing n-spin correlations in optical lattices. *Phys. Rev. A*, 76:023605, 2007.

[94] S. Fölling, F. Gerbier, A. Widera, O. Mandel, T. Gericke, and I. Bloch. Spatial quantum noise interferometry in expanding ultracold atom clouds. *Nature*, 434:481–484, 2005.

[95] T. Rom, Th. Best, D. van Oosten, U. Schneidera, S. FÖlling, B. Paredes, and I. Bloch. Free fermion antibunching in a degenerate atomic Fermi gas released from an optical lattice. *Nature*, 444:733–736, 2006.

[96] M. Greiner, C. A. Regal, J. T. Stewart, and D. S. Jin. Probing Pair-Correlated Fermionic Atoms through Correlations in Atom Shot Noise. *Phys. Rev. Lett.*, 94:110401, 2005.

[97] S. Wessel and M. Troyer. Supersolid Hard-Core Bosons on the Triangular Lattice. *Phys. Rev. Lett.*, 95:127205, 2005.

[98] R. G. Melko, A. Paramekanti, A. A. Burkov, A. Vishwanath, D. N. Sheng, and L. Barents. Supersolid Order from Disorder: Hard-Core Bosons on the Triangular Lattices. *Phys. Rev. Lett.*, 95:127207, 2005.

[99] S. R. Hassan, L. de Medici, and A.-M. S. Tremblay. Supersolidity, entropy, and frustration: t-t[sup [prime]]-v model of hard-core bosons on the triangular lattice. *Physical Review B (Condensed Matter and Materials Physics)*, 76(14):144420, 2007.

[100] C. Wu, W. V. Liu, J. Moore, and S. Das Sarma. Quantum Stripe Ordering in Optical Lattices. *Phys. Rev. Lett.*, 97:190406, 2006.

[101] L. Mathey, S.-W. Tsai, and A. H. Neto. Exotic superconducting phases of ulracold atom mixtures on triangular lattices. *Phys. Rev. b*, 75:174516, 2007.

[102] L. Pitaevskii and S. Stringari. *Bose-Einstein Condensation.* Oxford Science Publications, 1. edition, 2003.

[103] M. Erhard. *Experimente mit mehrkomponentigen Bose-Einstein-Kondensaten.* PhD thesis, Universität Hamburg, 2004.

[104] H. J. Metcalf and P. van der Straten. *Laser Cooling and Trapping.* Springer, 2. edition, 2002.

[105] C. Cohen-Tannoudji and J. Dupont-Roc. Experimental Study of Zeeman Light Shifts in Weak Magnetic Fields. *Phys. Rev. A*, 5:968–984, 1972.

[106] I. H. Deutsch and P. S.Jessen. Quantum-state control in optical lattices. *Phys. Rev. A*, 57:1972–1986, 1998.

[107] L. Santos, M. Fattori, J. Stuhler, and T. Pfau. Spinor condensates with a laser-induced quadratic Zeeman effect. *Phys. Rev. A*, 75:053606, 2007.

[108] F. Gerbier, A. Widera, S. Fölling, O. Mandel, T. Gericke, and I. Bloch. Phase Coherence of an Atomic Mott Insulator. *Phys. Rev. Lett.*, 95:050404, 2005.

[109] D. A. Steck. Rubidium 87 D Line Data, 2004.

[110] R. Grimm, M. Weidemüller, and Y. B. Ovchinnikov. Optical Dipole Traps For Neutral Atoms. *arXiv:physics*, (9902072), 1999.

[111] A. E. Siegman. *Lasers.* University Science Books, 1. edition, 1986.

[112] S. A. Self. Focusing of spherical Gaussian beams. *App. Opt.*, 22:658, 1983.

[113] P. Belland and J. P. Crenn. Changes in the characteristics of a Gaussian beam weakly diffracted by a circular aperture. *App. Opt.*, 21:522, 1982.

[114] T. A. Savard, K. M. O'Hara, and J. E. Thomas. Laser-noise-induced heating in far-off resonant optical traps. *Phys. Rev. A*, 56:R1095–1098, 1997.

[115] J. Kronjäger. Accurate tilt control of optical tables and applications, 2008.

[116] N. Poli, R. J. Brecha, G. Roati, and G. Modugno. Cooling atoms in an optical trap by selective parametric excitation. *Phys. Rev. A*, 65:021401(R), 2002.

[117] W. Ketterle, D. S. Durfee, and D. M. Stamper-Kurn. Making, probing and understanding Bose-Einstein condensates. In M. Inguscio, S. Stringari, and C. E. Wieman, editors, *Proceedings of the International School of Physics - Enrico Fermi*, page 67. IOS Press, 1999.

[118] L. T. Turner, K. F. E. M. Domen, and R. E. Scholten. Diffraction-contrast imaging of cold atoms. *Phys. Rev. A*, 72:031403(R), 2005.

[119] Martin Brinkmann. Optimierung der Detektion und Auswertung von ^{87}Rb-Spinor-Kondensaten. Diplomarbeit, Universität Hamburg, 2005.

[120] Lars Neumann. Hochauflösende Detektion von Bose-Einstein Kondensaten. Diplomarbeit, Universität Hamburg, 2006.

[121] I. N. Bronstein, K. A. Semendjajew, G. Musiol, and H. Mühlig. *Taschenbuch der Mathematik.* Verlag Harri Deutsch, 3 edition, 1996.

[122] K. Eckert, L. Zawitschowski, A. Sanpera, M. Lewewnstein, and E. S. Polzik. Quantum Polarization Spectroscopy of Ultracold Spinor Gases. *Phys. Rev. Lett.*, 98:100404, 2007.

[123] Y. Takahashi, K. Honda, N. Tanaka, K. Toyoda, K. Ishikawa, and T. Yabuzaki. Quantum nondemolition measurement of spin via the paramagnetic faraday rotation. *Phys. Rev. A*, 60(6):4974–4979, Dec 1999.

[124] I. Carusotto and E. J. Mueller. Imaging of spinor gases. *J. Phys. B*, 37:S115–S125, 2004.

[125] G. Klose, G. Smith, and P. S. Jessen. Measuring the quantum state of a large angular momentum. *Phys. Rev. Lett.*, 86(21):4721–4724, May 2001.

[126] H. F. Hofmann and S. Takeuchi. Quantum-State tomography for spin-l systems. *Phys. Rev. A*, 69:042108, 2004.

[127] Wikipedia. Erdmagnetfeld — wikipedia, die freie enzyklopädie, 2007. [Online; Stand 22. Mai 2007].

[128] L. M. K. Vandersypen and I. L. Chuang. MR techniques for quantum control and computation. *Rev. Mod. Phys.*, 76:1037 – 1069, 2005.

[129] C. C. Gerry and J. H. Eberly. Dynamics of Raman coupled model interacting with two quantized cavity fields. *Phys. Rev. A*, 42:6805 – 6815, 1900.

[130] M. Albiez, R. Gati, J. Fölling, S. Hunsmann, M. Cristiani, and M. K. Oberthaler. Direct Observation of Tunneling and Nonlinear Self-Trapping in a Single Bosonic Josephson Junction. *Phys. Rev. Lett.*, 95:010402, 2005.

[131] S. Trotzky, P. Cheinet, S. Fölling, M. Feld, U. Schnorrberger, A. M. Rey, A. Polkovnikov, E. A. Demler, M. D. Lukin, and I. Bloch. Time-Resolved Observation and Control of Superexchange Interactions with Ultracold Atoms in Optical Lattices. *Science*, 319:295–299, 2007.

[132] V. Boyer, M. Godun, G. Smirne, D. Cassettari, C.M. Chandrashekar, A.B. Deb, Z.J. Laczik, and C.J. Foot. Dynamic manipulation of bose-einstein condensates with a spatial light modulator. *Phys. Rev. A*, 73:031402, 2006.

[133] Simon Stellmer. Solitonen in mehrkomponentigen Bose-Einstein Kondensaten. Diplomarbeit, Universität Hamburg, 2008.

[134] Ł. Dobrek et al. Optical generation of vortices in trapped bose-einstein condensates. *Phys. Rev. A*, 60(5):R3381–R3384, 1999.

[135] J. Stenger, S. Inouye, A. P. Chikkatur, D. M. Stamper-Kurn, A. P. Chikkatur, and W. Ketterle. Bragg Spectroscopy of a Bose-Einstein Condensate. *Phys. Rev. Lett.*, 82:4569, 1999.

[136] E. W. Hagley, L. Deng, M. Kozuma, M. Trippenbach, Y. B. Band, M. Edwards, M. Doery, P. S. Julienne, K. Helmerson, S. L. Rolston, and W. D. Phillips. Measurement of the Coherence of a Bose-Einstein Condensate. *Phys. Rev. Lett.*, 83:3112, 1999.

[137] K. Bongs, S. Burger, D. Hellweg, M. Kottke, S. Dettmer, T. Rinkleff, L. Cacciapuoti, J. Arlt, K. Sengstock, and W. Ertmer. Spectroscopy of dark soliton states in Bose-Einstein condensates. *Journal of Optics B: Quantum and Semiclassical Optics*, 5(2):S124–S130, 2003.

[138] Thomas Garl. Aufbau eines Bragg-Lasersystems fur Kohärenzuntersuchungen an Spinor-Bose-Einstein Kondensaten. Diplomarbeit, Universität Hamburg, 2004.

[139] Mathis Baumert. Schemata zur Manipulation von Bose-Einstein Kondensaten mit Laserlicht. Diplomarbeit, Universität Hamburg, 2008.

[140] R. W. P. Drever, J. L. Hall, F. V.Kowalski, J. Hough, G. M. Ford, A. J. Munley, and H. Ward. Laser Phase and Frequency Stabilization Using an Optical Resonator. *Appl. Phys. B*, 31:97–105, 1983.

[141] Sebastian Schnelle. Aufbau eines optischen Gitters für ein ^{87}Rb Spinor-Bose-Einstein-Kondensat. Diplomarbeit, Universität Hamburg, 2006.

[142] H. C. Lefevre. Single-Mode Fibre Fractional Wave Devices And Polarisation Controllers. *Electronics Letters*, 16:778–780, 1980.

[143] M. Prevedelli, T. Freegarde, and T. W. Hänsch. Phase locking of grating-tuned diode lasers. *Appl. Phys. B*, 60:S241–S248, 1995.

[144] C. J. Pethick and H. Smith. *Bose-Einstein Condensation in Dilute Gases*. Cambridge University Press, 2002.

[145] C. J. Myatt, E. A. Burt, R. W. Christ, E. A. Cornell, and C. E. Wieman. Production of two overlapping Bose-Einstein condensates by sympathetic cooling. *Phys. Rev. Lett.*, 78:586, 1997.

[146] D. S. Hall, M. R. Matthews, C. E. Wieman, and E. A. Cornell. Measurement of relative phase in two-component Bose-Einstein condensates. *Phys. Rev. Lett.*, 81:1543, 1998.

[147] T. Mayer-Kuckuk. *Atomphysik*. Teubner Verlag, 5 edition, 2007.

[148] I. I. Rabi. Space quantization in a gyrating magnetic field. *Phys. Rev.*, 51:652–654, 1937.

[149] G. Lindblad. On the Generators of Quantum Dynamical Semigroups. *Comm. Math. Phys.*, 48:119–130, 1976.

[150] C. V. Ciobanu, S.-K. Yip, and Tin-Lun Ho. Phase diagrams of F=2 spinor Bose-Einstein condensates. *Phys. Rev. A*, 61:033607, 2000.

[151] D.M. Stamper-Kurn and W. Ketterle. Spinor condensates and light scattering from Bose-Einstein condensates. In R. Kaiser, C. Westbrook, and F. David, editors, *Coherent Atomic Matter Waves, Les Houches Summer School Session LXXII in 1999*, page 137, New York, 2001. Springer.

[152] M. Erhard, H. Schmaljohann, J. Kronjäger, K. Bongs, and K. Sengstock. Measurement of a mixed-spin-channel feshbach resonance in ^{87}Rb. *Phys. Rev. A*, 69:032705, 2004.

[153] J. Kronjäger, C. Becker, K. Bongs, and K. Sengstock. To be published.

[154] N. W. Ashcroft and N. D. Mermin. *Solid State Physics*. Saunders College Publications, 1 edition, 1976.

[155] J. Mun, P. Medley, G. K. Campbell, L. G. Marcassa, D. E. Pritchard, and W. Ketterle. Phase Diagram for a Bose-Einstein Condensate Moving in an Optical Lattice. *Phys. Rev. Lett.*, 99:150604, 2007.

[156] M. Greiner. *Ultracold quantum gases in three-dimensional optical lattice potentials*. PhD thesis, Ludwigs-Maximilians-Universität München, 2003.

[157] F. Gerbier, S. Trotzky, S. Fölling, U. Schnorrberger, J. D. Thompson, A. Widera I. Bloch, L. Pollet, M. Troyer, B. Capogrosso-Sansone, N. V. Prokof'ev, and B. V. Svistunov. Expansion of a Quantum Gas Released from an Optical Lattice. *PRL*, 101:155303, 2008.

[158] F. Gerbier, A. Widera, S. Fölling, O. Mandel, T. Gericke, and I. Bloch. Interfernce pattern and visibility of a Mott insulator. *Phys. Rev. A*, 72:053606, 2005.

[159] V. A. Kashurnikov, N. V. Prokof'ev, and B. V. Svistunov. Revealing the superfluid-Mott-insulator transition in an optical lattice. *Phys. Rev. A*, 66:031601, 2002.

[160] P. Pedri, L. Pitaevskii, S. Stringari, C. Fort, S. Burger, F. S. Cataliotti, P. Maddaloni, F. Minardi, and M. Inguscio. Expansion of a Coherent Array of Bose-Einstein Condensates. *Phys. Rev. Lett.*, 87:220401, 2001.

[161] Yu. B. Ovchinnikov, J. H. Müller, M. R. Doery, E. J. D. Vredenbregt, K. Helmerson, S. L. Rolston, and W. D. Phillips. Diffraction of a released bose-einstein condensate by a pulsed standing light wave. *Phys. Rev. Lett.*, 83(2):284–287, Jul 1999.

[162] R. Jáuregui, N. Poli, G. Roati, and G. Modugno. Anharmonic parametric excitation in optical lattices. *Phys. Rev. A*, 64:033403, 2001.

[163] R. Roth and K. Burnett. Superfluidity and interference pattern of ultracold atoms in optical lattices. *Phys. Rev. A*, 67:031602, 2003.

[164] W. Yi, G.-D. Lin, and L.-M. Duan. Signal of Bose-Einstein condensation in an optical lattice at finite temperature. *Phys. Rev. A*, 76:031602, 2007.

[165] S. Fölling, A. Widera, T. Müller, F. Gerbier, and I. Bloch. Formation of Spatial Shell Structure in the Superfluid to Mott Insulator Transition. *Phys. Rev. Lett.*, 97:060403, 2006.

[166] D. van Oosten, P. van der Straten, and H. T. C. Stoof. Quantum phases in an optical lattice. *Phys. Rev. A*, 63:053601, 2001.

[167] K. Sengupta and N. Dupuis. Mott-insulator-to-superfluid transition in the Bose-Hubbard model: A strong coupling approach. *Phys. Rev. A*, 71:033629, 2005.

[168] J. K. Freericks and H. Monien. Strong-coupling expansions for the pure and disordered Bose-Hubbard model. *Phys. Rev. A*, 53:2691–2700, 1996.

[169] S. Wessels, F. Alet, M. Troyer, and G. G. Batrouni. Quantum Monte Carlo simulations of confined bosonic atoms in optical lattices. *Phys. Rev. A*, 70:053615, 2004.

[170] B. Capogrosso-Sansone, N. V. Prokof'ev, and B. V. Svistunov. Phase diagramm and thermodynamics of the three-dimensional Bose-Hubbard model. *Phys. Rev. B*, 75:134202, 2007.

[171] B. DeMarco, C. Lannert, S. Vishveshwara, and T.-C Wei. Structure and stability of Mott-insulator shells of bosons trapped in an optical lattice. *Phys. Rev. A*, 71:063601, 2005.

[172] K. Mitra, C. J. Williams, and C. A. R. Sa de Melo. Superfluid and Mott-insulating shells of bosons in harmonically confined optical lattices. *Phys. Rev. A*, 77:033607, 2008.

[173] P. B. Blakie and J. V. Porto. Adiabatic loading of bosons into optical lattices. *Phys. Rev. A*, 69:013603, 2004.

[174] G. Pupillo, C. J. Williams, and N. V. Prokof'ev. Effects of finite temperature on the Mott-insulator state. *Phys. Rev. A*, 73:013408, 2006.

[175] A. M. Rey, G. Pupillo, and J. V. Porto. The role of interactions, tunneling, and harmonic confinement on the adiabatic loading of bosons in an optical lattice. *Phys. Rev. A*, 73:023608, 2006.

[176] F. Gerbier. Boson Mott Insulators at Finite Temperatures. *Phys. Rev. Lett.*, 99:120405, 2007.

[177] T.-L. Ho and Q. Zhou. Intrinsic Heating and Cooling in Adiabatic Processes for Bosons in Optical Lattices. *Phys. Rev. Lett.*, 99:120404, 2007.

[178] D. B. M. Dickerscheid, D. van Oosten, P. J. H. Denteneer, and H. T. C. Stoof. Ultracold atoms in optical lattices. *Phys. Rev. A*, 68:043623, 2003.

[179] R. B. Diener, Q. Zhou, H. Zhai, and T.-L-Ho. Criterion for Bosonic Suprfluidity in an Optical Lattice. *Phys. Rev. Lett.*, 98:180404, 2007.

[180] Y. Kato, Q. Zhou, N. Kawashima, and N. Trivedi. Sharp peaks in the momentum distribution of bosons in optical lattices in the normal state. *Nature Physics*, 4:617–621, 2008.

[181] T. Gericke, F. Gerbier, A. Widera, S. Fölling, O. Mandel, and I. Bloch. Adiabatic loading of a bose-einstein condensate in a 3d optical lattice. *arXiv:cond-mat*, page 0603590, 2006.

[182] D. Jaksch, V. Venturi, J. I. Cirac, C. J. Williams, and P. Zoller. Creation of a Molecular Condensate by Dynamically Melting a Mott Insulator. *Phys. Rev. Lett.*, 89:040202, 2002.

[183] P. Kruger, Z. Hadzibabic, and J. Dalibard. Critical Point of an Interacting Two-Dimensional Atomic Bose Gas. *Phys. Rev. Lett.*, 99:040402, 2007.

[184] N. Elstner and H. Monien. A numerical exact solution of the Bose-Hubbard model. *arXiv:cond-mat*, page 9905367, 1999.

[185] G. K. Campbell, J. Mun, M. Boyd, P. Medley, A. E. Leonhardt, L. G. Marcassa, D. E. Pritchard, and W. Ketterle. Imaging the Mott Insulator Shells by Using Atomic Clock Shifts. *science*, 313:649–652, 2006.

[186] R. Hanburry Brown and Twiss R. Q. Correlation between Photons in two Coherent Beams of Light. *Nature*, 177:27–29, 1956.

[187] R. Hanburry Brown and Twiss R. Q. A Test of a New Type of Stellar Interferometer on Sirius. *Nature*, 178:1046–1048, 1956.

[188] Sören Dörscher. Dynamik von Solitonen und Korrelationsanalyse in Quantengasen. Diplomarbeit, Universität Hamburg, 2008.

[189] D.-S. Lühmann, K. Bongs, K. Sengstock, and D. Pfannkuche. Self-Trapping of Bosons and Fermions in Optical Lattices. *Phys. Rev. Lett.*, 101:050402, 2008.

[190] J. Heinze. private communication.

[191] E. Zaremba. Sound propagation in a cylindrical Bose-condensed gas. *Phys. Rev. A*, 57(1):518–521, Jan 1998.

[192] M. R. Andrews, D. M. Kurn, H.-J. Miesner, D. S. Durfee, C. G. Townsend, S. Inouye, , and W. Ketterle. Propagation of Sound in a Bose-Einstein Condensate. *Phys. Rev. Lett.*, 79:553, 1997a.

[193] E. A. Donley, N. R. Claussen, S. L. Cornish, J. L. Roberts, E. A. Cornell, and C. E. Wieman. Dynamics of collapsing and exploding Bose-Einstein condensates. *Nature*, 412:295, 2001.

[194] T. Tsuzuki. Nonlinear Waves in the Pitaevskii-Gross Equation. *J. Low Temp. Phys.*, 4:441–457, 1971.

[195] V.E. Zakharov and A.B. Shabat. Interaction between solitons in a stable medium. *Soviet Physics JETP*, 37(5):823, 1973.

[196] G. Theocharis, P.G. Kevrekidis, and D.J. Oberthaler, M. K. andFrantzeskakis. Dark matter-wave solitons in the dimensionality crossover. *Phys. Rev. A*, 76:045601, 2007.

[197] A. Dreischuh, D. N. Neshev, D. E. Petersen, O. Bang, and W. Krolikowski. Observation of Attraction between Dark Solitons. *Phys. Rev. Lett.*, 96:043901, 2006.

[198] G. A. Swartzlander, D. R. Andersen, J. J. Regan, H. Yin, and A. E. Kaplan. Spatial dark-soliton stripes and grids in self-defocusing materials. *Phys. Rev. Lett.*, 66:1583, 1991.

[199] D. Foursa and P. Emplit. Investigation of Black-Gray Soliton Interaction. *Phys. Rev. Lett.*, 77(19):4011–4014, 1996.

[200] Y. S. Kivshar and W. Krolikowski. Lagrangian approach for dark solitons. *Opt. Commun.*, 114:353 – 362, 1995.

[201] Eva-Maria Richter. Simulation der Dynamik mehrkomponentiger Bose-Einstein Kondensate. Diplomarbeit, Universität Hamburg, 2008.

[202] V. E. Zakharov and A. B. Shabat. Interaction between solitons in a stable medium. *Soviet Physics JETP*, 37:823, 1973.

[203] G. Huang, M. G. Velarde, and V. A. Makarov. Dark solitons and their head-on collisions in bose-einstein condensates. *Phys. Rev. A*, 64(1):013617, 2001.

[204] S. Burger, L. D. Carr, P. Ölberg, K. Sengstock, and A. Sanpera. Generation and interaction of solitons in Bose-Einstein condensates. *Phys. Rev. A*, 65:043611, 2002.

[205] L. D. Carr, J Brand, S. Burger, and A. Sanpera. Dark-soliton creation in Bose-Einstein condensates. *Phys. Rev. A*, 63:051601, 2001.

[206] P. Engels and C. Atherton. Stationary and Nonstationary Fluid Flow of a Bose-Einstein Condensate Through a Penetrable Barrier. *Phys. Rev. Lett.*, 99:160405, 2007.

[207] G.-B. Jo, J.-H. Choi, C. A. Christensen, T. A. Pasquini, Y.-R. Lee, W. Ketterle, and D. E. Pritchard. Phase-Sensitive Recombination of Two Bose-Einstein Condensates on an Atom Chip. *Phys. Rev. Lett.*, 98:180401, 2007.

[208] R. Dum, J. I. Cirac, M. Lewenstein, and P. Zoller. Creation of Dark solitons and Vortices in Bose-Einstein Condensates. *Phys. Rev. Lett.*, 80(14):2972–2975, 1998.

[209] W. Zhang, Ö. E. Müstecaplioglu, and L.You. Solitons ina trapped spin-1 atomic condensate. *Phys. Rev. A.*, 75:043601, 2007.

[210] P. Navez. private communication.

[211] H. Saito and M. Ueda. Diagnostics for the ground-state phase of a spin-2 Bose-Einstein condensate. *Phys. Rev. A*, 72:053628, 2005.

Danksagung

Die Durchführung dieser Doktorarbeit und aller damit verbundenen kleinen und großen Projekte wäre ohne die tatkräftige Unterstüzung vieler hilfsbereiter Menschen nicht möglich gewesen. Ich schätze mich glücklich in einer Arbeitsgruppe mitgewirkt zu haben, innerhalb derer einerseits immenses fachliches Wissen und andererseits viel Zwischenmenschliches zum Tragen kamen und möchte hiermit allen Mitgliedern der Arbeitsgruppe Sengstock herzlich für ihre Unterstützung danken. Einigen, im Folgenden genannten Personen gilt besonderer Dank.

Als erstes möchte ich mich bei Klaus Sengstock bedanken, der es mir ermöglicht hat, meine Doktorarbeit in seiner Arbeitsgruppe anzufertigen. Er fand stets eine gesunde Mischung aus Unterstützung, Lob und dem Einfordern von Ergebnissen um das Beste aus unserem kleinen Team herauszukitzeln. Außerdem sei ihm für den stets gesicherten finanziellen Rückhalt für Doktorand und Projekt gedankt. Seine besondere Rücksichtnahme in Zeiten schwerer privater Probleme rechne ich ihm sehr hoch an.
Kai Bongs danke ich für ein stets – und damit meine ich wirklich stets – offenes Ohr für Probleme jeglicher Art und sein besonderes Interesse und seine Unterstützung bei der Verschriftlichung unserer Ergebnisse.
Ein ganz besonderer Dank geht selbstverständlich an meinen langjährigen Senior-Mitdoktoranden und Weggefährten Jochen Kronjäger. So ziemlich alles über gute experimentelle Arbeitsweise habe ich mir in all den gemeinsamen Jahren von ihm abschauen können. Mit schier unendlicher Geduld hat er versucht mir die Geheimnisse der Elektronik näher zu bringen. Gewisse Teilerfolge blieben nicht aus. Die gemeinsamen Diskussionen über unser Experiment haben in den entscheidenden Situationen meistens dazu geführt, dass ich das Richtige getan habe.
Meinen anderen Mitdoktoranden, Holger Schmaljohann, Michael Erhard und Parvis Soltan-Panahi danke ich ebenfalls für eine stets fruchtbare Zusammenarbeit. Darüber hinaus freue ich mich, dass Holger und mich seitdem eine zuverlässige, weit über Physik hinausgehende Freundschaft verbindet und er damals maßgeblich dafür gesorgt hat, dass ich mich von Anfang an in der Arbeitsgruppe wohlgefühlt habe. . All 'meinen' Diplomanden, Thomas Garl, Martin Brinkmann, Lars Neumann, Sebastian Schnelle, Simon Stellmer, Sören Dörscher, Mathis Baumert und später, schon nach meiner Zeit, Julian Struck, danke ich für ein stets sehr angenehmes Arbeitsklima. Darüber hinaus danke ich Simon and insbesondere Sören für eine weit mehr als selbstverständliche Unterstützung bei den Messungen und der Erstellung der Ergebnisse zur Dynamik von Solitonen. Mit Sebastian und Thomas verband mich auch über die Arbeit hinaus ein freundschaftliches Verhältnis. Auch Eva-Maria Richter möchte ich danken; dafür, dass sie stets mit Eifer bereit war, alle von mir zurechtgedachten Solitonen-Szenarien ohne Umschweife mit ihren Simulationen zu be- oder auch zu widerlegen.
Allen Leuten von KRb a.k.a. BFM insbesondere Phillip Ernst, Sören Götze und Leif Humbert sei für das freundschafttliche Klima auch nach Feierabend ausführlich gedankt.
Insbesondere möchte ich allen technischen Mitarbeitern des Instituts danken, exemplarisch sei Reinhard Mielck genannt, der mir immer mit Rat und Tat zur Seite stand, wenn es irgendwas auszutüfteln gab. Der Werkstatt im Standort Bahrenfeld danke ich ebenfalls für das erfrischende Maß an Normalität, welches die Zusammenarbeit stets mit sich brachte und natürlich auch für die unzähligen kleinen und großen Dinge, die sie im Laufe dieser

Arbeit in beeindruckender Perfektion gebaut haben.
Werner Neuhauser danke ich herzlich für die Übernahme des Zweitgutachtens.
Für das fleissige Korrekturlesen sei Sören Dörscher, Sören Götze und Parvis Soltan-Panahi gedankt.

Mehr als anderen gilt mein Dank meiner Familie und meinen besten Freunden. Insbesondere meine Eltern, meine Frau und seit einem Jahr auch meine Tochter mussten viel ertragen und auf Vieles verzichten, damit diese Arbeit entstehen konnte. Der Dank dafür kann schlecht in Worte gefasst werden.